

A NEW MID-INFRARED CAMERA FOR GROUND-BASED ASTRONOMY
AND AN INFRARED STUDY OF PLANETARY NEBULAE

by

Joseph Lee Hora

Copyright © by Joseph Lee Hora 1991

A Dissertation Submitted to the Faculty of the
DEPARTMENT OF ASTRONOMY
In Partial Fulfillment of the Requirements
For the Degree of
DOCTOR OF
PHILOSOPHY
In the Graduate College
THE UNIVERSITY OF ARIZONA

1 9 9 1

THE UNIVERSITY OF ARIZONA
GRADUATE COLLEGE

As members of the Final Examination Committee, we certify that we have read
the dissertation prepared by Joseph Lee Hora

entitled A New Mid-Infrared Camera for Ground-Based Astronomy
and An Infrared Study of Planetary Nebulae

and recommend that it be accepted as fulfilling the dissertation requirement
for the Degree of Doctor of Philosophy

<u>William F. Hoffmann</u> William F. Hoffmann	<u>9/17/91</u> Date
<u>John H. Biegling</u> John Biegling	<u>9/17/91</u> Date
<u>John Black</u> John Black	<u>9/17/91</u> Date
<u>James W. Liebert</u> James Liebert	<u>9/17/91</u> Date
<u>Marcia Rieke</u> Marcia Rieke	<u>9/17/91</u> Date

Final approval and acceptance of this dissertation is contingent upon the
candidate's submission of the final copy of the dissertation to the Graduate
College.

I hereby certify that I have read this dissertation prepared under my
direction and recommend that it be accepted as fulfilling the dissertation
requirement.

<u>William F. Hoffmann</u> Dissertation Director William F. Hoffmann	<u>9/27/91</u> Date
---	------------------------

STATEMENT BY AUTHOR

This dissertation has been submitted in partial fulfillment of requirements for an advanced degree at The University of Arizona and is deposited in the University Library to be made available to borrowers under the rules of the Library.

Brief quotations from this dissertation are allowable without special permission, provided that accurate acknowledgement of source is made. Requests for permission for extended quotation from or reproduction of this manuscript in whole or in part may be granted by the copyright holder.

SIGNED: _____

ACKNOWLEDGEMENTS

First, I want to thank all those who made this project possible by their support. The institutions listed in Appendix 1 and the grants provided the financial assistance that made this research possible. Our remote collaborators, Giovanni Fazio, Kandi Shivanandan, and Lynne Deutsch also had a major role in the results reported here, and I thank them for their contributions and assistance in preparing this dissertation. Lynne, you had your revenge on me for all the pesky comments that I sent you for your thesis. Your input was just what I needed, however, and it was a great help. Also, thanks for taking over proposing and observing the past few months while I have been writing.

The graduate students of Steward have been great friends the years that I have been here, and made coming to the desert from the frozen North an enjoyable experience. You know who you are-- the 10K racers, the Bratfesters, the Protostars (and EasyScores), and socialites of the observatory. My former class- and office-mate Tom Greene introduced me to the Gun Club and other fine music, and I am forever in your debt. Thanks to Joe and Karen Haller who have been great friends to us here.

I want to express my appreciation to my advisor, Bill Hoffmann, for the source of knowledge, guidance, and support that he has been to me over the past years. His encouragement of my work and commitment to whatever project we would undertake was inspiring, and has made the time I have spent here enjoyable. I could not have had a better advisor and colleague.

My parents have encouraged and assisted me constantly throughout my life, but especially in attaining this degree. Their belief in me has helped during times when I have doubted my own abilities, and they have helped out in many times of need. They had no idea that when they bought me my first telescope I would become an astronomer, but they have always helped me pursue my goals.

Finally, I want to thank my wife, Penny, who has patiently waited for me to finish school and to get a real job. That, of course, will not happen since I will work in astronomy, but at least I will be compensated properly. Without her help I could not have worked so hard for so long.

TABLE OF CONTENTS

LIST OF ILLUSTRATIONS	12
LIST OF TABLES	17
ABSTRACT	19
 PART 1: THE MID-INFRARED ARRAY CAMERA	 21
1.1 Introduction	21
1.1.1 MIRAC program goals	22
1.1.2 Astronomical Applications	23
1.1.3 Definitions of terms	26
1.2 MIRAC Dewar and components	28
1.2.1 Cryostat	28
1.2.2 Optics	31
1.2.3 Electric wiring, connections	35
1.2.4 Actuators, Filter Motors and Control	37

	6
1.3 Detector	41
1.3.1 General description	41
1.3.2 Array Format and Packaging	43
1.3.3 The CRC-444A Readout	44
1.4 Electronics	48
1.4.1 Detector Bias Supplies	49
1.4.2 Preamplifier	50
1.4.3 Digital Controller	51
1.4.3.1 Timing, addressing	52
1.4.3.2 Controller and processor timing	54
1.4.3.3 Controller logic	56
1.4.4 Signal Processor (SP)	58
1.4.4.1 Analog Section	58
1.4.4.2 A/D Sample Modes	59
1.4.4.3 Fast Coadder	61
1.4.4.4 FIFO Memory	62
1.4.5 Command and Data Link to	63
1.4.6 Temperature Controller	66
1.4.6.1 Temperature Controller Operation and Test Results	67
1.4.6.2 Temperature Controller Performance	70
1.4.7 Power Supply and Grounding	72
1.4.7.1 Power Supply	72

	7
1.4.7.2 Grounding	75
1.5 MIRAC Computer and Interface	76
1.5.1 Data and Command Interface/Local Controller	76
1.5.2 Array Processor Board (APB)	76
1.5.3 MIRAC PC Control Program	79
1.5.3.1 MIRAC Program Structure	80
1.5.3.2 MIRAC Data Files	83
1.5.3.3 Telescope Control	84
1.5.3.4 Image Display and Processing	86
1.6 Guider Box	88
1.6.1 Optics - Dichroic, Optical Flats	88
1.6.2 Mechanical Coupling of Dewar and Box to Telescope	90
1.6.3 TV Guider Port	91
1.7 MIRAC Test Results and Performance Evaluation	92
1.7.1 Initial Tests, Corrections to Reduce Noise	92
1.7.2 Background Measurements Using Calibrated Detector	97
1.7.3 Optimization of MIRAC Detector	97
1.7.4 Performance Results: Noise, Sensitivity	102
1.7.5 Standard Star Observations, Calibration	106
1.7.6 Sky Noise and Chop Frequency	113
1.7.7 Optics Alignment and Evaluation	114

	8
1.8 Future Directions	119
1.8.1 Future Detectors	119
1.8.2 High Spectral Resolution Imaging	120
1.8.3 Fast Shift and Coadd	122
FIGURES-PART 1	124
 PART 2. AN INFRARED STUDY OF PLANETARY NEBULAE	 177
2.1 Introduction	177
2.1.1 Planetary Nebulae Formation, Structure	179
2.1.2 Infrared Emission from Planetary Nebulae	184
2.1.3 The Planetary Nebulae in This Study	186
2.1.4 Observing Procedures and Data Reduction	191
2.1.4.1 Near-IR Observations	191
2.1.4.2 Mid-IR Observations	194
2.1.5 Presentation of the Planetary Nebulae Observations	195
2.2 BD+30°3639	197
2.2.1 Observations: BD+30°3639	198
2.2.2 Discussion: BD+30°3639	199
2.2.2.1 BD+30°3639 2.2 μ m Image	199
2.2.2.2 BD+30°3639 Mid-IR Images	201

	9
2.2.2.3 BD+30°3639 Temperature, Optical Depth Images . .	203
2.2.4 Conclusions: BD+30°3639	208
2.3 J 900	210
2.3.1 Observations	210
2.3.2 Results and Discussion: J 900	211
2.3.3 Conclusions: J 900	213
2.4 IC 418	214
2.4.1 Observations and Data Reduction: IC 418	215
2.4.2 Results and Discussion: IC 418 NIR Emission	217
2.4.2.1 IC 418 Morphology and Sizes	217
2.4.2.2 IC 418 Central Star Subtraction	219
2.4.2.3 Comparison, Discussion of Previous Studies of IC 418	223
2.4.2.4 Sources of Near-IR Emission in IC 418	224
2.4.2.5 IC 418 Halo Emission	228
2.4.3 IC 418 Mid-IR Emission	229
2.4.4 Dust Emission in IC 418	231
2.4.5 Conclusions: IC 418	233
2.5 NGC 6543	235
2.5.1 Observations: NGC 6543	236
2.5.2 Discussion: NGC 6543	237

	10
2.5.3 Conclusions: NGC 6543	240
2.6 NGC 2392	241
2.6.1 Observations: NGC 2392	242
2.6.2 Results and Discussion: NGC 2392	243
2.6.3 Conclusions: NGC 2392	244
2.7 AFGL 2688	246
2.7.1 Observations: AFGL 2688	248
2.7.2 Discussion: AFGL 2688	248
2.7.3 Comparison to Other Observations, Models of AFGL 2688 .	253
2.7.4 Conclusions: AFGL 2688	255
2.8 M 2-9	256
2.8.1 Observations: M 2-9	257
2.8.2 Results and Discussion: M 2-9	257
2.8.2.1 Size and Shape of M 2-9	258
2.8.2.2 Structure of M 2-9	260
2.8.3 Conclusions: M 2-9	261
2.9 Comparison of the Planetary Nebulae Properties	262
2.9.1 BD+30°3639, J 900, and IC 418	263
2.9.2 NGC 2392 and NGC 6543	267
2.9.3 AFGL 2688 and M 2-9	269

	11
2.10 Conclusion	275
FIGURES - PART 2	278
APPENDIX 1. MIRAC SYSTEM RESPONSIBILITIES AND FUNDING SOURCES	354
APPENDIX 2. MIRAC FILTERS	356
APPENDIX 3. CRC 444A ROW DECODER CODE	368
APPENDIX 4. MIRAC ELECTRONICS COMMAND SUMMARY	370
APPENDIX 5. PHOTOMETRY OF SAO STARS	375
REFERENCES	379

LIST OF ILLUSTRATIONS

1.1. The MIRAC cryostat.	125
1.2. MIRAC Optics ray diagram	130
1.3. Hughes IBC detector cross section	132
1.4. Hughes IBC 20x64 detector layout	133
1.5. Hughes Si:As IBC detector spectral response	134
1.6. Wire bond diagram for the CRC 444A readout	135
1.7. CRC 444A Decoder	136
1.8. CRC 444A unit cell and detector	137
1.9. MIRAC block diagram	138
1.10. MIRAC Bias supply representative circuit	139
1.11. Preamp circuit diagram	140
1.12. MIRAC Controller block diagram	142
1.13. MIRAC PAL timing diagrams	143
1.14. MIRAC Coadder Memory Map	148
1.15. MIRAC Signal processor block diagram	149
1.16. Typical analog output from the detector	150
1.17. Pixel-level timing diagram for delta reset	151
1.18. MIRAC cooldown	152
1.19. MIRAC temperature and heater power	154
1.20. MIRAC temperature while changing filters	155

	13
1.21. MIRAC detector temperature and heater power	156
1.22. Block diagram of the Sky board	158
1.23. Flowchart of the SKY program	159
1.24. MIRAC program main screen	161
1.25. Sample MIRAC output	164
1.26. MIRAC Guider box assembly diagram	165
1.27. MIRAC Guider box dichroic holder	167
1.28. MIRAC dewar mounting plate	168
1.29. MIRAC Lab test setup	169
1.30. Mirac optimization measurements	170
1.31. MIRAC noise as a function of background flux	172
1.32. Sky noise as a function of chopper frequency	173
1.33. Photograph of reticle through MIRAC optics	174
1.34. MIRAC pinhole profiles	175
1.35. MIRAC optics distortion measurement	176
2.1. Planetary nebulae types and models	279
2.2. CCD images of the planetary nebula BD+30°3639	280
2.3. Contour images of the planetary nebula BD+30°3639	281
2.4. Contour image of BD+30°3639 at 2.2 μm	287
2.5. Profiles of the 2.2 μm image of BD+30°3639	288
2.6. Contour image of BD+30°3639 at 4.885 GHz	290
2.7. Profiles of the mid-IR images of BD+30°3639	291
2.8. Temperature image of BD+30°3639	293
2.9. Dust opacity image of BD+30°3639	294

2.10. Contour image of the 12.8 μm feature of BD+30°3639	295
2.11. Contour image of the 11.2 μm feature of BD+30°3639	296
2.12. Profiles of BD+30°3639 in the [NeII] and UIR feature	297
2.13. Profiles of the 2.2 μm star-subtracted image of BD+30°3639	299
2.14. Contour images of BD+30°3639, from Roche (1989)	301
2.15. Contour images of the PN J 900	302
2.16. Contour images of the PN J 900, in which the central star has been subtracted	304
2.17. Grayscale images of the PN J 900	306
2.18. CCD images of IC 418	308
2.19. H β contour image of IC 418	309
2.20. Calibrated contour images of IC 418 at J, H, and K	310
2.21. Grayscale images of IC 418	313
2.22. Profiles of IC 418	315
2.23. Theoretical nebula profile for IC 418, J image.	316
2.24. PSF-subtracted profiles of IC 418	317
2.25. PSF-subtracted profiles of IC 418	320
2.26. Profiles of IC 418 halo	323
2.27. Contour image of IC 418 at 11.7 μm	324
2.28. Observed surface brightness of IC 418 at 11.7 μm	325
2.29. Surface brightness of IC 418, from Hoare (1990)	326
2.30. Images of the planetary nebula NGC 6543	327
2.31. Contour images of the planetary nebula NGC 6543	328
2.32. Grayscale image of NGC 6543 in the K filter	330

2.33. Model of the structure of NGC 6543	331
2.34. CCD images of NGC 2392	332
2.35. Contour images of NGC 2392	333
2.36. Grayscale images of NGC 2392	335
2.37. Optical image of AFGL 2688	337
2.38. Contour images of AFGL 2688	338
2.39. Grayscale images of AFGL 2688	342
2.40. Profiles through the major axis of AFGL 2688	345
2.41. Contour image of AFGL 2688 at K showing the halo	346
2.42. Model of AFGL 2688	347
2.43. Mid-IR contour images of M 2-9	348
2.44. Source profiles of M 2-9 at 8.8 and 9.8 μm	350
2.45. Overlay of 8.8 μm image of M2-9 on negative optical image	352
2.46. UIR correlation plot	353
A2.1 2.2 μm filter.	357
A2.2 3.8 μm filter.	358
A2.3 4.6 μm filter.	359
A2.4 8.8 μm filter.	360
A2.5 9.8 μm filter.	361
A2.6 11.7 μm filter.	362
A2.7 12.5 μm filter.	363
A2.8 7.9-14.5 μm CVF.	364
A2.9 8-13 μm filter ("N" band).	365
A2.10 MIRAC KrS-5 window.	366

A2.11	MIRAC ZnSe window.	367
-------	----------------------------	-----

LIST OF TABLES

1.1	MIRAC Filters	34
1.2	Pupil stop positions	35
1.3	Hughes IBC Detector Characteristics	42
1.4	MIRAC Bias Voltages	45
1.5	MIRAC Power Supplies	73
1.6	Transimpedance Determination	94
1.7	Responsivity Determination	96
1.8	MIRAC Optimization Data	100
1.9	MIRAC Sensitivity Calibration	
	Steward Observatory 1.5 m Telescope	106
1.10	MIRAC Sensitivity Calibration	
	Steward Observatory 2.3 m Telescope	108
1.11	Comparison of Instrument Sensitivities	111
2.1	General Characteristics of the	
	Planetary Nebulae In This Study	189
2.2	Observations of BD+30°3639	199
2.3	Sizes of BD+30°3639	203
2.4	Photometry of J 900	212
2.5	IC 418 Observation Log	215
2.6	PSF Standard Stars for IC 418 Observations	216

	18
2.7 Observed Parameters of IC 418	219
2.8 IC 418 NIR Component Fluxes	227
2.9 Photometry of NGC 6543	237
2.10 Photometry of NGC 2392	244
2.11 AFGL 2688 Lobe Parameters	250
2.12 AFGL 2688 Fluxes	251
2.13 Photometry of M 2-9	258
A3.1 CRC 444A Row Decoder Code	369
A4.1 MIRAC Electronics Command Summary	372
A4.2 Available Bandwidth Filters	373
A5.1 SAO STAR PHOTOMETRY	375
A6.1 IR Standard Star Magnitudes	377
A6.2 Adopted Fluxes for Zero Magnitude	378

ABSTRACT

This dissertation is composed of two parts. The first part is a description of the Mid-Infrared Array Camera (MIRAC), a new camera for ground-based astronomy. The second part of this dissertation is an infrared study of planetary nebulae utilizing observations with the new camera.

MIRAC is a collaborative effort among the University of Arizona, Smithsonian Astrophysical Observatory, and Naval Research Laboratory. It currently utilizes a Hughes 20x64 Si:As IBC detector array, which is sensitive to infrared (IR) radiation from 2 to 26 μm . The camera is equipped with 10% bandwidth filters at 2.2, 3.8, 4.6, 8.8, 9.8, 11.7, and 12.5 μm , and a wide band 8.0 to 12.8 μm "N" filter. There is also a 20% filter at 20.5 μm , and a 8-14 μm CVF with a resolution of 1.8%. The MIRAC electronics provides timing signals and coadds successive frames at a maximum rate of 10 KHz for the full array, and higher rates for a partial array readout. The data are transferred via a serial interface to a PC for storage and further processing. The camera recently achieved a NEFD of .010 Jy/arcsec² at 8.8, 11.7, and 12.5 μm for a 900 second on-source integration on the Steward Observatory 1.5 m telescope.

Planetary Nebulae (PN) are formed when a star is in the post-Asymptotic Giant Branch stage of evolution. The ejection of circumstellar material is an important enrichment mechanism for the interstellar medium. In many PN, there is an excess of emission in the IR, indicating the presence of dust. There are several different components seen in the IR emission, including a family of unidentified IR (UIR) emission features at 3.3, 6.2, 7.7, and 11.3 μm . Images in the near- and mid-IR are presented here for the following PN: IC 418, BD+30°3639, J 900, NGC 2392, NGC 6543, AFGL 2688, and M 2-9. In IC 418 and BD+30°3639, the SiC and UIR emission is seen to be spatially distinct from the IR continuum. In NGC 2392 and NGC 6543, evidence for excess emission is seen in the distribution of the near-IR flux. In the bipolar nebulae AFGL 2688 and M 2-9, structures in the IR emission are seen that could be related to the equatorial density enhancements that have caused the bipolar morphology.

PART 1: THE MID-INFRARED ARRAY CAMERA

1.1 Introduction

The first part of this dissertation describes the Mid-Infrared Array Camera (MIRAC). The introduction discusses some results from previous instruments and possible astronomical applications of the camera. Then each component of the camera system is described in detail, including the cryostat, optics, detector array and electronics, the computer interface and control program, and the guider box. Following the camera description are the results of several tests of the system carried out in the lab and on the telescope. The final section describes ongoing and future projects that will add to the capabilities and effectiveness of MIRAC.

MIRAC is a collaborative program among the University of Arizona (U/A), Smithsonian Astrophysical Observatory (SAO), and the Naval Research Laboratory (NRL). The principal investigators are William Hoffmann (U/A), Giovanni Fazio (SAO), and Kandiah Shivanandan (NRL). The responsibilities for each institution and the sources of funding are outlined in Appendix 1. With William Hoffmann as my graduate advisor, I participated in the parts of the program that were carried out at U/A. These include the review of the dewar design by Infrared Labs, the initial tests of the detector with the prototype electronics, the installation and alignment of the dewar optics, the testing and

optimization of the final controller and signal processor electronics, and the subsequent lab tests and astronomical observations using MIRAC described here. I developed the microprocessor program for the array processor, which provides the interface between the MIRAC electronics and the IBM PC-compatible computer and controls the telescope chopper motion while coadding images in memory. I also developed the MIRAC program for the PC which controls the camera operation and the display and recording of data.

1.1.1 MIRAC program goals

MIRAC was designed for mid-infrared imaging of astronomical sources from ground-based telescopes using normal bandwidth infrared (IR) filters, without saturating the readout or detector, and to achieve a sensitivity comparable to or better than the best discrete or array detector systems currently in use. It was intended to replace the system that we had been using, the Goddard Space Flight Center (GSFC) 10 μm Camera, which was used to obtain broad-band mid-IR images of a variety of sources (Hoffmann *et. al* 1987). MIRAC was to allow us to obtain similar images with the state-of-the-art mid-IR arrays currently being developed.

There were a number of other goals for the new camera system. We wanted to take advantage of the increased spectral range of the available Si:As array to observe at wavelengths in the 20 μm atmospheric window and at near-

IR wavelengths, as well as the 8-13 μm atmospheric window. In addition to broad band imaging (at a resolution of ~ 10), we wanted the ability to image sources at higher spectral resolution of ~ 50 with a CVF filter, and resolutions of up to 10000 using a Fabry-Perot spectrometer (FPS) currently being modified to use with MIRAC. The MIRAC had to have the proper scales to image large emission regions on the sky efficiently, yet allow us to obtain high resolution images of compact sources. The camera also had to be easily configured and transported to the different telescopes we were likely to use, including the Steward (IRTF), and the Cerro Tololo Inter-American Observatory (CTIO) 4 m telescope, as well as the Kuiper Airborne Observatory (KAO) or the Stratospheric Observatory for Infrared Astronomy (SOFIA) and the 6.5 m Multiple Mirror Telescope replacement. The dewar and electronics had to be free from extraneous noise and as efficient as possible to allow us to use the detector to its full capability.

1.1.2 Astronomical Applications

There are many astronomical applications for which this camera is well suited. The study of planetary and protoplanetary nebulae conducted with the GSFC 10 μm camera has yielded valuable information on the nature of the dust emission in several nebulae (Arens *et. al* 1985, Tresch-Fienberg 1985, Jaye *et. al* 1989, Hora *et. al* 1990, Deutsch 1990, Deutsch *et. al* 1991). Many of these nebulae exhibit emission from the "unidentified" infrared (UIR) features, usually

attributed to carbonaceous dust or molecules. Images in the mid-infrared have shown the spatial distribution of emission from the UIR features to differ from the emission from the ionized zone of the nebula. Determining the location of the emitting regions relative to the central star is important in evaluating models of dust formation, composition, and evolution. Because of its better sensitivity, the MIRAC will allow this study to be extended to many more nebulae, including nebulae in later stages of evolution, which are spatially more extended and diffuse. Its increase in spectral sampling and coverage will enable a more thorough investigation of the UIR features near $10\text{ }\mu\text{m}$ and the cool dust emission at $20\text{ }\mu\text{m}$. High spectral resolution images of the [NeII] ($12.8\text{ }\mu\text{m}$) line will yield information on the velocity structure and dynamics of these nebulae.

Another area of interest is star-formation regions. Observations with a mid-infrared camera are very effective in determining the spatial distribution, color temperature, and optical depth of warm dust emission surrounding young star-forming regions. Circumstellar disks, which are predicted by stellar formation models and indicated by the observed emission at far-infrared wavelengths, may be resolvable in the mid infrared in nearby protostellar regions. If the camera is used in conjunction with a high resolution FPS, observations of H_2 lines at 12.279 and $17.034\text{ }\mu\text{m}$ would permit the study of shocked gas in these regions at high spatial resolution. Images of the sources in the lines would yield the distribution and velocity structure of shocked gas in these star forming regions.

A third area of investigation is star formation processes in extragalactic nuclei. Mid- and far-infrared studies of galaxies have shown that strong star formation may be common in the nuclei of normal spiral galaxies. Studies of two IR-bright galaxies M82 and NGC 253 (Rieke *et al.* 1980, Ho *et al.* 1988) have shown that the infrared emission is associated with indicators of recent star formation. In active galactic nuclei, non-thermal sources of emission may contribute to the mid-infrared flux from these objects. In the Seyfert galaxy NGC 1068, two point-like sources have been detected in the central kiloparsec at several mid-infrared wavelengths (Tresch-Fienberg *et al.* 1986), one at the center of the nucleus and the other 100 pc to the northeast. This spatial and spectral information is important in understanding the processes taking place in galactic nuclei.

These are examples of some of the many possible uses of the MIRAC. The camera was designed with these and other potential uses in mind, maximizing the flexibility and usefulness of the instrument. In the description of the camera below, I have tried to point out as much as possible how these goals influenced the decisions made in the design of the camera. Many of the choices made are compromises between opposing opportunities, because of the impossibility of doing everything at once, and the practical limits of cost and ability. However, we believe that the instrument that has resulted from this effort will prove to be extremely useful and a productive astronomical camera.

1.1.3 Definitions of terms

There are a number of definitions that I will make here to clarify the descriptions of the data and image processing below. The array is composed of 20 **columns** by 64 **rows** of discrete detector pixels. Each signal processor board contains 2 **channels**, and each channel is connected to a single column on the array. A **frame** is an image consisting of the pixels from a single readout of the entire array. A **coimage** is several frames added together in the coadder buffer of the signal processor board. An **observation** is a number of coimages that have been added together in the array processor board (APB). This could consist of two phases of a chop pair, etc. A data file on the PC contains one complete observation. A **picture** or **image** is a set of coimages from an observation or many observations that have been processed in the PC computer to be displayed on the screen. Two chop phases could have been subtracted, and/or the picture flat-fielded or masked.

The following terms designate regions of the infrared spectrum. Near-IR denotes the region from 1-5 μm , mid-IR is the region from 5-25 μm , and far-IR is above 25 μm . The following direction abbreviations are used: N=north, S=south, E=east, and W=west. All images presented here have N at the top and E to the left, unless otherwise noted. Position angles (PA) of source structures are defined, unless otherwise noted, as degrees E of N, relative to the center of the source. All personnel mentioned by name are U/A, unless stated otherwise. The symbol " = arcsec. The unit of flux Jansky (= $10^{-26} \text{ W m}^{-2} \text{ Hz}^{-1}$) is abbreviated Jy, and .001 Jy = 1 mJy.

1.2 MIRAC Dewar and components

1.2.1 Cryostat

The MIRAC dewar, shown in Figure 1.1, is a modified HD-3 cryostat built by Infrared Laboratories Inc. (IR Labs). The modifications were designed by Bob Kurtz of IR Labs. The case is a standard 6-inch inside diameter (I.D.) aluminum cylinder with hexagonal outer surface, with liquid nitrogen (LN_2) and liquid helium (LHe) reservoirs that occupy the entire upper section of the dewar. A 7-inch I.D. extension holds all the optics, electronics, and mechanisms in the camera. The support for the reservoirs and the mechanisms in the extension is provided by a rigid support structure between the cryogen vessels and the top of the dewar. A radiation shield extends from the nitrogen vessel and encloses the helium vessel and shield. Inside the helium temperature shield, the volume is divided into two parts by a plate that separates the section containing the detector and filter wheels and the section containing the optics. The optics (described below) are mounted inside a housing mounted to the plate that divides the sections. A baffle tube with a baffle on both ends extends from the housing to the helium temperature shield. A second baffle tube extends from the nitrogen shield to near the helium temperature shield and tube. Inside the housing is the pupil stop mechanism. The only opening into the upper section where the detector is located is through the selected pupil hole.

The array, mounted on a 68 pin chip carrier, is inserted into a socket on

a circuit board as shown in Figure 1.1b. There are two 31 pin miniature connectors on the circuit board where the electrical connections are made, one for the bias voltages and clock signals, the other for the analog output signals from the detector. A heater resistor and temperature sensor diode are stycast to the bottom of the copper detector mount to provide for detector temperature monitoring and control.

The volumes of the nitrogen and helium reservoirs are 0.8 and 2.0 liters, respectively, allowing for a hold time of 17.5 hours for the liquid helium and 18 hours for LN_2 . This is sufficient for more than an entire night of observing without having to interrupt to fill. The position of the nitrogen fill tube also allows for tilting the telescope to high airmass without unnecessarily spilling LN_2 . Our method of measuring a gain matrix involves taking images of blank sky at low and high airmass, so this feature is important, especially at the beginning of the night when the dewar is full.

The MIRAC dewar was designed so that the filters, magnification positions, and pupils can be changed externally, minimizing the need for disassembly under normal operating conditions. However, a dewar is always opened much more often than planned, so the dewar was also designed for ease of disassembly and reassembly. The disassembly proceeds from the bottom, first by removing the bottom plate and the lower case extension. Next the LN_2 and helium shields are removed. This exposes the optical housing and the area where the detector is mounted. At this point all major mechanisms and

components are exposed. The detector stage can be removed, wiring checked and repaired, filter wheel mechanisms examined, optics adjusted, etc. Everything within the helium shield is attached to a plate which is in turn attached to the bottom of the helium reservoir. If desired, this plate can be removed from the cold plate by removing six bolts. The entire assembly can then be removed. This is useful when aligning the optics or working on the filter wheel mechanisms, or to protect the array and optics when working on the upper section of the dewar.

Another design goal was to have a portable dewar. This was achieved by designing the dewar to be as compact as possible, and protecting the connectors and external actuators from damage. The 6-inch I.D. IR Labs dewar was chosen for compactness, instead of the 8-inch I.D. dewar. If the bottom plate with the actuators and filter motors is replaced by a blank plate, the MIRAC dewar meets airline size restrictions for carry-on luggage. The actuator mechanisms and the vacuum valve are mounted on the bottom plate of the dewar. The dewar stand attached to the bottom plate has the same profile as the dewar extension, and along with the standoffs used to attach it forms a cage which protects the mechanisms. The electrical connectors are mounted on the top, and act as a stable support when the dewar is inverted on the workbench.

1.2.2 Optics

The MIRAC optics were designed with the following goals in mind: to provide two different magnifications, to enable use of the full 2-20 μm range of detector sensitivity, and to be as simple, compact, and efficient as possible. The optics also had to be easily configurable to the different telescopes with which MIRAC may be used. For all magnifications and pupil sizes to be used, the geometrical image size had to be much less than the 100 μm pixel size over the full array. An additional constraint was to allow for the potential use of larger format arrays in the MIRAC dewar without significant modifications. The optics were designed by William Hoffmann and the ellipsoid element was fabricated by Dick Sumner.

A drawing of the MIRAC optics is shown in Figure 1.2. The optical elements are a gold-coated flat and a tilted off-axis ellipsoid mirror, and a pupil stop. The central ray enters the dewar through the window and passes through baffles to the flat inside the optical housing. The ray is reflected first down to the ellipsoid, then directly upward, normal to the work surface of the dewar. The ray passes through the center of the pupil, filter wheel 1 and 2, and intercepts the center of the array normal to the surface. The only opening to the compartment of the dewar where the detector is located is through the pupil stop. This minimizes the amount of off-axis radiation reaching the detector. The inside of this compartment, along with the optics housing, is painted black to reduce scattering of stray light on to the detector.

A reflective system has many advantages over a refractive system. The reflective optics accommodate the wide range of wavelengths that the detector is sensitive to without need for adjustment. This simplified the design considerably and reduced the volume necessary inside the dewar to contain the optics. There is only one active element, an off-axis ellipsoid located at the bottom of the optics housing. Propagation losses through the system are minimized by having only two gold-coated reflective surfaces. Any system of lenses would have reflective losses from the lens surfaces and absorption loss in the lens material. Changes in magnification are accomplished by moving the position of the detector and refocusing the telescope. This allows the optics to remain fixed and aligned, and eliminates the need for a mechanism to slide or shift the optical elements. One drawback of having a single off-axis ellipsoid is that it causes a small amount of pincushion distortion at the detector. The amount of distortion, however, is small (see §1.7.7 below) and has been calibrated, so the distortion can be removed in the data reduction process.

Since the central ray is normal to the work surface, the array can be translated vertically to change magnifications. The low magnification position is when the detector is moved to the closest position to the pupil stop, 19.95 mm, and in high magnification, the array is moved farthest from the pupil stop, 40.84 mm. The detector image focus is located outside the dewar for both magnification positions, 13.72 cm for low and 1.176 cm for high magnification.

The optical design was optimized for minimum image blur at the edges

of the array at the $f/36$ IRTF. This was a compromise between the $f/45$ of the Steward telescopes and the faster telescopes on which the MIRAC could be used. The design has a calculated maximum rms image blur of $8\ \mu\text{m}$ over the array at low magnification, and $5\ \mu\text{m}$ at high magnification. The maximum pincushion field distortion at the corners is $45\ \mu\text{m}$ at low magnification and $23\ \mu\text{m}$ at high magnification. The pixels are $95\ \mu\text{m}$ square, on $100\ \mu\text{m}$ centers.

The filter wheels, shown in Figure 1.1e, are made from 12.7 cm diameter aluminum gears in which counterbored holes have been machined on a 8.052 cm diameter to hold the filters. The wheel nearest the pupil stop holds nine .953 cm diameter filters and blockers and the CVF segment. The second wheel holds 10 1.588 cm filters. Figure 1.1e shows the position of the filter wheels in the dewar. The filter wheel containing the CVF is located as close to the pupil as possible, to provide a sharp wavelength-defining aperture. It is also desirable to have the other filters near the pupil stop.

Table 1.1 gives a list of the filters in the MIRAC dewar. In each wheel there is a position with no filter installed, and in both wheels there is an aluminum blank installed in one position. The filters were all purchased from Optical Coating Laboratories, Inc. (OCLI), and the information is based on data supplied by OCLI, except for a few filters and the dewar windows which were measured at room temperature with the Beckmann Acculab 6 Spectrophotometer at NOAO. See Appendix 2 for a spectral scan of each of the filters.

Table 1.1 MIRAC Filters

Wavelength ¹ [HP width] (μm)	Trans- mission ² (%)	Substrate	Size (cm)	Blocker ³	Comments
Wheel #1					
8.82 [.87]	75	Ge	.959	CaF ₂	OCLI "O" astr.
9.8 [.96]	76	Ge	.959	BaF ₂	OCLI "P" astr.
11.7 [1.13]	72	Ge	.959	BaF ₂	OCLI "R" astr.
12.5 [1.16]	64	Ge	.959	BaF ₂	OCLI "S" astr.
10.6 [4.8]	80	Ge	.959	BaF ₂	OCLI W10575-9
4.62 [.59]	85		.959		OCLI W04711-4
Sapphire			.959		1 mm thick
7.9-14.5 CVF [~1.8%]	70	Ge	1.37 ⁴		OCLI 15-1395-970
Wheel #2					
2.17 [.35]	67		1.715		OCLI W02206-7
3.85 [.62]	92		1.715		OCLI "L" astr.
20.6 [4.2]	31		1.715		OCLI W-19500-9, L18180-8A
N.D.	.33		1.715		
N.D.	1.0		1.715		
N.D.	5.0		1.715		
N.D.	20		1.715		
		BaF ₂	1.715		1 mm thick

¹The wavelength data from the OCLI 295°K scans were shifted to adjust for a temperature of 4K. The OCLI 77°K data were not adjusted, since most of the wavelength shift occurs from room temperature to 77°K. All of the scans were multiplied by the detector response to derive the effective wavelength given here. N.D. = Neutral Density filter.

²For filters, effective peak transmission. For CVF, average peak transmission over the usable range. For N. D. filters, the trans-mission is the average value over the range 2-26 μm .

³The filters with blockers listed have a 1 mm blocker of the same diameter installed in the same wheel, separated by a .25 mm thick gold-coated copper spacer ring.

⁴The CVF is a 1.37 cm wide, 90° segment of a circle of diameter 8.052 cm (circle through the center of the CVF).

Two windows were fabricated for use with MIRAC, one of KrS5 and the other of ZnSe. The ZnSe window has good transmission from the near-IR to

approximately 18 μm . The KrS5 window transmits from the near-IR to beyond the 20 μm atmospheric window. The transmission through each of these windows is shown in Appendix 2.

The pupil stop slide is a set of pupil stops that are sized for the telescopes on which the MIRAC may be used. Table 1.2 shows the hole dimensions and the appropriate telescope.

Table 1.2 Pupil stop positions			
Pos. #	Hole Dia. (cm)	f/number	Telescope
blank
2	.167	45	SO 1.5, 2.3 m
3	.196	36	IRTF
4	.237	30	CTIO 4-m
5	.420	17	KAO
6	.470	15	MMT Upgrade

1.2.3 Electric wiring, connections

There are four electrical connectors at the top of the dewar, illustrated in Figure 1.1b. One provides the necessary bias and clock voltages to the detector. The second contains output lines from the detector to the external preamplifier electronics. The third connector is the temperature sensor and the heater connections. The fourth connector is attached to the home switches for control of the filter wheels. These connectors are mounted on the top of the dewar, pointed horizontally away from the center. The two detector connectors are each mounted on their own block, and the temperature sensor/heater and

the switch connector are mounted on a common block. The detector signal output block, at the top in Figure 1.1b, is as close as possible to the electronics, to minimize the length of the coaxial analog cables from the dewar to the preamp.

A number of steps were taken to insure minimal pickup of the digital signals on the detector and the analog output lines. First, there are three separate shielded cables in the dewar for the detector connections, one each for the clocked row addresses and reset, bias voltages, and analog outputs. The analog signals are segregated on their own connector at the top of the dewar, and at a separate connector at the circuit board where the detector is mounted. At the circuit board near the detector, filter capacitors were mounted on all the bias lines to reduce potential digital pickup. The connection to the detector is made by two 31-pin miniature connectors on the circuit board on the detector mount.

The cables used were made at the Naval Research Laboratory specifically for cryogenic applications using detectors of this type. The cable is a ribbon consisting of alternate strands of insulated Constantan wire separated by nylon insulator. The flat cable is then wrapped in superinsulation which provides shielding and protection of the conductors. The beneficial characteristics of this cable are that it is very compact and flexible, has relatively low capacitance, and low thermal conduction. The capacitance of the cables was measured as installed in the dewar (approximately 30 inches) to be 130 pf for each conductor

to ground, and 30 pf from one conductor to the next. The cables are taped to the LN₂ reservoir, pass under a slot in the radiation shield, and then are taped to the liquid helium reservoir. This insures that the wires do not provide a source of heat inside the helium shield. There is a 10 cm loop in each cable from the connector to the LN₂ shield to reduce heat input.

An additional 6-pin connector is used to connect the temperature monitor and heater resistor located on the detector slide. There is enough free length in the cables between the mounting slide and the point where the cables are fastened to the cold plate so that there is not excessive strain on the cables when switching from high to low magnification.

1.2.4 Actuators, Filter Motors and Control

There are four mechanisms that are controlled by external actuators which enter the dewar from the base: the pupil stop slide, the detector mounting slide, and two filter wheels. The filter wheels are driven by stepper motors that drive the wheels through a series of linkages and gears. The other two actuators are kept pulled out of the dewar into a recess in the dewar case, except when the slides are being changed. Their location is shown on the bottom plate of the dewar in Figure 1.1c.

Each filter wheel is rotated by an Anaheim Automation Co. #23D108S

stepper motor and SMC20BC controller system. The motors are mounted on the base of the dewar, shown in Figures 1.1a and 1.1c. The shafts of the motor are connected through an adapter to a ferrofluidic feedthrough that transmits the rotation to the vacuum of the dewar. This feedthrough device is model #SB-250-A-N-086, part #50C103237, manufactured by Ferrofluidics Corporation. The vacuum seal consists of a permanent magnet, pole pieces, a magnetically permeable shaft and a magnetic fluid, or ferrofluid. The structure of the magnets creates a field which is concentrated between the stationary magnet and the shaft. The ferrofluid is trapped in this region, and forms a "liquid O-ring" seal between the shaft and the stationary housing. There are several stages of ferrofluid seals in the feedthrough, separated by air gaps. Each stage can sustain a pressure difference of 0.2 atmospheres, and the stages act in series to provide the total pressure capability of the seal. The feedthrough is designed to sustain a total pressure differential of >2 atmospheres, providing a safety margin.

The feedthrough shaft extends through the vacuum inside the dewar to a nylon bushing that is captured in the nitrogen shield. The nylon bushing provides thermal insulation from the warm shaft to the nitrogen temperature shield. From the nitrogen shield, a shaft extends into a nylon bushing connected to the helium temperature gear which turns the motor. This provides thermal isolation between the nitrogen and helium shields.

The motors drive the wheels from the edge using a smaller gear with a

(32/3):1 reduction. The motor controller accepts ASCII command strings from the PC via a RS-232 interface. The motors can be stepped any number of steps in either direction, at the user selected speed. The stepper motors have 400 steps per revolution, which gives 4267 steps for one revolution of the filter wheel. This corresponds to a positioning accuracy of .007 μm in wavelength for the CVF filter.

Mounted on top of the filter wheel right at the edge is a small block which defines the initial reference, or "home" position. Two microswitches are mounted on a stand on the cold plate so that they are positioned just above the wheels. To move the wheels to the home position, the controller rotates each wheel until the block mounted on the wheel comes in contact with its home switch. This position is centered on one of the filters. To move to other filter positions, the motors are stepped the appropriate number of steps, determined by the filter spacing.

The normal position of the other actuators is fully withdrawn outside the dewar into a cylindrical recess in the dewar case. When the pupil stop slide or detector mount needs to be moved, the actuator is pushed into the dewar. The end of the shaft enters the nitrogen shield through a hole which is covered by flexible aluminized mylar that is slotted in an "X" pattern to allow the actuator to pass through. The actuator is pushed into a flexible nylon coupling that is connected to the mechanism. For the pupil stop slide, the actuator is rotated and a rack and pinion gear causes the slide to move. A spring loaded

ball bearing presses against the slide and falls into a detent at each slide position. The slide positions are described above, in Table 1.2.

The array mount slide is engaged by pushing the actuator in until it enters the coupling, shown in Figure 1.1b, and then twisting to lock it in. Then the array position is changed by pushing or pulling it to the other position. Two spring-loaded balls on either side of the mount fall into detents which define the correct position, similar to the pupil stop mechanism.

The center of the chip socket has been cut out and a copper finger extends through to provide the surface where the detector chip carrier is mounted. A 2.29 cm square of .254 mm thick indium foil is placed between the chip and the copper to insure good strain-free thermal contact. The detector is held in place in the socket by a copper bracket that presses the chip from the front side into the socket, shown in Figure 1.1b. The bracket also acts as a radiation baffle; the top side and the cavity on the side facing the detector is painted black, and the opening is just large enough to expose the sensitive area of the array. The copper mount is thermally isolated from the slide by a block of G-10. The mounting bracket that connects to the cold plate has two stainless steel shafts on which the detector mounting assembly slides, pulled or pushed up or down by a third rod connected to an external actuator. Thermal contact between the detector mount and the cold plate is made by a flexible copper foil strap which has been optimized to provide sufficient cooling so that when the detector is running with no heater the temperature of the array is 6.5 K.

1.3 Detector

This section describes the detector array currently used in MIRAC. We received much assistance from Grant Albright, Skip Augustine, and Stone Klengler of Hughes from their comments and suggestions on electronics design and in the initial testing phase of the detector in the MIRAC dewar.

1.3.1 General description

The detector used in the MIRAC is a arsenic-doped silicon (Si:As) Impurity Band Conduction (IBC) 20x64 pixel array, bonded to a capacitive transimpedance amplifier (CTIA) readout, designated CRC 444A, serial number AR6. This detector was developed by Hughes Aircraft Co. of Carlsbad, CA. The relevant parameters are summarized in Table 1.3.

Fowler and Joyce (1990) provide a general description of the Hughes Si:As IBC arrays. The array is a hybrid device consisting of a readout circuit that is "bump-bonded" to the detector array using indium "bumps". Figure 1.3 shows the IBC detector cross section. It consists of a high resistivity substrate, a transparent contact, the heavily doped IR active layer, a lightly doped blocking layer, and aluminum contacts on the top, with an indium bump for connection to the readout.

Table 1.3 Hughes IBC Detector Characteristics

Material	Si:As
Operating Wavelength (μm)	2-26
Number of Pixels	20x64
Pixel size (μm)	95x95
Pixel spacing (μm)	100
Readout Mode	Parallel
(# of lines)	(20)
Peak QE ¹	0.4
Well Size (e^-) ²	1×10^5
Read Noise (e^-) ³	80

¹Hughes test report data²MIRAC measurement 2/9/91³MIRAC measurement 2/9/91

Stetson *et. al* (1986) give a description of the operating principle of this detector type. In the heavily doped IR detecting layer, acceptor impurities exist which are ionized. The negative charges associated with acceptor sites are fixed, but the positive donor sites "D+" are mobile, and can migrate through the crystal when the acceptor sites are sufficiently close. When a positive bias is applied to the top Al contact, a field is created which drives the pre-existing D+ sites toward the substrate. The undoped blocking layer prevents the injection of additional D+ charges, so a region depleted of D+ charges is created near the top contact. A negative space-charge is left in the depleted region, since the negative charges are immobile. When an incident IR photon is absorbed, it

creates a mobile D^+ charge and a conduction band electron. The applied field sweeps the electron out through the blocking layer where it is collected by the top contact. The D^+ charge travels in the opposite direction and enters the undepleted region of the detecting layer.

This design has advantages over a standard photoconductor in reducing the noise due to the detector. In the depleted region there are almost no empty states below the conduction band to trap electrons, so the collection efficiency is extremely high. Also, the conduction band electron concentration under these conditions is virtually zero, making the D^+ charge collection efficiency high. The high collection efficiency of the charge carriers minimizes noise due to carrier recombination. Since the detecting layer is highly doped, it can be made thin while keeping the quantum efficiency high. The thin detecting layer lowers the sensitivity to incident charged particles.

1.3.2 Array Format and Packaging

The detectors are arranged as two sub-arrays of 10×64 pixels, separated by one pixel in the short direction and offset by half a pixel in the long dimension. This is illustrated in Figure 1.4. The spectral response of the detector material is shown in Figure 1.5. The full range is from approximately $2 \mu\text{m}$ to $26 \mu\text{m}$, peaking at a quantum efficiency of approximately 0.4 at $22 \mu\text{m}$. Much of this range, however, is limited for ground-based astronomy by

atmospheric absorption.

The wire bonding diagram is shown in Figure 1.6. The detector itself is bonded to a ceramic "chip carrier", which has 68 contacts on the four sides. Pin 1 of the carrier is an "L"-shaped pad shown in the upper left of the diagram, and the numbering proceeds counterclockwise as viewed from above the detector, 17 contacts to a side. The metalization of the outer pads wraps around from the top to the sides of the carrier, allowing electrical contact to be made from the edge as well as from the top. The numbers marked on the chip carrier contacts on the edge are the numbers of the pads of the detector that they are connected to.

1.3.3 The CRC-444A Readout

The CRC 444A decoder is shown in Figure 1.7. This uses 8 address bits to specify 64 pixels. The addresses are coded such that four bits are always 1 and four bits are always zero. The detector and readout use negative logic, with "0" = 0 V and "1" = -4 V. Also, consecutive addresses differ by two bits, and require changing one address line from a zero to a one, and another address line from one to zero. One advantage of this scheme is that the address clocking is very uniform, and cases where all the bits toggle simultaneously are avoided, preventing possible noise pickup problems. The code is shown in Appendix 3, Table A3.1. For each pixel, four of the address lines are connected as shown in Figure 1.7 to enable the reset and the output

for that pixel.

The CRC 444A unit cell is shown in Figure 1.8. The RESET CLOCK and ENABLE CLOCK are from the decoder in Figure 1.7. The bias voltages are labeled with a capital V and the current supplies are labeled with a capital I. The values used for each of these are shown in Table 1.4. The currents are consistent with the sum of the currents approximately equal to zero.

Table 1.4 MIRAC Bias Voltages

Bias Name	Volts	Current ¹ (μ Amp)
V _{SUB}	9.00	.36
I _{SS1}	5.00	172
V _{SS0}	3.00	260
V _{DD3}	0.00	3248
V _{SSC}	0.00	<.02
I _{SS3}	0.00	-11.7
V _{CL}	0.00	<.02
V _{SSD}	-1.00	36.8
V _{CAS}	-2.00	<.2
V _{DD2}	-2.00	-249
V _{DET}	-2.60	<.02
V _{DD1}	-3.00	-3651
V _{RST}	-4.00	-2.0
V _{EN}	-4.00	-40.0
V _{ADJ}	-6.00	-2765

¹Current measured on 7/19/90, at 7.5 MHz clock rate, reading out 32 of 64 rows, 8.8 μ m, 20% ND looking at room temperature radiation, detector temperature = 12.4°K. The current was calculated from measurements of the voltage drop across series resistors.

The detector pixel and readout unit cell consists of the circuit from the left edge of the diagram to the point where the ENABLE CLOCK is connected. This circuit exists for every pixel. The part of the unit cell labeled "Current

mirror/output driver" is part of the column readout circuit, and there is one for every 64-pixel column. The point labeled V_{OUT} is the output of the detector chip, and the "typical output load circuit" is implemented on the MIRAC Preamp board.

The readout circuit is a Capacitive TransImpedance Amplifier (CTIA) whose output voltage is proportional to the integral of the input current flowing into the feedback capacitor from the detector. The transimpedance of the amplifier, defined as the ratio of the output voltage to the charge on the input capacitor, in Volts/Coulomb, is equal to the reciprocal of the feedback capacitance, assuming negligible parasitic capacitance and gate leakage current. For the remainder of this dissertation, I will use units of millivolts/electron for the transimpedance. The overall transimpedance for the array is the output source follower gain divided by the CTIA feedback capacitance.

There are two advantages of using the CTIA circuit. First, the bias on the detector is held constant during charging of the feedback capacitor, resulting in detector linearity. The second advantage is that the input voltage gain at the source follower effectively suppresses noise introduced after the amplifier input. The input voltage gain is the ratio of the detector and parasitic capacitance to the feedback capacitance, which for this array is approximately 4.

The reset pulse dissipates the charge which has built up in the capacitor,

allowing for another integration. The difference in voltage output levels between the "before reset" and the "after reset" is proportional to the flux incident on the detector during the integration time. This linear relation holds until the charge building up on the capacitor exceeds the "well size" value given in Table 1.3 above. At this point the pixel saturates, or the response curve flattens out and eventually does not rise with increasing flux. Therefore, as the flux level increases, to keep the detector from exceeding the well size each pixel must be reset more often.

The peak of a 300K blackbody curve is near 10 μm , so the ambient temperature telescope radiates strongly in the mid-IR. The atmosphere also radiates in the mid-IR. The combination of the thermal telescope and sky emissivity result in backgrounds that are often larger than the source signal by a factor of 10^6 . For the backgrounds present in the mid-IR from ground-based telescopes using 10% bandwidth filters, typically a rate of 10 KHz is required to operate the detector in its linear range.

1.4 Electronics

The MIRAC electronics were designed to perform the necessary tasks to operate the detector properly, sample the analog signals synchronously and convert them to digital values, store these values as pixels in a frame, coadd multiple frames, and transfer the stored coimages to the computer. These functions had to be accomplished within the design goals of low noise, multiple sampling modes and options, subject to size and cost constraints. In addition to the electronics associated with the detector array, a temperature controller and monitor were necessary to maintain a constant detector temperature, and an interface was necessary to transfer the images from the camera electronics to the computer.

The electronics were designed by William Hoffmann, Larry Coyle, and John Geary and constructed and initially tested at Smithsonian Astrophysical Observatory Central Engineering. Peter Crawford of SAO assembled the signal processor boards and the power supply. A block diagram of the MIRAC system is shown in Figure 1.9. The Figure is divided into three main sections, the cryostat, the electronics at the camera, and the equipment in the telescope control room. There are six main components of the electronics: the bias voltage supply, the preamplifiers, the signal processors (20 channels total, one for each column of the array), the digital controller, the temperature monitor and controller, and the filter wheel controller and motors.

1.4.1 Detector Bias Supplies

There are 14 separate bias supplies necessary to run the detector and its readout. The operating bias voltages are listed above in Table 1.4. These voltages are generated on a separate bias voltage board, which is enclosed in its own shielded box to separate it from the other electronics components. The voltages are derived from regulated ± 10 and ± 15 volt supplies on the bias board.

Figure 1.10 shows a representative bias voltage circuit. In series between 10 and -10 V are a fixed resistor R1, a 1K 10-turn potentiometer (pot), and a second fixed resistor R3. The resistance values R1 and R3 are chosen so that when the 1K pot is set to the middle of its range, the voltage is at the nominal value, with a total range of ± 1 V about this value. The voltage from the adjustable pin of the pot then goes to a buffer amplifier of unity gain. The output of the amplifier goes to a small series resistor, and then directly to the detector via a shielded cable to the top of the dewar and then through the dewar wiring. The points labeled T1 and T2 are test points that are wired to a connector on the side of the bias box, where a breakout board can be plugged in to monitor voltages. There are bypass capacitors in a small box in the cable leading to the dewar, as well as on the circuit board with the detector chip socket in the dewar. These are to eliminate noise due to digital pickup on these lines.

Two of the "bias" supplies (I_{SS1} and I_{SS3}) are actually current sources. These supplies have an additional series resistors of 38.3 k Ω and 51.1 k Ω , respectively, at the point labeled (R5). The detector bias V_{DET} is also equipped with an additional series resistor of 24.3 k Ω , to provide protection against high currents through the detector. V_{ADJ} does not go to the detector itself, but provides the voltage for the output MOSFET source follower amplifiers' source resistors which are located on the preamp board.

1.4.2 Preamp

The preamp acts as a buffer and an amplifier of the signal coming from the detector. Twenty separate signals come from the detector to the top of the dewar, and are connected to the preamp inputs via a short coaxial shielded cable. The preamp electronics are housed in a separate shielded box near the top of the electronics enclosure, with separate power regulators inside, to prevent extraneous noise pickup from other parts of the MIRAC electronics.

The preamp circuit is illustrated in Figure 1.11. Two inputs for every channel enter the preamp: the signal, which is the source of the array output MOSFET source follower, and signal reference. The signal reference is connected to analog ground in the preamp for every channel. The signal is connected to a unity gain buffer amplifier, and through a 30.1K source follower resistor to V_{ADJ} . The output of the unity gain amplifier is connected to a second

amplifier with a gain of -4. An offset bias of +3.2 V is also added at this stage. This bias, along with the preamp gain and gain on the signal processor, were selected to match the array output, which has a range of approximately -1.2 to -.2 V, to the A/D input range of ± 2.5 V.

The "+" input of the second op amp (gain -4) is connected through a 4.99 k Ω series resistor to the detector return, which are the coaxial shield of the signal cables and are all tied together at the preamp board. This point is then connected to analog ground on the board. The output of this stage is connected through coaxial shielded cable to the input of the signal processor board.

1.4.3 Digital Controller

The main functions of the digital controller are indicated in the MIRAC block diagram, Figure 1.9. A more detailed block diagram of the controller is shown in Figure 1.12. The serial interface receives commands and parameters from the PC, and it sends the data from the "first in first out" (FIFO) memory on the signal processors to the PC. A number of camera parameter registers exist where the current values are stored. These parameters control the operation of the timing on the controller and signal processor. Two programmable array logic (PAL) chips (denoted as "PAL1,2 Timing Generator" in the diagram) create the reset pulse and the control signals for sampling the

data. Other counters and timing signals keep track of the number of frames in the coimage, the transfer of the coimages to the FIFO memory, and clearing the frame memory on the signal processor between coimages.

1.4.3.1 Timing, addressing

There are a total of nine clocked signals driving the array readout: eight address lines and a reset pulse. The row address is generated by a counter that starts at zero and counts up to the maximum row ($n-1$). It is then reset to zero to start the next cycle. This row address is used to specify the address of the coadder memory, as well as to clock the array. The 6-bit row address is converted to the 8-bit array address using an electronically erasable programmable memory (EEPROM) chip, and then is sent through optical isolators to the dewar.

All timing on the controller is specified by the master clock, which is derived from a 30 MHz crystal oscillator. This is divided by two for a maximum clock rate of 15 MHz, which can be further divided by factors of two, based on the value in the clock rate register. A single pixel select time is divided up into 24 master clock cycles. At the clock frequency of 15 MHz, this is 67 nsec per clock cycle or 1.6 μ sec per pixel. This corresponds to .1 msec for a full 64 row frame and .05 msec for half frame. The rate at which the detector is read out is command selectable to 16 different rates. The frame rate is

derived from counting down the master clock by powers of 2 to obtain the desired value. This gives a range of frequencies of 15 MHz down to 457 Hz.

The controller has several different modes of clocking the detector. The usual mode is selecting each pixel from 1 to 64 in sequence and resetting each one. When number 64 has been reset, the controller begins again at 1, with no pause in between. Another possible mode is to clock through half the addresses, 1 to 32, before starting again at 1. This mode has been used exclusively since June 1990, when it was discovered that one of the address lines was malfunctioning, and only half the array could be read out correctly. It was decided not to attempt to repair this device since no replacement array was available at that time.

Another possible readout mode is a "burst" mode, where the pixels are read out quickly in succession, but there is a delay time between frames. The delay can be set to be an integer number of pixel readout times. This mode is useful in low background conditions, when a longer integration time is possible. It also synchronizes the integration periods of each pixel, making them closer to simultaneous. The range of delay values is 0 to 65536, making the readout rate range .05 msec to 3.3 sec at 15 MHz clock frequency, or much larger frame times for lower clock frequencies.

The controller directs the data sampling synchronously with the clocking of the detector. There are four different modes possible: single sample, with

the sample taken during the pixel select just before the reset; delta reset - taking a sample before and after the reset, finding the difference between the two, and sending the difference to the computer; double sample - taking two samples as in delta reset, but sending both to the computer; and triple sample, where samples are taken before, during, and after the reset, and all three samples are sent to the computer. See the signal processor section below for a more detailed description of these modes.

1.4.3.2 Controller and processor timing

There are two PAL chips on the controller. The PAL timing diagrams are shown in Figure 1.13. The first PAL device, called PAL1 here, has as input the master clock (referred to as BITCLK), a control line called PIXWAIT which can be used to stop the clocking of the array, and SMODE00 and SMODE01, two bits which control the sample mode. The outputs of the PAL1 are the detector reset pulse DRST/, the CVRT/ pulse which causes the A/D's to take a sample, PIXCLK2/ that signals the start of a new pixel on the downward transition, and five control lines CT0-CT4 which are inputs to the second PAL (PAL2). The slash "/" after the names above indicates that it is negative logic, e.g., for the DRST/ pulse, the reset occurs when the signal in the timing diagram goes low. These control lines are used by the second PAL to generate control signals for the coadding of data.

The control line PIXWAIT is used to turn the detector reset pulse off, along with the other coadder logic. This is used when the camera is being operated in the burst mode, when the detector clocking is suspended for a number of pixel read times after each frame. Otherwise, the detector is continuously reset and clocked whenever the electronics power is on, even when not imaging. This insures a steady state in the detector and eliminates noise due to detector temperature drift which would result if the readout was not constant. The DRST/ and CVRT/ outputs are different for the various sample modes, due to the different number of A/D samples necessary.

Four separate diagrams are shown in Figure 1.13b-e for PAL2, one for each of the different sample modes. The DRST/ and CVRT/ signals are not inputs to PAL2, they are shown for reference. The outputs perform the following functions. COADST is the signal that latches the coadder memory row address for a particular pixel. COADDA is the signal that causes a "coaddition" to be latched in preparation for storing the value to memory. There are two coadditions necessary per sample, one each for channel A and B on the signal processor. COA8A is the signal that selects between channel A and B on the signal processor. COA7A and COA6A are the highest bits of the coadder memory address. For a particular row address, there can be up to three samples stored for triple sample, and these are stored in different areas of memory based on the value of COA6A, COA7A and COA8A. This is shown in the coadder memory map diagram in Figure 1.14.

ADDSUBA is used to control whether the coadders are adding or subtracting the numbers. For the Δ reset mode, this is used to subtract the post-reset sample from the pre-reset sample, and only the difference is stored and transferred to the PC. OFFBLKA and OFFBLKB are address bits for the fast offset function of the signal processors, which has not been implemented.

1.4.3.3 Controller logic

The controller uses the signals generated by the PALs to control the processes of sampling the data on the signal processors and storing the coimages in coadder and FIFO memory. The timing is based on the following user-selected parameters: the clock frequency, the number of frames per coimage, and the number of rows per frame, or the portion of the array being read out.

The control of the data taking and coimage generation is accomplished using the PAL signals described above, along with a number of other signals derived from these on the controller. Some of these are described below:

FIRSTROW - This is true during the first pixel read of a frame, or when the row address = 1.

LASTFRAME - This is true when the last frame of the coimage is being coadded by the signal processor. If there is only one frame per coimage, this is true all of the time.

TOFIFO - This is the result of LASTFRAME AND COADDA/. This is used to direct the data to the FIFO memory during the last frame of the coimage. During this period, the coadder memory is filled with zeros. If there is only one frame per coimage, then the image always goes to the FIFO and the coadder memory is not used to store the frame.

A typical integration would proceed as follows: first, the controller receives the START COIMAGE command from the PC. As soon as the row address reaches the maximum value and toggles back to 1, the flag IMAGING is set. This enables the coadder timing and starts the data taking process. Also, the frame counter is initialized to the number of frames per coimage. Based on the selected sample mode, each pixel row is read out by the signal processors under the direction of the controller, and the frame stored in the coadder memory. After all of the rows have been read, the row address is reset to 1, the frame counter is decremented, and the next frame proceeds in the same way, with the current frame being coadded to the previous result in coadder memory. This proceeds until the frame counter reaches zero. When this occurs, LASTFRAME is set and the image is transferred to the FIFO memory by writing the result of the coadder to the FIFO instead of the coadder memory. The coadder memory is simultaneously loaded with zeros, to prepare for the next integration. After the last frame is completed, the IMAGE READY flag is set, the frame counter is initialized and the next integration begins.

If a STOP COIMAGE command has been sent during a coimage, the data taking process continues until the last frame has completed and the IMAGE

READY flag is set. At this point, the IMAGING flag is turned off and the data taking stops until the next START COIMAGE command is received. The imaging process will stop only after the last frame has been completed, so to take a single frame, START and STOP COIMAGE commands must be sent consecutively before the frame has completed.

1.4.4 Signal Processor (SP)

The function of the SP board is to sample the analog waveform from the detector at one or more places per pixel to determine the voltage due to flux on the detector. This information must be converted to a digital value and stored in memory. Successive frames are coadded, according to the observing mode selected, and saved in memory. The data is transferred as requested to the controller board when the PC directs the transfer of images. A block diagram of the signal processor is shown in Figure 1.15. There are five main sections to the SP board: the analog section, the A/D sampling, the fast coadder, the coadder memory, and the FIFO memory.

1.4.4.1 Analog Section

The analog portion of the SP consists of an amplifier stage and a voltage over-range protection circuit. The amplifier stage includes a unity gain buffer

with programmable bandwidth, and a second amplifier with unity gain. The bandwidth selection allows the maximum bandwidth in the sampling to be set to the optimum value, based on the operating frequency. The available bandwidths are given in Appendix 4, in Table A4.2. Noise can be filtered out in this way without loss of signal, decreasing the read noise, hence increasing the dynamic range for background noise limited operation.

The voltage over-range circuit is to protect the A/D converters from unintentional inputs that exceed the safe operating range of the converters. The maximum input range for conversion is ± 2.5 V, and the maximum safe voltage is ± 3.5 V. The voltage protector circuit clips the voltage at 3.0 V so that the safe range of the converters is not exceeded. The output of this stage is connected to the input of the track and hold device, which is controlled by the A/D converter.

1.4.4.2 A/D Sample Modes

The analog-to-digital conversion is directed by signals from the controller board and is synchronized with the addressing of the detector to insure the samples are taken at the appropriate time. The output voltage level from the detector is proportional to the amount of flux incident on the detector, so to measure the flux, the output level must be measured accurately. After the analog signal is sampled and converted to digital numbers, these numbers must

be added (or subtracted) and stored until read out by the computer. When the CONVERT pulse arrives from the controller, the A/D converter commands the track and hold chip to hold the current input value, and then converts the input voltage to a digital value, which it transfers to its output bus. The data word from the 12-bit A/D chip goes through a latch to an input to the coadder chips.

Figure 1.16 illustrates a typical column output signal and the relevant timing. Three pixel reads are shown in this figure, the middle pixel being illuminated by a point source and the two pixels to either side illuminated by a faint background. When the pixel output is selected, the output rises to the signal level. The reset pulse causes a spike to appear in the output. The output level then falls to the reset level. The signal is then the difference between the signal level and the reset level.

There are several sampling options available. The simplest mode available is "single sample", where one sample is taken before the reset pulse. This mode generates one data word per pixel. This mode cannot be used effectively for taking data in most cases, since it depends on the absolute stability of the output level from frame to frame, which is subject to drift.

A second type of sampling available is "double sample", where two samples are taken per pixel, one immediately before and one after the pixel reset. The first sample measures the pixel output after the integration, and the

second sample measures the output level after resetting the pixel. The difference between these two levels is the signal due to flux on the detector. There are actually two modes available for this, one named "delta reset" and the other "double sample". The delta reset timing is shown in Figure 1.17. Both take samples in the same way, but in the delta reset mode, the two samples are subtracted immediately in the fast coadder and stored as a difference. The advantage to this mode is that the number of data words that must be transferred to the computer is cut in half, making fast frame rates possible. The delta reset mode is the one used most often on the telescope when using the mid-infrared 10% bandpass filters.

Another available mode is "triple sample", where three samples are taken per pixel reset, one just before, one during, and one after the reset. The sample taken during reset is clamped to a constant reference voltage. This mode is potentially useful for relatively long integrations for near infrared observations and for high spectral resolution mid-infrared observations with a Fabry-Perot interferometer (see section 1.8.2).

1.4.4.3 Fast Coadder

The coadder adds successive frames and stores the result in the coadder memory. The SP block diagram in Figure 1.15 shows the general path of the data. The 12-bit data from the current row being read out is added to the 24-

bit coimage currently in the memory (the memory values are zero if this is the first frame). The result of this operation is then stored back in the coadder memory, overwriting the previous result. During the last frame of the coimage, the result is transferred to the FIFO memory, and the coadder memory is loaded with zeros from the second set of tri-state buffers which are connected to ground (digital zero).

The 24-bit coadder memory can store a coimage with as many as 4096 frames (12-bit per pixel) without overflowing. This means that a much slower image transfer rate between the camera and the computer can be used. For example, if the camera is operating at the maximum full frame rate of 9766 Hz, the transfer rate to the PC can be as slow as 2.4 Hz if performing the maximum number of coadds. Usually, the number of frames per coimage and the transfer rate is determined by the time for a telescope secondary half "chop" cycle, typically .05 seconds.

1.4.4.4 FIFO Memory

The FIFO memory is where the image is stored until the PC reads the data. The use of separate coadder and FIFO memory gives the camera the capability of taking a second image while preserving the first image. The read and write operations to the FIFO can be asynchronous and can be done simultaneously. The camera can therefore be continuously taking data, with

no "dead time" between images. No conflict will arise if the second image is completed before the first image is completely read out.

The implementation of the FIFO memory on the SP uses the Cypress Semiconductor CY7C421, a 512x9 bit FIFO memory. Three are used per channel, or six per SP board. 24 bits out of the total of 28 are used for data, and two bits are loaded with the current area of coadder memory, based on the sample mode. This gives a total of 26 bits of valid input. The MSB input is set to GND. There are two flag outputs of the FIFOs, a FIFO full flag and a FIFO empty. The first flag is set when a WRITE TO FIFO operation is attempted when the memory is full, and the second flag is set when a READ FROM FIFO operation is attempted when the memory is empty. These two flags are appended to the output word from the FIFOs when being read out, to make a total of 28 bits that are transferred to the PC.

1.4.5 Command and Data Link to PC

The MIRAC controller is linked to the array processor board (APB) in the PC by a serial transmission line using the "Manchester" data encoding format at 1.25 Mbit/sec. This is accomplished using two 1551 encoder/decoder chips manufactured by Harris. One chip is in an interface box connected via two 16-bit I/O cables to the APB, and the other is on the controller. One Manchester-encoded word is 32 bits long. All of the operating parameters of the camera

are set by the computer sending commands through this interface, and all data are received from the camera through this interface in the opposite direction. Appendix 4 gives a list of the commands used.

The APB sends commands to the controller through its parallel I/O bus to the interface box. The command to be sent is written by the APB as two 16-bit words, which are latched to a 32-bit bus in the interface box. The useable size of a transmitted word is 28 bits, the other bits are used in the Manchester encoding format for synchronization bits and parity. The 1551 chip then reads the data in through a parallel to serial shift register, encodes the data word, and sends it to the 1551 chip on the controller in the MIRAC electronics. Command words are accepted asynchronously by the 1551 chip on the controller and are decoded and output as a serial stream consisting of the original word sent. The data enter a serial-to-parallel shift register and are clocked in a set of latches.

The command segment of the word is sent to a decoder chip which determines which command is being sent. Based on this, the data, if any, can be sent to the appropriate latches to store the parameter just sent. For example, if the command being sent is to set the number of frames per coimage, the upper 5 bytes that carry the command will be decoded to select the frames per coimage command, and the lower 12 out of 23 bits will contain the number of frames/coimages to use. These data are latched into a register in the controller, which is used to determine when the coimage is finished by being compared to the "number of frames completed" counter. Other commands, such as the

FIFO reset, do not require any data bits in the command.

There are two types of commands that can be sent to the electronics controller from the computer, "Group 1" or data functions and "Group 2" or parameter setup functions. See Appendix 4 for a summary of the commands available. The first group of commands are always active (i.e., the controller will respond regardless of its state). These commands include the RESET commands for the controller and the SP FIFO memory, and commands to control the image recording and transferring to the computer. The second group can only be set when the camera is not "imaging", or currently sampling and storing data. This is to prevent the parameters from inadvertently being changed during an observation.

The transmission of data from the camera to the APB proceeds in a similar way, except it is initiated by a command from the APB requesting a number of words based on the current data sampling mode (1 word per pixel for single sample and delta reset, 2 for double sample and 3 for triple sample). The camera then sends the requested number of words to the APB, which places the data in memory to be used by the PC. Data words are sent in a similar way as from the APB, with the data first loaded into a shift register, clocked into the 1551 chip serially, and then transmitted to the 1551 chip on the interface, where they are decoded and sent to the computer. The image data words are 24 bits long, with the upper 4 bits used for transmitting the area of coadder memory used and the FIFO full and FIFO empty flags. These latter

flags can be used to monitor the condition of the memory to insure that images are not being overwritten.

The serial encoding chips now in use have a 1.25 Mbit transmission rate. The data words sent are 32 bits long (with 28 bits valid data), so an entire frame of 20 columns and 64 rows can be transmitted in .033 sec, or a rate of 30 Hz. For single sample or Δ reset mode, this gives a maximum chop frequency of 15 Hz (2 frames per chop cycle) when reading out the entire array.

1.4.6 Temperature Controller

The detector sensitivity and uniformity are functions of the detector operating temperature, so in order to calibrate the observations properly and to reduce noise due to drifts, the detector temperature must be maintained constant. There are four factors which affect the detector temperature: the detector self-heating, the power dissipated by the heater resistor, radiative and conductive cooling to the helium temperature cold plate, and the flux incident on the detector.

The direct connection of the detector mounting block to the cold plate is through a flexible copper heat strap attached to the base of the mounting block. The block is attached to the slide of the mounting bracket via a block of G-10 which acts as an insulator. This is done to thermally isolate the detector stage

from the cold plate so that the detector can be operated near 10K, and to insure that the dominant cooling is through the heat strap and therefore can be easily controlled by changing the size of the strap. The thermal connection can be adjusted in this way to insure that the minimum amount of extra heating is required to maintain the temperature at the proper value, minimizing the amount of helium boil-off and heat dissipation inside the dewar.

The temperature controller monitors the temperature at the detector by measuring the voltage across a calibrated diode (Lakeshore Cryogenics DT-470-SD-12) which is attached to the detector block on the sliding mount. The heater resistor is also attached to the same block. The diode calibration is valid for a 10 μ Amp current, which when at a temperature of 10K results in approximately 1.2 V across the diode. The MIRAC program, described below, continuously monitors the temperature sensor and displays the current detector temperature in real time.

The controller has two modes, a "manual" mode where the heater voltage is set directly without feedback, and the "auto" mode where the controller sets the heater voltage to maintain a selected temperature. The controller can control the temperature in the range of about 8K to 16K with a stability of .003°K rms. The controller was designed by William Hoffmann and Barry McLendon and assembled in the Steward electronics shop.

1.4.6.1 Temperature Controller Operation and Test Results

Figure 1.18 shows the cool-down of the dewar from room temperature, first after the pre-cool using LN_2 , and then after filling with helium. The time required to cool from room to LN_2 temperature is approximately 4 hours, and the time for cooling from nitrogen to helium temperature is approximately 75 minutes. Since the detector block presumably has the weakest connection to the helium reservoir, the detector temperature should be a good indicator of the complete cooldown of the system.

Figure 1.19 shows the effect of the controller being turned on and set to reach a desired temperature, and the effect when changing temperatures. Initially the heater turns full on, to heat the detector block from LHe temperature to the goal of near 8.5 K. The controller increases the heater power initially to a value greater than necessary to maintain the desired temperature, to reduce the time necessary to reach it. As the detector heats and gets near the goal, the heater power is reduced until the temperature settles on the desired value. Similarly, if reducing the temperature, the heater will reduce its power input to a value below what is required to maintain the goal temperature, in order to minimize the time necessary to reach the new temperature. If the new temperature value is drastically different from the current one, there may be some overshoot in the temperature, but it will still reach the new temperature much faster than if the heater had simply been set to the equilibrium value.

When increasing the temperature slightly, as was done from seconds 320-500 in Figure 1.19, the overshoot is less severe and the temperature stabilizes quickly. When reducing the temperature slightly, from 700-900 seconds, the heater turns off completely and the cooling time is dominated by conduction through the copper strap attached to the detector block.

The flux incident on the detector has an effect on the heating, although not a direct one. When the output level of the detector changes, it changes the amount of power being dissipated in the output MOSFET source follower. When the detector is operating under low flux conditions and the output signal is low, the voltage drop across the source follower is high, dissipating more power on the detector readout. Therefore, less heater power is required to maintain the temperature. When the detector is operating under high flux, less power is dissipated by the output source follower, so more heater power is required. This has the curious effect that when going from blanked off to fully illuminated, the heater power has to be increased, which is the opposite one would expect if the detector was being significantly heated by external radiation.

This effect is illustrated in Figure 1.20, where the detector temperature and heater power are plotted as the filters are changed between the 8.8, 9.8, and 11.7 μm filters. As the filters are changed, the detector is momentarily blanked off, the self-heating increases, and the detector temperature rises. The controller tries to compensate to this by dropping the heater power. When the new filter

is in place, the self-heating returns to close to its previous value, and the heater power rises again. The net effect of this is that about 150 seconds are necessary for the detector to stabilize between filter changes, or any other changes that increase the output level of the detector, such as changing the delay or frame rate. It should be noted that this test was performed before the temperature controller was properly optimized, so this is perhaps a worst case.

Since these tests were done, several changes were made in the thermal connections of the detector stage. The heat strap was making poor contact with the cold plate because of loose connections, so the strap was tightened and had to be significantly reduced in size. Also, the detector cover was not properly tightened, so parts of the detector stage were not thermally connected. When these changes were completed, the heat transfer properties were measured by monitoring the temperature in the 8-12 K range under changing heater power inputs. The thermal conductivity to the LHe cold plate from all paths was determined to be 5.7 mW/K. The contribution to the conductivity from the heat strap was determined from measuring the total conductivity as the width of the strap was reduced. The conductivity of the strap currently being used is 3.6 mW/K. The heat capacity of the detector block is 2.77 J/K, for a time constant of 485 sec.

1.4.6.2 Temperature Controller Performance

The temperature controller circuit was optimized for the MIRAC dewar before the most recent observing run from June 1-3, 1991. The relevant parameters of the dewar are the heat capacity of the detector block and the cooling power of the copper strap in the temperature range near 10K. The strap had recently been modified so that the self-heating of the array would bring the temperature to 8.5 K for a V_{ADJ} of -5 V, so that the extra heater power required would not be excessive yet allow good control of the temperature near 10K.

The temperature of the detector and the heater power at the time of each observation are recorded in the observation file header. Several hundred observations are taken on a night with good weather. From these data, a record of these parameters can be compiled for the entire night. This was done for the night of June 3, 1991, and the results are displayed in Figure 1.21. The first graph shows the temperature of the detector, and the second graph shows the heater power. Except for a few short spikes, the temperature for each observation can be seen to be within a total range of about .005°K. Excluding the first 50 minutes of the night, the average temperature is 10.022°K, with a standard deviation of .003°K. The largest variations can be understood as changing flux levels incident on the detector. During the first 40 minutes of the night, flat field integrations were being taken, which involves obtaining images at many different filter positions and two different sky positions. During the

rest of the night, the variations can be caused by filter changes, or when the telescope is pointed at a different source. When the pointing of the telescope is changed to a new object, the telescope can momentarily point at the dome, which saturates the detector.

1.4.7 Power Supply and Grounding

Each subsystem of the MIRAC electronics is separated, in most cases into its own shielded enclosure, to prevent additional noise on the detector signal. Each of these separate systems has its own power supplies, in order to isolate it further from the other subsystems. In total, eight separate supplies are necessary. For the portability requirement for MIRAC, the supplies were designed to be easily portable and convenient to set up. The power supply was designed by Frank Laccata and assembled by Peter Crawford at SAO.

1.4.7.1 Power Supply

The DC power supplies for the controller, signal processor, preamp, bias supply, and temperature controller electronics are housed in a single suitcase style aluminum case, approximately 43 x 53 x 19 cm. The power supplies are from Power One, Inc., and are summarized in Table 1.5. The voltage of each supply is higher than what is necessary for the components on the board,

allowing for a voltage drop in the power cable and on-board voltage regulators.

Table 1.5 MIRAC Power Supplies

Electronics Subsystem	Power One Model #	Output Volts	Voltage On Board	Amp Rating
Preamp	HAA24-0.6-A	± 24	± 15	.6
Bias	HAA24-0.6-A	± 24	$\pm 15, \pm 10$.6
Camera Clock	HB12-1.7-A	-12	-4	1.7
A/D Converters	HB12-1.7-A	-12	-5.2	1.7
Analog Processor	HN24-3.6-A	24	15	3.6
Analog Processor	HN24-3.6-A	-24	-15	3.6
A/D and Fast Coadd Logic	HE12-10.2-A	12	5	10.2
Detector Heater	HAD15-0.4-A	± 15	± 12	.4

All of these supplies are mounted to the panel in the lower half of the power supply case. There is an ELCO connector on the front panel for the power cable, a number of power supply status LED indicators, a multiple-pole switch and two test points where currents can be monitored, power switches for electronics and temperature monitor and heater power, and a standard 3-prong A/C power cord.

An interlock circuit prevents the power supply from providing power to the camera electronics if the power cable is not plugged in properly, or if the detector is above the maximum safe operating temperature. This prevents accidental damage of the detector if the dewar has for some reason warmed up. This circuit also provides a short time delay after the A/C power to the supplies is turned on, to allow them to stabilize to their proper output values and to prevent any voltage spikes from propagating to the camera electronics.

As mentioned above, there are on-board voltage regulators that provide a stable, low noise voltage of the proper value. This provides isolation of the electronics from noise pickup on the long power cable, as well as isolation between the various systems on the same board. This is especially important on the controller and signal processor boards. The clock signals necessary to run the detector are generated on the controller, and separate voltage regulators and optical isolators prevent pickup from the digital signals on the controller. On the signal processor, the analog section and the A/D converters use a separate voltage regulator from the digital logic of the fast coadder and FIFO. This prevents noise from being introduced before the A/D conversion takes place.

An additional benefit of separate supplies and regulators on the boards is that when problems occur, they are relatively isolated and can be located easily. For example, there were a few bypass capacitors that failed on the signal processor boards after several hours of use. The output at the computer

quickly shows which signal processor boards are not working. There was no short when tested with an ohm meter, but when power was turned on, the voltage drop across the regulator indicated that the current had reached the regulator's maximum rating.

1.4.7.2 Grounding

The grounding within the MIRAC electronics has been carefully designed to prevent noise and ground current loops within the system. The camera and electronics are isolated and all electrical connections to the telescope control room are through the power cable. The dewar is isolated from its mounting plate and the telescope through G-10 spacers and nylon washers. The camera is isolated from the computer through optical isolators on the serial transmission line.

All of the power supply returns are brought out to the electronics separately in the power cable. Earth ground is also brought out on a separate line and connected to the electronics backplane. The power supply returns (except for the biases, isolated clock drivers, and preamp), earth ground, and the electronics chassis are connected together at the electronics backplane. The dewar case is connected to the electronics chassis via its mechanical mounting. The returns for the bias supplies and isolated clocks are connected to the dewar case at the top of the dewar near the connector. The return from the detector

is also connected to the dewar at this point. The preamp return is connected to the electronics chassis. On the SP boards, the analog and digital returns are also tied together at the A/D converter.

1.5 MIRAC Computer and Interface

1.5.1 Data and Command Interface/Local Controller

The interface between the MIRAC electronics and the APB discussed above also serves as a "local controller" that enables commands to be sent without the computer. The interface detects whether it is connected to the PC. If not, the encoder switches to local mode, where the commands are entered using a set of thumbwheel switches and a push button to send the command. All the commands may be sent in this way to initialize the camera to the desired operating parameters.

1.5.2 Array Processor Board (APB)

All communication to the MIRAC electronics as well as control of data transfer and chopping is done through an AT-compatible coprocessor board called the SKY 321-PC array processor, made by Sky Computers, Inc. This board utilizes the Texas Instruments TMS 32010 digital signal processor, a 25-MHz fixed-point 16-bit processor, with a 32-bit accumulator, 16x16 bit hardware multiply instruction, 4K program memory and 144 bytes of on-chip RAM. A block diagram of the SKY board is given in Figure 1.22. It has several registers that can be assigned to I/O ports on the PC, and 64K of data RAM which is memory-mapped onto the PC address space. This results in increased

speed and flexibility, since no explicit data transfer is necessary between the SKY board and the PC -- the data are just read and written directly to memory by both the PC and SKY board. The SKY board is also equipped with two 16-bit auxiliary ports for input and output, based on an extension of the DT-Connect format, a protocol designed by the Data Translation Corp. for use with their A/D and frame processing boards. These ports are used to communicate with the camera through the local controller/interface. There are a few additional I/O bits that provide control of the data I/O to the interface and from the camera, and four digital outputs, one of which controls the chopping of the telescope. Programs for the SKY board are written in TMS 32010 assembly language and are compiled on the PC. The object code is then written to the program memory on the board directly by the PC.

The operation of the SKY APB program is shown in Figure 1.23a. There are three main functions of the APB program: to receive command words from the PC to send to the camera electronics, to coadd images and alert the PC when the image is finished, and to receive commands from the PC to set parameters within the APB program. After initialization, the APB enters a main "polling" loop where it checks the status of registers and takes the appropriate action. In the first function, the APB enters into a mode where it transfers all data received from the PC to the camera, until the mode is terminated by the PC. Control of this transfer is through the STCREG, or status and control register, and the data are transferred through the COMREG register. The camera initialization and operating parameters are set in this

mode, as well as sending the BEGIN and END COADD. Depending on the observing mode, the PC also sets variables in the APB program. These include whether to chop or not, how many coimages in the image, how many coimages per chop cycle, the chop wait time, etc. These are set by writing the parameters to the shared data memory, then commanding the APB processor to read these parameters into its on-chip memory.

Figure 1.23b illustrates the operation of the image transfer and coadd routine. There are two basic data taking modes which the APB controls, the "Grab" mode and the "Chop" mode. (For wobbling the telescope, the PC does a series of GRAB or CHOP images.) In the grab mode, the APB constructs a single image from the coimages sent from the camera. When the required number of coimages has been recorded, the camera is sent the STOP command. In the chop mode, two separate images are constructed at the same time, one for each chop beam. In between each chop phase, the camera is stopped, the chop beam changed, time is allowed for the chopper to settle, and the START COIMAGE command must be sent. This procedure is repeated until the desired integration time on source is reached. In both modes, when the number of coadds has been taken, the APB halts the camera and notifies the PC that the image is ready. When the PC is done storing the data, it signals the APB to continue observing, or to wait for the next command.

Figure 1.23c shows the procedure on the APB and on the PC for transferring command words from the PC to the APB. Three flag bits and one

8-bit data port is used to transfer the 16-bit command words. The routine to send commands to the electronics from the PC is similar. When the data word is received from the PC, the APB calls the subroutine to send the word to the electronics, then returns to this procedure to accept the next word from the PC.

1.5.3 MIRAC PC Control Program

The main tasks of the PC control program are to send the operating parameters to the APB and the camera, to initiate the data taking and store the images, and to display the images and provide simple data analysis functions. Also, since image accumulation times are often several minutes, it is desirable to be able to perform display and analysis functions while the camera is taking data. An additional goal was to make the program relatively simple to operate, so that it could be used by new observers with minimum instruction and possibility for user-generated errors.

These designs were implemented in the control program called MIRAC, written in Turbo Pascal v. 5.0 for an MS-DOS computer. The program will run in any IBM-compatible PC running DOS v. 3.3 or above, with 640K RAM and an available 8-bit slot for the APB and available address space between 640K and 1 MB. The program can be run on any PC without the APB to use the data analysis and display functions on previously obtained data. A hard drive is recommended for fast storage and retrieval of data. If a math coprocessor

is in the system, the program will use it to increase the speed of calculations. The program uses overlays to swap out parts of the program that are not currently being used, allowing the program and data space to be larger than 640K. The unused code is stored in expanded memory and swapped as needed. If the PC has no expanded memory, the overlays are swapped to the disk. The overlay operation is completely automatic and transparent to the user. The computer now used is a Gateway 2000, a 25-MHz 386 IBM PC-compatible, with 4 MB of RAM, 150 MB hard drive, 80387 math coprocessor, and a monochrome VGA display.

1.5.3.1 MIRAC Program Structure

The user interface structure in the MIRAC program consists of a command line menu across the top of the screen, with pull-down menus for each general heading. See Figure 1.24 for an illustration of the program's main screen. There are several command line menus, each containing pull-down menus and entries to move between the command lines. There are four command lines: OBS (Observe), DISP (Display), PRN (Printer), and UTIL (Utilities). The OBS menu controls the camera operating parameters and observing modes. The filter can be selected, general features of the program set up (i.e., the directory where images are stored, initializing the APB, etc.), and the user can start the process of taking data. The DISP menu includes choices of how the observations are displayed, including using a gain matrix

and/or flat field automatically. Simple data reduction can be done, such as flat fielding and adding images together using offsets to construct a mosaic image. Previously stored images can be read in and displayed. The PRN menu controls the hardcopy functions, usually to a grayscale image printed on a HP laser printer. Figure 1.25 shows an example of this printout. All of the relevant header parameter values are printed at the top of the output. Below that are various statistics on the image, including the total source counts and background RMS. The UTIL menu provides access to DOS functions, file output utilities, macro definitions, and system information.

The current camera and program operating parameters are stored in a default file on the PC. All of these are collectively called the "header", since this information is written to the beginning of every image file stored. The header information may also be stored to other files and read in from the program by name, making it possible to keep default files for different telescopes or observing conditions.

The most common display mode used is one that displays the most recent image taken, shown in Figure 1.24. At the top of the screen, below the command line, are some of the current camera parameters. The temperature of the detector is measured and displayed once a second, to allow for monitoring. The image is displayed in the center of the screen with a 16-level grayscale that can be autoscaled or the limits fixed to user-supplied values. For chopped images and nod sets, the off-source images are automatically

subtracted. If a gain matrix or flat field has been chosen, it is applied to the image before being displayed. A summary of statistics of the image is given below, including the average and RMS for the whole map, as well as for any source in the image and the background. This gives a quick indication of the signal to noise of each image. If a source is detected in the image, a gaussian profile is fit to the source in both directions, and the source position and FWHM are displayed. The numbers labeled "SKY FLUX" are the level of one of the off-source images in the chop pair or nod set, and that number compared to the last several images. This gives an indication of the absolute sky flux, and can be used to indicate when the sky is varying rapidly.

At the bottom of the display screen are two status lines. The first displays the time, date, and the current object name. The camera status is also displayed. The status can be "DATA" for taking an image, "IDLE" for no activity, "STORE" for writing an image to disk, "WAIT" for pausing during an observation. If observations are being taken, the time left in the current observation is displayed compared to the total time, and the current observation number compared to the total number to be taken. The second line displays information on the current data being displayed: the time and date of the displayed observation, and the source and file name.

1.5.3.2 MIRAC Data Files

The images from the camera can be viewed only, viewed and saved, or only saved. The data file names are chosen automatically, in a format which includes the date and image number, for example, "C910528A.001", which is the first data file saved on May 28, 1991. The image files all start with the letter "C", followed by the last two digits of the current year, two digits each for the month and day, and an index letter that starts at "A". The file extension is a number that begins at "001" and increments automatically until 999. At this point, the index letter is incremented from "A" to "B" and the numbers go to zero. The file is therefore fully specified by the date, index letter, and number. The "header" of the data file includes all the information on camera parameters, program operating modes, and source information. The data are stored without change directly from the APB. For example, if the camera is being operated in double sample mode, both the "before reset" and "after reset" values are stored for each pixel in the image. In addition, if the image is taken in the chop or nod mode, all the images in that set are stored in the same file. When the picture is retrieved from disk, all the necessary arithmetic, such as subtracting off-source images and multiplying by a gain matrix, is done automatically, according to the information in the file header. This can also be overridden, and each individual frame in the file displayed separately.

While observing, a log file can also be kept automatically by the program. This is a text file that keeps track of the images taken during a night

of observing. The file begins with a listing of the current header parameters. After this information, one line is written for every observation, with the following information: File number, date, time, wavelength, integration time, object name, and offsets. This file can be viewed from within MIRAC, in case one needs to double check the observations that have been performed during that particular session. If the program is terminated, when the program is started again the new observations are appended to the old list for that session, unless a new file is started. A new file is automatically started for a new night of observing.

1.5.3.3 Telescope Control

The MIRAC program has a number of options to control the operation of the telescope. The chop signal is generated by the APB and the output is located on the local controller/interface box. This is a 0 to 5 V logic level, with 0 specifying the first chop beam and 5 V the second chop beam. The "on-source" beam is software selectable.

There are a number of different options for controlling the telescope wobble motion. One option is to output a logic level to specify the beam. This can be used on the SO 2.3 and 1.5 m telescopes, which have a wobble interface that accepts a logic level input. This output is provided on the A/D breakout box (the same box that connects to the dewar temperature monitor). Another

possibility is to trigger the telescope wobble using a logic pulse. This is necessary for the IRTF telescope control. Either a positive (0 - 5 - 0 V) or negative-going (5 - 0 - 5 V) pulse can be selected.

On the SO 2.3 and 1.5 m telescopes, the telescope can also be controlled by sending ASCII commands via a RS232 interface to the mount micro. In addition to the wobble beam control, other telescope parameters and commands can be sent, such as setting the guide and drift rates, RA and Dec bias rates, setting offset and wobble vectors, and various telescope motion commands.

The MIRAC PC program has the ability to control the telescope offsetting for a series of observations, in order to construct a mosaic image. The offsets may be entered in an "absolute" mode, where a zero point is defined and all offsets are relative to that initial position, or a "relative" offset, where the offsets are relative to the previous observation. All offsets can be entered in units of pixels or arcsec RA and DEC, and the program, using the plate scale of the telescope and the camera magnification, calculates the offset in RA seconds of time and Dec arcsec. Before each observation, the observer has a chance to enter the desired offsets, and the PC then sends the offsets, moves the telescope, and after an appropriate delay starts the observation. These offset values are saved to the image file header, so when the images are combined these offsets can be used to align the images.

1.5.3.4 Image Display and Processing

There are a number of built-in display capabilities in the MIRAC program. These include contour images, grayscale maps, and "cuts", or a plot of a single row or column. The current image can be displayed, or previous images read from disk files. These displays can be printed, and there are additional printout options, such as printing out the values in a map, or doing statistics on the rows or columns. Figure 1.25 shows a typical printout of an image. All the camera parameters and observing conditions are displayed in the top section of the output. Some statistics of the image are displayed, similar to the observing screen. The grayscale image is printed at the bottom.

The MIRAC program has the capability to perform simple image processing tasks. Gain matrices and/or flat fields can be applied to an image, an image can be smoothed, and images can be added, subtracted, multiplied, or divided by constants or other images. A mosaic utility also exists, where the images can be combined using offsets from a number of sources. If the telescope was being controlled by the PC, the offsets stored in the file header can be used. The user may also type in offsets, or select to have them read in from a file. The offsets can also be calculated by the mosaic routine, by aligning the peak values, calculating the centroid, or a cross-correlation calculation. The images are shifted and averaged.

For additional processing, a utility exists within the MIRAC program to

convert the image files to FITS format, and can be read directly by IRAF or another image processing program. The utility program reads in the image file and performs the subtractions and gain matrix arithmetic, and can also expand the map into subpixels for more accurate registration of the images. The images are written to FITS files on the PC, which can be transferred to other computers by copying to disks or using ethernet, if available.

1.6 Guider Box

The Guider box has two main functions: to provide the mechanical connection from the dewar and TV monitor to the telescope, and to bring the telescope beam into these instruments. Figure 1.26 illustrates the basic design of the guider box. It is a rectangular, anodized aluminum box, with a round flange on the top for mounting to the telescope. The beam exits the telescope at the Cassegrain focus and enters the guider box through a hole in the top. There is a large mirror that can be rotated into the beam near the midpoint of the guider box. This mirror can be used with an eyepiece attached at the viewport, but is usually in the stow position, out of the field of view of the camera. The telescope beam first encounters a beamsplitter, which reflects the IR radiation to the side where the MIRAC is mounted. Some of the optical light passes through the beamsplitter and is reflected by other mirrors into the TV guider. This design allows for simultaneous viewing of the source for guiding while the IR image is being taken. The guider box design was modified and fabricated by Tom Tysenn, and the coupling between the dewar and guider box was designed by Dick Young.

1.6.1 Optics - Dichroic, Optical Flats

The beamsplitter and mirrors in the guider box are shown in Figure 1.26, along with the two telescope focus positions for the MIRAC high and low

magnification settings. In order for the TV guider to be in focus at each of the positions, two folding flats are used to provide additional optical path length, and the third flat changes positions to add or remove these mirrors from the path. When the rotating flat is in position shown in Figure 1.26a, the telescope beam is reflected directly from the rotating flat into the TV guider relay optics. For the high magnification case, the mirror is rotated into the position shown in Figure 1.26b, and the telescope beam is reflected from the lower two mirrors first before being reflected by the rotating mirror into the TV guider optics, thereby adding 12.54 cm to the path length to allow the TV to remain in focus. The moving mirror rotates on a shaft mounted in bearings pressed into the side of the guider box, and each position is defined by a hard stop. The position of this hard stop is adjustable using a screw mechanism attached to a knob outside of the guider box.

The dichroic mirror is mounted in a cell in which the tilt of the mirror is adjustable using a spring-loaded "floating" mirror holding bracket. This cell moves above a fixed plate that is connected to the outer walls of the box. This is illustrated in Figure 1.27. One corner of the mirror holder rests on a steel ball on which it can pivot. There are recesses in the plates where the ball sits, and the two plates are pulled together by three springs. In the two corners next to the corner with the ball, springs pull the mounting plate against adjustment screws that are linked to knobs outside the guider box. Turning the knobs causes that corner of the mirror to rise or fall, resulting in an almost pure E-W and N-S adjustment of the beam.

1.6.2 Mechanical Coupling of Dewar and Box to Telescope

The guider box is connected to the telescope by at least three 5/8" bolts that connect the mounting flange to the Cassegrain mount of the telescope. The dewar is connected to the guider box via the interface illustrated in Figure 1.28. A mounting plate is bolted to the dewar using G-10 spacers and nylon sleeves around the bolts to achieve electrical isolation from the telescope. The surface of the mounting plate that attaches to the telescope has a slot in the center and a stainless steel tooling ball mounted near the top. Two captive bolts on either side of the slot are mounted in the plate. The guider box has a steel block near the top with a hemisphere recess in the top to accept the ball on the dewar mounting plate. About midway down the guider box there is a block with a ridge which fits into the slot on the mounting plate, and two threaded holes in which the captive bolts on the plate attach.

This design makes it easy to mount the dewar on the telescope. To attach the dewar, the dewar is lifted to the guider box, tipping the top forward slightly. The ball is inserted into the hole and the slot is aligned with the ridge, and the dewar is slowly lowered to lock it into place. At this point the dewar is held to the box, and the two captive attachment screws can be tightened to secure the camera.

1.6.3 TV Guider Port

The TV camera mounts on the guider box on the opposite side from the dewar. The camera bolts to a tube that extends out from the face of the box. This tube contains reimaging optics to focus the image of the star on the TV, accounting for the longer optical path and the focus of the TV camera. The TV camera focus is almost even with the plane of the front surface of the mounting flange, and the telescope is focused for MIRAC, which has its focus at 13.72 cm in front of the dewar window for low magnification, or 1.176 cm for high magnification. This puts the telescope focus in front of the dichroic for low magnification, and a few centimeters past the dichroic for high magnification.

1.7 MIRAC Test Results and Performance Evaluation

1.7.1 Initial Tests, Corrections to Reduce Noise

Before the current electronics system was built, the detector was operated with a prototype controller and bias board, with one completed preamp board and no digital processing. The detector output was monitored at the output of the dewar and preamp, using a frame "synch" pulse generated on the controller board which could be used to determine the pixel address that was being reset.

There were a few initial problems with the electronics that had to be overcome before the detector could be successfully operated. One problem was that V_{CSD} , a detector test point, had to be left floating for the detector to operate properly, whereas it was at first set to 0 V initially with its own bias power supply amplifier. The other problem was that the detector reset pulse was the wrong polarity. To reset properly it must be held at logic 1 (-4 V) throughout the integration and pulsed to logic 0 (-1 V) during reset. Initially, the electronics were designed to do the opposite.

A number of noise problems were observed in these tests. First, digital pickup on the bias supply circuit at the controller board was measured to be on the order of 300 mV. This noise signal was present on all power supplies, ground planes, and bias supply outputs. There was no single digital chip or

line that was causing the noise. When we attempted to determine the source of the noise by removing the digital chips one by one and measuring the noise at each stage, the noise was reduced by approximately an equal amount for every chip removed. No amount of filter capacitors or rerouting of digital lines could reduce the noise significantly. Filter capacitors built into the bias supply cable leading to the dewar also did not eliminate the noise. It was because of this result that the decision was made to place the detector bias supplies in a separate box that was shielded completely from the digital electronics.

Even when shielded in this way, the detector bias supply voltages and the clock signals come in close proximity, since they share a connector on the top of the dewar and a connector at the detector mount in the dewar. As a precaution, the filter capacitors in the bias cable were left in place, and as recommended by Hughes, additional bypass capacitors were installed on the connector board inside the dewar. The capacitors installed were Vitramon #VJ2321A223 GFA, type NPO. These low temperature coefficient capacitors have a value of $.022 \mu\text{F}$ ($\pm 2\%$) and were supplied by Hughes. With the permanent controller board and self-contained bias supply currently in use, carried out with the grounding protocols described above, the bias line noise problems did not occur.

Several detector parameters were measured during these tests. These measurements should be considered to be preliminary and approximate. The mean transimpedance of the array was determined by measuring the voltage

across a current sensing resistor in the V_{DET} line for the pupil blanked off and for the pupil open to f/45, 8.8 μm , and the 20% neutral density filter. This is a measure of the total detector current for the 1280 pixels. The results are summarized in Table 1.6.

Table 1.6 Transimpedance Determination			
Current sensing resistor	$R = 24.3 \text{ K}\Omega$		
Resistor voltage	Blanked	Open	
Total array current	.045	2.55	mV
	.0019	.105	μA
Number of pixels	1280		
Total current difference per pixel	.0805	namps	
Integration time	100	μsec	
Integrated charge per pixel	8.05×10^{-15}	coulomb	
	5.03×10^4	electron	
Detector output voltage difference (for a "typical" pixel)	.31	V	
Transimpedance (V/Q)	$1/.026$	pf^{-1}	
	6.2×10^{-6}	Volts/electron	

The saturation voltage difference for a typical pixel (column 6 row 34) was measured to be .9 V, with a linear range of .75 V. In terms of electrons, the full well is 1.45×10^5 and the linear range is 1.25×10^5 electrons.

The responsivity of the detector in amp/watt and e-/photon at the four mid-infrared filter wavelengths was determined from the measurement of the output of a "typical" pixel (column 6 row 34) with the calculated photon flux and the flux calibration performed with the Hughes calibrated detector. The solid angle was estimated from the design pupil size and pupil-to-detector

spacing at low magnification. The area of the pixel was taken to be $(.95 \mu\text{m})^2$. The result of this calculation is shown in Table 1.7. The measurements of signal correspond to the signal difference between a 319K blackbody and the chopper blade at a temperature of 295K. The calculated QE agrees reasonably well with the expected value of approximately .23 at $10 \mu\text{m}$. The significance of Table 1.7 is not so much a determination of detector properties as a check on the consistency of the values used for filter transmission, camera solid angle, optics efficiency, etc. The reference detector mentioned is the Hughes calibrated reference detector.

Table 1.7 Responsivity Determination

Integration time	$t = 100 \mu\text{sec}$			
Solid angle at detector	$\Omega = 4.6 \cdot 10^{-3} \text{ ster}$			
Area of pixel	$A = 9.03^{-5} \text{ cm}^2$			
Window Transmission	$t_w = .8$			
Optics Reflectivity	$t_o = .9$			
Attenuator	$t_A = .20$			
	Filter wavelength (μm)			
	8.8	9.8	11.7	12.5
Output (volts)	.34	.6	.54	.7
Output ($10^4 \text{ e-}/\text{pix-read}$)	5.5	9.7	8.7	11
Output ($10^{-9}\text{amp}/\text{pixel}$)	.088	.16	.14	.18
Filter bandwidth (μm)	.82	.93	1.03	1.07
Peak transmission	.83	.81	.81	.71
Planck power ($10^{-11} \text{ W}/\text{pixel}$)	3.6	4.2	4.3	3.7
Planck photon rate ($10^5 \text{ photons}/\text{pixel-read}$)	1.6	2.2	2.7	2.4
Response (amp/watt)	2.4	3.8	3.2	4.9
Response (e-/photon)	.33	.45	.32	.47
Detector electron gain = 1.4				
Calculated QE	.23	.32	.23	.34
Reference detector calibration				
Output ($10^{-9}\text{amp}/\text{mm}$)	3.2	6.2	7.6	7.8
Output ($10^{-11}\text{amp}/\text{pixel}$)	3.2	6.2	7.6	7.8
Ratio of array to reference detector	2.8	2.6	1.8	2.3

These calculations do not take into account the detailed shape of the filter transmission curve and the detector response. Also, the emission of the dewar window, and the known undersize of the f/45 pupil add some uncertainty to the calculations.

1.7.2 Background Measurements Using Calibrated Detector

The background level in the dewar was checked independently by using a calibrated detector loaned to us by Hughes. At the time of this test, the gold plated surfaces inside the optics housing, the filter wheels, and detector section of the helium-shielded area had not yet been painted black, and not all baffles were in place. The measured background with both filter wheels and the pupil blanked off was $1.5 \cdot 10^9$ photons $\text{cm}^{-2} \text{sec}^{-1}$. This is compared to $1.2 \cdot 10^{15}$ photons $\text{cm}^{-2} \text{sec}^{-1}$ for a 77K source, or $1.4 \cdot 10^{18}$ photons $\text{cm}^{-2} \text{sec}^{-1}$ for a 295K source (π ster). These photon fluxes are for the full bandwidth of the Si:As detector which peaks at 22 μm and has a cutoff at 25 μm .

Other measurements were made with various attenuator and filter combinations. It was found that the ND attenuators did not reduce the flux by the expected amounts, and it was consistent with approximately 2% of the flux that passes through the first filter wheel bypassing the second wheel. This was attributed to radiation reflected from the gold coated surfaces and reaching the detector. All surfaces have since been painted black, so the background is likely to be lower than reported here, with less radiation bypassing the filters.

1.7.3 Optimization of MIRAC Detector

An optimization of the detector was performed by first choosing a

method to measure signal to noise, and then varying each of the parameters independently from their canonical values and measuring the effect on signal to noise (S/N). The parameters could of course be interrelated in some complex way and would require changing several parameters simultaneously. However, one would hope that testing each one individually would identify the critical parameters on which to concentrate.

The test setup is illustrated in Figure 1.29. The blackbody source was positioned behind a plate with a hole. A chopper which is controlled by the observing program is placed in front of the hole. The signal measured was the difference between the blackbody and the room temperature chopper blade. Chopping was done at .585 Hz. The camera was operated at 7.5 MHz clock frequency, Half Array mode, 6400 coadds per chop phase, and a detector temperature of 11.52K. The signal was measured at .5 Hz, and the noise measurements were done at 12.2 Hz, 7600 coadds per chop phase. The data were obtained in the following way: at a particular parameter setting, three chop sets were done. In each of these chop sets, the off-source (chopper blade) frame was subtracted from the on-source (blackbody) frame and the result was multiplied by a gain matrix. The average of the resultant maps gave the "signal" used in the S/N calculations. The noise was measured by turning off the mechanical chopper, increasing the chop frequency to 12.2 Hz, and taking six images staring at the blackbody. The RMS of all pixels in the flat-fielded chop difference was calculated for each of the six measurements, and the average was taken to be the "noise" in the S/N calculations. The detector was

tested at 8.8 μm , with the 20% neutral density attenuator, a blackbody temperature of 310K, chopper temperature of 295K, and a frame rate of 9765 frames/sec. This background closely approximated the expected background at the telescope, and the chopping frequency was chosen to be close to the 9-12 Hz rates used on the telescope.

Table 1.8 lists the results of the optimization test. For each of the bias voltages, the S/N was measured for the "nominal" case, equal to the bias values recommended by Hughes. The S/N was also measured at the two other voltages given on that line, which are a small amount above (+) and below (-) the nominal value. The voltages are all given in the three columns marked "Settings", for the "-", "nominal", and "+" case. The second set of three columns give the S/N for each of the settings. The middle column S/N ratios were all measured at the same nominal settings, so it gives an indication of the scatter in the S/N values. The average nominal S/N is 3990, with a standard deviation of 85 (2%), so S/N ratio differences of a few percent are not significant. In the "-" and "+" columns, the S/N measured is given, along with the percentage change from the nominal S/N in that row.

Table 1.8 MIRAC Optimization Data

Parameter	SETTINGS			S/N at		
	-	Nominal	+	-	Nominal	+
V _{SUB}	8.89	9.0	9.29	4147 (+.39%)	3992	4021 (-1.7%)
I _{SS1}	4.85	5.05	5.25	3953 (-1.7%)	4021	4094 (+1.8%)
V _{SS0}	2.832	3.032	3.232	4176 (+6.6%)	3918	4176 (+6.4%)
V _{DD2}	0.319	0.518	.717	3804 (-4.0%)	3962	4045 (+2.1%)
V _{SS3}	-.102	0	.100	4064 (+2.2%)	3975	4030 (+1.4%)
V _{SSD}	-1.229	-1.029	-.829	5111 (+28.6%)	3973	4142 (+4.3%)
V _{CAS}	-2.216	-2.016	-1.816	3942 (-0.7%)	3971	3835 (-3.4%)
V _{DD2}	-2.217	-2.017	-1.817	3926 (+0.4%)	3911	4008 (+2.4%)
V _{DD1}	-3.222	-3.022	-2.822	4000 (+3.9%)	3851	4008 (+4.1%)
V _{DET}	-2.820	-2.620	-2.420	4077 (+2.7%)	3969	4055 (+2.2%)
V _{RST}	-4.22	-4.02	-3.82	4042 (-1.8%)	4115	4034 (-2.0%)
V _{EN}	-4.19	-3.99	-3.79	4070 (-3.0%)	4199	4052 (-3.5%)
V _{ADJ}	-7.02	-6.02	-5.02	3917 (-2.6%)	4023	4188 (+4.1%)

Other parameters:

Bandwidth (relative to 1400 KHz)			
(KHz)	175	350	700
S/N	3899	4072	4082
% change	+2.3	+6.8	+7.1
Temperature (relative to 11.52K)			
°K	10.23	10.54	11.52
S/N	4097	4008	3938
% change	+3.9%	+1.8%	...
			12.51
			3755
			-4.6%

The tests confirmed that the system parameter settings used were close to optimum, and in most cases there were no indications that changes were necessary. One exception seems to be V_{SSD} where an increase of 28% is shown, but it was discovered that the readout was saturating at the high background position, so that the noise was not being sampled properly. There is evidence for a trend towards higher S/N at lower temperatures, so a new operating temperature of 10.0K was chosen. This temperature was chosen since it was a canonical value used by Hughes. The behavior of the array was well understood at this temperature and it would be easier to compare our tests with previous results.

Additional tests were performed on V_{ADJ} and V_{DET} , illustrated in Figure 1.30. The S/N measured for the V_{DET} values shown in Figure 1.30a seemed to be fairly flat across a range from -2.8 V to -2.2 V, and then dropped sharply down outside this range. The slight peak at -2.2 V is inside the scatter seen at -2.6 V where several measurements were taken, so is not considered a significant S/N peak. We concluded that V_{DET} could be left at -2.6 V. Similarly, the response of S/N to V_{ADJ} shown in Figure 1.30b seems to be flat across the range tested, all points within the scatter at -6.0 V. Two other factors affect our choice of V_{ADJ} . Making V_{ADJ} more negative dissipates more power in the detector, increasing the self-heating. Making V_{ADJ} more positive lowers the voltage across the output MOSFET source follower and reduces the bandwidth of the readout. It was decided to reduce V_{ADJ} to -5.0 V, to reduce the detector self-heating. This also allows the temperature controller to regulate

the temperature more effectively. Reducing this any further would begin to limit severely the bandwidth and reduce our ability to run at high frame rates.

1.7.4 Performance Results: Noise, Sensitivity

During the evaluation and testing of the electronics with the final version of the controller board and the new multilayer printed circuit signal processor boards, much effort was put into reducing the extraneous noise sources in an attempt to keep the noise without the array to less than one least significant bit (LSB) of the A/D converter. The main sources of noise were determined to be "pickup" in the analog section of the signal processor of the digital signals present on the same board.

The noise in the analog section was occurring even though the analog circuit had been segregated into the front corners of the board with a separated ground plane. The magnitude of the pickup was extremely sensitive to the distance the analog component was from the nearest digital line. Several digital data printed circuit traces were incorrectly located under the analog section of the board. When these were re-routed with wires above the board and the original traces connected to analog ground, the noise was greatly reduced. In addition, there was one particular node (connected to the summing input of the second amplifier stage on the SP board) which exhibited extra noise that could not be reduced. This node had to be bypassed, mounting the

components above the circuit board. After these modifications, our noise goals were met, with a typical single sample noise of .35 LSB rms (.11 mV rms at the preamp input) with a 1 MHz signal bandwidth.

Additional testing was conducted to demonstrate the background-limited noise performance of the array. Measurements were made in the lab of the noise as a function of flux, using different filters and neutral density attenuators to achieve a variety of flux levels. The noise was determined for each pixel and then averaged over all pixels in the column. The noise was defined as the standard deviation of the value of a pixel in 100 consecutive coimages, each coimage formed from an average of 1500 consecutive frames. The standard deviation was then multiplied by the square root of 1500 to obtain the standard deviation expected from a single frame. The array was operated at a 0.1 msec frame rate and 3.2 μ sec pixel sample interval. Images were combined in a "pseudo-chop" mode at 32 Hz, where consecutive 16 msec long coimages were alternately added and subtracted. This was to suppress any drift in the background or electronics during the integration.

The results of these measurements are shown in Figure 1.31. The measurements are of two quantities, the background voltage and the noise voltage. The transimpedance of the array (g) is known from the measurements presented above. Noise results in the signal from the random nature of the conversion of photons to electrons and the motion of charge carriers through the detector. Assuming Poisson statistics, the number of noise electrons n_e is

a function of the number of signal electrons N_e :

$$n_e^2 = N_e \quad (1)$$

The photons are converted to electrons at a ratio given by the quantum efficiency of the detector. The detector has an electron gain, represented by G , which gives the rate at which photoelectrons are multiplied within the detector. The current due to these electrons is amplified by the CTIA of the readout and is measured as a voltage at the output, V . The following equation gives the relation between the detector properties and the output voltage:

$$V = N_e G g \quad (2)$$

The noise electrons n_e are amplified by the same processes that the signal electrons are, so the output noise voltage v is given by

$$v = n_e G g \quad (3)$$

Using the above relations, a relation for the noise voltage as a function of the measured parameters can be written:

$$v^2 = V g G \quad (4)$$

This relation is strictly true only for each individual pixel. The difficulty in measuring these quantities is that g and G cannot be measured for each

individual pixel. In the detector array, each pixel will have a slightly different value, and the measurement will yield the average of these over the array, \bar{g} and \bar{G} . When the average values are used, the right side of equation 4 contains a "dispersion" term of the form $(\bar{g}^2 \bar{G}^2 / (\bar{g} \bar{G})^2)$. If the variances of these quantities are small, the dispersion term will have a value near 1. The array is relatively uniform and so it is assumed here that this dispersion term is unity.

In addition to this electron noise term, there is a read noise term n_R that is independent of the signal level. Therefore, the total measured output noise n_T is given by

$$n_T = \sqrt{n_R^2 + V g G} \quad (5)$$

The dashed curve in Figure 1.31 is a best fit of equation 5 for the data, excluding the two highest background points where saturation is occurring. This fit was done assuming a transimpedance $g = .0063$ mV/electron. The fit gives a fixed readout noise $n_R = .65$ mV, and detector electron gain $G = 1.41$. These data were taken at a detector temperature of 10.52K, $V_{DET} = -2.6$ V, $V_{ADJ} = -5$ V, in delta reset mode. The readout noise n_R measured at the preamp input corresponds to a read noise of 188 μ V at the detector for double sample, or 133 μ V per sample. This implies a broad band noise of 133 nV Hz^{-1/2} at the

detector.

1.7.5 Standard Star Observations, Calibration

Several stars of known magnitude were observed with MIRAC to determine flux calibration and sensitivity through the available filters at the telescope. The total counts in the image due to the source were added, and the background noise was estimated by calculating the RMS of a nod set taken off the source. The star β And was observed on December 8, 1990 at the SO 1.5 m telescope at 8.8, 9.8, 11.7, and 12.5 microns. Table 1.9 gives the results of these measurements. The on-source integration time was different for each wavelength, ranging from 15 to 60 seconds, so the sensitivity values presented in Table 1.9 have been scaled to 1 second and 900 seconds on-source by multiplying by the square root of the ratio of 1 and 900 seconds to the actual on-source observing time.

Table 1.9 MIRAC Sensitivity Calibration
Steward Observatory 1.5 m Telescope¹

Air Mass = 1			
NEFD (Jy/arcsec ²)			
Wavelength (μm)	Background (Jy/arcsec ²)	(1 sec on-source, 4 sec total)	(900 sec on-source, 1 hour total)
8.8	2600	.28	.009
9.8	7338	.49	.016
11.7	4657	.31	.010
12.5	4665	.31	.010

¹Measurements made 12/6/90, -4°C outside temp., humidity 24%.

The second column labeled "Background" is the flux from the "blank sky". The flux at 9.8 μm is high because of high atmospheric emissivity at that wavelength.

During the design of MIRAC we calculated a sensitivity based on measurements or estimates of the detector quantum efficiency, camera optics transmission, filter transmission and bandwidth, telescope transmission and emissivity, and sky emissivity. For the 1.5 m telescope, 900 seconds on source, 1 hour total time chopping and nodding, this calculation gave a noise equivalent flux density (NEFD) of .012 Jy/arcsec² at 8.5 μm and .013 Jy/arcsec² at 12.5 μm . These predictions agree with the observed sensitivity of .010 Jy/arcsec² at 12.5 μm , within the uncertainty of the calculations.

Similar observations were performed at the Steward Observatory 2.3 m

telescope, using α Boo as the calibration source. Table 1.10 lists the results of these observations. There were high cirrus clouds during these observations, in addition to the relatively high humidity measured at the telescope, so these achieved sensitivities are likely to be poorer than what can be achieved under better conditions.

Table 1.10 MIRAC Sensitivity Calibration
Steward Observatory 2.3 m Telescope¹

Air Mass = 1

NEFD (Jy/arcsec²)

Wavelength (μ m)	Background (Jy/arcsec ²)	(1 sec on-source, 4 sec total)	(900 sec on-source, 1 hour total)
8.8	2166	.21	.007
11.7	3417	.21	.007
12.5	5580	.38	.013

¹Measurements made 6/2/91, 11°C outside temp., humidity 40%.

These sensitivity values can be compared with those attained with other instruments. Several other instruments exist which can obtain images in the 8-13 μ m range. Since sensitivity values, if they are reported, are often in different units and different wavelengths, bandpasses, integration times, and telescopes, it is hard to make an absolute comparison. Other parameters, such as conditions of the site and the weather will have an influence on the results. Despite these difficulties, it is meaningful to make a comparison, since the measured sensitivities reveal the total effectiveness of the instrument, including all the transmission losses, emissivities, sources of extra noise, and other non-optimal behavior of the system. In this way it is more realistic than a

theoretical calculation of the performance of an instrument, and demonstrates what can actually be achieved.

The instruments described were chosen to be representative of past or current array cameras that were designed for broad spectral band, high spatial resolution mid-IR imaging. The instruments were used on different telescopes under a variety of atmospheric conditions. Therefore, the sensitivity is compared here in terms of surface area brightness in $\text{Jy}/\text{arcsec}^2$, rather than source flux density in Jy. The surface area brightness value is more directly related to the camera performance, while the source flux density is dependent on image quality, which can be adversely affected by the telescope image quality, telescope tracking, and atmospheric seeing.

Table 1.11 gives the sensitivities of a number of instruments, from values reported in the literature. The reference given for each instrument is where the observational result was reported. First, the reported sensitivity value is given, along with the details of the observation, including on-source and total time, pixel scale, wavelength, bandpass, and telescope. In the second half of this table, an attempt is made to "normalize" the values to compare the instruments. The assumption made for the normalization is that the instrument is background noise limited, that is the noise is dominated by statistical fluctuations in the photon conversion to electrons. If an instrument is system noise limited, then this normalization would not be correct.

Four normalizations are performed successively, as appropriate. First, the value is divided by the reported number of sigma and multiplied by the square root of the integration time in seconds to normalize the result to 1 second. The value is also multiplied by the square root of two times the ratio of the on-source time to the total time in order to normalize to a total time equal to twice the on-source time. Then the value is divided by the pixel scale to normalize to 1 square arcsec. The value is then multiplied by the square root of the ratio of the surface areas of the telescope used to the IRTF, to normalize the result to the IRTF. No attempt is made to allow for differences in the telescope and site IR properties. Finally, the result is multiplied by the square root of the bandpass in μm , to normalize the result to a 1 μm bandpass. If the value is already in the proper time, scale, or telescope units, no normalization is applied at that step.

Table 1.11 Comparison of Instrument Sensitivities

Instrument (pixels) [‡]	Reported Sensitivity	On-Source Int. Time	Total Time	"/pix	$\lambda(\mu\text{m})$	$\Delta\lambda(\mu\text{m})$	Telescope
1. MIRAC (20x64)	.31 Jy/(") ²	1 s	4 s	1.0	11.7	1.1	SO 1.5 m
2. GSFC AMCID Camera (16x16)	.15 Jy/pix	60 s	240 s	.79	11.2	.9	IRTF
3. Berkeley Mid-IR Camera (10x64)	.8 Jy/(") ²	32 s	64 s	.39	12	1.2	SO 2.3 m
4. NASA-MSFC Bolometer Array (5x4)	3.1 mJy/pix**	2.95 hr	5.9 hr	4.2x4.3	10.8	5.3	IRTF
5. GSFC 5-17 μm Camera [†] (58x62)	10 mJy/pix	60 s	120 s	.26	10.0	1	IRTF
6. Berkeley Mid-IR Camera* (10x8)	15 mJy min ^{-1/2} (") ^{-1/2}	23 min	46 min	.39	10.6	5	IRTF
7. NRL IR Camera (10x50)	.5 Jy/pix	5 min	10 min	1.65	10	1	WIRO ^{††}
8. UCSD Golden-Gopher (20x64)	5 mJy hr ^{-1/2} (") ^{-1/2}	30 min	60 min	.93	8.5	1	Mt.Lemmon 1.5 m

Table 1.11 (cont.)
Comparison of Instrument Sensitivities

Instrument	Sensitivity Normalization			Final (Jy/($''$) ²) Bandpass to 1 μ m
	Int. Time to 1 sec ^{‡‡}	Scale to 1 ($''$) ²	Telescope to 3 m	
1. MIRAC	.22 Jy/($''$) ²	.22 Jy/($''$) ²	.11 Jy/($''$) ²	.11
2. GSFC AMCID Camera	.82 Jy/pix	1.04 Jy/($''$) ²	1.04 Jy/($''$) ²	.99
3. Berkeley Mid-IR Camera	4.5 Jy/($''$) ²	4.5 Jy/($''$) ²	3.5 Jy/($''$) ²	3.8
4. NASA-MSFC Bol. Array	.32 Jy/pix	.075 Jy/($''$) ²	.075 Jy/($''$) ²	.17
5. GSFC 5-17 μ m Camera	.077 Jy/pix	.30 Jy/($''$) ²	.30 Jy/($''$) ²	.30
6. Berkeley Mid-IR Camera	.12 Jy/($''$) ²	.12 Jy/($''$) ²	.12 Jy/($''$) ²	.27
7. NRL IR Camera	8.7 Jy/pix	5.3 Jy/($''$) ²	4.0 Jy/($''$) ²	4.0
8. UCSD Golden-Gopher	.3 Jy/($''$) ²	.3 Jy/($''$) ²	.15 Jy/($''$) ²	.15

Notes to Table 1.11:

The sensitivities reported are the value given in the reference for the Noise Equivalent Flux Density (NEFD), or the RMS noise in the image background. This comparison does not consider point source sensitivity, which may give quite different results because of image resolution and smearing due to atmospheric seeing and instrumental effects.

There are two entries for the Berkeley camera for different observations reported, one a 1 μm bandpass observation on the SO 2.3 m telescope, and the other a 5 μm bandpass observation on the IRTF.

† Camera described in Gezari *et al.* 1988.

‡ Pixels given are portion of the array being read out.

* Camera described in Keto *et al.* 1991b.

** Sensitivity achieved for reported observations, although 1-2 mJy for 6 hrs integration time claimed typical.

‡‡ Normalized to 1 sigma, 1 second on source, 2 seconds total time.

†† Wyoming Infrared Observatory 2.3 m telescope

References for Table 1.11:

2. Hoffmann *et al.* 1987
3. Bally *et al.* 1987
4. Telesco *et al.* 1990
5. Gezari *et. al* 1991
6. Keto *et al.* 1991a
7. Odenwald, Shivanandan, and Thronson 1991
8. Puetter, Jones, and Pina 1990

It can be seen from the above comparison that the MIRAC is a vast improvement over the performance of the GSFC AMCID array camera, and is competitive with other systems currently in operation.

1.7.6 Sky Noise and Chop Frequency

A test was also carried out on the 1.5 m telescope at 12.5 μm to

determine the chopper frequency required to keep $1/f$ sky noise below the background photon shot noise. The total noise for an observation will be the sum in quadrature of these two noise sources. If the constant A represents the photon shot noise and B/f the " $1/f$ " component of sky noise, the total noise observed $n(f)$ at a given sky background will be given by

$$n(f) = \sqrt{A^2 + \left(\frac{B}{f}\right)^2}$$

where A and B are constants, and f is the chop frequency. In our observational test, the noise was determined from a time sequence of 50 1-second chopped images, and was taken to be the average of the standard deviations of each pixel over the 50 images. The results of these observations are shown in Figure 1.32. The dashed line through the data is a fit to the data of the above function $n(f)$ in units of mV. The best fit parameter values for A and B are 2.1 mV and 3.3 mV, respectively. Converted to Janskys and scaled to the chop-nod mode, 1 sec on source (4 seconds total), these parameters are .34 and .52 Jy/arcsec². From these data it was concluded that a frequency of 10 Hz was sufficient to avoid sky $1/f$ noise, at least for the filters at wavelengths where the atmosphere is relatively transparent. It is preferable to run the chopper at the slowest speed necessary to avoid sky $1/f$ noise, in order to maintain good image quality in the chopped beam, and to decrease the amount of "dead time" as a result of waiting for the chopper to settle. These parameters will be very dependent on local sky conditions, but it appears there will always be times when background limited performance can be achieved at high chopper speed

(~10 Hz) and not at lower rates.

1.7.7 Optics Alignment and Evaluation

The optics were first aligned at IR labs when they were installed in the dewar, before the array was installed. The elements were placed in their holders and moved to the design spacing. It was confirmed that a pinhole light source at the focus in front of the dewar was imaged on the center of the array holder in the dewar. The focus and scale were evaluated by placing an illuminated reticle at the position of the array in the dewar, and measuring the size and quality of the image at the focus outside the dewar using a comparator with reticle.

To position the optics correctly, first the ellipsoid was adjusted to focus the pupil at the distance of the secondary. To do this, the position of the array in the dewar was illuminated, and the image of the back-illuminated pupil was viewed with an eyepiece in the darkened room. The ellipsoid was positioned so that the pupil was in good focus at the distance of the IRTF secondary, 884 cm. The focus was also evaluated using a "chop" technique. The central 1/3 of the mask on the optics housing was covered, leaving 1/3 of the area uncovered on either side. Then the pupil image was again viewed at the desired focus position, while a card was used to alternately block one side or the other of the baffle. At the correct focus position, the pupil image should

not move as it is chopped. If not at the correct position, the pupil will move side to side as the mask is chopped. When the ellipsoid was set properly, the image was steady as the mask was chopped when viewed from the distance of the IRTF secondary.

The direction of the beam was then adjusted so it is normal to the dewar window. A white card with a crosshair was placed at the position of the array, and the card was illuminated from the side. A crosshair was also placed on the baffle on the outside of the optics housing. A mirror was attached to the front face of the optics housing. A telescope was used at a distance of approximately 10 feet, looking at the dewar and into the optics. The telescope was positioned so that its reflection was visible in the mirror, on center with the outer baffle. Then the ellipsoid was tilted slightly so that the two sets of crosshairs were aligned as viewed through the telescope.

The image quality was documented by photographically recording the image sharpness. An eyepiece reticle with a .1 mm spaced ruling was placed at the low magnification array position, and illuminated from behind. A mask of 4x8 mm was placed over the reticle to show the approximate size of the array. Then a camera (with the lens removed) was placed at the focus, determined from the sharpest image in the camera. A photograph from this test is shown in Figure 1.33. Several photos were taken at small displacements from this position, but this was the position with the best focus over the field.

The optics quality was also evaluated by observations with the detector on March 12-15, 1991. The tests were done using a "pinhole" source positioned at the optics focus outside the dewar. A 150 μm diameter pinhole was used for all measurements except with the 20 μm filter, where a 300 μm pinhole was used. The pinhole was mounted on a XYZ micrometer stage, which allowed for accurate positioning and measurement. The pinhole was illuminated from behind by a 40W high intensity bulb painted black. A chopper was placed between the source and the pinhole. Images were taken with the MIRAC program and normalized with a gain matrix.

Some results of these measurements are shown in Figure 1.34 which shows the observed pinhole profiles at three different wavelengths. The pinhole was adjusted to attempt to center it on the pixel in row 14, column 1. The profiles have been normalized so that the peak value is 1. The image size increases with wavelength due to diffraction. In the 2.2 μm profile, almost all of the energy is contained in the peak pixel, with some spillover into the neighboring pixels. These profiles show the optics are close to the calculated performance, showing no signs of unexpected scattering or image spread.

The measured optics distortion is shown in Figure 1.35. This was obtained by moving the pinhole source to center it on different pixel positions and then measuring the displacements on the positioning micrometers. The scale was measured by assuming no distortion between pixels 31 and 24 (where the distortion effects will be the smallest) and positioning pixels 2, 9, and 16

based on this scale. All of these pixels are in column 11 of the array. In this figure, the dotted lines are the pixel edges, so the data square is in the center of the square on the plot if it is not distorted. Pixels 24 and 31 are perfectly centered in the plot because of the assumption of no distortion between these pixels. The largest distortion is for pixel 2, which is shifted to the left and downward of a perfectly linear displacement, as expected. To the accuracy of this measurement, the optics distortion is consistent with the calculated distortion from the optics design.

The optics distortion is removed in the data processing by calculating a new image from the original data using the measured distortion. Typically, the new image has 16 "subpixels" for each instrumental pixel. Each subpixel is assigned a value taking into account the distortion to produce an undistorted image. These images can then be simply shifted and added together to produce the final image.

The efficiency of the MIRAC optics will be high, since the optics consists of gold-coated reflective elements. In the calculations of MIRAC performance, the reflectivity of each element has been assumed to be 98%. The performance observed was almost identical to the calculations (described above), so this assumption for the reflectivity is consistent with the performance achieved with MIRAC.

1.8 Future Directions

The MIRAC system has been designed to be easily adaptable to keep pace with advances in detector technology and instrumentation. Three possible areas of future improvements and additions are in improved detectors, addition of a Fabry-Perot interferometer for high spectral resolution imaging, and fast shift and coadding of images to achieve diffraction-limited performance.

1.8.1 Future Detectors

The MIRAC dewar and electronics were designed for the Hughes detector and readout currently being used. This unit is no longer being produced, and there are no available spares, so in order to replace the current detector the current system must be modified. There are several reasons why it would be advantageous to replace the current detector. First, since the address line failure occurred as described above, only a 20x32 pixel segment of the array can be read out. Changing to a different detector would enable us to use the full 20x64 format. Secondly, the current array is not anti-reflection coated, which results in a degradation of quantum efficiency. Finally, advances are continually being made in detector quality, including increased quantum efficiency, lower read noise, increased well size, and more pixels. An improved detector would provide higher sensitivity and allow the MIRAC to be used more efficiently on the telescope.

For future arrays using a similar 20x64 format, the hardware changes in the dewar would be minimal. There are a few spare wires available if the detector required additional bias or address lines. The routing of bias and address lines to the chip carrier would most likely be different. Changes could be implemented by using a new circuit board on the detector stage, or by rewiring the cable connections at the digital controller and bias supplies. Both of these are wire-wrapped, so changes are easy to implement. The PAL timing generators and EEPROM address converter can be replaced with reprogrammed chips for the new device.

Larger format arrays would require changing the baffle shape from the current rectangular form to one matching the new detector shape. Also, significant changes in the controller and signal processors might be necessary for different numbers of detector outputs.

1.8.2 High Spectral Resolution Imaging

A Fabry-Perot spectrometer (FPS) is currently being prepared for use with the MIRAC. This spectrometer was originally developed by Nishimura, Low, and Shivanandan (1984, 1985). The FPS is capable of achieving resolutions ($\lambda/\Delta\lambda$) of ~1000-10000, and is well suited for use with MIRAC because of its low background levels when cooled to LHe temperatures.

The FPS uses superconducting actuators that control the alignment and tuning of the actuators at LHe temperatures, dissipating little power within the instrument. The mechanism consists of two main assemblies, the xy-unit and z-unit. The xy-unit controls the relative tilt between the etalons, and the z-unit controls the tuning by displacing the second etalon along the optical axis. Both units are driven by superconducting Nb:Ti wire coils in magnetic fields produced by rare-earth cobalt magnets. This mechanism is housed in its own helium temperature dewar, which can be connected to the MIRAC dewar at the window port.

The FPS has previously been used with the 10 μm AMCID camera on the SO 2.3 m telescope. The FPS and camera dewar were mated, sharing a common vacuum, and the common instrument was used to observe several standard stars. Later tests done in the lab showed that the FPS could be tuned successfully for a single wavelength over the entire array when scanning over a small wavelength range. The system is now being prepared for use with the MIRAC. The coil current source and control electronics have been rebuilt, and a second spectrometer is being prepared for inclusion in the spectrometer dewar. The MIRAC LHe and LN_2 radiation shields have been equipped with threaded apertures to enable baffle tubes to be attached that will mate with the Fabry dewar.

1.8.3 Fast Shift and Coadd

Another possible direction is to improve the camera efficiency and sensitivity by using a different method of observing. One problem with the current observing technique is that during an integration lasting several seconds to minutes, there are drifts in the telescope position as well as the seeing motion which combine to spread the image out on the array into several pixels. This decreases the maximum resolution that can be achieved on the telescope, and also effectively degrades the sensitivity of the camera, since the source flux is spread out over more pixels and is more difficult to detect for a given NEFD. A possible solution to this problem is to determine the offsets introduced by these effects, so that the data can be corrected and the performance improved.

One possible method for determining the offsets is to measure the position of the source on the array and then to determine the offset needed to align it with some reference image of the same object. This is essentially what is done now with IR-bright sources ($S/N > 10$) that are visible in a single MIRAC observation. The separate observations are aligned using the centroid, or by a cross-correlation algorithm, and the observations are shifted before coadding to form the final image. This usually yields more accurate offsets than those derived from the record of the offsets sent to the telescope. The problem with the current method is that it still does not remove the effects of telescope drift on short timescales, and does not treat the seeing broadening of the image.

Also, the source must be detectable in a single observation.

One possible method of improving this for the brightest IR sources would be to perform this centroid and shift operation as the frames are stored in the array processor board. Each coimage transferred from the camera would have the offsets corrected in real time as the integration is taking place. This could be performed at the chopping rate of 10 Hz, and would remove the effects of telescope drift and seeing. The major drawback of this method is that it would work for only the brightest sources, clearly detectable in a single coimage of 1/20 sec.

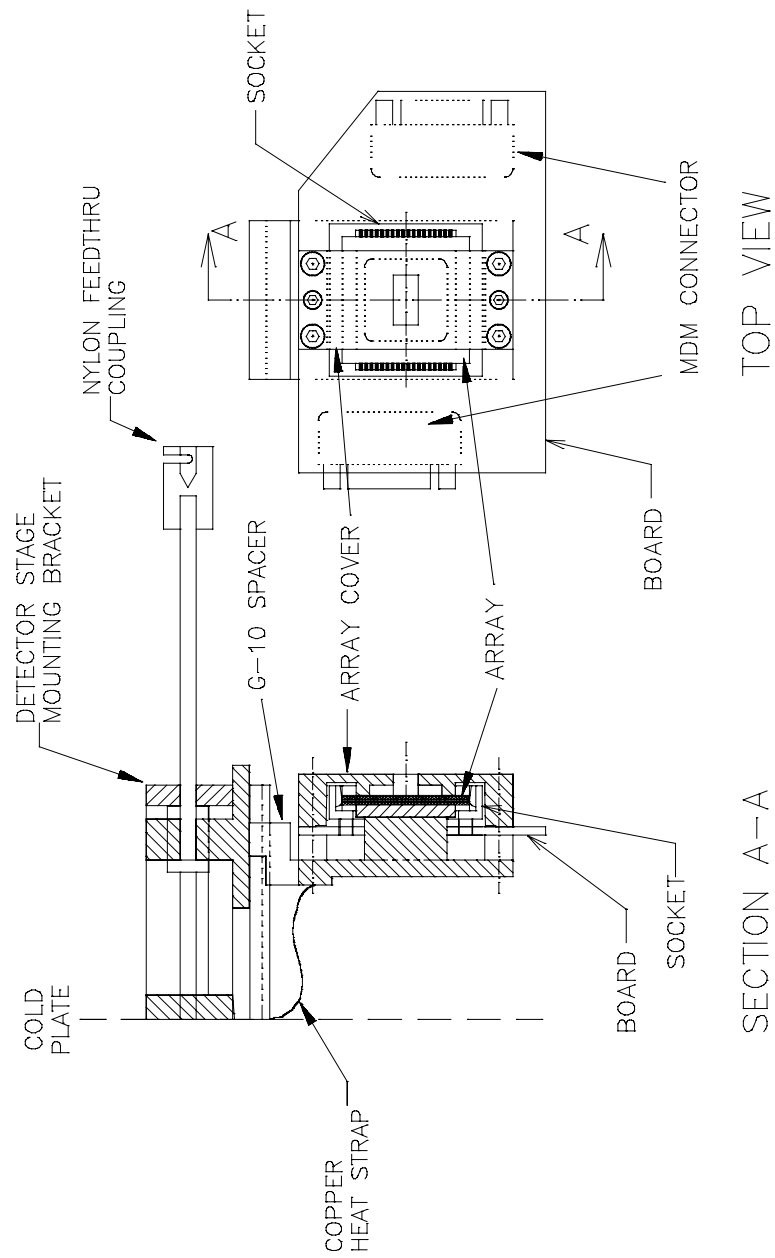
An alternative to using the IR image as the reference image is to use the optical image of a source in the TV guider. The source could be the same as the IR source, or another nearby star could be used, if the field of view is wide enough and the TV camera sensitive enough. The centroid would be calculated for the optical source, and assuming that the IR and optical centroids are the same, the offsets would be used to align the IR images. This could be utilized with the present method of observing, for those IR sources that are not detectable in a single observation. A more powerful method would be to use the optical image of a guide star to determine offsets for the individual coimages as they are being coadded in the array processor. This has the potential of achieving diffraction-limited images for any IR source as long as a star can be found in the field to provide the offsets.

FIGURES-PART 1

Figure 1.1. The MIRAC cryostat. All dimensions shown are in inches.

1.1a. Cutaway view from the side, showing the internal mechanisms. A ray tracing of the optical beam is shown entering the dewar from the left. The array sliding stage is shown in the low magnification position; below it are the filter wheels and then the pupil stop slide, which moves perpendicular to the plane of the paper. The actuators are shown partially inserted-- during normal operation, these are withdrawn outside the LN_2 radiation shield to eliminate unnecessary heat load.

Figure 1.1b. MIRAC array mounting assembly. The array is mounted in a socket on top of the stage. A copper "finger" extends through the socket and makes direct contact with the backside of the chip carrier, through a piece of indium foil. The copper mount that holds the array and circuit board is insulated from the rest of the dewar by a G10 spacer, and the thermal connection is made using a flexible copper strap below the stage. Detents and spring-loaded balls define the two magnification positions.



MIRAC Detector Stage

Figure 1.1b

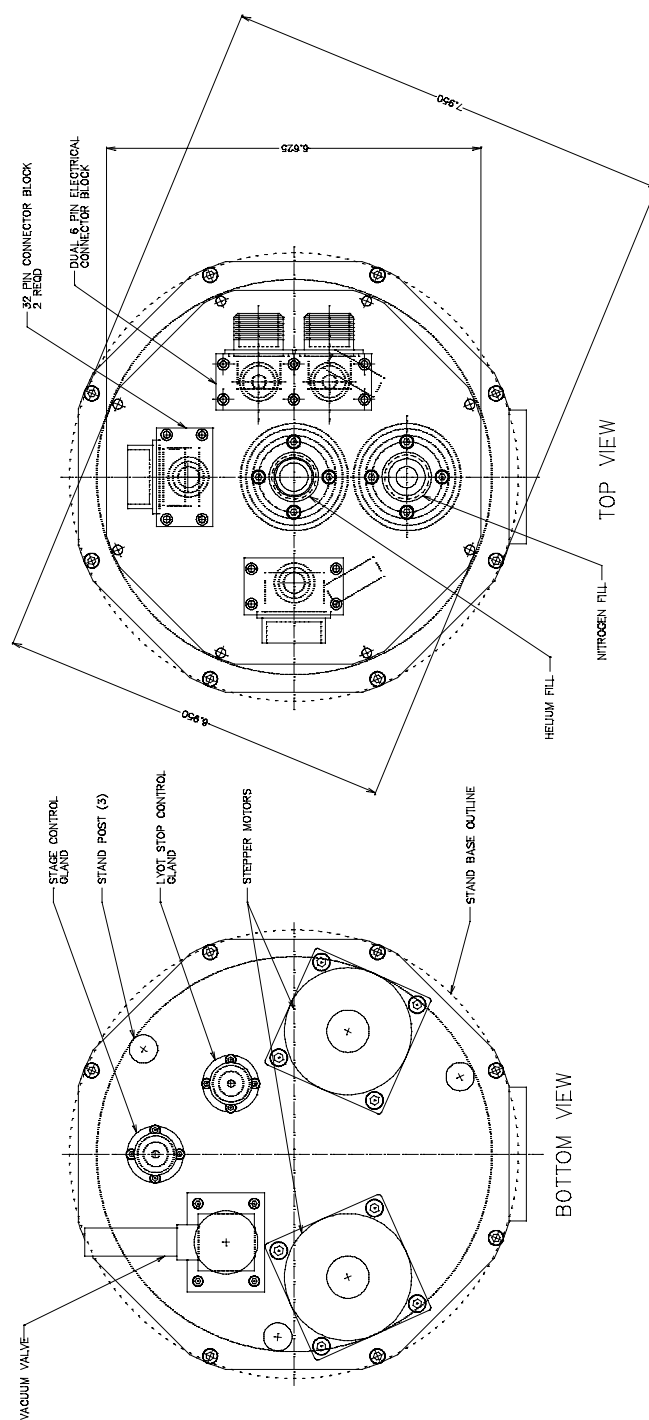


Figure 1.1c The MIRAC cryostat, top and bottom view.

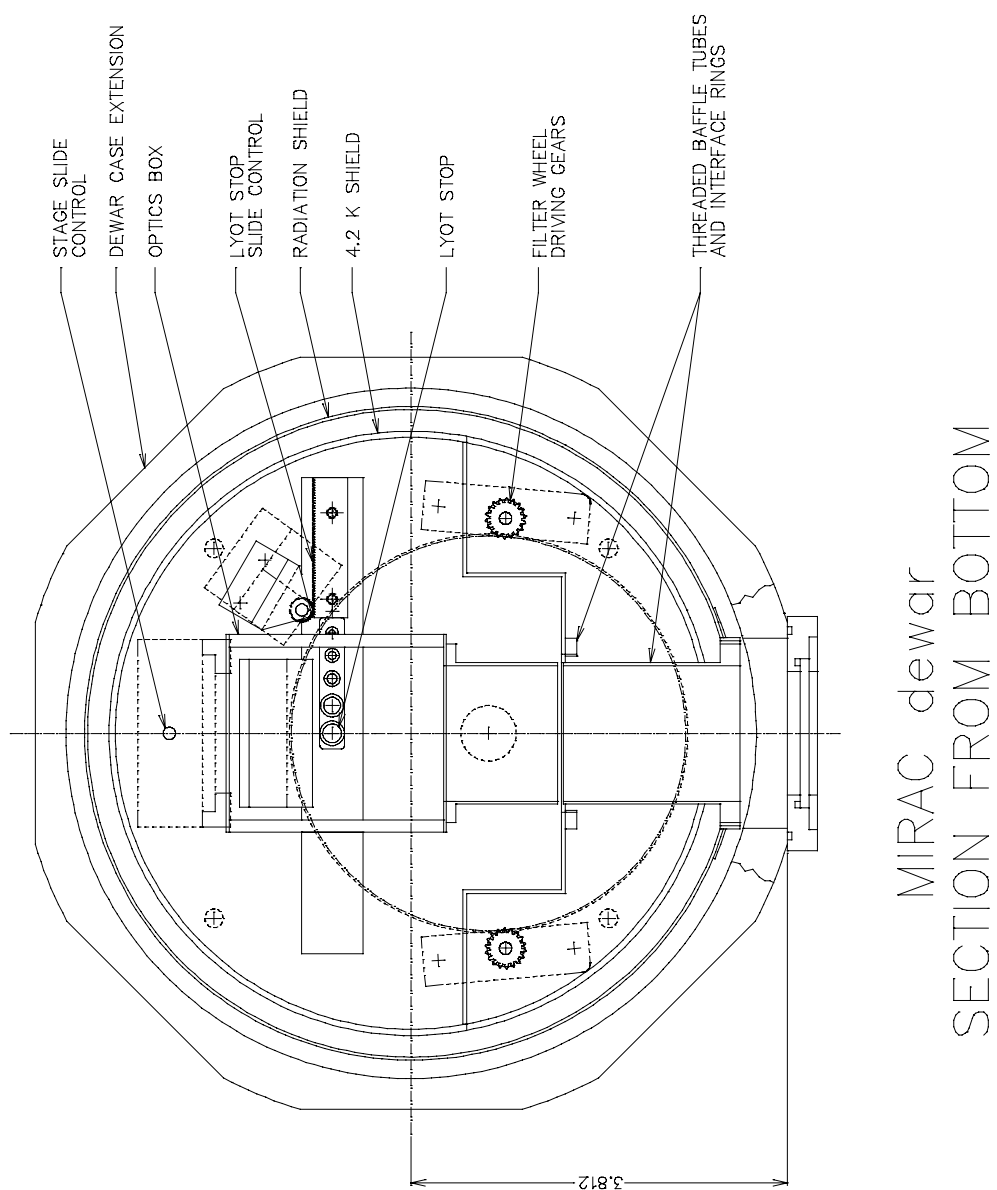


Figure 1.1d. The MIRAC cryostat, cutaway section view from the bottom.

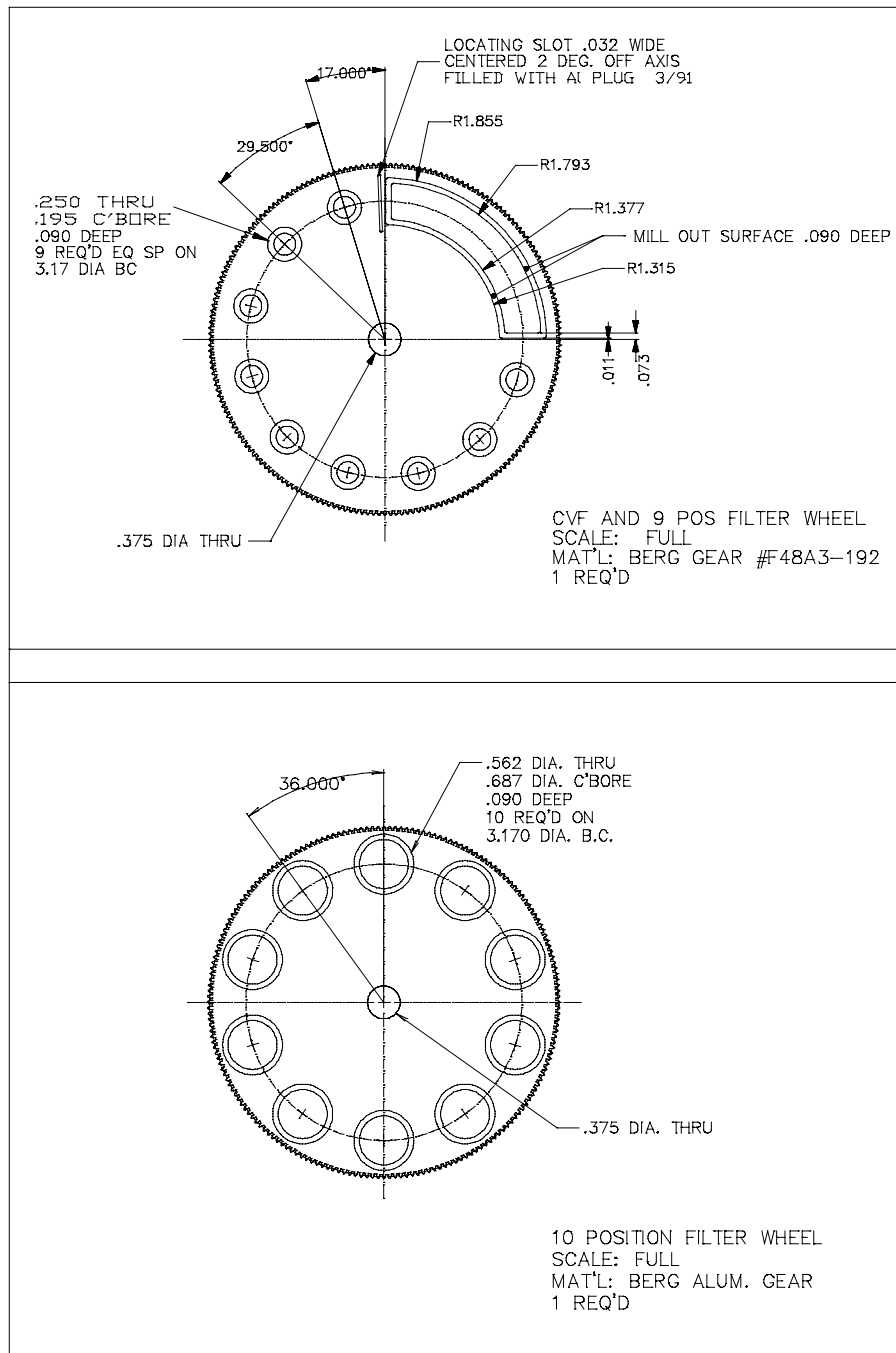


Figure 1.1e. MIRAC filter wheels, number 1 on the top and number 2 on the bottom.

Figure 1.2. MIRAC Optics ray diagram. The position of the dewar window and radiation shield baffles are indicated. The units are in cm. In changing from low to high magnification, the only change is in the position of the array and the focus position outside the dewar.

1.2a. Low magnification position.

MIRAC Low Magnification

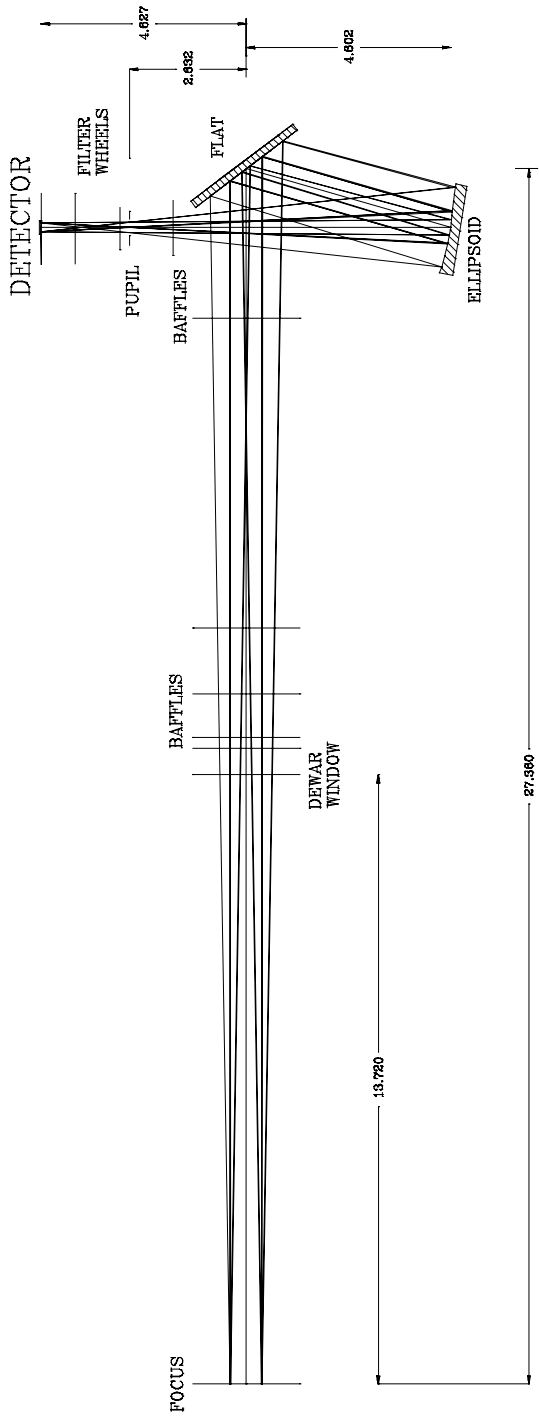


Figure 1.2a.

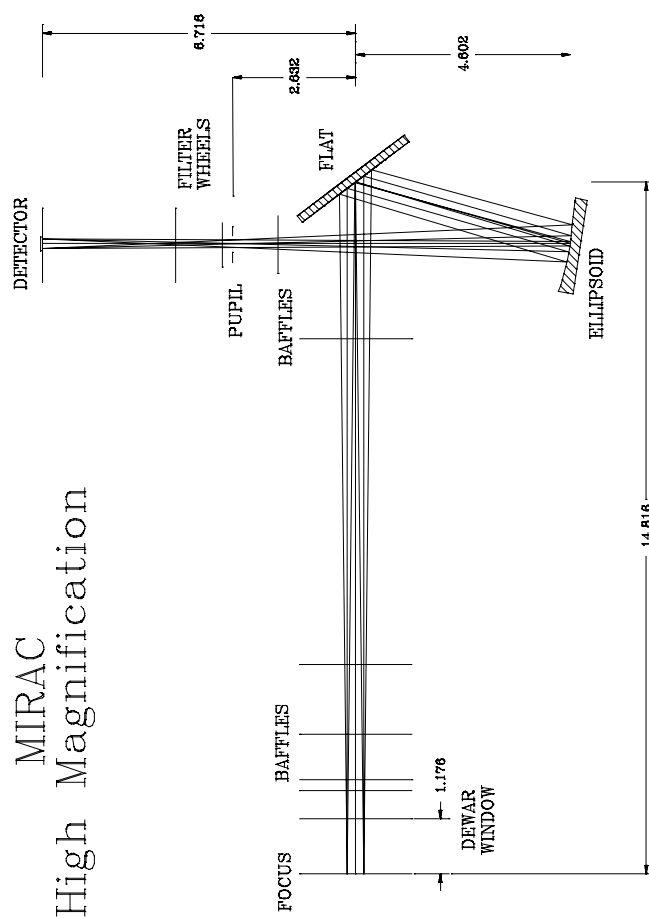


Figure 1.2b. MIRAC optics High magnification position.

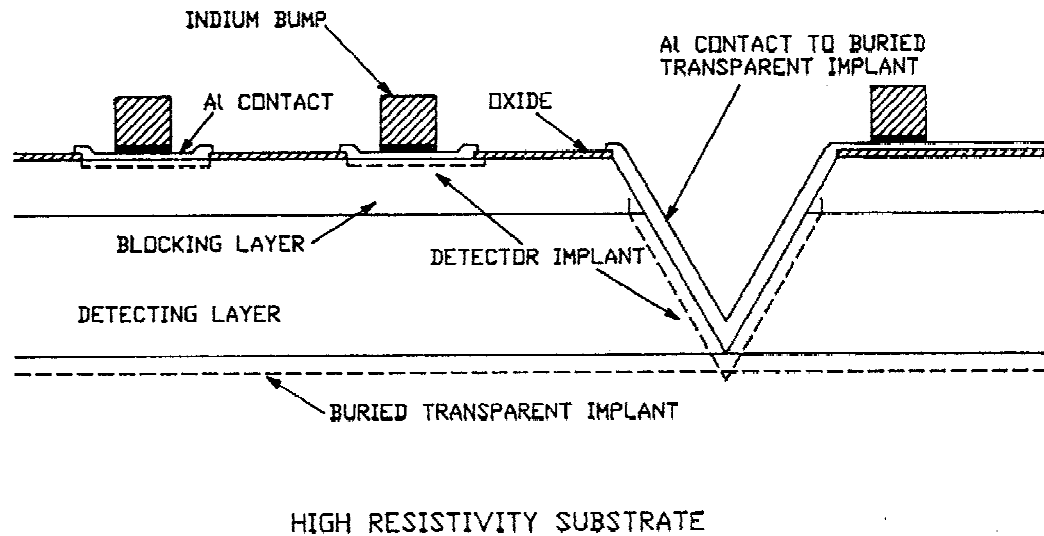


Figure 1.3. Hughes IBC detector cross section, from a figure provided by Hughes and published by Fowler and Joyce (1990). Two pixels are shown on the left, and the guard ring and electrode are shown on the right. The indium bumps allow for bonding to the readout array.

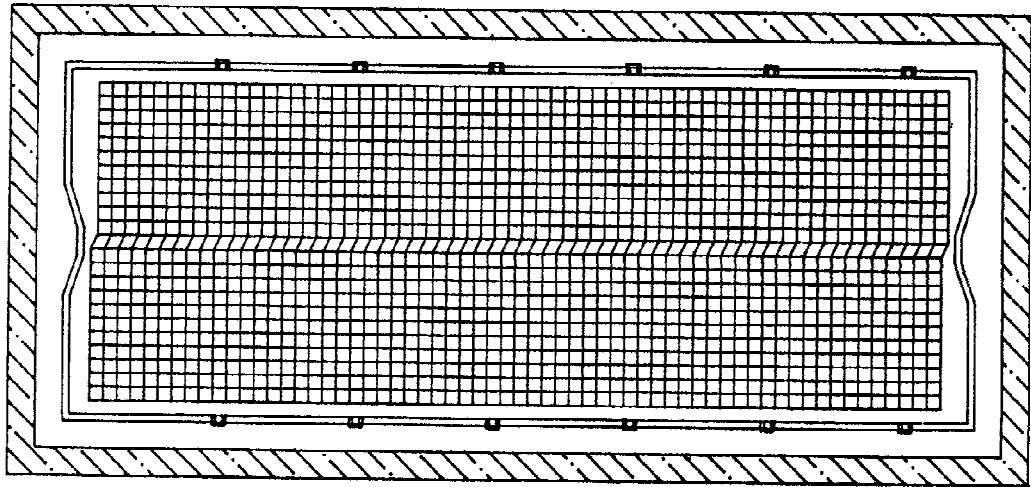


Figure 1.4. Hughes IBC 20x64 detector layout, from a figure provided by Hughes and published by Fowler and Joyce (1990). The array is organized as two 10x64 sub-arrays, separated by a pixel and offset by a half pixel in the long dimension, surrounded by a guard ring.

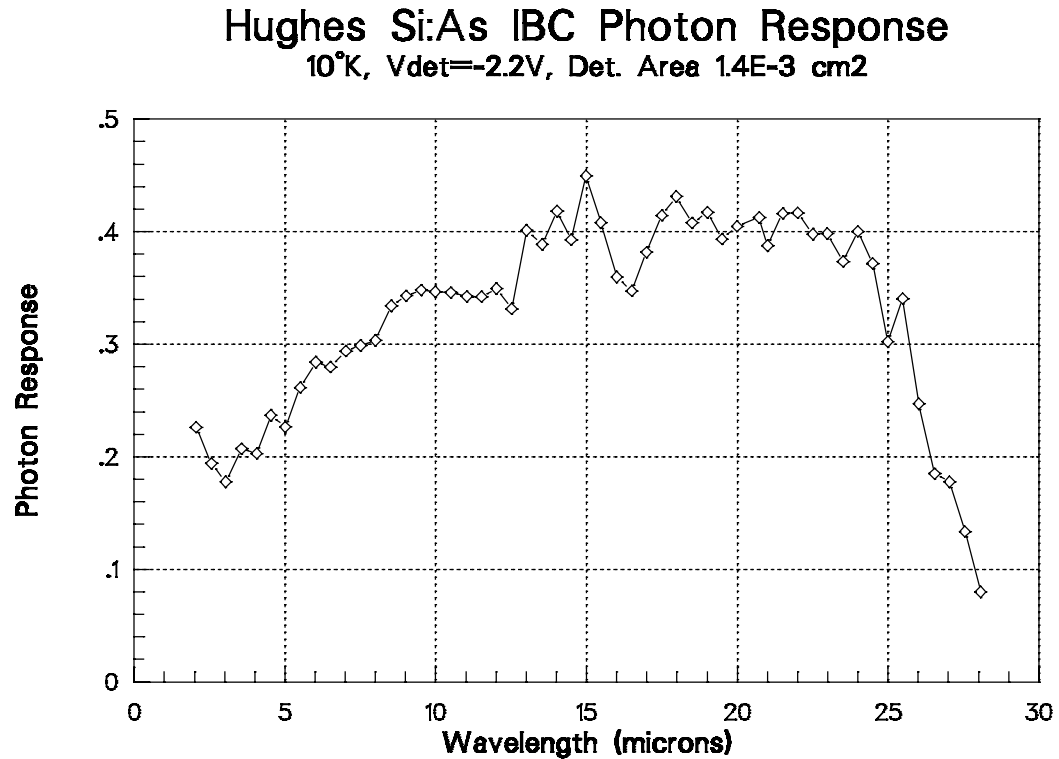


Figure 1.5. Hughes Si:As IBC detector spectral response, from data supplied by Hughes. This response was not measured for the particular device used in MIRAC, but represents the general response of this detector material. The "photon response" or quantum efficiency is plotted as a function of wavelength in microns. The data were supplied as relative photon response compared to the peak at 15 μm . In this plot, the data have been scaled so that the 22 μm response is equal to .42, based on results reported by Hughes.

PATHS CARLSBAD VERSION 3/4 BONDING DIAGRAM

CRC 344 &
CRC 444

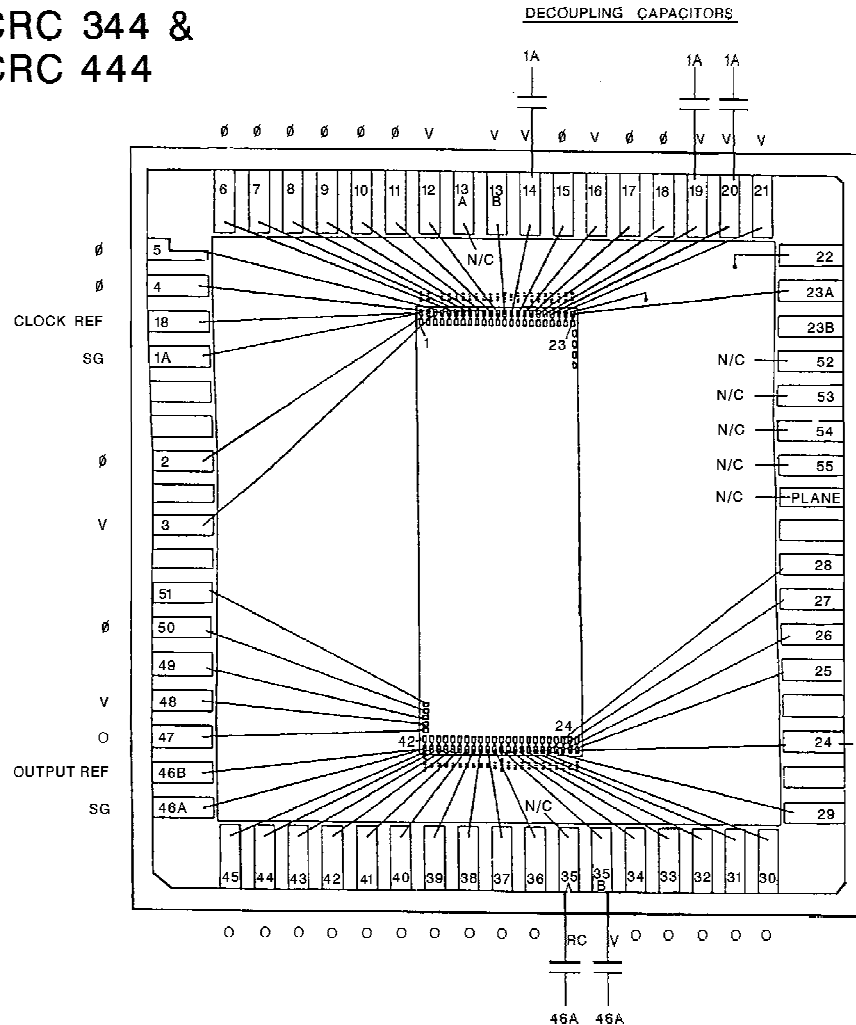


Figure 1.6. Wire bond diagram for the CRC 444A readout (figure courtesy Hughes). This shows the electrical connections between the readout and chip carrier. The number on each pad corresponds to the connection number on the readout. The pads are marked with the following symbols: "V" - bias voltage, "φ" - clock (address or reset), "SG" - system ground, "RG" - reference ground, "O" - output, "N/C" - no connection. The length of the readout is 332 mils, the size of the cavity in the chip carrier where the readout is mounted is 430 mils, and the pixel size is 100 μm.

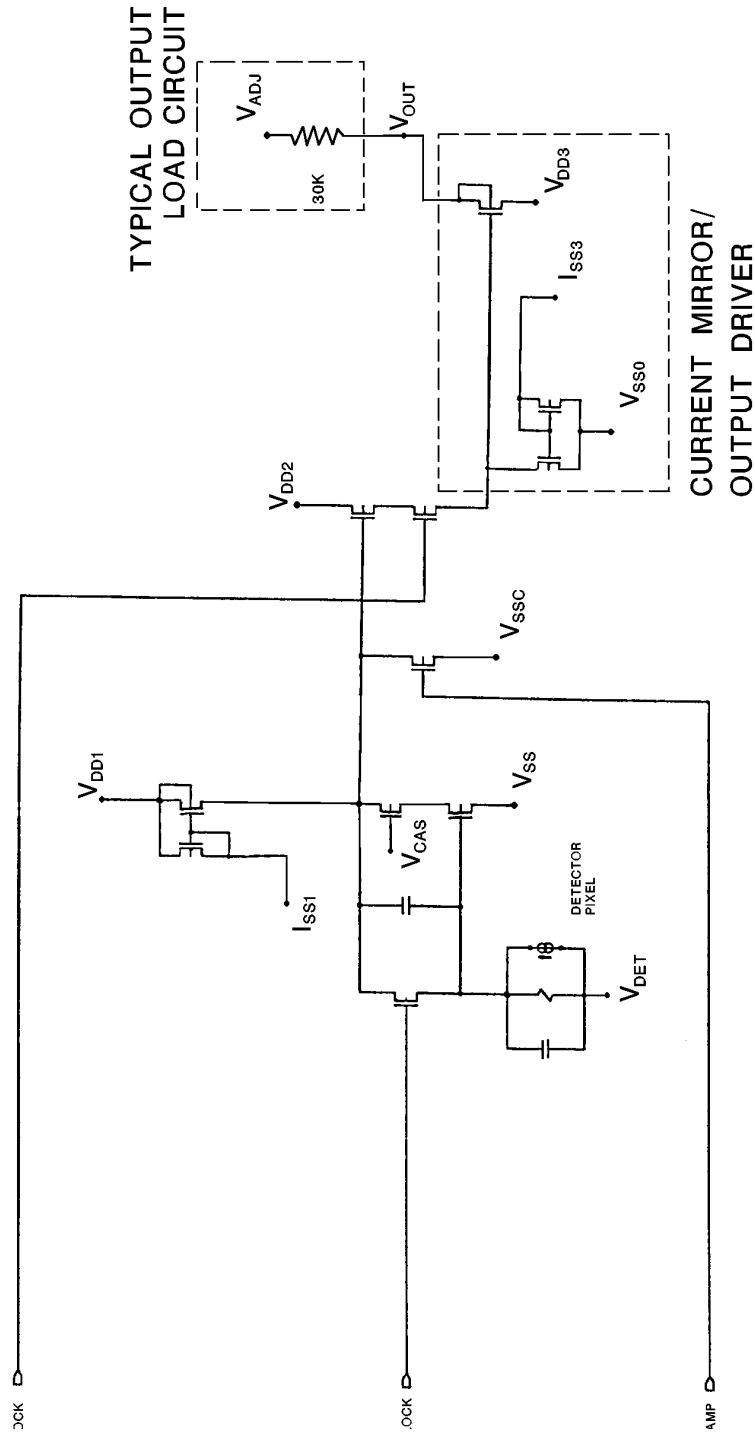


Figure 1.8. CRC 444A unit cell and detector (figure courtesy Hughes). The ENABLE and RESET clocks are from the CRC 444A decoder (see Figure 1.7). When the pixel is addressed, the ENABLE clock connects the pixel to the output for that column, and the RESET clock is allowed through. There is a separate unit cell circuit for every pixel, except for the components inside the dashed boxes, for which there are 20 in total, one for each column. The "Current Mirror/Output Driver" is on the readout, and the "Typical Output Load Circuit" is on the preamp card.

Figure 1.9. MIRAC block diagram. The diagram is divided into three main sections as indicated by the dashed lines: the cryostat, the electronics at the camera, and the equipment inside the telescope control room. The items in the cryostat section are all the components that are inside the dewar. In the electronics section, the functions in the signal processors and controller board are shown, and these are enclosed by the dotted rectangle. There are ten identical signal processor boards, each with two channels. One is shown in the diagram. Nine clock signals and 14 bias voltages are supplied by the electronics to the detector. Twenty outputs, one from each detector column, are amplified by 4 and enter the inputs of the signal processor boards. The data are transferred to the controller via a 28-bit parallel bus, and are sent to the computer to a 1.25 Mbit/sec serial Manchester transmission line. Commands are also sent from the PC to the camera over this serial line to set the camera parameters. Analog signals from the temperature controller are read by an A/D board inside the PC, and the PC sends commands to the filter motor controller via a RS-232 serial link.

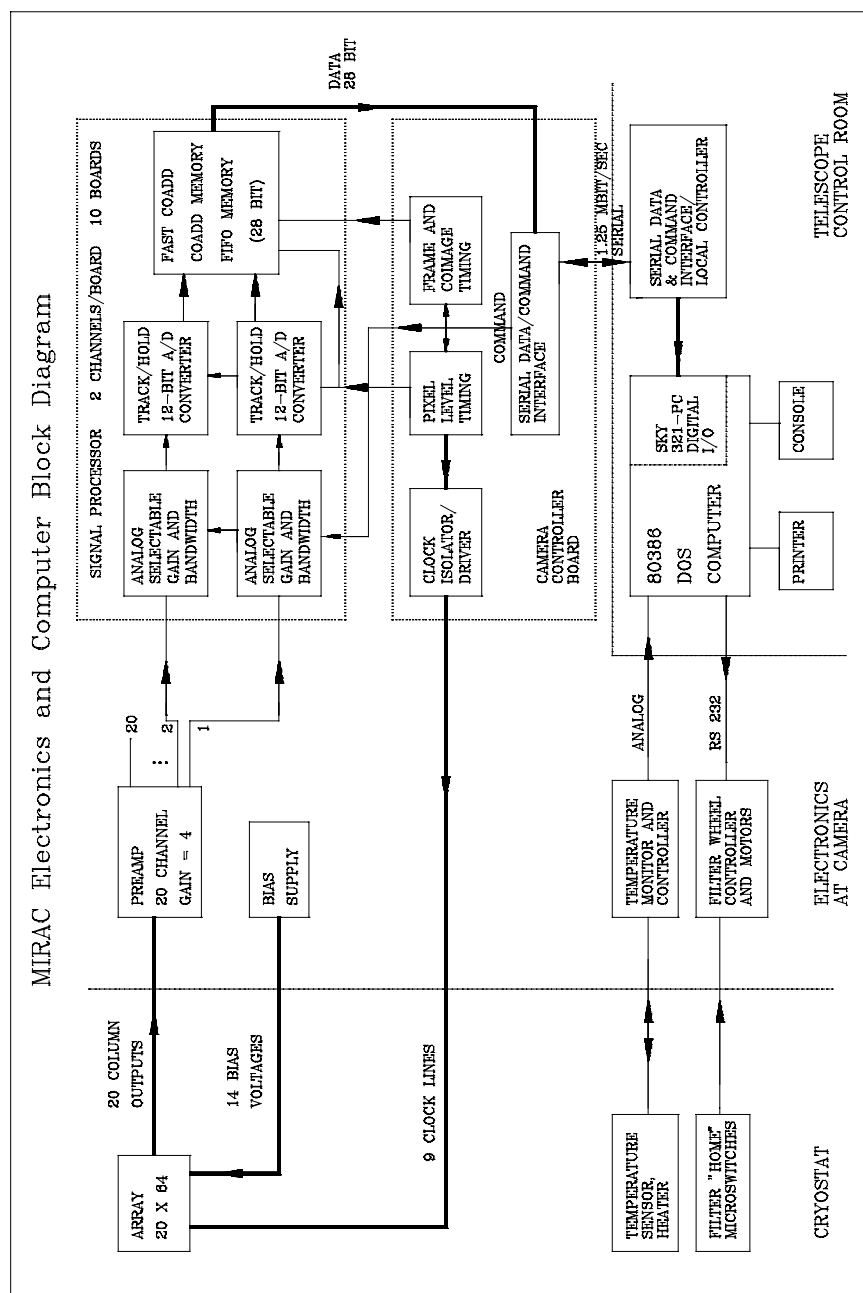


Figure 1.9

MIRAC BIAS SUPPLY

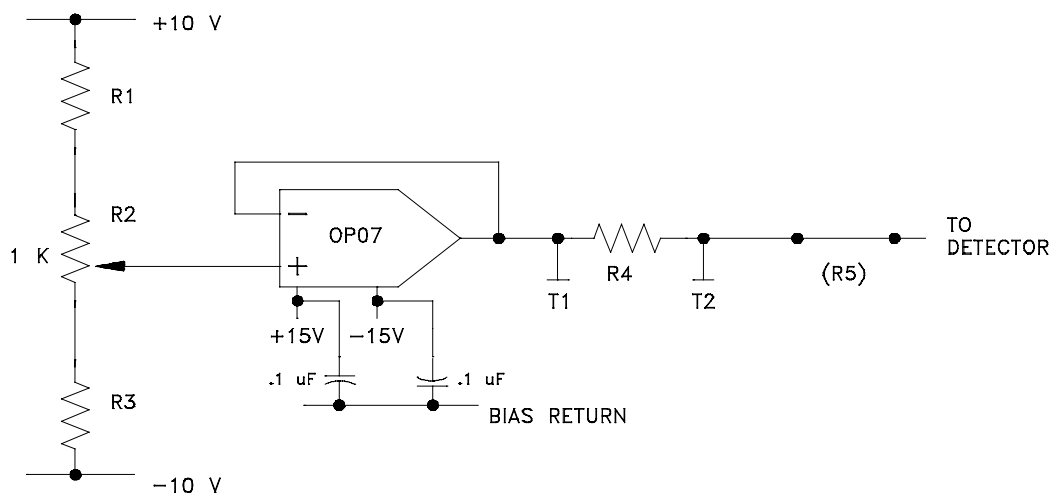
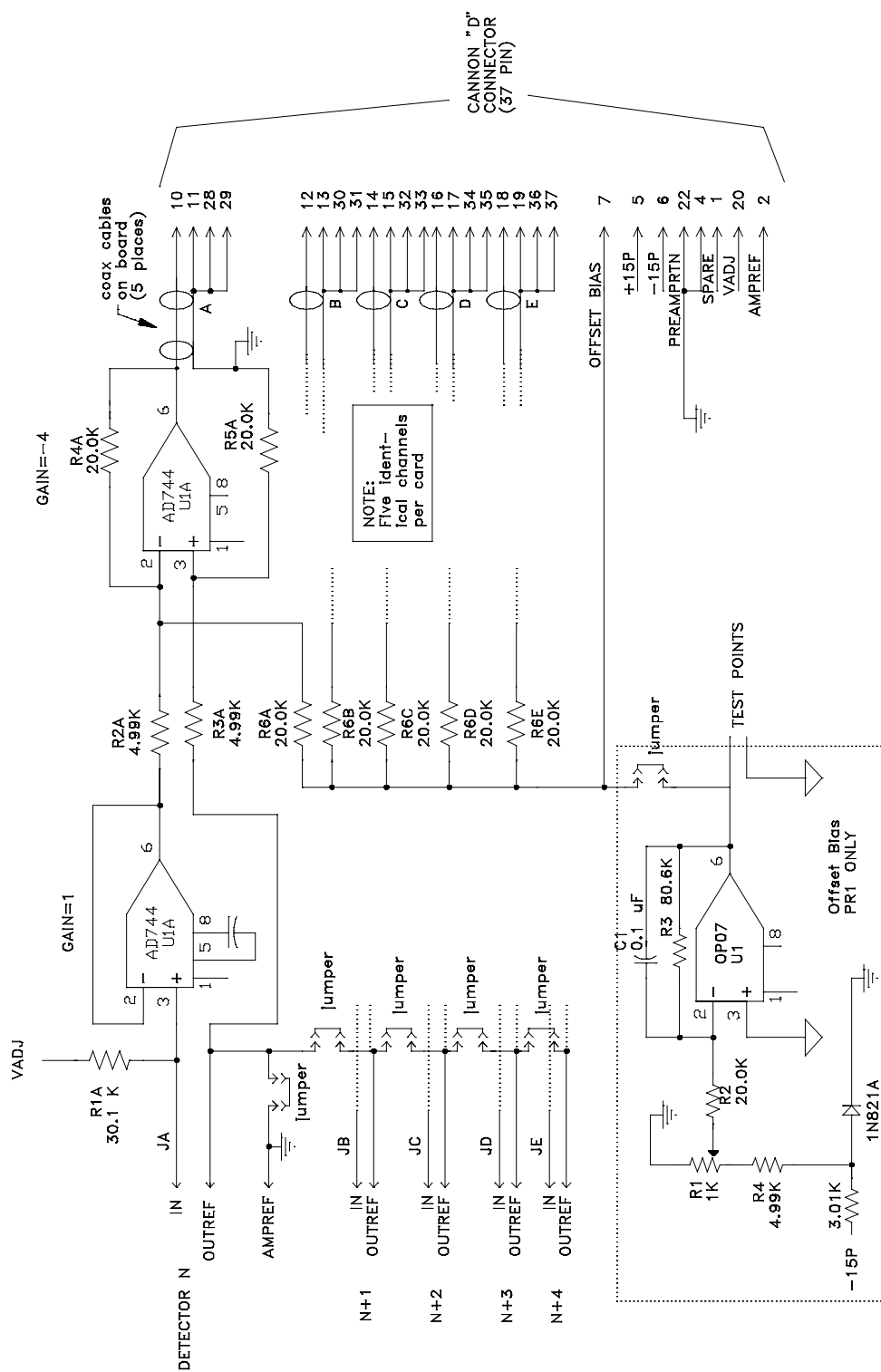


Figure 1.10. MIRAC Bias supply representative circuit. For ISS1, ISS3, and VDET, an additional series resistor is added at the point marked (R5) on the right side of the diagram.

Figure 1.11. Preamp circuit diagram. There are four preamp boards, with five channels on each board.

1.11a. Preamp main circuit. The circuit enclosed by the dotted lines in the lower left for the offset bias is only installed on the first preamp board. The five inputs JA-JE are subminiature connectors where the coaxial cables that carry the detector output are attached.

MIRAC PREAMP



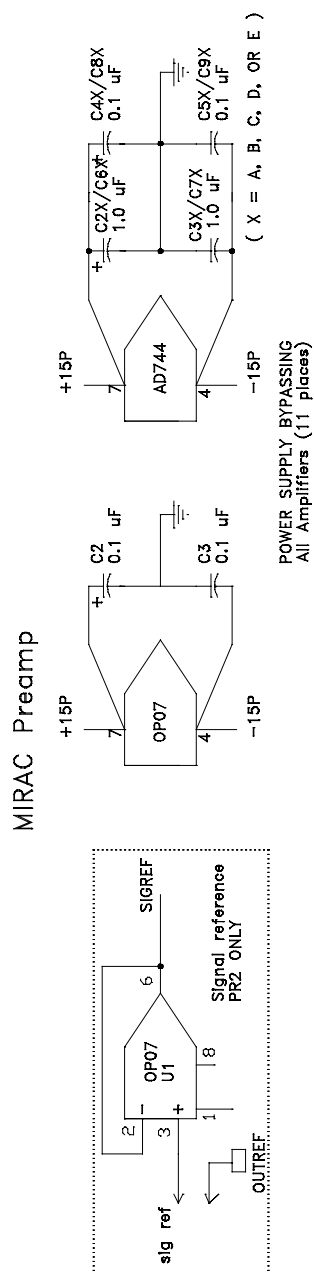


Figure 1.11b Preamp circuit, signal reference and power supply bypassing. The signal reference circuit is implemented on circuit board 2 only.

Figure 1.12. MIRAC Controller block diagram. On the left are the connections to the computer, the command and data lines which are serial transmission lines, and IMGRDY which is a logic level. The Serial Encoder/Decoder decodes command words sent from the PC and received by the Manchester serial encoder/decoder. The command word is separated into command and data segments and sent to the command decoder and registers. There are two types of commands, one which performs a function, such as to START imaging, and another which loads a camera parameter register with a data value. The values in these parameter registers specify how the controller timing operates. Control signals are sent to the signal processors, and address and reset signals are sent to the detector.

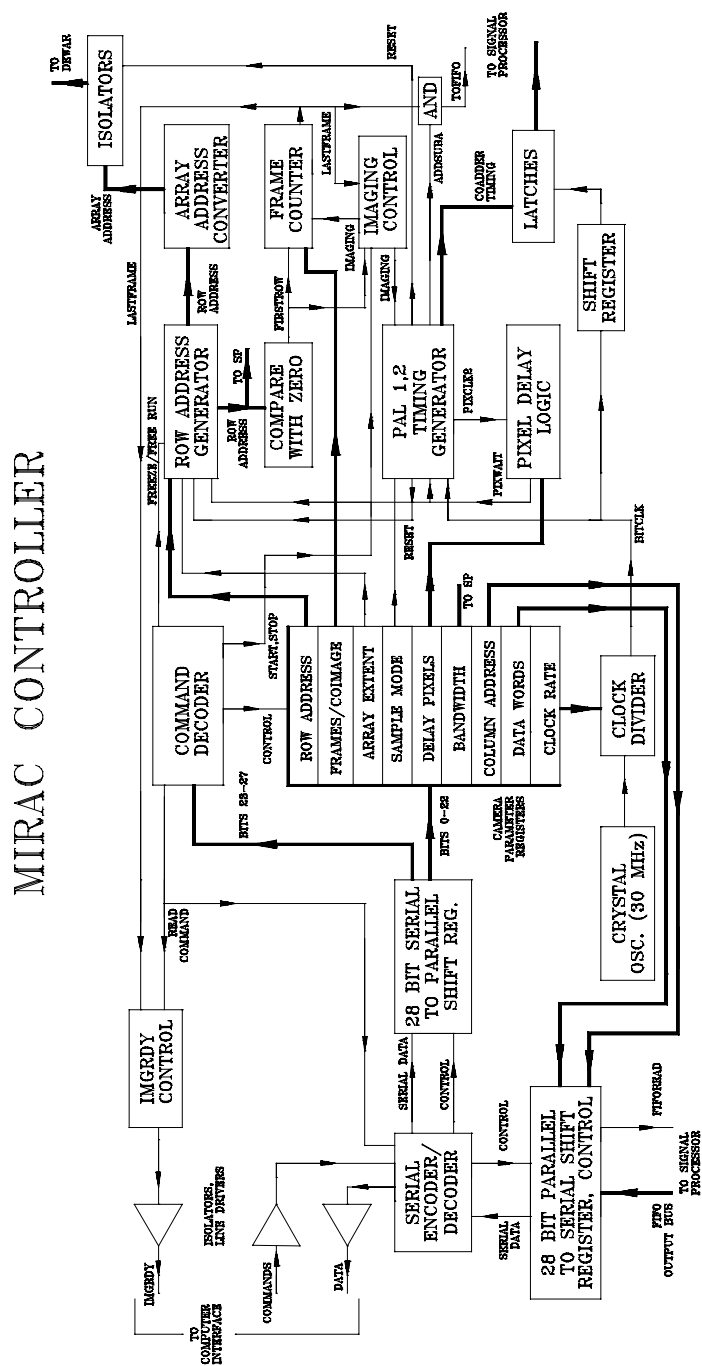


Figure 1.12

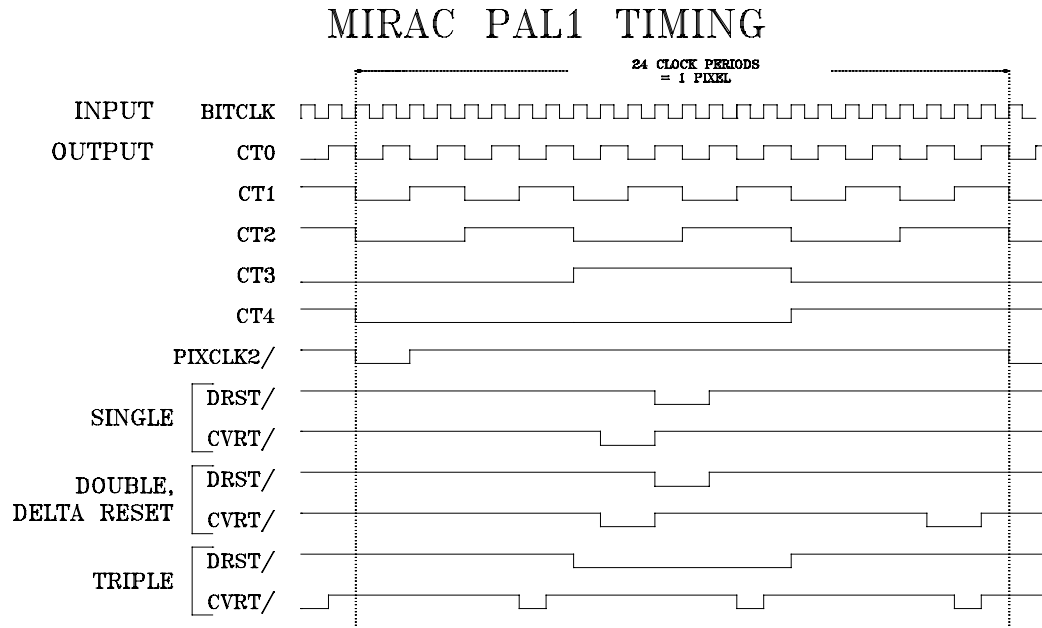


Figure 1.13. MIRAC PAL timing diagrams. The timing for the section labelled "PAL1" refers to U215 (PAL16R8), and "PAL2" is U216 (PAL22V10). The inputs to both PALs include BITCLK, PIXWAIT, and SMODE00 and SMODE01. BITCLK is the counted-down master clock, PIXWAIT is a control line that can be used to stop some of the PAL output, and SMODE00 and SMODE01 determine the sample mode.

1.13a. PAL1 timing. When PIXWAIT is high, the outputs have the following values: DRST/ = High, CVRT/ = High. The others are unchanged.

MIRAC PAL2 TIMING – SINGLE SAMPLE

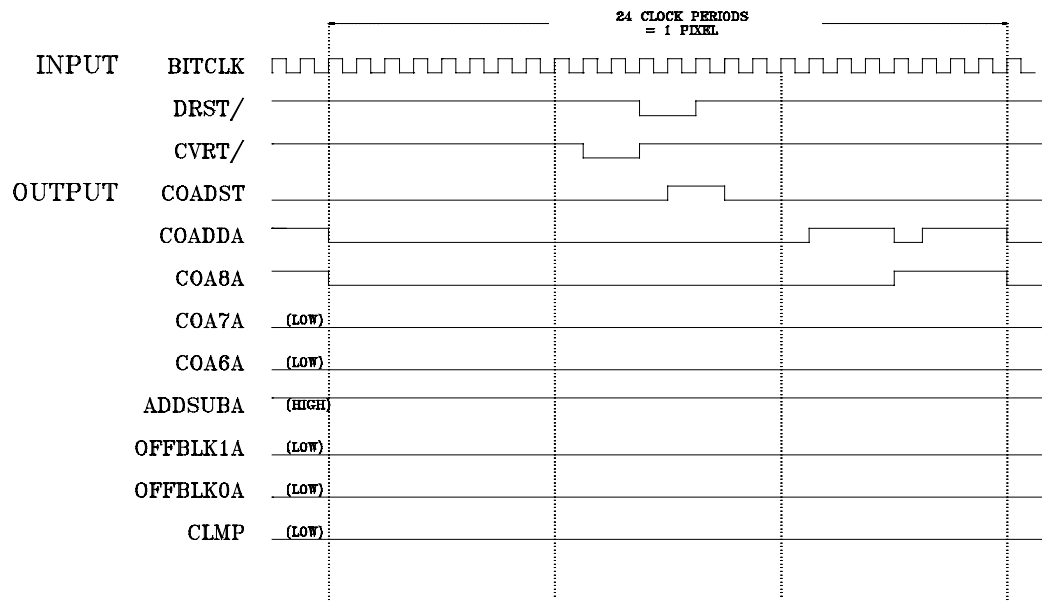


Figure 1.13b. PAL2 timing, single sample mode. PAL2 has several inputs in addition to the ones common to all PALs: CT0-CT4 from PAL1, and IMAGING. When PIXWAIT is high, or IMAGING is false for any of the sample modes, the outputs have the following values: COADST, COADDA, COA8A, COA7A, COA6A, OFFBLK1A, OFFBLK0A, and CLMP = low, ADDSUBA = high.

MIRAC PAL2 TIMING – DOUBLE SAMPLE

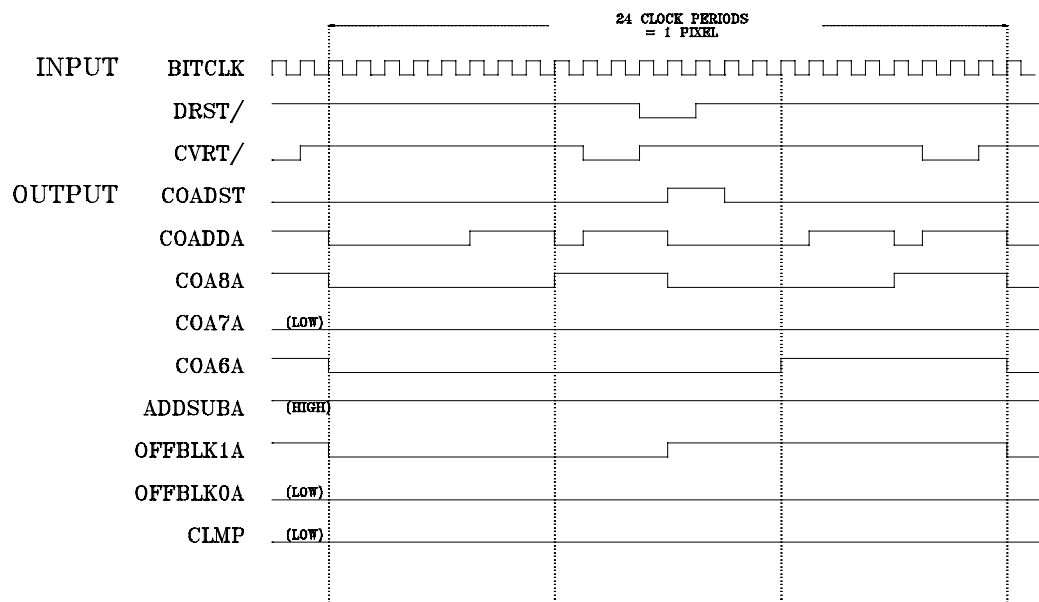


Figure 1.13c. PAL2 timing, double sample mode. See caption to Figure 1.13b.

MIRAC PAL2 TIMING – DELTA RESET

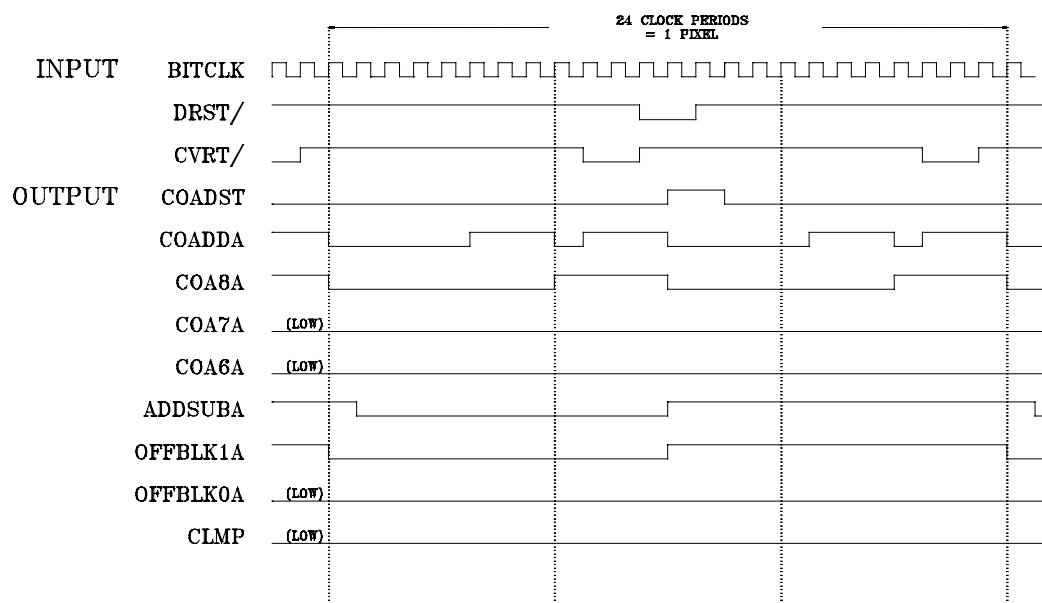


Figure 1.13d. PAL2 timing, delta reset mode. See caption to Figure 1.13b.

MIRAC PAL2 TIMING – TRIPLE SAMPLE

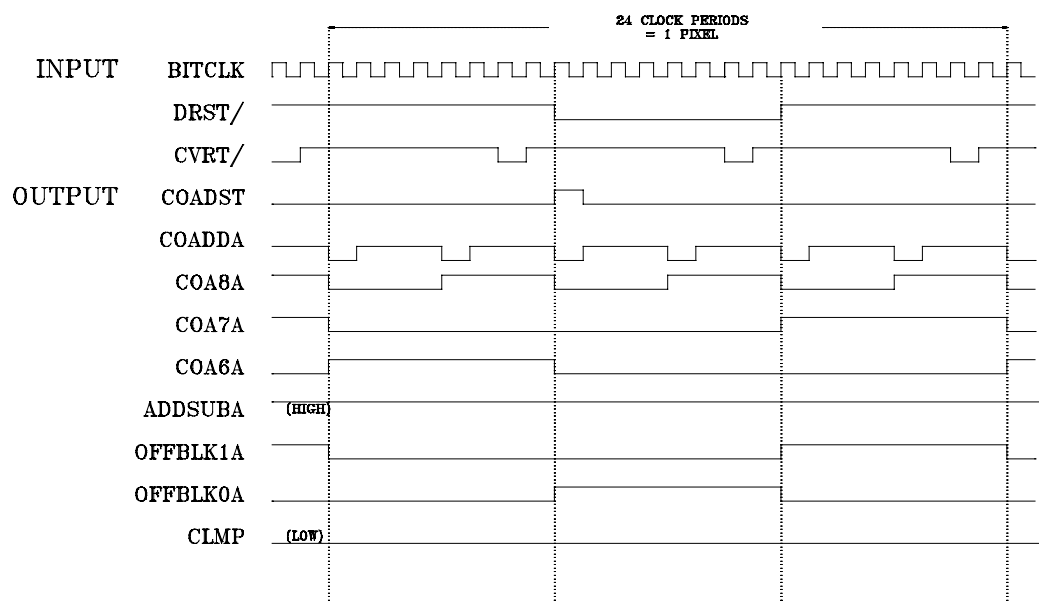


Figure 1.13e. PAL2 timing, triple sample mode. See caption to Figure 1.13b.

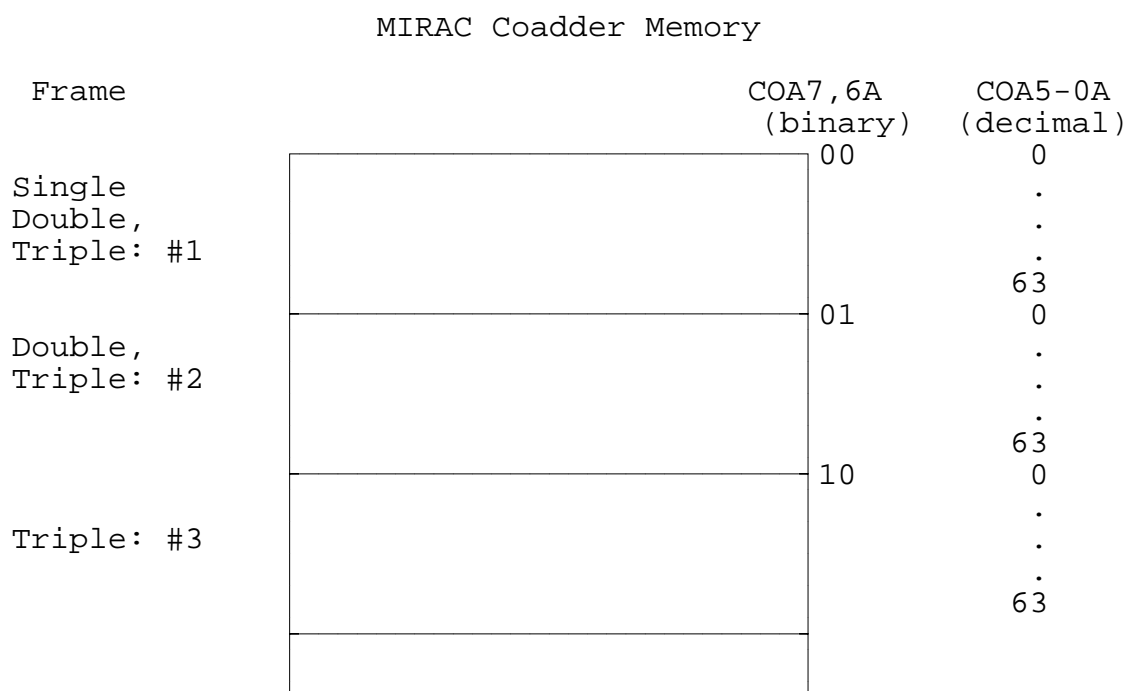


Figure 1.14. MIRAC Coadder Memory Map. This shows the segmentation of the memory space where the coimage is stored during an integration. Two of the above segments exist on each SP board, one for each channel. The channel is selected with the COA8A address line.

Figure 1.15. MIRAC Signal processor block diagram. The inputs on the left edge of the diagram are from the Preamplifier outputs. All the addresses and timing signals are from the controller, except for the end of conversion (EOC) signal from the A/Ds, which insures that the data words from the A/Ds are not used before it becomes valid. The data is transferred to the controller from the FIFO memory output bus, shown in the lower right corner.

MIRAC SIGNAL PROCESSOR

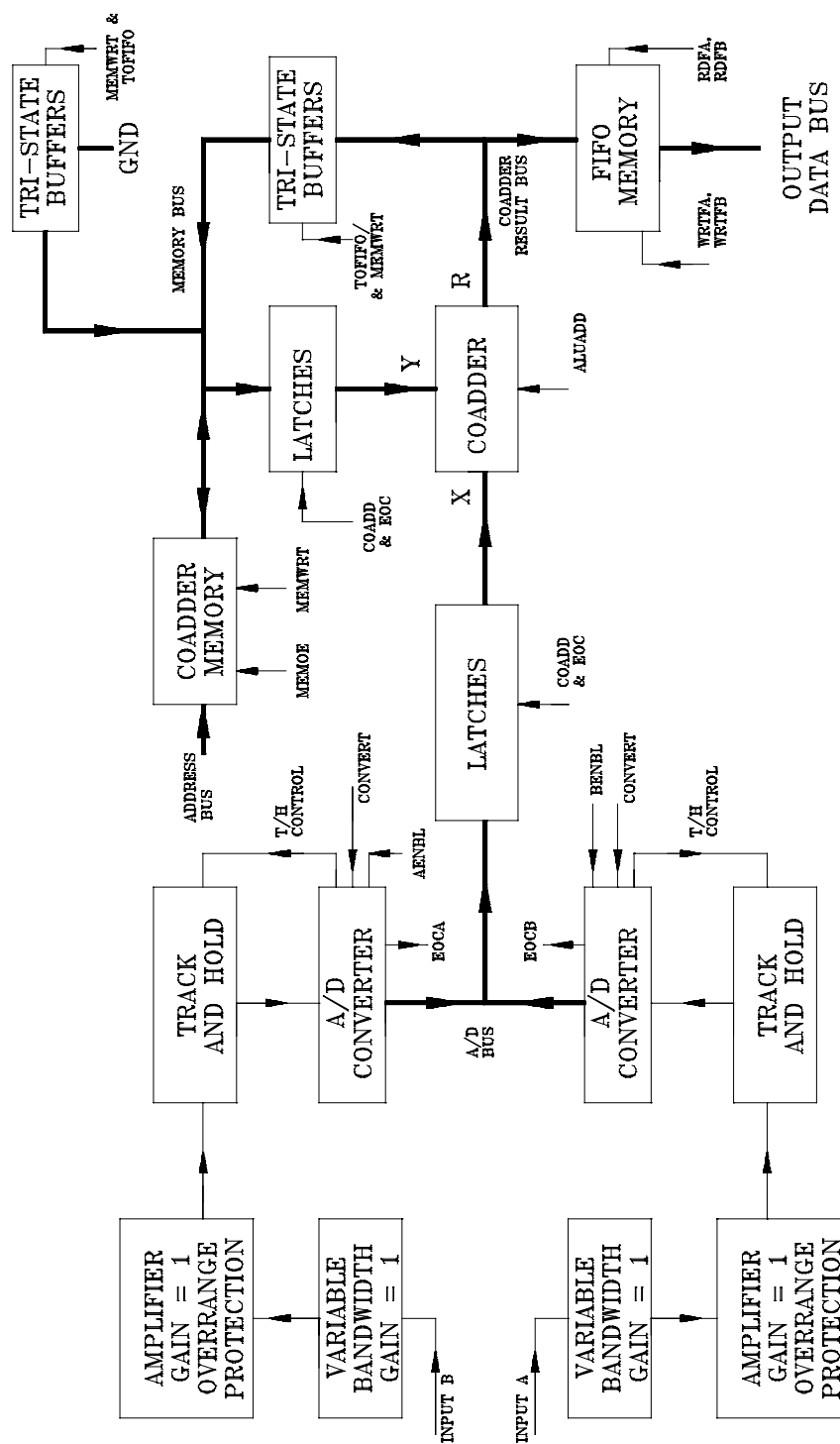


Figure 1.15

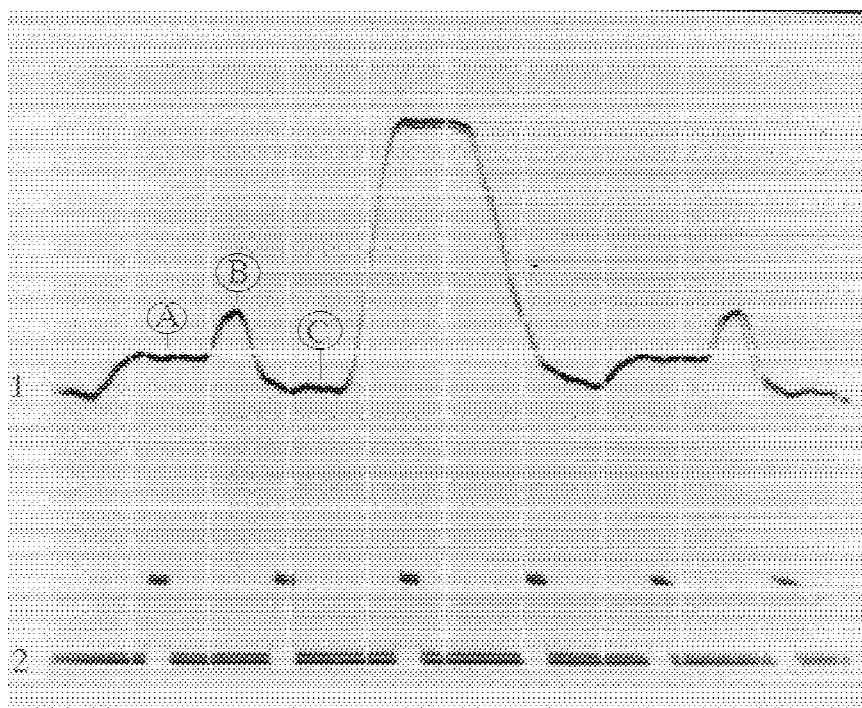


Figure 1.16. Typical analog output from the detector column, shown at the preamp output. This trace is labeled "1". The trace labeled "2" is the CONVERT pulse on the signal processor. The second pixel is being illuminated by a pinhole source, the other two pixels show the background level and the reset feedthrough. The following sample positions are labeled for the first pixel: A - before reset, B - during reset, and C - after reset. The spike at B is referred to as the reset feedthrough. The horizontal axis scale is $.5 \mu\text{sec}$ per division, and the vertical scale is 1 V per division for trace 1 with zero at the top, and 5 V per division for trace 2 with zero at the bottom.

Figure 1.17. Pixel-level timing diagram for delta reset sample mode. Several relevant timing signals are shown at the top of the diagram, and the signals that control the signal processor are shown at the bottom. The hatched regions indicate the limits of the asynchronous conversion completion, according to the specifications of the A/D converter device.

MIRAC DELTA RESET MODE TIMING

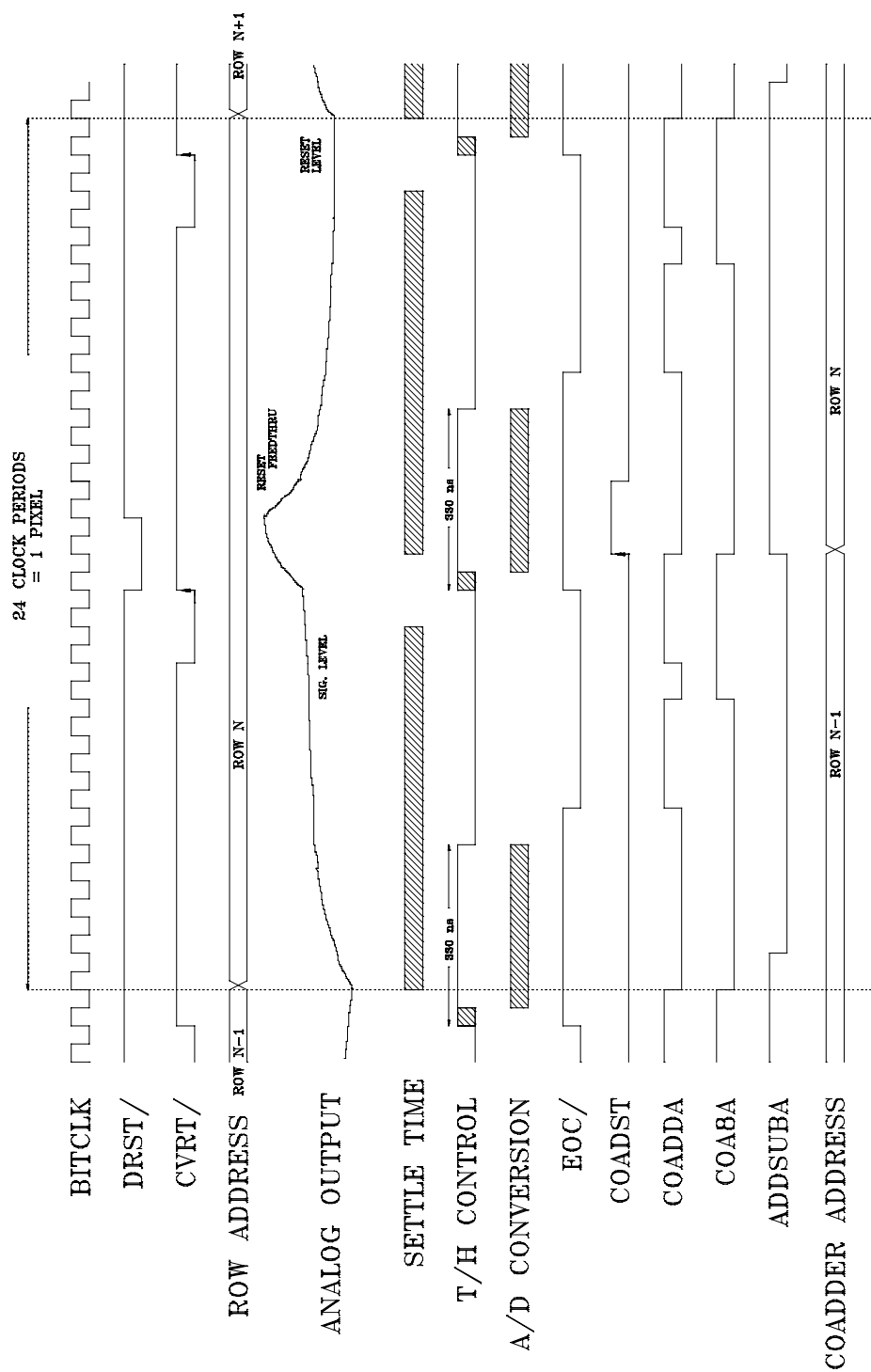


Figure 1.17

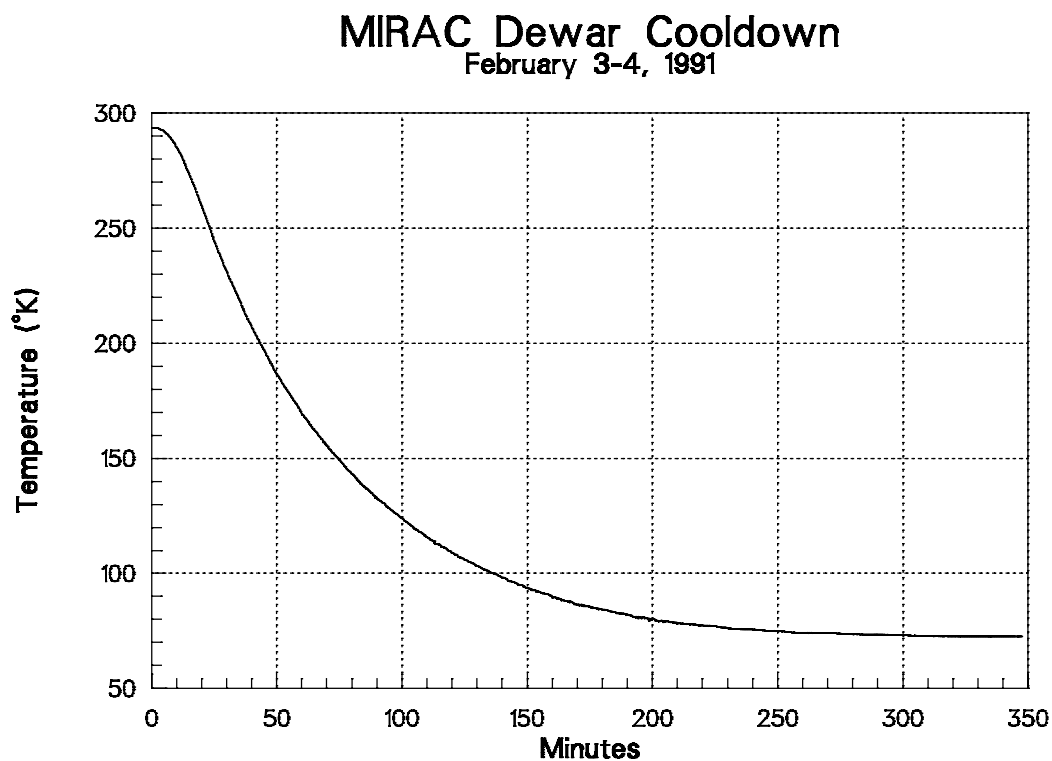


Figure 1.18. MIRAC cooldown from room temperature.

1.18a. With the dewar at room temperature, LN_2 is added to both the nitrogen and helium reservoirs at 0 minutes. The temperature is allowed to stabilize at 77K. Normally, the LN_2 would be removed from the helium reservoir and the LHe fill begun after the temperature drops below 100K.

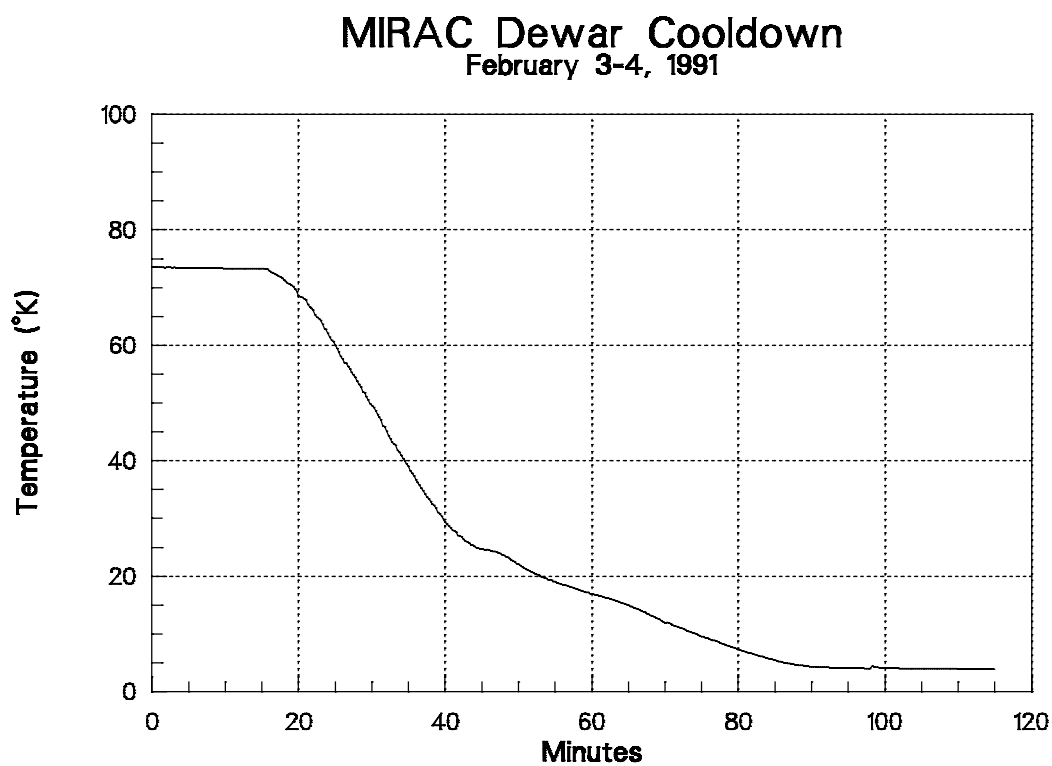


Figure 1.18b. The dewar has stabilized at 77K. At a time of approximately 15 minutes, the LN₂ is blown out of the helium reservoir, and it is filled with LHe. The temperature stabilizes at 4K in about 75 minutes.

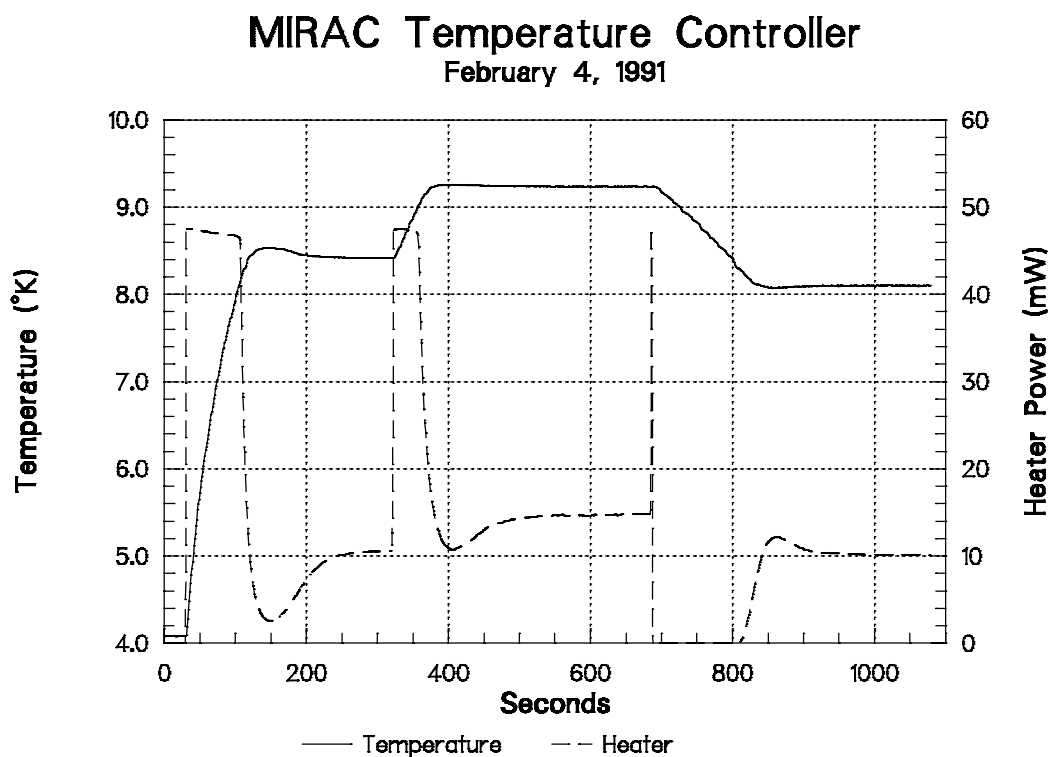


Figure 1.19. MIRAC temperature and heater power. The temperature controller was set at a goal temperature of 8.5 K and turned on with the detector block initially at 4.1K. At approximately 320 seconds into the test, the temperature goal was set to 9.2K. Then at approximately 680 seconds the temperature goal was set to 8.1K.

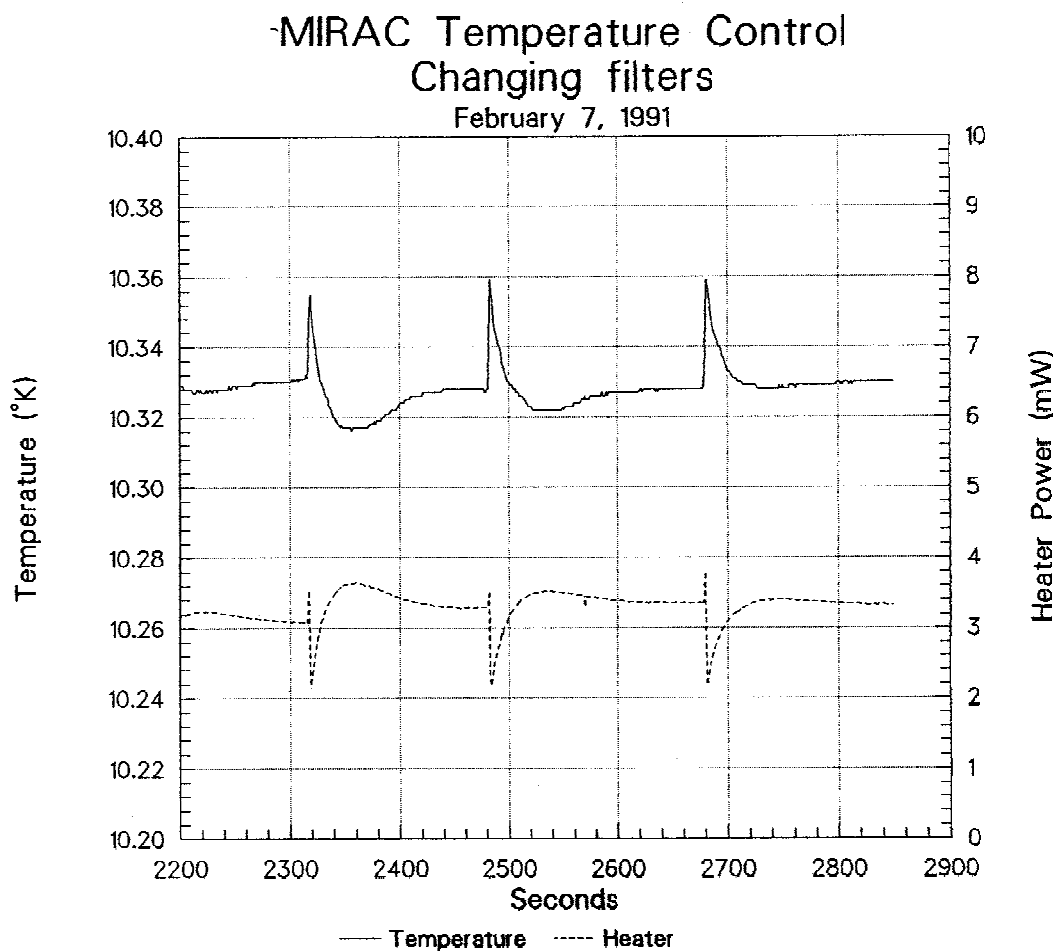


Figure 1.20. MIRAC temperature while changing filters. The initial filter was the 8.8 μm with the 20% neutral density, and the filter was changed successively to the next three adjacent ones, the 9.8, 11.7, and 12.5 μm . The filter wheel motors take approximately 5 seconds to move from one filter to the next. In the plot, a spike in the temperature occurs just as the filter is changed. This is because the detector is momentarily blanked off as the filter wheel turns to the next filter, and the self-heating of the array increases. This causes the temperature to increase, so the controller lowers the heater power. It takes approximately 150 seconds for the temperature to stabilize to the original value.

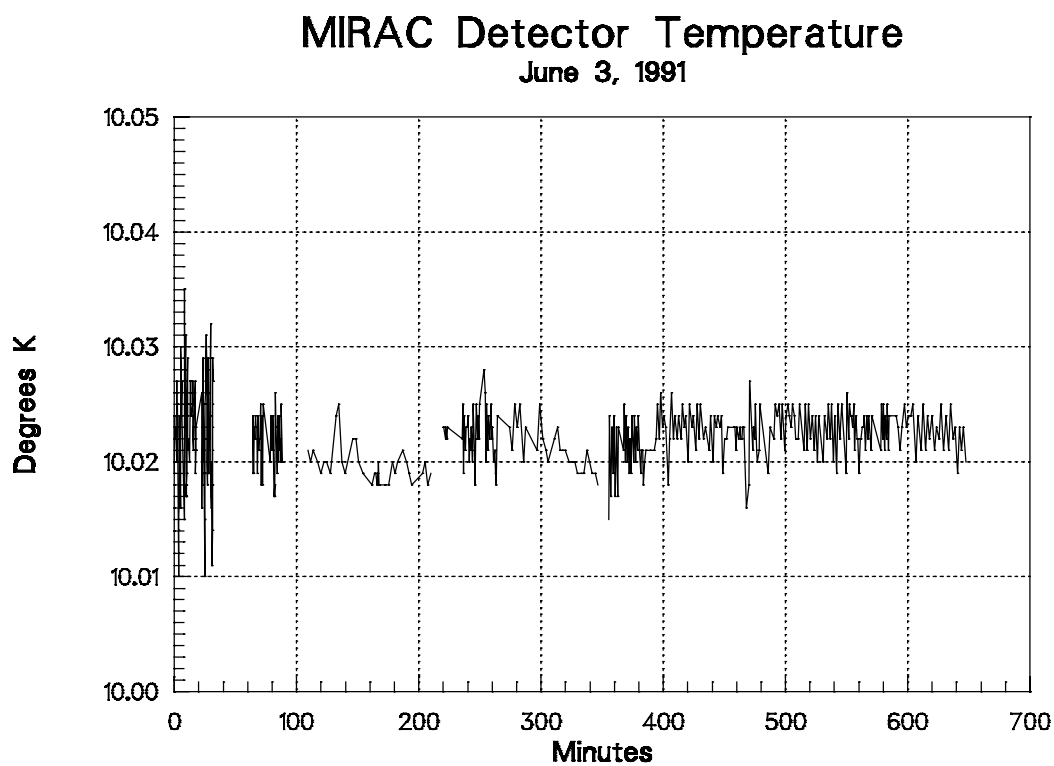


Figure 1.21. MIRAC detector temperature and heater power for June 3, 1991. The temperature was recorded at the beginning of each observation taken.
1.21a. Detector Temperature.

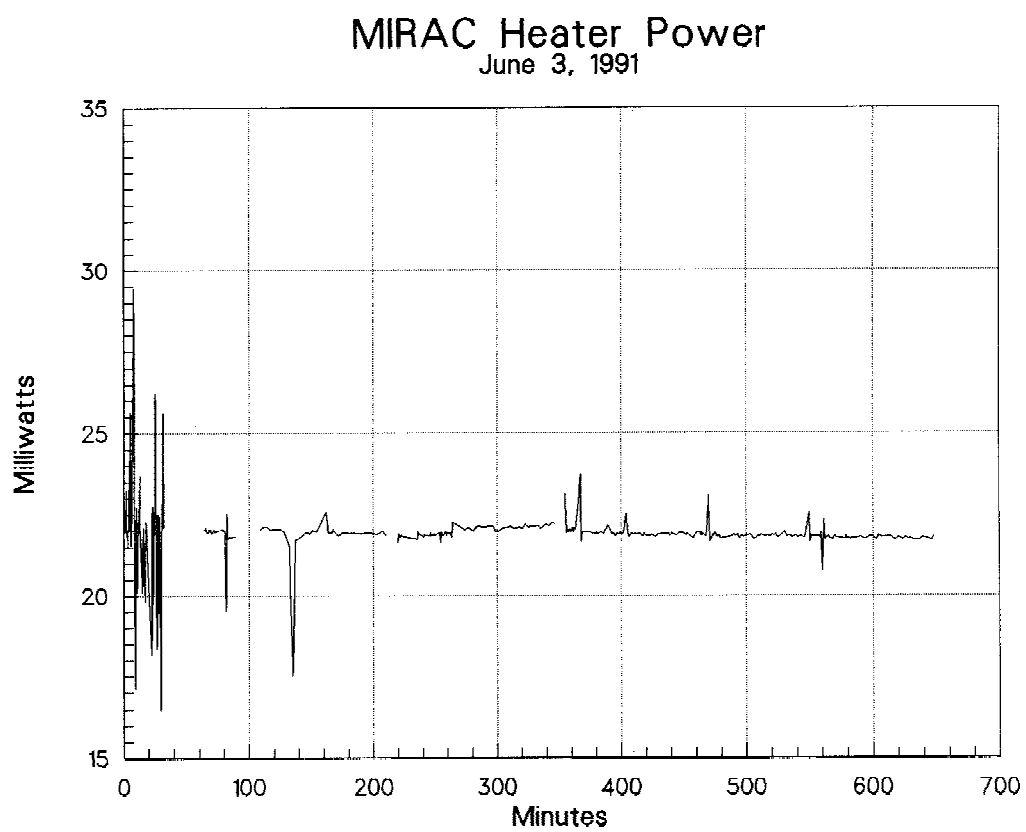


Figure 1.21b. Heater Power for June 3, 1991.

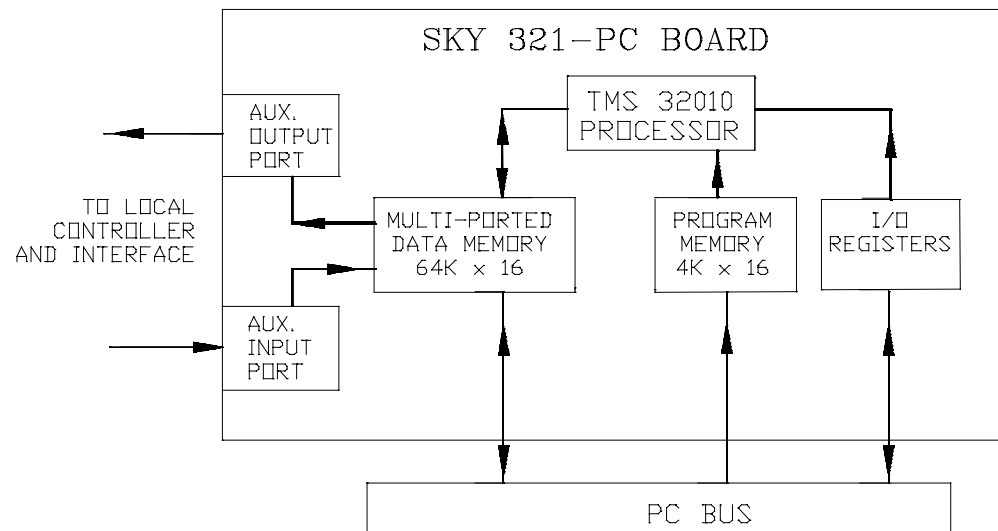


Figure 1.22. Block diagram of the Sky board. The PC can write to data and program memory and registers on the SKY board, and read registers and data memory. The TMS 32010 processor's program is read from program memory, and it can read and write from the data memory and registers. It can also direct transfers to and from the auxiliary input and output ports, which are connected to the local controller/interface which provides communication with the MIRAC electronics.

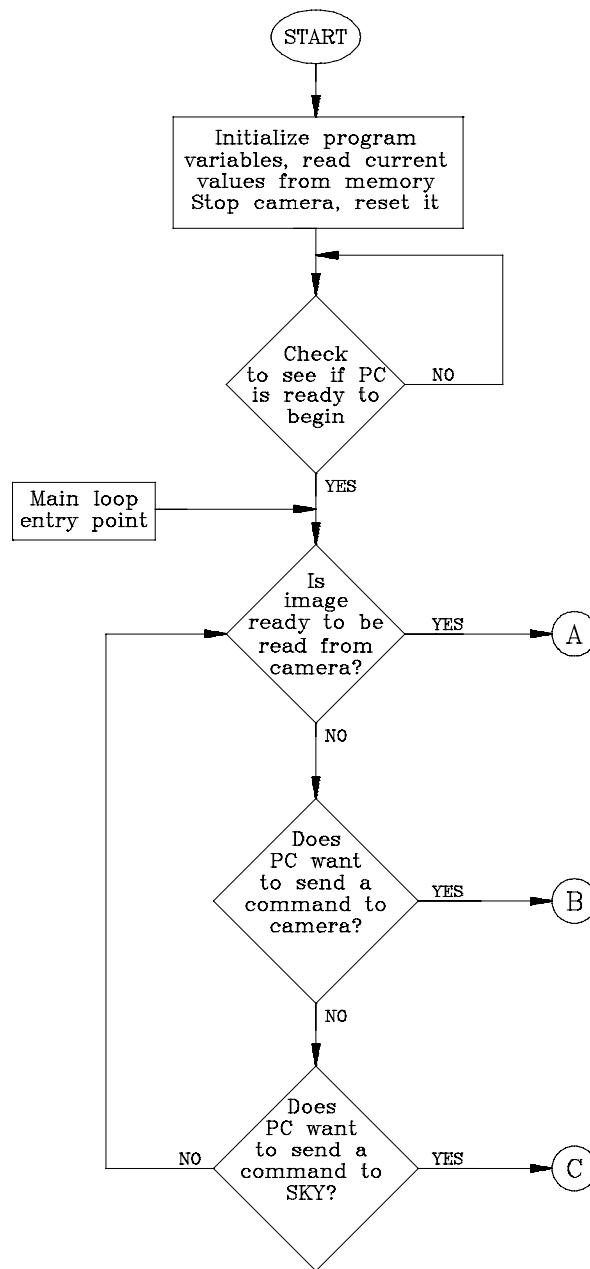


Figure 1.23. Flowchart of the SKY program. The letters (A), (B), and (C) refer to subroutines that return to this main loop at the point marked main loop entry point.

a. Main sky board loop.

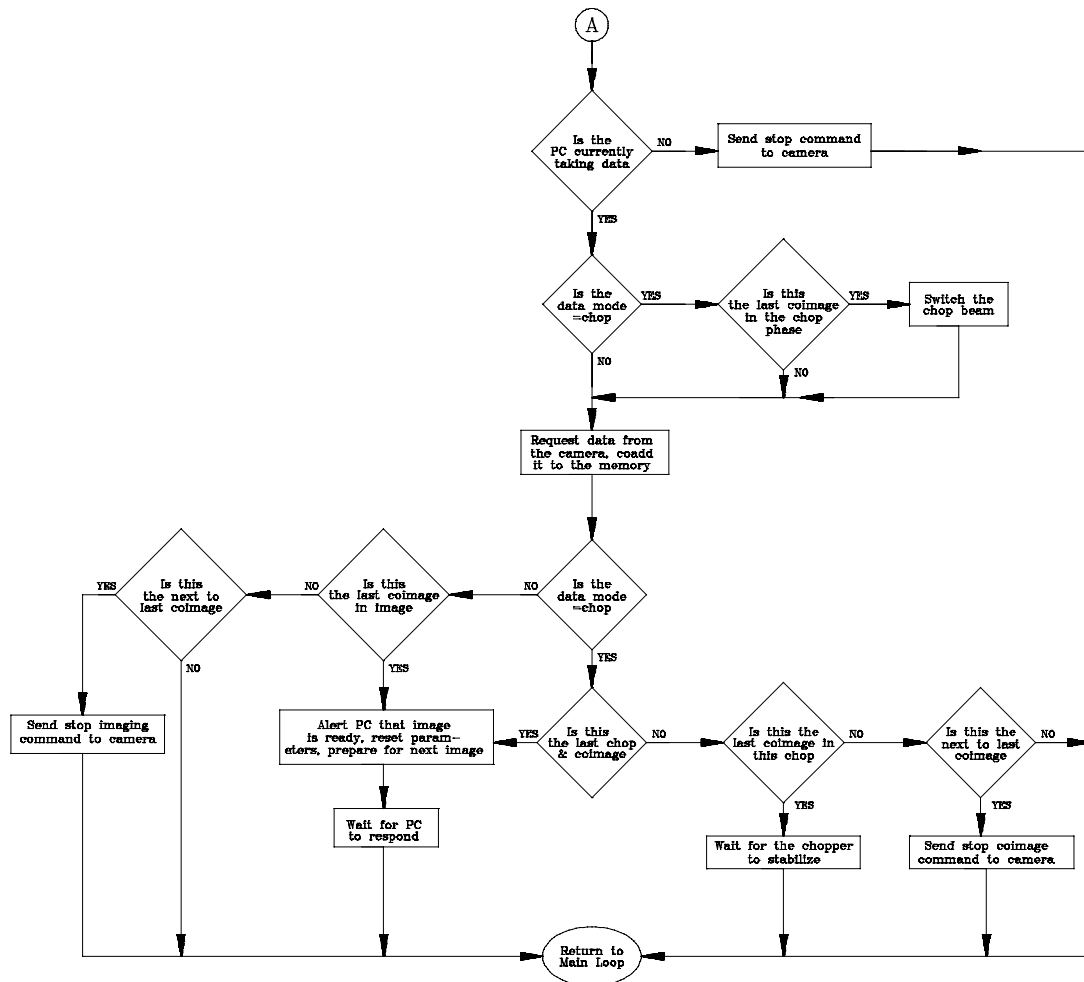


Figure 1.23b. image ready loop. This routine is executed at the point marked **A** in Figure 1.23a. Two different observing modes are handled, depending on whether chopping is active.

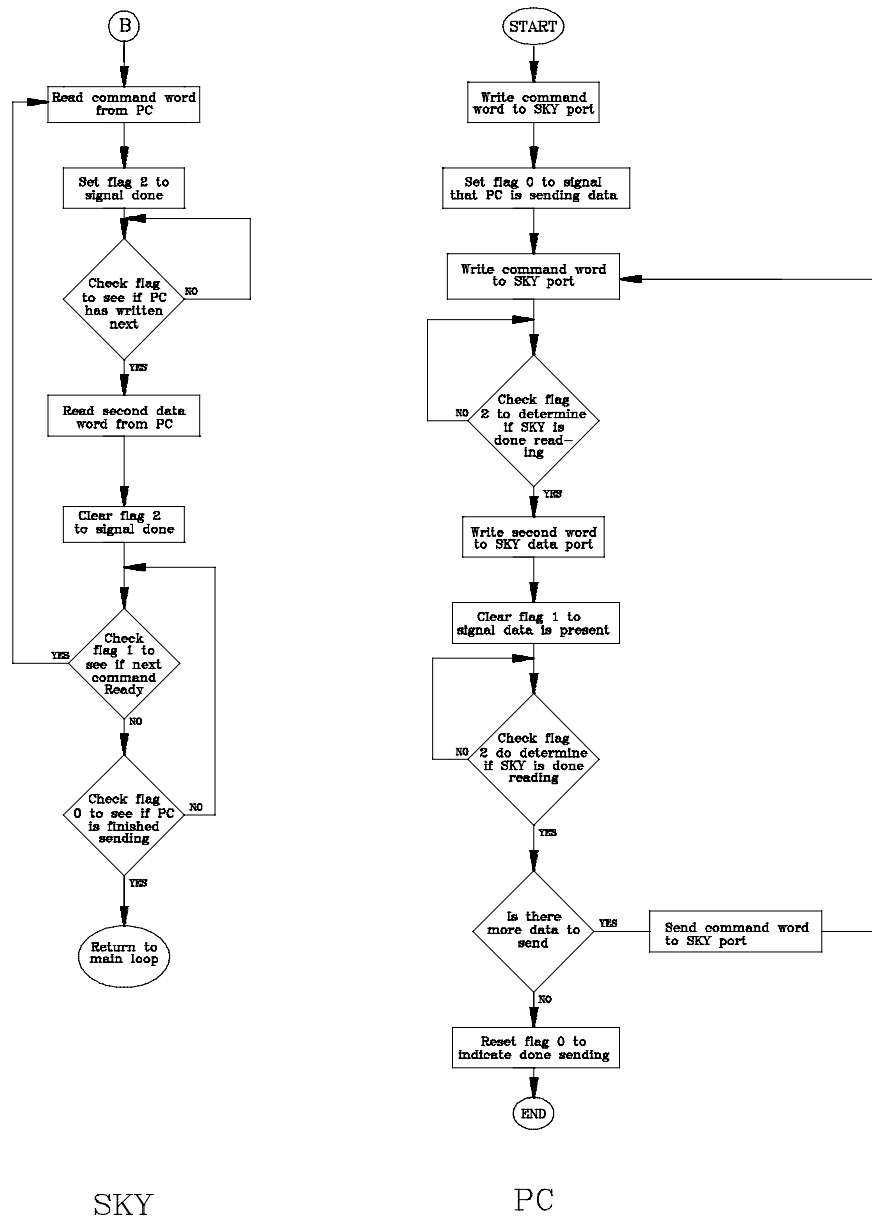
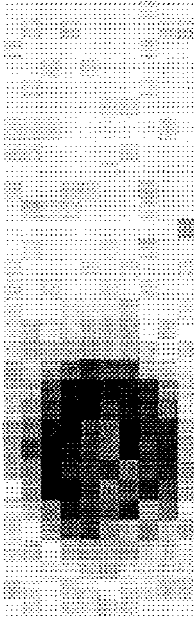


Figure 1.23c. PC to SKY board communication procedure. This routine is marked (C) in Figure 1.23a. The routine executed on the SKY board is shown on the left, and the corresponding procedure for the PC computer is shown on the right.

```

OBS:  Unit Mode Header Run Wait Save Filter Locat Disp Util Quit
      IntTime: 0.00 SampleM: 4 Reset Off_RA : 0.00
      ObsMode: Grab ClkRate: 15.000 MHz Off.Dec: 0.00
      Hwlgth : 13.20 Fr Time: 1.0240E-4 Filter 1: Nonstd
      Chop Fr: 0.15 ChpWait: 0.000ms Filter 2: Baf2
      ElcTemp: 0.00 DetTemp: 0.000

Dmax: 1.39 ( 12, 5 ) Dmin: -0.27 ( 31, 3 )
Fit= Max: 0.92 (11.08, 0.00) FWHM-X: 4.79 FWHM-Y: 0.00
Total RMS: 0.410 Avg: 0.21 Num: 318
Background RMS: 0.102 Avg: -0.08 Num: 89
Source Sum: 70.13 Num: 255 ( 3 )
Sky Flux: 0.0 RMS: 0.00 DIF: 0.0

OBS: 7-12-91 13:29:25 C910712A.001 IDLE 0:00/0:00 0/1
DISP: 6-02-91 9:45:15 f:\data1\C910602A.160 BD+30 3639

```

Figure 1.24. MIRAC program main screen.

1.24a. Main screen in OBS: command line with sample image.

```

OBS:  Init Mode Header Run Wait Save Filter Locat Disp Util Quit

IntTime: 4.82      SampleM:  A Reset      Off.RA : 0.00
ObsMode:  Chop-Mod ClkRate: 7.324 KHz      Off.Dec: 0.00
Wvlngth : 0.00     Fr Time: 1.0486E-1     Filt1:  Nonstd
Chop Fr:  4.35     ChpWait: 10.00ms       Filt2:  Open
ElcTemp: 0.00     DetTemp: 10.629

A. Filter          Nonstd
B. Filter          Open
Time (sec)         4.823
Total Coadds       46
Clock Rate         7.324 KHz
Sample Mode        A Reset
# of Raster Positions 0
Frames per Coimage 1
Frame Time         1.0E-0001
Magnification      0.58
Nod Line           4.00
Chop Frequency     4.353
Chop wait time (ms) 10.000
Per Chop phase     1

Dmax: 0.30 ( 63, 63)  Dmin: -0.13 ( 48, 63)
Total RMS: 0.047  Avg: -0.00  Num: 315
Background RMS: 0.030  Avg: -0.01  Num: 286
Source Sum: 2.89  Num: 29 ( 6)
Number of observations: 1.0
Sky Flux: 0.0  RMS: 0.00  DIF: 0.0

OBS: 2-25-91 16:27:51 C910225A.001 Blank sky      IDLE 0:00/0:24 0/1
DISP:02-14-91 10:35:11 e:\data12\m4151sh.nap NGC 4151

```

Figure 1.24b. A MIRAC program pull-down menu showing options.

7-12-91 14:07:16 File: ~tal\C910602A.160 7-12-91 14:06:52

Date: 6-02-91 Time: 9:45:15

Object information:

Name : BD+30 3639
R. A. : 19:32:47.50
Dec. : 30:24:20.00
Off.RA : 2.00 arcs
Off.Dec: 2.40 arcs

Camera parameters:

DtBias: -2.60 Offbuf : 0
ADTemp: -41.38 DelayCy: 0
ERTemp: 9.22 Row Cnt: 64
DtTemp: 10.03 Bndwdth:1400 KHz
HPower: 19.95 Gain : -1.00
Extent: Half Array : 32 x 10

Observing Parameters:

Filtr 1: Nonstd SampleM: Reset
Filtr 2: Nonstd TotCoad: 24600
Wvlgth : 12.80 IntTime: 10.08s
ClkRate: 1.875 MHz ObsMode: Chop-Nod
FrPerCo: 200 Fr Time: 4.0960E-4

Telescope:90-inch

Magnif.: 0.29
Chop Fr: 5.16
NodWait: 4.00s
T Scale: 1.99"/mm
ChpWait: 15.0ms

Mask : msk11_20.map
Gain Map : e:\data10\gain125.map
Comment : c910602a.160

Data Max: 1.39 (12, 5) Min: -0.27 (31, 3)
Display Max: 1.39 Min: -0.27
Fit> MAX: 0.92 (11.08, 0.00 FWHM-X: 4.79 FWHM-Y: 0.00
Total Sigma: 0.410 Avg: 0.21 Num: 318
Background Sigma: 0.102 Avg: -0.08 Num: 63
Source Sum: 70.13 Num: 255 (3)
Number of Observations: 1.0
Sky Flux: 1445.014 RMS: 0.833 DIF: 0.319

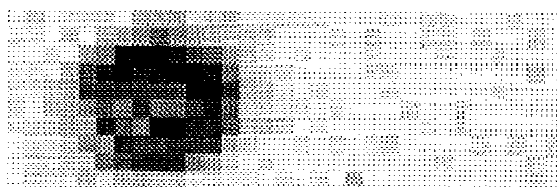


Figure 1.25. Sample MIRAC output, showing header information, map statistics, and image.

Figure 1.26. MIRAC Guider box assembly diagram, side view. At the top is the mounting flange that attaches to the telescope. The upper, largest mirror can be rotated into the beam to reflect it to a viewing port, but is usually stored in the vertical position to allow the beam to reach the dichroic. The MIRAC dewar and mounting mechanism are shown attached to the right side, and the TV can be attached to the port on the lower left. The position of the relay optics can be adjusted to properly focus the MIRAC and the TV on a common telescope focus. The magnification flip mirror has two positions, one for each magnification of the camera.

1.26a. Low magnification. After passing through the dichroic, the optical light is reflected directly into the TV relay optics.

MIRAC GUIDER BOX AND CAMERA MOUNT

Low Magnification

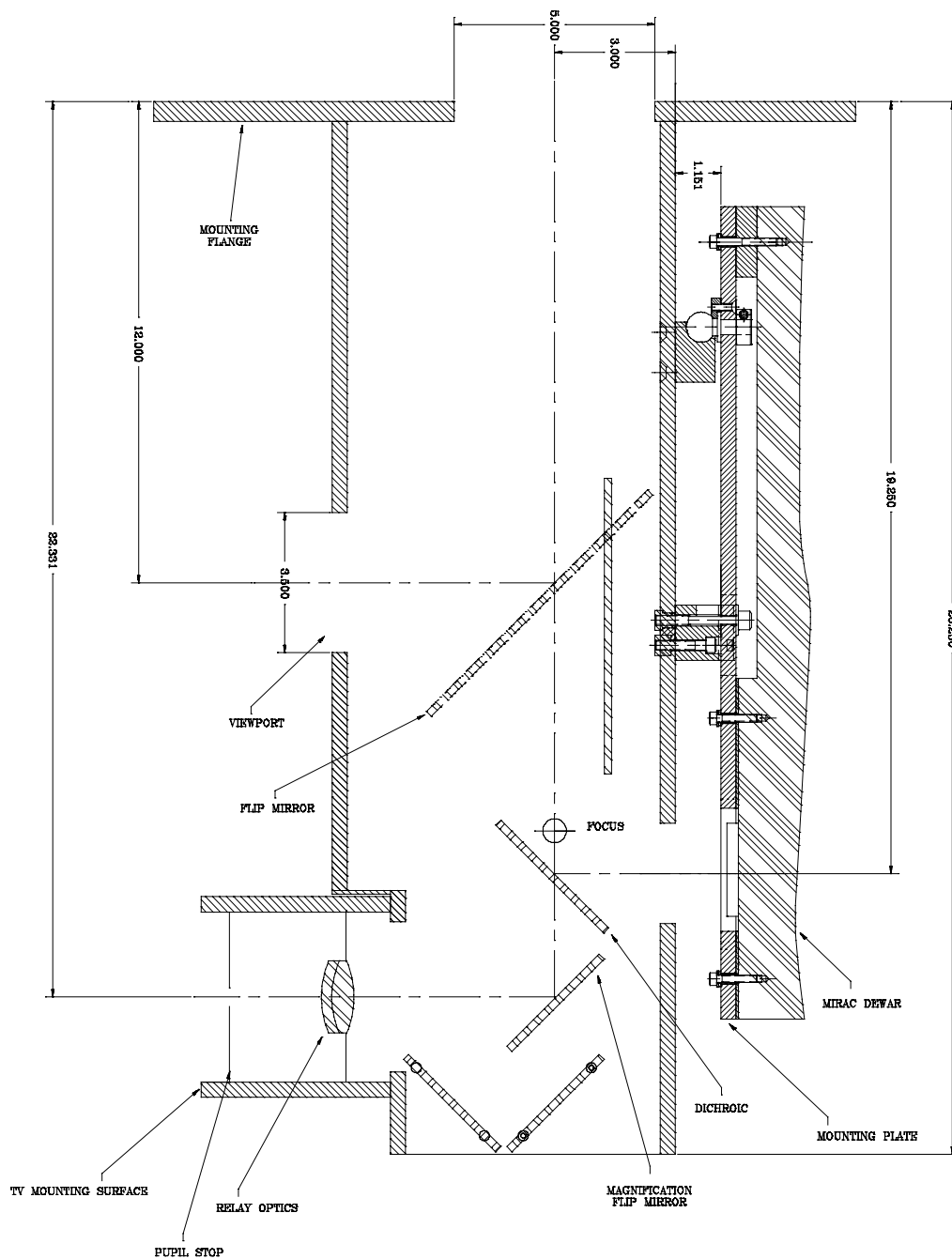


Figure 1.26a

Figure 1.26b. High magnification. The magnification flip mirror is rotated 90° clockwise in this diagram. The optical light is allowed to pass to the pair of mirrors at the bottom of the box. The beam is then reflected up to the flip mirror in its alternate position and then into the TV relay optics.

MIRAC GUIDER BOX AND CAMERA MOUNT

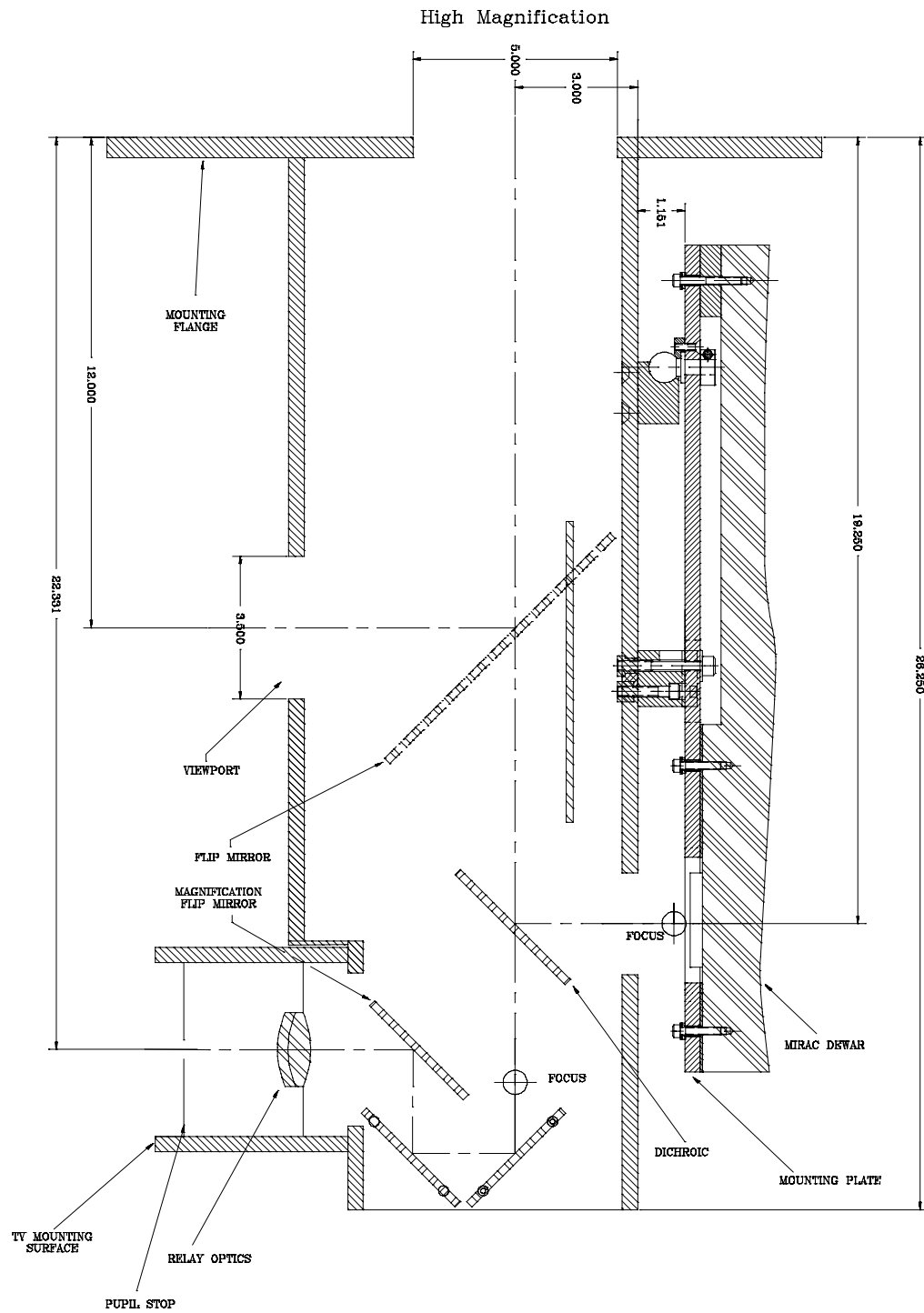


Figure 1.26b

Figure 1.27. MIRAC Guider box dichroic holder. The dichroic is mounted in a plate which "floats" above a larger plate which is attached to the inside walls of the box. The floating plate has three points of support, two pivot screws and a stainless steel ball, and is held in place by three springs pulling the plate against these points of support. By turning the pivot screws using knobs outside of the guider box, the alignment can be adjusted in R.A. and Dec.

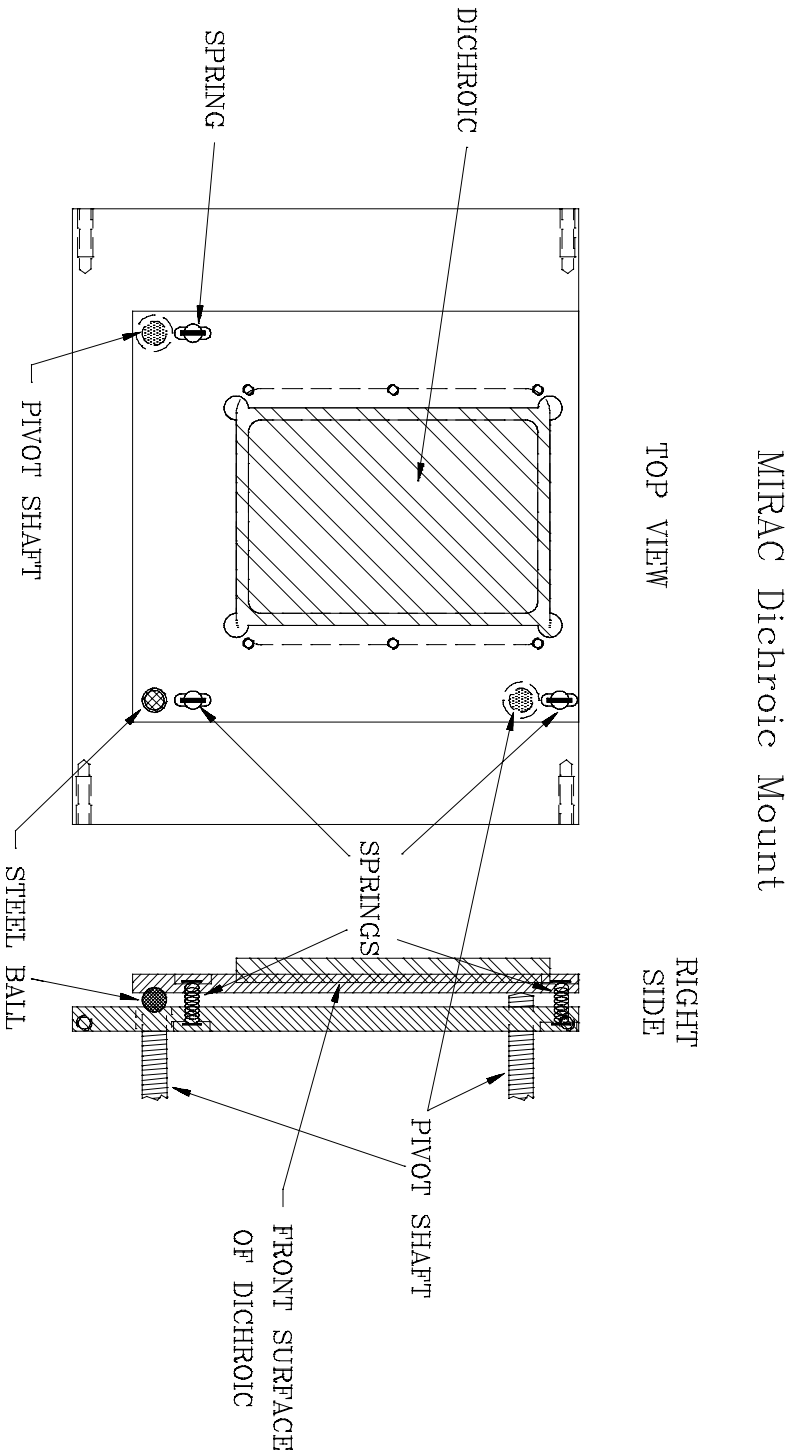


Figure 1.27

Figure 1.28. MIRAC dewar mounting plate. The side view shows the dewar and mounting plate on the left, and the guider box front plate on the right. The mounting plate is separated from the dewar by G-10 spacers and attached using nylon-insulated screws, isolating the dewar from the telescope. A round ball on the mounting plate fits into a socket on the guider box, and a rectangular post slips into a groove on the mounting plate to align the dewar laterally. Two screws on the mounting plate on either side of the post screw into the guider box to secure the dewar.

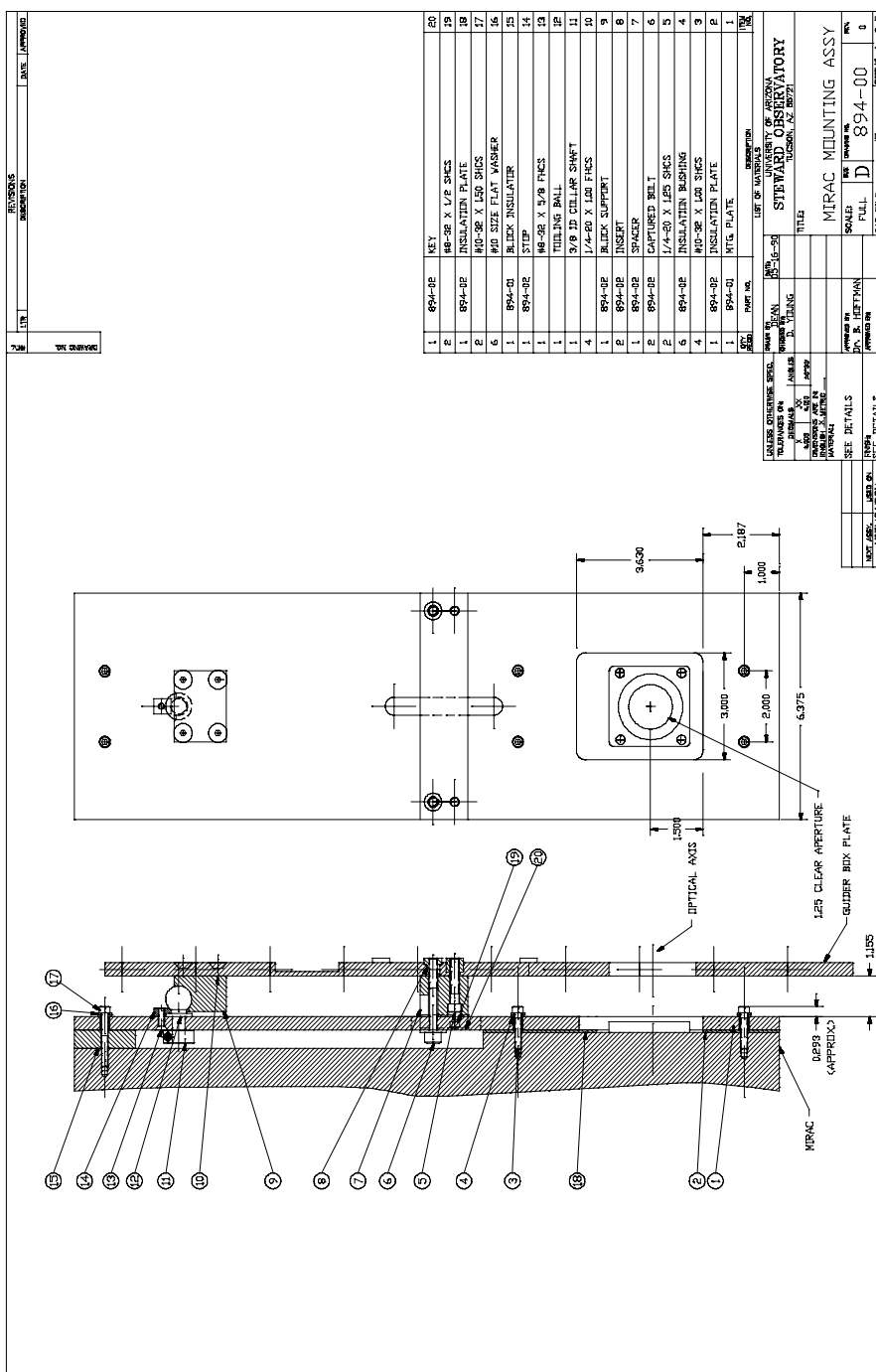


Figure 1.28

Figure 1.29. MIRAC Lab test setup. The pinhole and XYZ stage were present only for the optics evaluation. The chopper is controlled by the MIRAC computer with a logic pulse, just as it controls the chopper on the telescope.

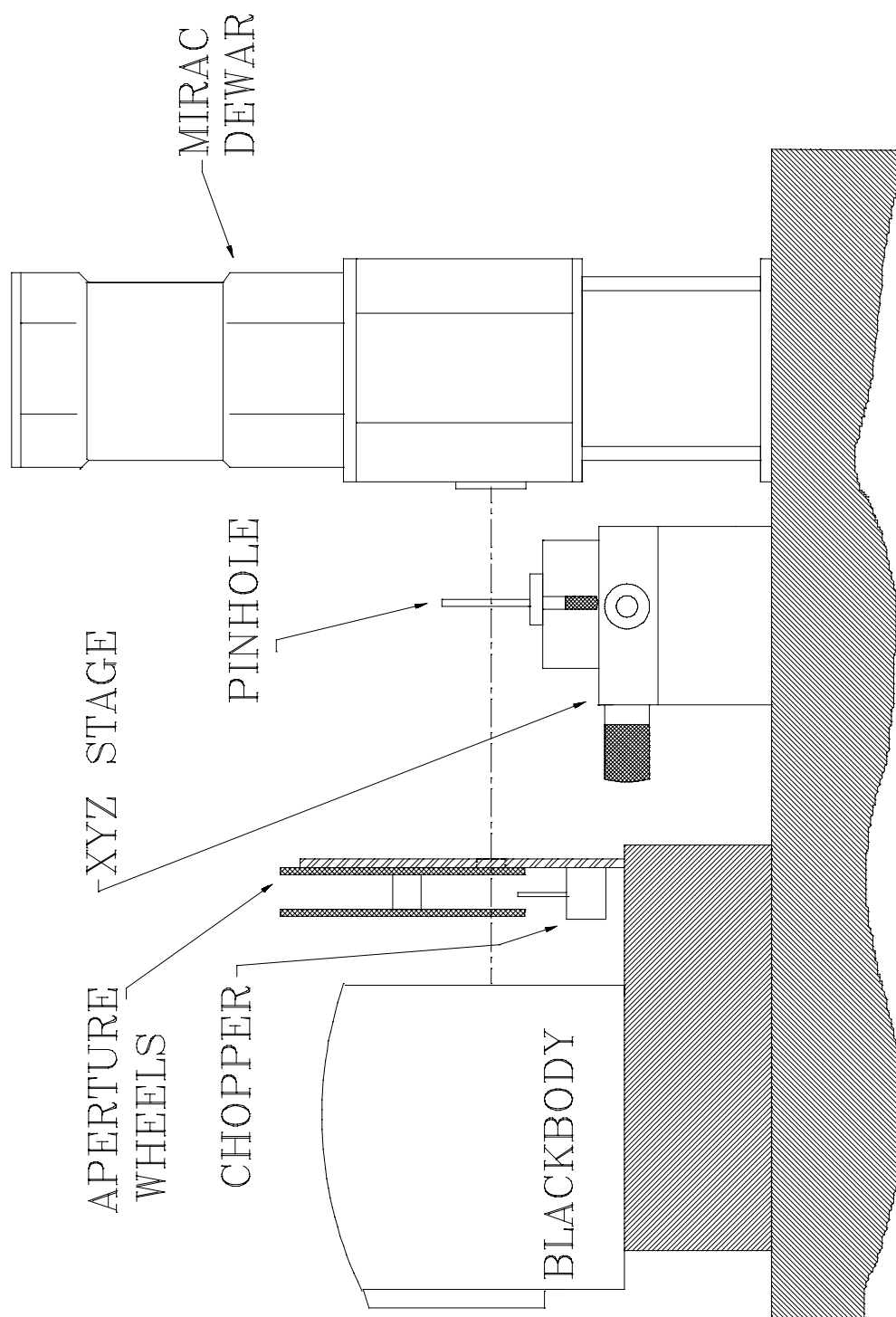


Figure 1.29

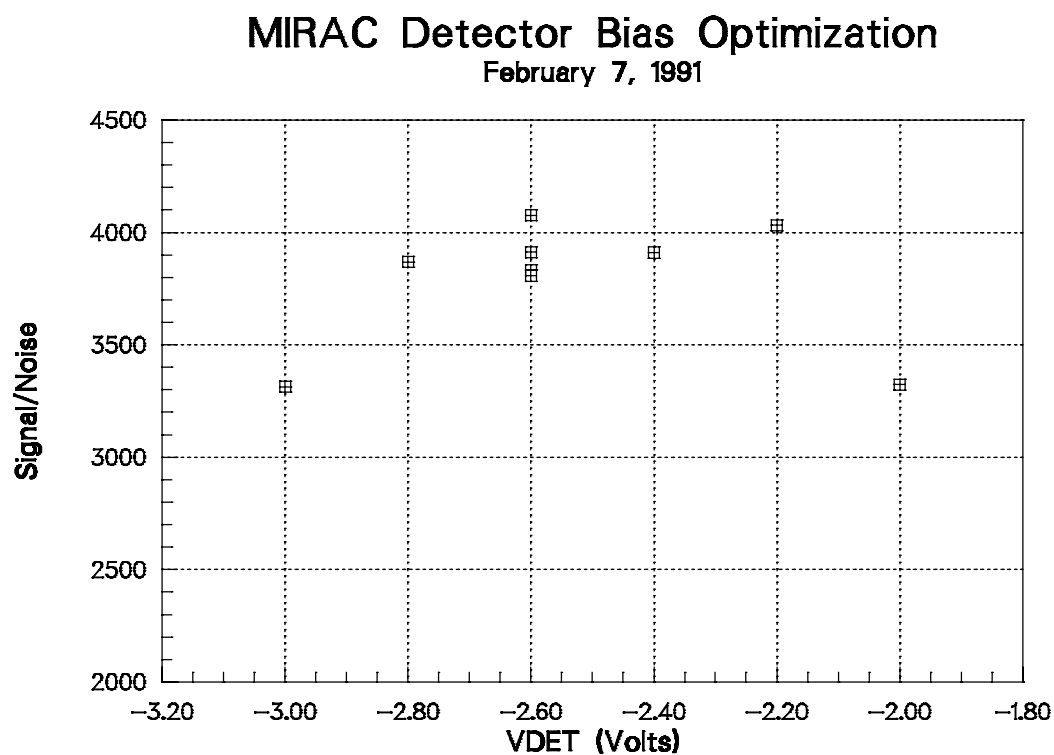


Figure 1.30. Mirac optimization measurements.

1.30a. Signal/Noise as VDET is adjusted from -3.0 to -2.0 V. The S/N is relatively flat over the range -2.8 to -2.2 V, with a definite downturn outside this range at -3.0 and -2.0 V.

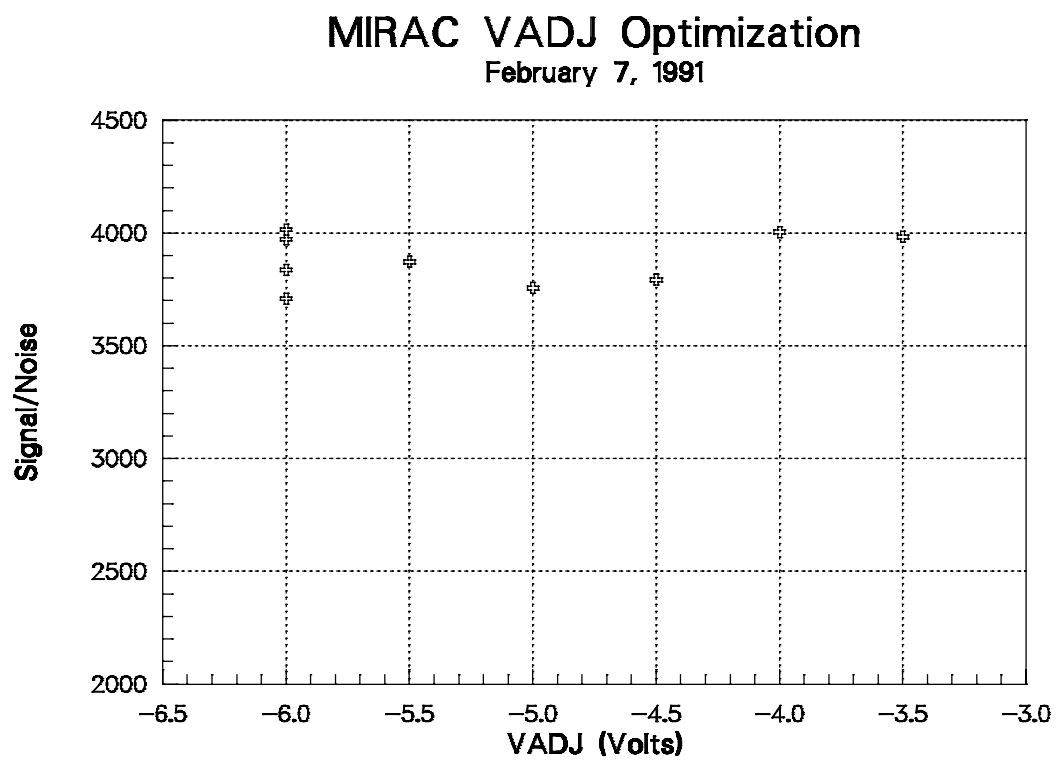


Figure 1.30b. Signal/noise as VADJ is adjusted over the range -6 to -3.5 V. Changes in VADJ has a negligible effect on S/N over this range.

MIRAC NOISE vs BACKGROUND

Feb 9, 1991

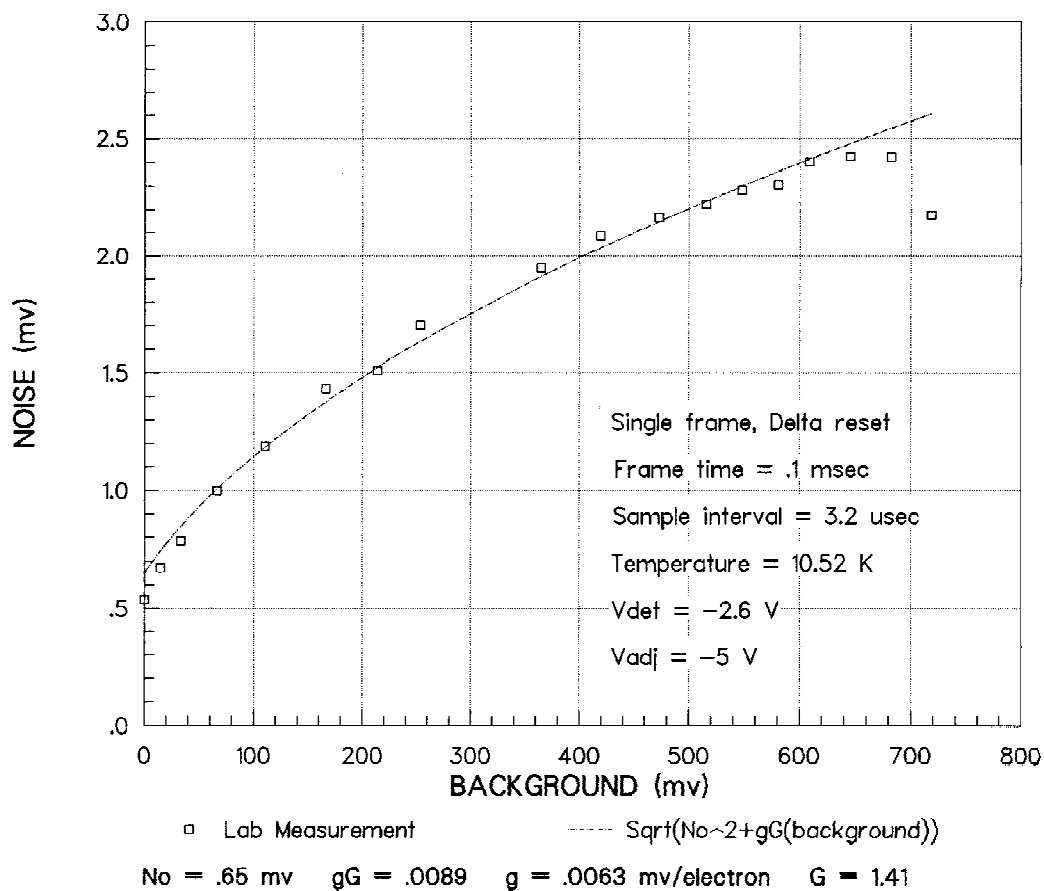


Figure 1.31. MIRAC noise as a function of background flux. The data were taken using various filter and attenuator combinations to achieve different backgrounds, using a 308K blackbody as a source. The noise was taken from an image formed by differencing successive frames, and taking the sum of all the differences. The noise was defined to be the standard deviation of this image.

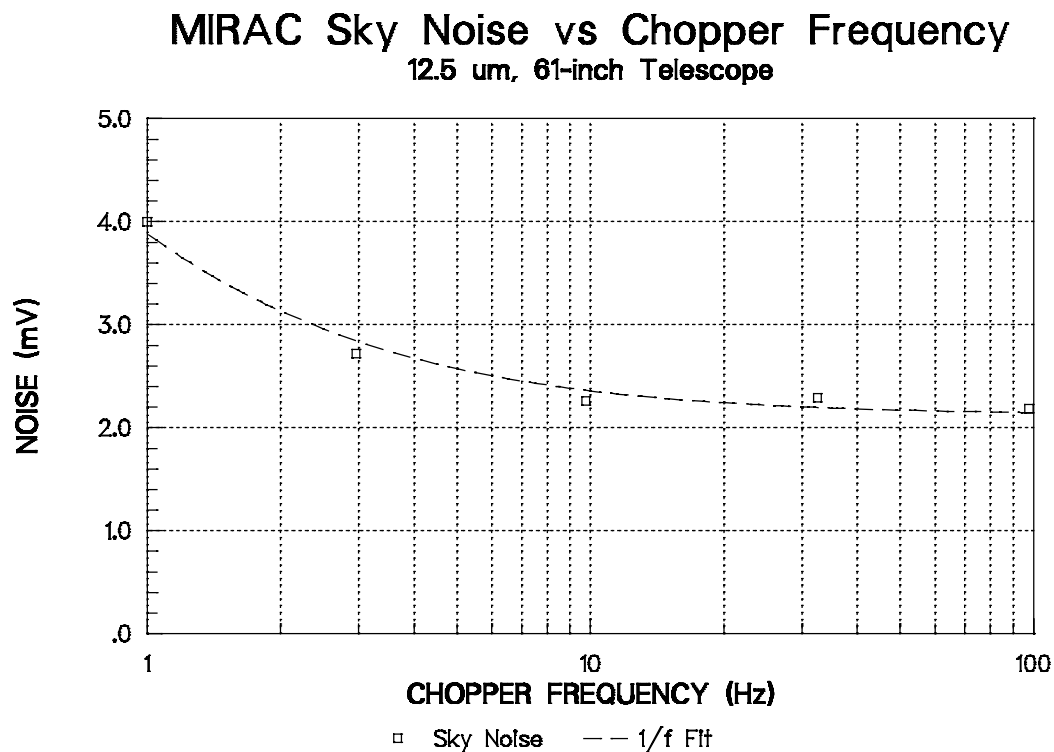


Figure 1.32. Sky noise as a function of chopper frequency at 12.5 μm . The noise was determined from a time sequence of 50 one-second chop pairs on blank sky at an airmass of 1. The curve is the best fit of the data to the function of the form $n = \sqrt{A^2 + B/f}$, where n is the noise, A and B are constants, and f is the chop frequency. The best fit values for parameters A and B are 2.1 mV and 3.3 mV, respectively.

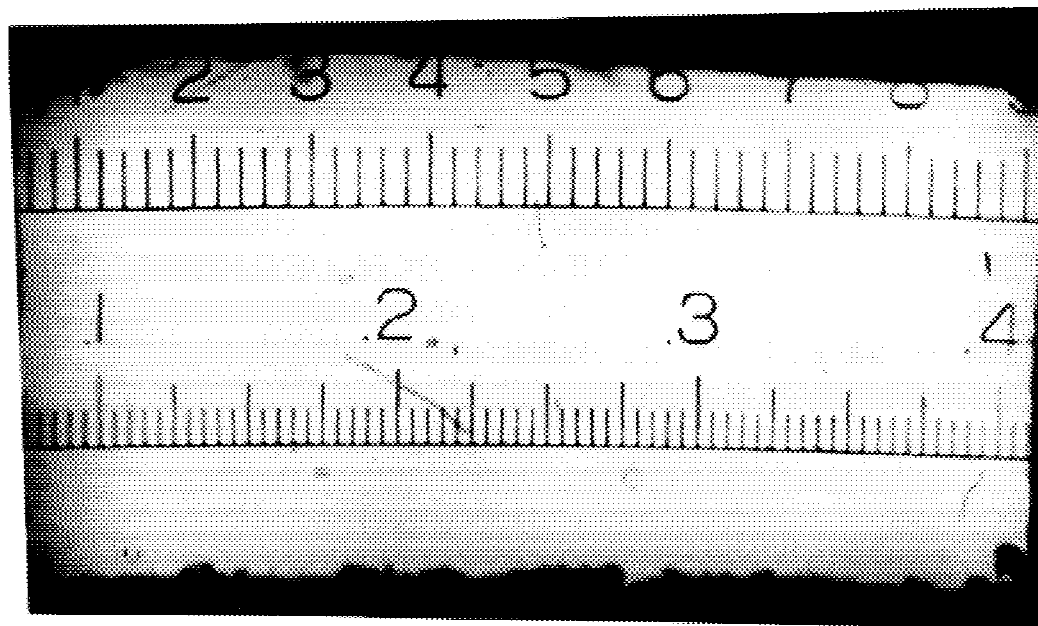


Figure 1.33. Photograph of reticle through MIRAC optics. The lower reticle scale is labeled in inches, with the smallest divisions being .005 inch. The upper scale is labeled in mm, with the smallest divisions being .2 mm (the detector pixel spacing is .1 mm). The reticle was masked to be roughly 4 mm x 8 mm and placed at the low magnification position and back-illuminated. The photo was taken at the focus position outside of the dewar with a 35mm camera with the lens removed. The f/35 MIRAC pupil was used, and the position was determined by achieving the best optical focus through the camera.

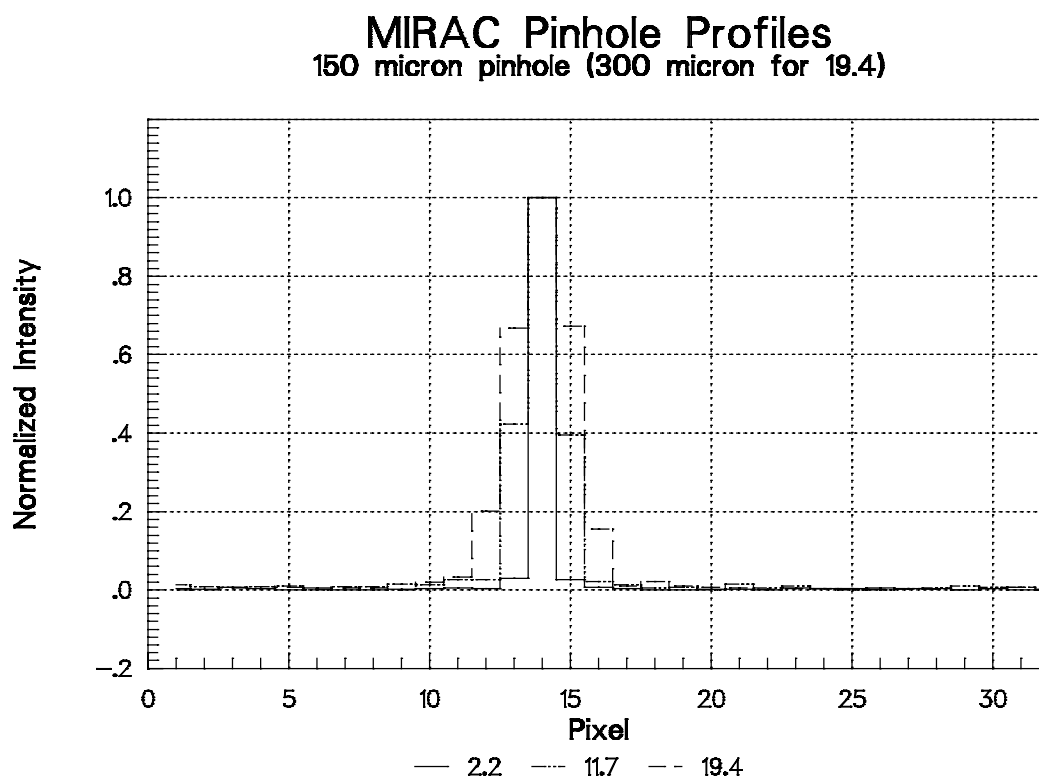


Figure 1.34. MIRAC pinhole profiles. This measurement was obtained in the lab, using the test setup illustrated in Figure 1.29. The profiles shown are 2 second chopped images which have been multiplied by a gain matrix. Each profile has been normalized to a peak value of 1.

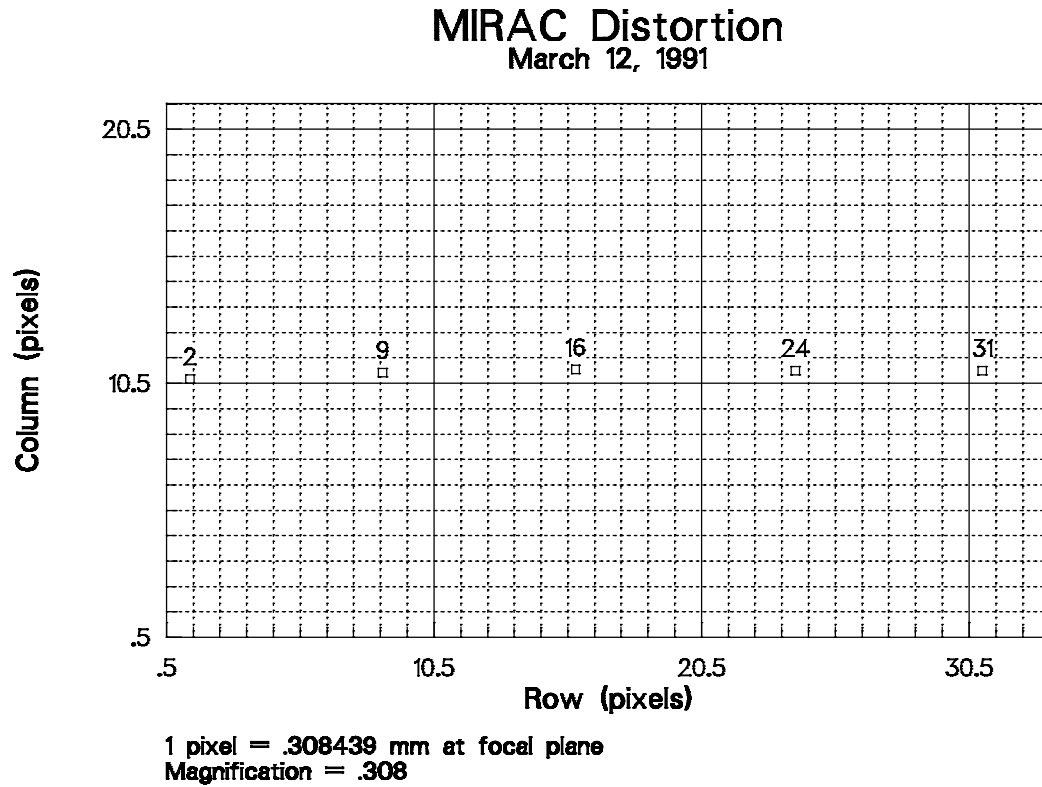


Figure 1.35. MIRAC optics distortion measurement, using 150 μm pinhole source. The camera was set to low magnification, and the pinhole placed at the focus outside the dewar, 14.2 cm from the case. The pinhole was centered on various pixels (2, 9, 16, 24, 31) of column 11, and the displacements were measured using the stage micrometers. The determination of the magnification assumes that there is no distortion between pixels 24 and 31.

PART 2. AN INFRARED STUDY OF PLANETARY NEBULAE

2.1 Introduction

Planetary nebulae (PN) are circumstellar clouds of gas and dust formed through the ejection of the stars' outer envelopes during their asymptotic giant branch (AGB) and post-AGB stages of evolution. The clouds are often in the form of a shell exhibiting some symmetry that expands outward from the central star. Multiple shells, filaments, and bright knots of ionized gas emission are common structures in these nebulae.

PN are an especially interesting and important class of objects for a number of reasons. First, the PN stage is the transition of stars from the AGB to white dwarfs. The nebulae are the ejected outer envelopes of these stars, so a knowledge of the properties of mass loss rates and time scales for ejection, and the composition of the ejected material will help in understanding this evolutionary process. As the nebula expands, it will encounter any material previously ejected by the star in earlier stages of evolution at lower velocities. Both the ejection process and the expansion into previously ejected material will affect the morphology of the nebula. Therefore, a study of PN morphology will provide information on both processes. Also, emission from dust grains and

large molecules has been observed in many PN. In some PN the conditions of grain formation such as composition, radiation from the central star, density of the nebula, etc. can be determined from observation, thereby shedding light on the processes of grain and large molecule formation, evolution, and destruction. Finally, PN are an important factor in the return of gas and dust to the interstellar medium (ISM). The total mass which they return to the Galaxy is about $0.5 M_{\odot}/\text{yr}$ (Knapp, Rauch, and Wilcots 1990).

It is difficult to discuss the general properties of PN since this class contains a wide assortment of objects of varied morphology, composition, and stage of development. In listing typical parameters, one would also wish to distinguish from objects that are observationally similar, but are not members of the class of PN because they don't represent this phase of stellar evolution. Kohoutek (1989) gives several "typical" properties of PN and their central stars. PNs usually display some symmetry in their emission structure: bipolar, circularly or elliptically symmetric disk or ring, with a sharp outer boundary. There are often multiple shells or haloes. The observed morphology is highly dependent on the angle of inclination of the nebulae and the wavelength of observation. Typical diameters range from 0.1 to 0.2 pc. Electron density is usually in the range 10^3 to 10^4 cm^{-3} , and electron temperatures from 9000K to 15000K. The total mass of the nebula is typically 0.1 to $0.2 M_{\odot}$. Expansion velocities are often non-isotropic and approximately 25 km/sec. PN spectra show mostly recombination lines of H and He, and collisionally excited lines of C, N, O, Ne, Mg, Si, S, Cl, and Ar. Continuum emission is observed from

free-bound, free-free, and two-photon processes. In the infrared, there is thermal emission from dust, along with emission features from silicon carbide (SiC) and other large molecules and grains, as well as unidentified infrared (UIR) emission lines. The central stars have the following typical properties: surface temperatures ranging from 25000K to 200000K, luminosity of approximately $5 \cdot 10^3 L_{\odot}$, radii of from 0.005 to 1.5 R_{\odot} , and progenitor masses of 0.8 to 6-8 M_{\odot} . Mass loss rates from the central stars are from approximately 10^{-10} to $10^{-7} M_{\odot}/\text{yr}$, although much higher rates of $\sim 10^{-4} M_{\odot}/\text{yr}$ may occur during the hypothetical "superwind" phase which creates the nebular shell (Schönberner 1987). Typical central star spectral types are WR, Of, OVI, cont. O, sdO, and peculiar. The central stars can be separated into two groups based on whether the atmospheres are H-rich or H-poor.

2.1.1 Planetary Nebulae Formation, Structure

There are two levels of models necessary to understand PN. The first is a model of the actual three-dimensional structure of the nebula to explain the observed morphology. A model is necessary since only the two-dimensional "projection" of the emission from the usually optically thin nebula can be observed, at some unknown inclination angle. Details of the nebular structure (including local density and temperature variations), obscuring gas and dust, and interaction with the ISM all combine to make this a non-trivial problem. The second level are models which seek to explain the process of nebula

formation and evolution: mechanisms for stellar mass loss, formation and shaping of the nebular shells by stellar winds, and the formation and evolution of dust and large molecules in the stellar atmosphere and the nebula. The two levels of models are closely linked, of course, since the morphology of the nebula is dependent on the mechanism of its formation.

Determining the actual three-dimensional structure of PN is not straightforward since it involves solving for the density, temperature, and velocity structure simultaneously. Also, one single model of PN structure cannot explain all of the observed nebular morphologies. However, many nebulae are similar in observed morphology and can be grouped into various classes. Balick (1987) has presented CCD images of 51 PN and organized them into three general groups: round, elliptical, and butterfly, shown in Figure 2.1. There are also three levels in each class: early, middle, and late, which suggest an evolutionary sequence within a class. An additional group of irregular and peculiar PN contain the examples that don't fit into the first three classes. Some of these nebulae, such as NGC 7027, may appear to be irregular at some optical wavelengths because of heavy obscuration near the source, but in IR or radio images can be seen to be a member of one of the three classes (elliptical for NGC 7027). Other nebulae, such as NGC 6543, show multiple shell structure when observed in some fine structure lines, but are single-shelled in others.

The second level of PN models must explain the formation processes that

produce the observed nebular properties and morphologies. One group of models that describe PN formation and evolution are interacting winds models (Lazareff 1981, Kahn 1983, Volk and Kwok 1985). The shapes and dynamical evolution of the nebulae are explained by the interaction between stellar winds emitted by the central star during its late stages of evolution. These models explain the formation of PN as resulting from a slow and fast wind stage. First, a red giant star nearing the end of the AGB sheds its envelope in a slow wind phase, with a mass loss rate of 10^{-5} to $10^{-4} M_{\odot}/\text{yr}$, and a velocity of ~ 10 km/sec. This process continues for approximately 10^4 yr, as the star evolves to a small radius, high effective temperature star. At this stage, the star generates a lower density fast wind, with mass loss rates of $10^{-8.5}$ to $10^{-6.5} M_{\odot}/\text{yr}$ and velocities of $1\text{--}2 \cdot 10^3$ km/sec. The fast wind encounters the material previously ejected in the slow wind, forming an inward-facing shock front on the inner edge. The gas at the shock is heated to approximately 10^5 to 10^7 K, and the pressure of the hot gas pushes the material into an expanding shell, forming the nebular structure.

A model with isotropic winds would be sufficient to explain only the simplest PN structures, such as round, highly-symmetrical nebulae such as BD+30°3639 or IC 418. In fact, most PN show more complex structure. Zuckerman and Aller (1986) studied the shapes of 139 PN and found that, in the spatially resolved PN, 50% showed bipolar symmetry, and 30% were elliptical. Many PN also exhibit filamentary radial structures, knots of emission, and multiple shells. Clearly this cannot be easily accounted for by an

isotropic wind expanding into free space.

There are several ways in which nonspherical nebulae could be produced. One possibility is anisotropies in the stellar wind from the central star. If the slow wind deposits much more material in the equatorial regions compared to the polar direction, or if the wind velocity is direction dependent, elliptical or bipolar structures can be created. When the fast wind begins to sweep the material into a shell, the density structure of the previously emitted envelope can determine the resulting nebular shape. Expansion will progress faster in the lower density polar regions, depending on the actual density gradient. A slight gradient will produce elliptical nebulae, whereas extreme gradients will produce bipolar nebulae, with very little expansion in the equatorial region.

Several mechanisms have been proposed to generate anisotropic winds. They can be separated into two groups: models that describe mechanisms for a single central star, and models that assume that the star is a close binary. For a single star, stellar rotation is one possible way in which an asymmetric wind can be produced. This mechanism is usually dismissed since, by the time a star expands to its AGB size where most of the mass loss is expected, the surface velocity is such a small fraction of the escape velocity that it cannot have a large effect on the mass loss rate (Soker and Livio 1989). However, D'Antona, Mazzitelli, and Sabbadin (1987) have suggested that there is a transfer of rotational momentum from the envelope to the core, which results in an enhancement of the equatorial magnetic field, causing more equatorial mass

loss. This process would be more efficient for high mass stars.

A second group of models assumes that the central star is a close binary, and anisotropic mass loss occurs from the interaction between the two stars (Livio *et al.* 1979, Morris 1981). When the primary in the system evolves to the red giant stage, it fills its Roche lobe and begins losing mass through the first Lagrangian point L_1 to the second star. The envelope of the second star expands and begins to lose mass through the second Lagrangian point L_2 , which leaves the binary system and forms the PN. One problem with this model is that only a few central stars of PN have been determined to be close binaries of the type necessary on this model. These identifications are difficult to make because the central star is often obscured by the nebula itself. Another difficulty was brought up by Zuckerman and Aller (1986), who showed that in a sample of 139 PN, there were too many exhibiting bipolar symmetry to be explained by the binary ejection mechanism alone.

The number of contrasting models is an indication of the uncertainty of how PN actually form. At present, only a few central stars have been confirmed to be close binaries of the type described in the models above. Also, the late stages of stellar evolution are as yet not well modelled, especially in the case of PN where significant mass loss occurs, either by a single star, or by a close pair. A better understanding of these processes will lead to a clearer picture of PN formation.

2.1.2 Infrared Emission from Planetary Nebulae

In some of the first infrared observations of PN, it was found that some nebulae have an "excess" of emission in the infrared over that which one would expect from recombination in the nebula and continuum flux from the central star (e.g., Gillett, Low, and Stein 1967, Woolf 1969, Willner, Becklin, and Visvanathan 1972). This excess was subsequently attributed to emission by dust, heated by Lyman α , other ultraviolet and visible line radiation, and Lyman continuum flux from the central star.

Measurements of the integrated flux from PN have shown that the IR spectrum typically peaks near 35 μm (Moseley, 1980). The characteristic dust temperatures are near 100K. However, the spectrum is usually not fit well by this single temperature blackbody at shorter wavelengths, having a spectral shape that indicates the presence of warm and hot dust components. There are also several recombination and fine-structure lines which can make significant contributions to the total flux in the near- and mid-IR.

In the near-IR, there are several components which contribute to the total flux. There is nebular emission from recombination and collisionally excited lines, and hydrogen bound-free continuum. In some nebulae, there is continuum emission from hot dust. Also, there is usually a significant emission component from the PN central star. In the mid-IR, possible components are a warm ($\approx 200\text{K}$) dust continuum, and emission lines due to [NeVI] (7.9 μm),

[ArIII] (9.5 μm), [SIV] (10.8 μm), [NeII] (12.8 μm), [NeV] (14.5 μm), and [NeIII] (15.5 μm), and possibly others. In some PN, there is a feature attributed to SiC grains near 11.3 μm , and in others, a silicate feature near 9.7 μm .

In addition to these sources of continuum and line emission, it was soon discovered that there were several broad emission lines at 3.3, 7.7, 8.6, and 11.3 μm (Gillett, Forrest, and Merrill 1973). Also associated with these lines is a broad emission "plateau" that extends from approximately 11.5 to 13 μm . These spectral features have been referred to as "unidentified infrared" (UIR) features, and have since been detected in many other PN, as well as other galactic and extragalactic sources (see reviews by Willner 1982, Puget and Leger 1989). The UIR features have been shown to correlate with each other, and with the nebular carbon to oxygen (C/O) ratio (Cohen *et al.* 1986). This correlation with the carbon abundance suggests that the features originate from carbon grains or molecules. Several possibilities have been studied, including polycyclic aromatic hydrocarbons (PAHs) (Leger and Puget 1984), quenched carbonaceous composites (QCCs) (Sakata *et al.* 1987), or hydrogenated amorphous hydrocarbons (HACs) (Duley 1985).

For PN that are less carbon rich ($\text{C/O} \approx 1$) the UIR features are relatively weaker and often a broad plateau of emission is seen from 10.5 to 12.5 μm , attributed to silicon carbide (SiC) (Willner *et al.* 1989, Barlow 1983). In oxygen-rich PN ($\text{C/O} < 1$), emission from silicates are seen with little or no SiC or UIR emission. When the PN is oxygen-rich, all the carbon is locked up in CO,

allowing only oxygen-rich grains to form, such as silicates. For PN with C/O unity or greater, the oxygen is then depleted by the formation of CO, allowing only grains containing carbon such as SiC, graphite, and the grains responsible for the UIR emission to form.

Many of the models of dust formation and fragmentation make specific predictions for the spatial distribution of the dust that can be readily evaluated by high-resolution IR observations. For example, if the emission at the various UIR wavelengths is caused by the same molecules or grains, then the spatial distribution of the emission should be the same. Also, if the carbon grains have an inhomogeneous spatial distribution, or are progressively destroyed in the PN as it ages as suggested by Natta and Panagia (1981), then studies of the spatial distribution of the dust emission will provide information about these grains. In addition, the infrared emission may be a good tracer of warm material external to the PN responsible for its shape, which may be in the form of circumstellar disks or clouds.

2.1.3 The Planetary Nebulae in This Study

The purpose of this study is to examine the spatial distribution of IR emission in various types of PN in order to gain a better understanding of the structure and evolution of these objects. This dissertation includes representative examples of several different types of nebulae, to provide an

overview of the characteristics of PN as viewed in the IR. The specific goals of this study are to determine the spatial distribution of emission from dust, UIR features, SiC emission near $11\ \mu\text{m}$, and forbidden line emission. Using the images of the nebulae at different wavelengths, the temperature structure of the dust can also be determined, and the emission features can be separated from the continuum emission. The spatial distribution of the emission can also be compared to the distribution in the radio continuum and emission lines in the optical, providing information on the structure of the PN. The IR structure may help explain the formation and shaping of the PN by stellar winds.

The PN were selected for this study based on a number of criteria. A few practical criteria limited the scope of the PNs to be studied. First, the nebulae had to have a small enough angular size on the sky ($<30''$) yet large enough to be clearly resolved with the IR cameras used ($>2-3''$). The nebulae also were chosen to be relatively bright in the IR so that images in several bands could be obtained in a short time so that several objects could be studied. Most of these PN have been studied before in the IR and at optical and radio wavelengths, so this information could be used to help interpret the new data.

The seven PN in this study can be divided into four groups, according to their IR characteristics. Three of the groups contain PN with different sets of IR emission features. The first group contains the IR-bright PN BD+30°3639 and J 900. The members of this group typically have a high C/O ratio (>1)

and exhibit excess IR emission at near-, mid-, and far-IR wavelengths. UIR feature emission is seen at most or all of the UIR wavelengths. There is usually a strong mid-IR continuum emission from these PN. These nebulae are in the same class as NGC 7027. The second group, which contains IC 418, has a different IR signature. These objects, which have a C/O ratio typically ~ 1 , show weak or no UIR feature emission and a weaker mid-IR continuum. An emission feature attributed to SiC is seen in these nebulae near $11\ \mu\text{m}$. The PN NGC 6572 is also in this group. The third group contains the PN NGC 2392 and NGC 6543. These nebulae have C/O ratios usually < 1 and except for the far-IR show little or no "excess" IR emission that can be attributed to dust. There is no evidence of UIR or dust continuum emission in the mid-IR, and little or no emission in the near-IR in excess of the central star and recombination emission from the nebula. The fourth group in this study is separated by morphology and presumably, by evolutionary sequence. The objects in this group, M 2-9 and AFGL 2688, are bipolar nebulae (BPN) and are usually considered to be proto-planetary nebulae (PPN) or PN in their early stages of formation.

Table 2.1 summarizes some of the observational characteristics of these nebulae, collected from the literature. The PNs NGC 7027 and NGC 6572 are also included for comparison. Some parameters (e.g. the distance) are not well determined, with the values in the literature varying for a particular nebula by as much as a factor of 2 or more. The values given here have not been evaluated for their quality, but whenever possible the values are from the same source, for consistency.

Table 2.1 General Characteristics of the
Planetary Nebulae In This Study

Parameter	BD+30° 3639	J 900	NGC 7027	IC 418	NGC 6572	NGC 6543	NGC 2392	AFGL 2688	M2-9
Distance (kpc)	0.6 {3}	3 {2}	1.1 {4}	0.42 {6}	0.42 {3}	0.53 {4}	0.94 {7}	1.0 {14}	0.9 {20}
V (km/sec)	26 {6}	18 {6}	18 {6}	12 {6}	16 {6}	20 {6}	54 {6}	100 {23}	7 {24}
T(e-) (10 ⁴ K)	0.80 {6}	1.15 {6}	1.4 {6}	0.85 {6}	1.05 {6}	0.83 {6}	1.3 {6}
Central star type	WC9 {6}	Of {6}	Of+WR {6}	O7+WR {6}	O7f {6}	F5 Ia {16}	B1 {19}
Morphology class	E	E	E	E	DL	P	E	BP	BP
Central star temp. (10 ³ K)	27 {18}	...	310 {9}	32 {18}	60 {18}	45 {18}	...	6	44 {18}
Dust Temp(°K)	175 {6}	...	90 {25}	190 {6}	180 {6}	125 {6}	95 {6}	200 {17}	140 {21}
C/O ratio	1.6 {10}	4.0 {13}	3.1 {14}	1.3 {11}	1.1 {12}	2.2 {12}	0.58 {12}
Mass Loss rate (10 ⁻⁶ M _⊙ /year)	20 {1}	30 {1}	81 {1}	6.6 {1}	6.7 {1}	13 {1}	...	3 {23}	33 {22}
INP IRE	5.46	1.39	...	1.9	1.98	2.37	1.16	...	68.5
INP Dust Temp (°K)	109	104	...	130	125	92	75	...	98
INP Distance (kpc)	.73	1.8241	.47	.64	1.22	...	2.37

References:

1. Taylor, Pottasch, and Zhang 1987
2. Gathier, Pottasch, and Pel 1986
3. Pottasch 1983
4. Acker 1978
5. Zuckerman and Aller 1986
6. Pottasch 1984
7. Natta and Panagia 1981
8. Morris 1981
9. Walton et. al 1989
10. Pwa, Pottasch, and Mo 1986
11. Torres-Peimbert and Pena 1981
12. Flower and Penn 1981
13. Aller and Czyzak 1983
14. Knapp et al. 1982
15. Ney et al. 1975
16. Crampton et al. 1975
17. Forrest et al. 1975
18. Kaler and Jacoby 1991
19. Calvet and Cohen 1978
20. Kohoutek and Surdej 1980
21. Kwok, Hrivnak, and Milone 1986
22. Kwok et al. 1985
23. Kawabe et al. 1987
24. Bachiller, Martin-Pintado, and Bujarrabal 1990
25. Moseley 1980

Explanations to Table 2.1:

The first column (Parameters) lists the particular nebular characteristic. The other columns give the value of the parameter for each nebula. There are two rows for each parameter. The top number gives the value of the parameter, and the number below it in brackets gives the reference for that value, referring to the list given above. The following are parameter abbreviations used in the table: V - expansion velocity, relative to rest frame of PN, LNP - Lenzuni, Natta, and Panagia 1989, IRE - Infrared Excess, defined as the ratio of the IR luminosity to the Ly α luminosity. The morphological classes given are as follows: E = Elliptical, BP = Bipolar, P = Pecular, DL = Double lobed. Note that members of the E class may also have two lobes of emission superimposed on the overall elliptical shape.

2.1.4 Observing Procedures and Data Reduction

The observations presented here were carried out on Steward Observatory telescopes by a number of observers including myself. Also participating in the near-IR observations were William Hoffmann and Giovanni Fazio. In the mid-IR observations with the MIRAC, the other observers were William Hoffmann, Giovanni Fazio, Lynne Deutsch, and Jeff Regester.

2.1.4.1 Near-IR Observations

In the following sections, near-IR images of the following nebulae are presented: IC 418 at J, H, and K; BD+30°3639 at K; NGC 2392, NGC 6543, and J 900 at H and K, and AFGL 2688 at J, H, K, and Br γ . All of these observations were obtained with the 64x64 Hg:Cd:Te array camera (Rieke, Rieke, and Montgomery 1987) on the Steward Observatory 2.3 m telescope at Kitt Peak. The general observing procedure was to take a short (5 to 40 sec.) exposure on the source, followed by an exposure at a telescope offset of 60" off the source of the same duration. The two images were then differenced to remove signal from the sky. A number of these image pairs were taken at each wavelength for the object being observed.

The following sequence was followed for each PN observed. First, images were taken of the standard star used for the flux calibration. These

exposure times were relatively short (2 to 10 sec.) to avoid saturation, since the calibration stars are fairly bright. Next, images were obtained of an SAO catalog star near the PN (about half the number to be taken on the PN). The purpose of these observations was to obtain a measurement of the point spread function (PSF) of the array at the time of the PN observations. The SAO star would be typically a few arcmin from the PN, so this would provide a good measurement of the PSF for that time and part of the sky. Next, images of the PN were taken. Typically 32-64 images were obtained at each filter, at 20-60 seconds per image, depending on the magnitude. For all of the PN presented here, the sizes of the nebulae were smaller than the field-of-view of the array, so each on-source frame contained an image of the entire nebula. After these images were taken, more images (about half the number taken on the PN) were taken of the SAO catalog star nearby. Finally, more images of the flux standard star at the same wavelength were obtained.

The data were reduced in the following way: first, "bad" pixels were removed from all the images by linearly interpolating between neighboring "good" pixels. The bad pixels were identified by their large digital values compared to the average value of the remainder of the image, or by showing no response to different flux levels. The number of bad pixels was typically 5-10 in the 64x64 pixel image, and were isolated in separate parts of the array. A gain matrix was calculated for each filter used, for each PN. The gain matrix was calculated by taking the reciprocal of the average of all the off-source images taken in the PN observations, normalized to the average value. Then

for all the on- and off-source pairs, the off-source image was subtracted from the on-source image, and the difference multiplied by the gain matrix. The result is an image where the instrumental inhomogeneities and background have been removed, leaving the source on a flat background. This process is frequently called a "flat field correction". In this description, I refer to the off-source image of blank sky as a "flat field". The matrix that corrects for the pixel-to-pixel gain variations in the flat field-subtracted images is referred to as the gain matrix.

The images were then reformatted by expanding each instrumental pixel to 4x4 subpixels, to allow for shifting the images by 1/4 pixel increments when aligning and averaging the images. The offsets between the images were determined by a two-dimensional cross correlation algorithm (Barnea and Silverman 1972, Tresch-Fienberg 1985). The images were registered to the nearest 1/4 pixel and averaged together to obtain the final image. Since there are small offsets between images, the extreme edges of the final image have slightly less integration time than the center of the image where the PN is located, but all points on the nebula have the same amount of on-source integration time. The images of the standard stars were then evaluated with the IRAF routines in DAOPHOT to determine the calibration factors to use with the PN images. Fluxes for the near-IR standards observed were taken from Elias *et al.* (1982).

2.1.4.2 Mid-IR Observations

In the following sections, mid-IR images of the following PN are presented: IC 418 at 11.7 μm ; BD+30°3639 at 10.0, 11.2, 12.4, 12.8, and 13.2 μm ; and M 2-9 at 8.8 and 9.8 μm . These images were obtained with MIRAC. The wavelengths were chosen to sample the warm dust continuum and the [NeII], UIR features, and SiC emission in these nebulae. The procedures used to obtain images are different because of the large telescope and sky background contributions, and noise in the sky background. Gain matrices were calculated from blank sky images taken at 1 and 2 airmass, in the "Grab" mode where a single image is taken with tracking off and no telescope modulation. The average image at 1 airmass is subtracted from the average image at 2 airmass to obtain the signal. The reciprocal of each pixel is taken and the image normalized so that the average value is 1. This procedure is done for each filter or CVF position used during the night of observing. This gain matrix compensates for all pixel-to-pixel gain variations in the array itself, along with sensitivity variations across the field dependent on the telescope.

When observing the sources, a combination of chopping the secondary and "wobbling" or "nodding" the telescope was used. The source is placed in the first chop beam and a short (5-20 sec on-source) pair of integrations are taken. The chopper throw was typically 20-30", usually toward the north, at a frequency of 5-10 Hz. Then the telescope is pointed at the second nod beam position completely off the source, and another chop pair is taken. These four

images are combined into a single "observation" by taking the difference between the image in each chop pair, and then the second chop difference is subtracted from the first. The result is then multiplied by the gain matrix. This produces an image for which the sky and telescope background have been removed and the instrumental response of the camera have been corrected. At this point, the data reduction process proceeds in the same manner as the near-IR reduction described above, where the images are registered to the nearest $1/4$ pixel and combined to produce the final picture.

2.1.5 Presentation of the Planetary Nebulae Observations

In the following sections, the observational results and analysis are presented. All the images presented are oriented with N at the top and E at the left, unless otherwise noted. The axes around the image show arsec Right Ascension along the bottom of the image, and arcsec Declination along the left edge. The contours are labeled with letters that are described in the caption for each figure.

Each of the following sections describes the results for a single object. The first part of each section briefly describes the general characteristics of the nebula, including its morphology, optical or radio images, continuum and line emission, or other relevant data. A short summary of the IR characteristics of the nebula is also given, describing the near- and mid-IR photometry and

previous imaging studies. A brief description of the observations is given, providing details about the data taking that were not covered in the above summary of observing methods, and information such as the date, direction of chopping and nodding the telescope, and integration time. The calibrated images are then presented, along with an analysis of the data. At the end of each section is a conclusion which summarizes the most important results discussed in that section.

Following the sections that cover the individual objects there is a section that compares the nebulae as members of three different groups. The groups are defined by their near- and mid-IR emission characteristics and their optical and IR morphology. The nebulae are also compared to other PN which have been observed in the infrared. The implications of these observations concerning the various models of dust formation and UIR emission are also discussed.

2.2 BD+30°3639

The PN BD+30°3639 is an optically bright, round, highly symmetric low-excitation nebula (see Figure 2.2). The nebula is usually considered young, because of its high surface brightness, symmetric shape, and small inferred intrinsic size. The distance to BD+30°3639, however, is very uncertain, with estimates ranging from 0.5 to 2.8 kpc (Pottasch 1983, Taylor *et al.* 1987, Martin 1987, Masson 1989). Radio continuum images (Basart and Daub 1987, Masson 1989) have shown that the structure is double-lobed, with peaks at the north and south positions of a nebular ring.

The infrared emission from BD+30°3639 has been studied extensively. Early observations showed the nebula to have excess IR emission (Woolf 1969, Gillett and Stein 1969). Russell, Soifer, and Merrill (1977) observed the UIR features around 3.3 μm in their near-IR spectrum. Moseley (1980) observed far-IR continuum emission, along with a strong feature near 30 μm . Aitken and Roche (1982) obtained an 8-13 μm spectrum showing UIR and [NeII] emission features, which were confirmed in the IRAS measurements of BD+30°3639 (Pottasch *et al.*, 1986). Results of near-IR imaging of BD+30°3639 by Roche (1989) and Smith *et al.* (1989) are reported, and mid-IR imaging studies of BD+30°3639 have been carried out by Bentley *et al.* (1984), Hora *et al.* (1990) and Ball *et al.* (1991).

2.2.1 Observations: BD+30°3639

The planetary nebula BD+30°3639 was observed in the K band on December 14, 1989 at the 2.3 m telescope on Kitt Peak, with the Steward Observatory 64x64 Hg:Cd:Te array camera. Images were not obtained at other NIR wavelengths on this run due to poor weather. The images were taken as alternating on- and off-source 25 sec integrations. Off-source frames were obtained by nodding the telescope 1 arcmin to the north. Small (0.5 to 2") offsets were introduced before each on-source frame. The final image at each wavelength was constructed from 16 of these individual images. The IR standard star HD 203856 was used for flux calibration. The PSF standard was a field star in the same frames as BD+30°3639.

The PN BD+30°3639 was also observed on June 2-3, 1991 using MIRAC at the Steward Observatory 2.3 m telescope on Kitt Peak. Images were obtained at 10.0, 11.2, 12.4, 12.8, and 13.2 μm using the CVF. Ten columns were read out during these observations, and the telescope was rastered across the source. The images presented here are a mosaic of the 35-40 individual 10 second nod sets taken at each wavelength.

Images at each of the six wavelengths are shown in Figure 2.3. Table 2.2 gives the measured fluxes of BD+30°3639 at each of the six wavelengths. The total time listed is on-source time in seconds. In the case of the 2.2 μm image, the flux of the central star has been given, and the nebular flux is the total flux

measured from the system minus the central star contribution (the image at 2.2 μm with the central star subtracted is presented below). The resolution given is the measured FWHM of the profile of the standard star used for the flux calibration at that wavelength.

Table 2.2 Observations of BD+30°3639

Wavelength (μm)	Total Time(sec)	Nebula Flux(Jy)	Stellar Flux(Jy)	Resolution (arcsec)
2.2	400	.448	.084	1.3
10.0	540	51.0	...	1.5
11.2	400	96	...	1.5
12.4	220	89	...	1.7
12.8	240	138	...	1.7
13.2	420	88	...	1.6

2.2.2 Discussion: BD+30°3639

2.2.2.1 BD+30°3639 2.2 μm Image

The image of BD+30°3639 at 2.2 μm contains contributions from recombination emission, continuum emission from hot dust, and emission from the central star. Since the properties of the nebular emission are being studied, it is useful to remove the emission from the central star. The raw images of BD+30°3639 contained another star in the field, which made alignment of the individual images very accurate, and as a result, also provided a good measure of the instrumental PSF. This reference star was scaled and subtracted from the

raw image, and the result is shown in Figure 2.4. Source profiles of both the original and central star-subtracted images are shown in Figure 2.5. The E-W profile is slightly irregular in the central part of the nebula due to a slight mismatch of the profiles, but overall the central star is well subtracted to reveal the nebular structure.

The image of BD+30°3639 in Figure 2.4 shows the nebular emission to be in a ring shape, with two bright lobes, in the northern and southern portions of the ring. The northern lobe is slightly brighter than the southern one. This is very similar to the spatial distribution of emission seen in radio continuum images of this nebula (Basart and Daub 1987, Masson 1989). The 4.885 GHz image of BD+30°3639 from Masson (1989) is reproduced here in Figure 2.6 for comparison. The images match very closely, with the only significant difference being an extension of the northern lobe to the east in the mid-IR images (e.g., at 11.2 μm shown in Figure 2.3c), suggesting another concentration of emission in the northeast portion of the ring. As seen in the distribution of the mid-IR flux described below, there is also an enhancement of the emission in this location in several of the images, which also points to an origin in dust emission.

2.2.2.2 BD+30°3639 Mid-IR Images

Mid-infrared images of the PN BD+30°3639 have been published previously, by Bentley *et al.* (1984), who scanned a single element detector across the nebula at several wavelengths, by Hora *et al.* (1990) using the AMCID camera, and most recently by Ball *et al.* (1991). Our previous observations using the AMCID camera (Hora *et al.* 1990) were carried out on the IRTF, with a pixel scale of 0!78/pixel, compared to 0!66/pixel on the 2.3 m with the MIRAC. The diffraction-limited image size on the IRTF is approximately 1" at 10 μm , and the effects of atmospheric seeing and image alignment errors can be expected to slightly increase the point source image size. However, due to charge-spreading effects that were characteristic of the AMCID array, the actual FWHM of a point source image was spread anisotropically to approximately 1!5 in R.A. and 2!7 in Dec. The AMCID images were deconvolved using maximum entropy, which removed some but not all of the effects of this non-circular PSF. In addition, the AMCID observations used broad band filters (approximately 10-15% bandwidth) which were not centered on the UIR features or placed at continuum wavelengths. The present observations were chosen to sample the UIR feature at 11.3 μm , the [NeII] line at 12.8 μm , and continuum wavelengths around these features.

One issue addressed in previous studies has been the spatial distribution of the spectral features in the nebula, relative to the continuum emission. This is important to models of the dust formation and destruction. Some possible

carriers of the UIR emission may be destroyed within the ionized zone. Bentley *et al.* and Hora *et al.* find that the UIR emission was slightly more extended than the continuum emission, although by a small amount. Ball *et al.*, however, report finding no difference in the spatial extent of the UIR or [NeII] feature emission compared to the continuum image.

To address this issue, the spatial distribution of the emission has been compared in several ways. First, the source profiles of the images, both in R.A. and Dec, are compared. These are shown in Figure 2.7. The profiles have been normalized so that the peak value is 1, and shifted so that the eastern peaks are aligned. In general, the profiles are very similar in size and shape between wavelengths. The eastern lobe in the E-W profiles, and the northern lobe in the N-S profiles are the brighter lobes. There is a central minimum in each of the profiles, with some differences in the detailed location and structure between the main lobes. However, several significant differences exist in the spatial extent of the nebula at the wavelengths observed. For example, in both R. A. and Dec., the 11.2 μm profile has the greater extent than the profiles in the continuum wavelengths of 10.0 and 13.2 μm . The difference is small, but the 11.2 μm image is consistently among the largest size for each set of profiles, both in width of the profile, and the separation between peaks. The image at 11.2 μm also had one of the smallest resolutions reported (see table above) so the larger size is probably not related to an instrumental effect. Table 2.3 summarizes the profile sizes from the data in Figure 2.7.

Table 2.3 Sizes of BD+30°3639

Wavelength (μm)	E-W FWHM size (arcsec)	S-N FWHM size	Distance between peaks (E-W)	(S-N)
2.2	5.6	5.2	3.6	3.4
10.0	5.7	5.1	3.5	2.6
11.2	6.2	5.4	3.8	3.0
12.4	6.2	4.7	3.6	2.8
12.8	6.1	5.0	3.8	2.8
13.2	5.9	5.0	3.3	2.8
UIR ¹	6.5	5.6	3.6	3.8
[NeII] ²	6.8	5.2	4.0	3.3

¹Calculated from the 11.2 μm image minus a scaled 10.0 μm image

²Calculated from the 12.8 μm image minus a scaled 13.2 μm image

These results compare well with the conclusion of Bentley *et al.*(1984) and Hora *et al.* (1990) that found the emission at UIR wavelengths to be spatially more extended than at continuum wavelengths. A new result is the observations at 12.8 μm which shows a larger extent in the E-W profiles, but a S-N profile that is very similar to the continuum wavelengths. The similarity between the 13.2 μm and the 10.0 μm image profiles confirms that the distribution of the continuum emission is accurately measured.

2.2.2.3 BD+30°3639 Temperature, Optical Depth Images

By assuming that the IR radiation at 10.0 and 13.2 μm is thermal emission from dust grains, a temperature image for the nebula can be calculated. This calculation was performed in 4x4 sub-pixel bins (each bin equal in area to 1

detector pixel) for those regions where the S/N was greater than 10 in both images. Expressing the intensity of emitted radiation by a modified Planck law $Q_\lambda B_\lambda(T)$ per unit wavelength, where $Q_\lambda \propto \lambda^{-n}$ is the wavelength-dependent emissivity of the grains, the temperature T , can be calculated from solving the following equation for T :

$$\frac{I_{13.2\mu m}}{I_{10.0\mu m}} = \frac{Q_{13.2\mu m} B_{13.2\mu m}(T)}{Q_{10.0\mu m} B_{10.0\mu m}(T)} \quad (7)$$

For this calculation, the emissivity exponent n was taken to be 2, consistent with graphitic grains (Dwek *et. al* 1980). The result of this calculation for is shown in Figure 2.8. The points of highest temperature are on the ring of emission, with a central minimum, similar to the intensity images. However, the minimum temperature is not at the position of the central dip of the intensity map, but is located at the position of the southern lobe. The temperatures in the region calculated range from approximately 160K to 190K, and the average temperature over the region is $172K \pm 10K$. This is in excellent agreement with the value calculated based on mid-IR spectral data from the nebula obtained previously (Pottasch *et al.* 1986). It is also interesting to note that the highest temperature region is in the eastern lobe of the nebula, although there is another peak at the position of the northern lobe. The eastern lobe is where additional UIR emission is observed.

From the observed intensity and calculated temperature images, the opacity distribution of the dust can be determined. Assuming that the

radiation from the nebula at a particular frequency I_ν is from dust grains at a temperature T emitting a blackbody spectrum $B_\nu(T)$, and that the temperature T accurately represents these grains, the following transfer equation can be solved:

$$I_\nu = \left(1 - e^{-\tau_\nu^{\text{warm}}}\right) B_\nu(T) e^{-\tau_\nu^{\text{cold}}} \quad (8)$$

where τ_ν^{cold} is the absorption optical depth of dust between the nebula and the observer, and τ_ν^{warm} is the optical depth of the emitting grains in the nebula. Figure 2.9 shows an image of BD+30°3639 where the quantity τ_ν^{warm} was calculated from the 10.0 μm image and the temperature image from Figure 2.8 for all points where the temperature is defined, assuming that the quantity τ_ν^{cold} is zero. The emission is optically thin everywhere in the nebula, with an average opacity of $6.3 \cdot 10^{-4} \pm 1.3 \cdot 10^{-4}$. There are density enhancements along the ring of the nebula, with the brightest peaks in the north and south positions. Instead of a central minimum, however, there seems to be a slight enhancement in the center of the nebula.

Between the 11.3 μm UIR feature and the 12.8 μm [NeII] feature, BD+30°3639 exhibits an emission "plateau", seen in many different sources and predicted by many PAH emission models (e.g., d'Hendecourt and Léger 1987, Tielens *et al.* 1987). The emission of BD+30°3639 from the 12.4 μm image therefore includes a contribution from this emission plateau, which is a much smaller spectral feature than the 11.3 μm or 12.8 μm feature. As seen from the

source profiles, the image is larger than the continuum region in the E-W direction, but smaller in the N-S (FWHM size; the distance between the peaks is similar to the continuum images). This is consistent with the 12.4 μm emission resulting mainly from the warm dust continuum, with a small contribution from the UIR emission plateau.

2.2.2.4 BD+30°3639 [NeII], UIR Feature Images

The image of BD+30°3639 at 12.8 μm is centered on the bright [NeII] feature in this PN. Using the image at 13.2 μm , the contribution of the continuum flux can be subtracted from the image and obtain an image of the spatial distribution of the [NeII] flux in the nebula. The continuum level at 12.8 μm was estimated from the 13.2 μm image by assuming that the continuum flux follows the temperature derived from the 10.0 and 13.2 μm images. The result of this calculation is shown in Figure 2.10. The image shows that the [NeII] emission is primarily concentrated in the northern and southern parts of the nebular ring. This image shows a strong similarity to the distribution of the 6 cm continuum emission from the nebula, as seen in the VLA images by Masson (1989). The [NeII] emission, as a tracer of the emission from the ionized gas regions, confirms the peaks of emission in the northern and southern regions as shown by the radio images. Comparison of the 12.8 μm image with the continuum and UIR feature image at 11.2 μm shows that the distribution of [NeII] emission is similar to the dust emission, but the

enhancements of emission in the eastern and western regions of the dust images are not present in the [NeII] image.

Similarly, an image in the UIR feature at $11.2\ \mu\text{m}$ can be constructed by subtracting the $10.0\ \mu\text{m}$ continuum image from the $11.2\ \mu\text{m}$ image. This result is shown in Figure 2.11. As with the [NeII] image, the flux is from the outer edge of the ring, with peaks in the northern and southern parts of the nebula. However, a feature present here that is not in the [NeII] image is the enhancement in the east lobe of the nebula. Figure 2.12 shows profiles through these two images, with the profile of the $10.0\ \mu\text{m}$ continuum image included for comparison. Here the profiles have not been shifted, but are properly aligned to the correct position on the sky. The UIR profiles are larger than the continuum in both profiles, in FWHM size and position of the peaks. The [NeII] image is close to the same size as the continuum in the S-N profile (FWHM is similar, although the peaks have a larger separation), but is larger in the E-W profile, almost the same as the UIR profile. One ambiguity about the [NeII] image is that at $12.8\ \mu\text{m}$, the image may have a contribution from the $11\text{--}13\ \mu\text{m}$ emission plateau, which is not subtracted out by the $13.2\ \mu\text{m}$ continuum image. This would have the most effect in the E-W profile, since it passes through a minimum of the [NeII] emission. The broadening of the profile in this direction therefore may be related to this effect.

Near-IR images of BD+30°3639 have been published previously. The images from Roche (1989) are reproduced here in Figure 2.14. Two images are

shown, one at Br γ , and the other at 3.28 μm , the position of the UIR feature emission. The image at Br γ is very similar to ours at K, showing peaks to the north and south of the central star. Their image at 3.28 μm is different, showing an enhancement in the NE part of the emission ring. This is where an enhancement of the emission also appears in the 11.2 μm feature map (see Figure 2.11 above). This indicates that the 3.28 and 11.2 μm features have a similar spatial distribution, and provides evidence that the UIR emission is from a single population of grains.

2.2.4 Conclusions: BD+30°3639

The PN BD+30°3639 has been observed at six IR wavelengths. Calibrated images are presented, along with derived temperature, dust opacity, and [NeII] and UIR feature emission images. The following conclusions can be drawn:

1. The spatial distribution of the emission is similar in each of the mid-IR images. However, slight differences in source size and structure are observed, with the 11.2 μm image, which includes emission from the UIR feature at 11.3 μm , appearing slightly more extended than the continuum images. Subtracting the continuum image at 10.0 μm from the 11.2 μm image shows the UIR emission coming from the outer rim of the ring.
2. The calculated temperature image shows that the average nebular

temperature is 172K, with the highest temperature regions along the ring of the nebula. The opacity image shows the emission to be optically thin throughout the nebula, with opacity maxima in the northern and southern regions on the ring.

3. The [NeII] feature image shows the flux to be located in the nebular ring, with peaks in the northern and southern lobes. This is in excellent agreement with the radio images of the nebula, confirming that the ionized gas emission peaks are in these lobes. The mid-IR continuum emission, although also present in these N and S lobes, differs in that there is also significant emission from the E and W lobes of the nebula.

4. The image of BD+30°3639 at 2.2 μm shows the spatial distribution of the emission to be in a ring, with intensity maxima in the N and S lobes. The spatial distribution matches the radio image very closely, except for an additional peak in the NE part of the nebular ring. This is consistent with the emission resulting from recombination emission from the ionized gas, along with a contribution from hot dust.

2.3 J 900

The PN J 900 (PK 194 +2°1) is a circularly shaped high-excitation nebula of small angular size (approx. 5" FWHM). It was determined from JHK photometry to have a significant contribution from dust emission (Whitelock 1985). The excess emission was observed to be higher in K than in H. Mid-IR spectrophotometry (Aitken and Roche 1982) showed that the spectrum of J 900 is very similar to those of other nebulae such as NGC 7027 and BD+30°3639, with UIR features at 11.3, 8.6, and 7.7 μm . In addition, there are fine structure lines of [S IV] at 10.52 μm and [NeII] at 12.8 μm .

2.3.1 Observations

The PN J 900 was observed in the H and K band on December 14, 1989 with the 64x64 Hg:Cd:Te array camera on the SO 2.3 m telescope. The images were taken as alternating on- and off-source 40 sec integrations. Off-source frames were obtained by nodding the telescope 1 arcmin to the north. Small (0.5 to 2") offsets were introduced before each on-source frame. The final image at each wavelength was constructed from 45-50 of these individual images. The IR standard stars HD 44612 and HD 40335 were used for flux calibration. The nearby star SAO 095673 was observed as a PSF reference for the nebula observations.

2.3.2 Results and Discussion: J 900

Calibrated contour images of J 900 are presented in Figure 2.15. The emission is dominated by the central star of the nebula, so that the nebular structure is not easily separated out in these images. It is evident, however, that the nebula is extended to the NW and SE of the central star, with the NW extension the brightest. The nebula is roughly 5" in diameter, measured along a line passing through the major peaks.

The central star was removed from these images by subtracting a scaled image of a star that was in the same field as the J 900 observations, which gave an especially accurate determination of the PSF for the image. The star was aligned with the image of the nebula using a cross-correlation algorithm, and scaled according to a model that assumes the emission results from three components, the central star and the two lobes. Contour images of J 900 with the central star subtracted are shown in Figure 2.16, and grayscale images are shown in Figure 2.17.

The structure of the nebula is seen to be double-lobed, with the brightest lobe to the NW of the central star. It is also evident that the lobes are in slightly different positions in the H and K images. A line passing through both peaks is at a PA of 24° W of N in the H image, and a PA of 16° W of N in the K image. The lobe separation is also different, with the H lobe peaks separated by $2!85$ and the K lobe peaks separated by $2!07$.

Table 2.4 lists the results of the J 900 photometry, for the entire source, and for the central star separated from the nebula.

Table 2.4 Photometry of J 900				
Filter	Flux (10^{-2} Jy)		Magnitudes	
	Star + Nebula	Star	Star	Nebula
H	2.81	.180	14.9	12.0
K	9.68	.860	12.7	10.2

The correlation studies of the UIR bands by Cohen *et al.* (1986) showed that J 900 also exhibited UIR emission in the 3.3 and 6.2 μm bands, in addition to the 7.7, 8.7, and 11.3 μm bands observed by Aitken and Roche (1982). The relative band strengths matched well with the general correlations of band strengths. Cohen *et al.* also compared the fraction of nebular far-IR luminosity with the C/O ratio and found a strong correlation, with J 900 having the highest value of both for six nebulae, the others being NGC 7027, BD+30°3639, IC 5117, IC 418, and NGC 6572.

Of these five, J 900 is closest in its IR characteristics to BD+30°3639 and NGC 7027, the common IR emission factors being high intrinsic UIR emission, high C/O ratio, high excitation, and near-IR excess. In addition, the observations presented here have shown that the IR spatial structure is also similar, with two lobes of emission around the central star. The asymmetry in the flux between the two lobes is larger here than in the other nebula, but the larger distance to J 900 makes the spatial structure and the geometry of the

source more difficult to determine. The observed asymmetry could be from either an intrinsic difference in luminosity, a higher relative extinction in the SE lobe than the NW lobe, or an inclination of the source that causes the NW lobe to appear brighter.

2.3.3 Conclusions: J 900

We have observed the PN J 900 at H and K with a resolution of $0''.56$ per pixel. Calibrated images are presented showing the distribution of near-IR flux. The following conclusions can be drawn:

1. The nebula is seen to have a double-lobed structure at both wavelengths. The images in which the central star have been subtracted show that the NW lobe is brighter than the SE lobe at both wavelengths.
2. There are slight differences in the PA and position of the lobes at the different wavelengths, which may be in part due to the geometry of the source.

2.4 IC 418

The PN IC 418 is a young, low-excitation, elliptically shaped nebula with bipolar symmetry (see Figures 2.18, 2.19). This bright shell is enveloped in a much larger faint halo. A good review of the observational characteristics of IC 418 is given by Hoare (1990). The distance to IC 418 is not well known, with values in the literature ranging from 0.42 kpc (Pottasch 1984) to 2.0 kpc (Méndez *et al.* 1988).

The infrared emission from IC 418 shows several distinct components. The near-IR emission shows an excess from what is expected from the nebular gas and the star itself (Willner, Becklin, and Visvanathan 1972). A second component in the near- and mid-IR is the UIR features, seen at 3.3, 3.4 (Russell, Soifer, and Merrill 1977), 6.2, 7.7 (Cohen *et al.* 1986) and possibly 11.3 μm (Willner *et al.* 1979). There is also a broad feature at 11.2 μm which is attributed to SiC emission (Willner *et al.* 1979). In addition, there is a broad feature which peaks near 30 μm (Moseley 1980, Forrest, Houck, and McCarthy 1981) which has been attributed to magnesium sulfide by Goebel and Moseley (1985). There is also another component responsible for the continuum emission in the mid- and far-IR, which is assumed due to carbon grains that are larger than those responsible for the near-IR emission (Hoare 1990).

2.4.1 Observations and Data Reduction: IC 418

The planetary nebula IC 418 was observed at both near- and mid-IR wavelengths, on the Steward Observatory 2.3 m and 1.5 m telescopes. Table 2.5 lists some details of the observations.

Table 2.5 IC 418 Observation Log					
Date	Inst [†]	Wavelength (μm)	Scale (" / pix)	Telescope	On source Int. time(sec) [‡]
12/13/89	1	1.6 (H)	.58	2.3 m	320 (20)
12/14/89	1	2.2 (K)	.58	2.3 m	680 (40)
3/ 6/90	1	1.2 (J)	.58	2.3 m	560 (40)
12/ 6/90	2	11.7	1.0	1.5 m	60*(10)

[†]Hg: Cd: Te array camera, 2=MIRAC

[‡]The number in parenthesis is the number of seconds in a single integration

*Average integration time for a position on mosaic image

The J, H, and K images were taken as alternating on- and off-source 40 sec integrations. Off-source frames were obtained by nodding the telescope 1 arcmin to the north. The final image at each wavelength was constructed from 32-48 of these individual images.

Two standard star observations were done in each wavelength before and after the nebular observations. First, a flux standard was observed in the same manner as the PN, except that the integrations were typically 5 seconds to avoid saturating the detector. Second, a nearby SAO star was observed as a point source reference. Frames were taken at the same operating parameters

as the PN observations. Table 2.6 details which standards were used for the PN observed. The FWHM size is given for both the RA and Dec profiles of the PSF standards. These image sizes are for the final images, the sum of all the individual integrations, so the effects of seeing, errors in image registration, and telescope drift are included.

Table 2.6 PSF Standard Stars for IC 418 Observations				
Filter	Star	FWHM (")		Dec
		RA	Dec	
J	SAO 150440	1.31	1.32	
H	SAO 150445	1.56	1.55	
K	SAO 150445	1.18	1.16	
11.7 μm	α Boo	2.5	2.5	

For the MIRAC observations at 11.7 μm , the camera was equipped with four signal processor channels, so a 4x32 section of the array was used. The on-source integration time of each observation was 10 sec. Chopping was 23" to the north, and the telescope was nodded 30" N between each chop pairs. The array was scanned across the source in approximately 1.5" steps in Dec (along the short dimension of the array) to cover the entire nebula. A total of 5 separate scans were performed, along with a number of integrations with the nebula centered on the array. In the final coadded image, each position has an average of 60 seconds on-source integration time. Alpha Boo was used as a flux calibration reference.

2.4.2 Results and Discussion: IC 418 NIR Emission

Calibrated contour images of IC 418 at J, H, and K are shown in Figure 2.20. The general features of the nebula are the same in each image: the overall shape of the nebula is ellipsoidal, with emission lobes on either side of the central star. In all of the images, the east lobe is brighter than the west lobe, and the central star is the brightest point on the nebula. The K and H images are very similar, with similar relative intensity and position in the lobes, and a break in the ring structure northwest from the central star. Grayscale images of IC 418 at J and K are shown in Figure 2.21, for comparison to the optical image.

2.4.2.1 IC 418 Morphology and Sizes

There are important similarities between the NIR images presented here and the images at optical wavelengths in Louise *et al.* (1987). In their H β image, there are two main lobes of emission. A line drawn between these lobes passing through the center of the nebula has a position angle (PA) of 68° , similar to the PA for the H and K images of 70° and 76° , respectively. The separation of the peaks of the lobes is $8.8''$, close to that observed in the J image. The image at [OII] by Louise *et al.* shows a similar double-lobed structure, with the peaks of emission at approximately the same location and separation.

Despite the similarity between the near-IR images, however, significant differences are seen. The largest differences are between the J image and the H and K images. One difference is that the brightest lobe of emission from the nebula in J is rotated approximately 45° from the position of the brightest lobe in the H and K images, at a PA of 25° . In addition to the rotation, the E lobe in the J image also appears to be located slightly closer to the center of the nebula, compared to the H and K images. Another difference between the images is in the local minimum in the ring structure visible in the northwest part of the H and K images, as well as the optical images. This minimum is absent in the J image -the ring structure extends through this region without any break. The smaller west emission lobe also differs in the J image. This lobe is not present as a discrete local maximum in the J image. Instead, the intensity varies smoothly from the northern part of the nebula along the west side to the southern part, where there is a local minimum common to all the images.

These differences in spatial distribution of the flux can also be seen in the source profiles. Figure 2.22 shows the profiles for each of the images, normalized to the level of the brightest (E) lobe of emission and centered on the central star. The profiles are at a PA of 70° , and averaged over a width of $1.56''$. The spatial extent of the near-IR emission is similar in each of the bands, but it can be seen that there is a trend of larger source extension with increasing wavelength for the NIR images: the J image is smallest, then the H and finally

the K image being the largest. The FWHM of the J source profile is 1!1 narrower than the K source profile, and 1!2 narrower measuring between the local maxima (the peaks corresponding to the nebula ring) of the source profile on either side of the central star. Table 2.7 gives the fluxes of IC 418 and the size at each wavelength as measured from these profiles through the main lobes.

Table 2.7 Observed Parameters of IC 418

Filter	Flux (Jy)	FWHM size (")	Nebular peak separation (")
J	.82	11.33	8.58
H	.73	12.25	9.24
K	1.24	12.47	9.76
11.7 μ m	29	11.59	7.31

Also apparent in these profiles is the trend in the relative brightness of the emission near the central star, relative to the emission in the nebular ring. The J image has the brightest central emission relative to the lobes, followed by the H and then K image. This shows the increasing flux contribution of the nebula at the longer wavelengths.

2.4.2.2 IC 418 Central Star Subtraction

One would like to be able to separate out from the nebular flux the flux

emitted by the central star. One approach is to use the standard star observations to determine the instrumental PSF, and assume the central star is contributing to the image in this way. The standard star image would then simply be scaled properly and subtracted from the observed image to give an image of the nebula alone. However, for the IC 418 images at J, H, and K, the central peak of the nebula is wider than the standard star image, and so the central peak cannot be totally subtracted from the nebula image.

This is illustrated in Figure 2.23, which shows a profile of the nebula data at J with the theoretical profile of the nebula without contributions from regions near the central star. The nebular profile assumes that the nebular emission is from an optically thin ellipsoidal shell. When the central star is subtracted to this level, however, the resulting profile does not match the theoretical profile of Figure 2.23. Instead, two peaks remain on either side of the central position, indicating that the wings of the peak are not being matched well by the standard star.

This incomplete subtraction is shown in Figure 2.24, which presents three profiles at each wavelength: one with the star scaled and subtracted up to the point where it would begin to show a central hole (called "Case A" here for ease of reference), one with the central star subtracted to the level shown in Figure 2.23 ("Case B"), and one with the star subtracted so that the central hole goes to near zero ("Case C"). Case A corresponds to a residual emission peak at the position of the central star, Case B results in a central ring of emission

inside the main nebular ring, and case C shows that the wings of the central maximum are still not completely subtracted when the central flux is subtracted to zero. There is some irregularity in the profile in the central region after subtraction, due to errors in the image registration.

These three cases are not the only possibilities (the flux of the star could be intermediate between these discrete levels) but it is useful to examine these cases. Case C can be discarded immediately, since some nebular flux is expected from the central position of the nebula. In the Case B profiles of Figure 2.24 that show a double peak where the star was subtracted (corresponding to a inner ring of emission), the width of the double peaks are narrower than the instrumental PSF as measured by the standard star observations. The minimum size for any real feature should be the PSF width, so this indicates that the ring is an artifact caused by incorrect scaling of the subtracted star.

In the case where the PSF was scaled to produce a single central peak, the feature is approximately equal to or greater than the width of the PSF. Therefore, Case A is consistent with the observations and more likely to be valid than Case B. For the same reason, the flux of the residual peak is not likely to be smaller than the Case A profile. Therefore, the Case A profile represents a lower limit to the non-stellar central flux. Figure 2.25 shows three profiles in Case A for each wavelength: the original data, the standard star scaled to the proper value, and the resultant IC 418 profile when this star is

subtracted.

There are a number of ways in which this excess emission near the central star could be artificially created by the instrument or data reduction process. One possible cause of this effect is that the instrumental PSF in the nebula images was vastly different from that in the standard star observations. This is not likely, however, since several steps were taken to make sure the standard star images were prepared in the same manner as the nebula images. The observations of the PSF standard stars were taken immediately before and after the nebula observations at each wavelength. The integration times were similar, and a similar number of observations per source were done. The stars used were not excessively bright (see Appendix 4), so there is no reason to expect a flux dependent PSF difference between the stars and the nebula. When comparing the standard star images taken before and after the images of the nebula at a particular wavelength, there was no significant difference in the source profiles. This indicated that the conditions were stable throughout the observations at a particular wavelength.

In the data reduction, the standard star images were treated in the same way as the nebular images, using the same gain matrix and flat fielding technique. Offsets for the individual integrations were calculated using a spatial cross-correlation algorithm. This algorithm selected only the region near the central peak of the image to use in the calculation, so that in the nebular images, the fainter extended regions were not included. Therefore we conclude

that the differences in image profiles between the standard stars and the nebula are real and not an artifact of the instrument.

From the profiles of the PSF-subtracted nebula in Figure 2.25, it can be seen that the largest relative contribution of the central star to the flux in the central region is in the K image. The subtraction of the scaled standard star profile is nearly complete, with only a small residual left. The central residual is larger in the J and H images, with the peak still just over twice the intensity of the brightest lobe.

2.4.2.3 Comparison, Discussion of Previous Studies of IC 418

The fact that the size of IC 418 increases with wavelength in the near-IR has been noted before by Willner, Becklin, and Visvanathan (1972) and Phillips *et al.* (1984). Willner *et al.* used apertures of increasing size at H and K, and found that the flux continued to increase significantly even after the entire optical nebula was within the aperture. Phillips *et al.* scanned a photometer with a 5!4 beam across the nebula in right ascension to measure the source profile, and found the nebular size increased with wavelength, and was larger than their standard star profile at H, K, and L. However, their profiles showed no emission extended beyond the central star in the J band. In their H and K scans, extended emission was detected, however it was at a distance of 10" from the center of the nebula, twice the size of the images in Figure 2.20. Most

of the differences can probably be attributed to their lower spatial resolution and lower signal to noise. The faint nebular emission could have easily been lost in the wings of the bright central star profile at the shorter wavelengths.

This does, however, change their conclusions about the location of the temperature distribution of the dust. Phillips *et al.* (1984) had observed emission at K outside the ionized zone but no K-band emission inside that was not from the central star, and L-band emission that extends from near the central star to outside the ionized zone. They suggested that there was hot dust emission from outside the ionized zone and cooler dust emission from close to the central star. The images, however, show that there is emission in excess of the central star in J, H, and K, and no evidence of the temperature increasing with distance from the central star.

2.4.2.4 Sources of Near-IR Emission in IC 418

There are several components to the near-IR emission from IC 418. There is a component due to recombination emission from the nebulae. The total nebular flux between 2 - 4 μm is a factor of 2 greater than what is expected from the radio observations (Willner *et al.* 1979), implying the presence of hot dust. Willner *et al.* calculated a grain temperature of 1350 K for a 10" beam, and 950 K for a 44" beam, assuming a grain emissivity $Q_\lambda \propto \lambda^{-2}$. However, they

find it difficult to explain these high temperatures given the central star temperature of $\sim 3 \cdot 10^4$ K. Other mechanisms, such as free-free emission generated from interactions between electrons and H^- or H_2^- ions, or stellar radiation scattered from dust particles, were also not satisfactory to explain the excess.

Recently, Zhang and Kwok (1991) have measured the spectrum of IC 418 between 1.5 and 1.75 μm with a spectral resolution of $\lambda/\Delta\lambda = 1280$. The wavelengths measured cover the spectral region within the H band. There is an uncertainty in the measured flux from the nebula since the instrumental beam diameter was only 5", significantly smaller than the size of the nebula. They multiply the entire spectrum by a factor of 4 to correct for this; however, since the nebula shape is seen to differ as a function of wavelength, this will cause differences in the spectral shape as a function of position over the nebula. The main features of the spectrum in the wavelength region from 1.5 to 1.75 μm are the series of Brackett emission lines of hydrogen, superimposed on a continuum. There are also small flux contributions from emission lines of He and Mg.

Zhang and Kwok (1991) estimate that the total flux due to line emission is about 25% of the total H-band emission observed. From recombination line theory, an estimated 39% of the J band and 4% of the K band flux is from emission lines. Even after correcting for the line flux, there is still an emission excess over that expected from the nebular and stellar continuum. They

determine that the K excess could be accounted for by thermal radiation from 600 K grains, but the J and H excess implies a color temperature of 95000 K. One suggested possibility of a field star included in the aperture is ruled out by the images presented here, but does not rule out a close companion.

Another possibility for the flux excess is emission from small grains. These hot grains would be expected to be closer to the central star than the emission from the 600 K or the warm or cool dust emission seen at mid- or far-IR wavelengths. Since the temperature of the grains would have to be >1000 K, the emission from the hot grains would be greatest at J, and decreasing at H and K.

From the point-source subtracted profiles of Figure 2.25, one possible identification of the excess radiation is apparent in the central flux left after subtraction of the central star. The emission is located near the central star, only slightly more extended than the instrumental PSF. The excess is largest at J, smaller at H, and almost not present at K, implying a high temperature. It is helpful to separate the flux in each band into the nebular, stellar, and central excess components using the spatial information of the images presented here. Table 2.8 gives the flux for each separate component. The "halo" component is described in §2.4.2.5 below.

Table 2.8 IC 418 NIR Component Fluxes
(Flux in Jy)

Filter	Total	Nebula	Star	Central Excess	Halo
J	.823	.655	.086	.082	0
H	.732	.524	.064	.032	.112
K	1.24	.938	.073	.011	.218

Willner, Becklin, and Visvanathan (1972) calculated the expected flux at H and K based on radio observations to be .46 and .54 Jy, respectively. The excess flux does not seem to be emitted by a single spatial component as separated in Table 2.8. In fact, the emission from the nebula alone is above the expected values, implying that some of the excess emission must come from the nebular ring. The emission from the central region attributed to the star does not follow the expected blackbody spectrum for a 30000 K star-- the color temperature calculated from the J and H emission is ~2600 K. If the "central excess" flux is attributed to the star, this results in a J - H color temperature of ~3600 K. This effect could be caused by dust emission near the central star that has not been spatially resolved. Also, Zhang and Kwok's (1991) suggestion of a close companion is not ruled out.

Significant emission is also seen in the halo in the H and K bands. The relative flux in each band is ~17%, much less than what was suggested by Willner *et al.* (1989) in their multiple aperture photometry. The emission in the halo region could have contributions from thermal emission from grains, and from scattered starlight. Polarization observations of this region would aid in

separating out the components of emission.

2.4.2.5 IC 418 Halo Emission

There have been previous reports of evidence for an extended shell of emission around IC 418. Willner, Becklin, and Visvanathan (1972) showed that the flux continued to increase out to a beam size of 40" at K. Taylor and Pottasch (1987) detected neutral hydrogen in the circumnebular shell. Their observations showed 21 cm emission and absorption towards the nebula, with a velocity relative to the system of 13.2 ± 0.5 km/sec. Taylor, Gussie, and Goss (1989) mapped the 21 cm emission and found it to be extended by approximately 1 arcmin in Right Ascension and 2 arcmin in Declination. Monk, Barlow, and Clegg (1989) detected a faint halo in [OII] and H γ extending at least 110 arcsec in diameter. They attributed the emission to scattered light from small (< 0.03 μ m for carbon or silicate) particles.

We have shown in the source profiles in Figure 2.22 above that the nebula is more extended in the longer near-IR wavelengths, based on separation of the lobe peaks. There is also evidence for a low level emission from the nebula in the H and K images that extends well outside the ionized zone where most of the flux is emitted. Figure 2.26 shows the profiles of the images plotted again on a greatly magnified vertical scale. This shows the emission from the H and K bands extending out beyond the edge of the nebula,

to approximately 14" from the lobe peak. In contrast, the J emission terminates shortly after the edge of the major lobe of emission in the nebula, at no more than 7" from the lobe peak. The K emission is brighter than the H emission, relative to the lobes of the nebula. The J image is not as high signal to noise as the K and H images, but it is clear that, relative to the lobe peak, the emission drops much lower at a given distance.

The color temperature of the emission outside the ionized zone can be calculated using the H and K images. The resulting temperature image has a roughly flat distribution, with an average temperature of 1500K. If there is a significant contribution from scattered light in the halo, the relative contribution will be greater at H, so the temperature would be lower. Spatially resolved polarization images of IC 418 would help distinguish between thermal emission and scattered light in the nebula.

2.4.3 IC 418 Mid-IR Emission

The contour image of IC 418 at 11.7 μm is shown in Figure 2.27. This filter samples the spectral feature in the spectrum of IC 418 from 11 to 12.5 μm , which is attributed to SiC emission. Evidence of weak UIR emission at 3.3 and 7.7 μm has been detected (Willner *et al.* 1979), so there may be some weak contribution from the UIR feature at 11.3 μm , as well as from the UIR plateau feature. There is also a large contribution at 11.7 μm from mid-IR continuum

emission from the nebula. The relative importance of these contributions to the total emission are not known precisely, but the mid-IR continuum and the SiC feature contributions are approximately equal, with a minor contribution from the UIR features.

Significant differences between this image and the near-IR images are apparent. The signal-to-noise ratio is lower in the 11.7 μm image than in the J, H, and K images, but the major structure of the nebula is clearly visible. There is a small peak at the central star position, and other peaks around the ring of the nebula. There are E and W lobes corresponding to those seen in the J-K images, and two additional peaks in the N and S parts of the nebula.

A profile through the 11.7 μm image is shown in Figure 2.22, along with the near-IR profiles. The peaks of the 11.7 μm image fall inside of the peaks of the J image, which was the most compact of the J-K images. This would indicate that most of the SiC and warm dust emission is coming from within the region where the recombination and hot dust are emitting. The central emission peak in the 11.7 μm image is also interesting. There will be no significant flux from the star itself at 11.7 μm . Since we do not have an image of IC 418 in the continuum without contribution from the SiC feature, the flux from each separate component cannot be determined, only the total from both components.

The mid-IR emission detected from the position of the central star indicates the presence of dust or SiC. This is in the same position as the excess flux seen in the central regions of the J, H, and K images. Therefore, this provides additional evidence for the interpretation of the distribution of non-stellar near-IR flux as a central peak rather than a ring.

2.4.4 Dust Emission in IC 418

SiC has been thought to form in carbon star envelopes (Treffers and Cohen 1974, Merrill and Stein 1976). The envelopes of these stars have the conditions necessary for particles to form: high densities ($\geq 10^9 \text{ cm}^{-3}$) and cool temperatures (1000-2000K) (Salpeter 1974, Seab 1988). Experimental results by Frenklach, Carmer, and Feigelson (1989) have shown that SiC can form at higher temperatures (above 2800K) and therefore would be the first particles to form in C-rich envelopes. They have proposed that SiC may act as nucleation sites for larger carbon particles and formation of PAH molecules.

The observations at 11.7 μm presented here are consistent with this model of SiC formation and growth. Since the carbon abundance is not very high (C/O ratio ≈ 1.3) the carbon is locked up in CO and SiC, leaving little carbon for the formation of amorphous grains or PAHs. The UIR emission from IC 418 is in fact much weaker than in other IR-bright nebula, as shown by Cohen *et al.* (1986) who compared the 7.7 μm feature flux to total far-IR

luminosity. The spatial distribution of the $11.7\ \mu\text{m}$ emission also indicates that it is different from the UIR features or continuum that are located in or just outside the ionized zone (e.g., in NGC 7027 or BD+30°3639). The presence of emission near the central star indicates that the SiC at that location may have formed recently and may still be forming.

The SiC emission is only one component of the IR emission. The IR spectrum of IC 418 peaks near $30\ \mu\text{m}$, consisting of a broad thermal continuum with an emission feature near $30\ \mu\text{m}$ attributed to MgS. Models of the SiC emission have shown that it cannot account for the far-IR emission, by 2-3 orders of magnitude (Stephens 1980, Hoare 1990).

Hoare (1990) presents two different models for the mid- and far-IR emission. Both use SiC and MgS to create the spectral features at around 11.2 and $30\ \mu\text{m}$, and the continuum is produced by graphite emission in one model and amorphous carbon in the other. The amorphous carbon model fits the *IRAS* data slightly better than the graphite model, however both models have difficulty reproducing the near- and mid-IR continuum emission, where hot dust and UIR features will have a contribution. A plot of the surface brightness of IC 418 at 12 , 100 , and $450\ \mu\text{m}$ for the amorphous carbon model is shown in Figure 2.29. The model's $12\ \mu\text{m}$ surface brightness compares well with the observed surface brightness of the $11.7\ \mu\text{m}$ image, shown in Figure 2.28. This figure is a plot of the average surface brightness in an annulus as a function of increasing radius from the center of the nebula.

2.4.5 Conclusions: IC 418

The PN IC 418 was observed at J, H, K, and at 11.7 μm . Calibrated images are presented here, along with source profiles and ratio images. The following conclusions can be drawn:

1. The distribution of emission is very similar at J, H, and K, and is similar to the size of the H β image. However, there is a detectable difference in the size of the images, with the FWHM and the distance between the peaks increasing with wavelength in the near-IR.
2. There is a peak in the flux distribution of the nebula after subtracting out the flux contribution from the central star. This residual peak is strongest at J and is progressively weaker at H and K. This excess at the central position is coincident with the local maximum in the 11.7 μm image and perhaps indicates a compact shell interior to the main shell of emission.
3. The spatial distribution of the emission at 11.7 μm , attributed to SiC and continuum thermal emission from warm dust, is significantly different from the other images, being less symmetrical and having additional knots of emission. Also, the FWHM size is smaller than in the near-IR and optical images, indicating that the emission may be originating from within the ionized zone. Additional evidence of this is the emission peak at the position of the central

star.

4. Evidence for an extended halo is seen in the K and H images. The halo extends approximately 13" further than the peaks of the main lobes, for a total nebular diameter of 36" along the minor axis and 40" along the major axis of the nebula. Emission is not detected in the halo in the J band, or at 11.7 μm .

5. The location of the 11.7 μm emission within the ionized region is unique to IC 418, since in most nebulae exhibiting detectable 10 μm continuum emission, it is seen to be coextensive or located just outside the ionized zone. There are emission contributions from warm dust and possibly UIR features at this wavelength, in addition to the SiC emission feature. The other nebulae with UIR and dust continuum emission, however, do not exhibit emission near the central star position. This suggests that this central emission is from the SiC feature, which is expected to form at higher temperatures than the hydrocarbon carriers of the UIR emission, so it can be formed and survive closer to the central star.

2.5 NGC 6543

The PN NGC 6543 does not readily fit into any of the simple morphological classes that describe most PN (see discussion of classes in introduction above). Its appearance in optical low-excitation lines is that of two ellipses at nearly right angles to each other, centered on a star (Figure 2.30). Along with this large scale structure, there are tails and filaments of emission connecting the ellipses and extending out beyond them. In addition, there is a faint nebulosity of elliptical form that extends well beyond this bright inner structure. One difficulty in explaining the observed structure is that the appearance of the nebula is significantly different in the low-ionization emission lines, $H\alpha$, [OI], [O III], and radio continuum (Balick and Preston 1987).

Several models have been proposed to explain the observed morphology. The multiple shell appearance was first explained by helical structures (Munch 1968, Carranza *et al.* 1968). Phillips and Reay (1977) propose a triaxial closed shell model. Hippelein *et al.* (1985) suggest a simple wind-blown model and try to match it to the observations. Balick and Preston (1987) propose a model of two pairs of bipolar lobes with axes that intersect at the center of the nebula. This was based on their kinematic observations of NGC 6543 in $H\alpha$ and [N II]. The structure is very ordered but complex. The difficulty in interpreting these image is not only in determining the structure, but in proposing a possible mechanism to produce that structure.

2.5.1 Observations: NGC 6543

The planetary nebula was observed in the K and H bands on March 6, 1990 with the Steward Observatory 64x64 Hg:Cd:Te array camera. The images were taken as alternating on- and off-source 60 sec integrations. Off-source frames were obtained by nodding the telescope 1 arcmin to the north. Small (0.5 to 2") offsets were introduced before each on-source frame. The final image at each wavelength was constructed from 50 of these individual images. The IR standard star HD 136754 was used for flux calibration. The nearby SAO star 017713 was observed as a PSF reference.

Contour images of the PN NGC 6543 at H and K are presented in Figure 2.31. The near-IR nebular emission is dominated by a bright lobe of emission to the north of the central star. This lobe is present in both the H and K images, although in the K image the flux in this lobe is much brighter relative to the central star than in the H image. Table 2.9 summarizes the sources of emission from the nebula and the star. The second column lists the total flux from the system, including the star and the nebula. The third column gives total nebular flux, and the fourth column gives the total flux emitted by the central star. The fifth column lists the bright lobe excess, which is the difference between the flux from an 18 square arcsec region centered on the bright lobe, and the flux from the same size area centered on the fainter lobe south of the central star. The last column gives the percentage of flux emitted by the bright lobe, compared to the total nebular flux.

Table 2.9 Photometry of NGC 6543

Filter	Flux (Jy)				
	Star + Nebula	Nebula	Star	Bright Lobe excess	Percent in Br. lobe
H	.233	.203	.030	.008	4%
K	.211	.198	.013	.082	41%

In addition to the star and bright lobe, there is emission from the rest of the nebula roughly equivalent to the size and structure seen in optical images (e.g., Balick 1987). A grayscale image of NGC 6543 at K is presented in Figure 2.32. The basic structure is an ellipsoidal shell centered on the star, with the major axis oriented roughly E-W. In addition to this, roughly on the north and south edges there is a filament of emission extending north and to the east from the top of the nebula, and south and to the west from the bottom of the nebula. This has been referred to as a "pinwheel" structure because of these filaments. The structure could also be considered to be two overlapping ellipses, at right angles to each other.

2.5.2 Discussion: NGC 6543

Radio continuum images of NGC 6543 which show the distribution of the ionized gas are similar to the optical excitation line images, shown here in Figure 2.30. An image of NGC 6543 at 8.1 GHz (Terzian 1978) shows the same double elliptical shell structure seen in the optical images. Images at 20 cm and 6 cm by Bignell (1983) show the double elliptical shell appearance clearly, and

images at [SII] and [OIII] show a similar structure. Part of the larger elliptical shell seems to be separated from the nebula in the [OIII] image, but the image is fairly symmetrical.

The H and K images presented here have unique features compared to the images at radio and optical wavelengths. The basic underlying structure is similar, with the double ellipse structure seen in both H and K images. However, in the infrared images, the dominant nebular feature is the bright lobe north of the central star. As seen from the fluxes given in Table 2.9, the lobe accounts for 4% of the emission at H, and 27% of the total emission in K.

Some of the first near-IR observations of NGC 6543 (e.g., Willner *et al.* 1972) indicated that there was little evidence for a near-IR emission excess that could be attributed to dust. However, if the IR emission was from the same sources as the radio or optical emission, one would expect the emission to have a similar relative distribution of flux. These images therefore provide evidence that there is a near-IR excess of emission that is not well mixed with the ionized gas and is localized in a lobe north of the central star. The amount of excess emission is estimated by the values in Table 2.9, column 3. Based on the values in Table 2.9, the average color temperature of this region is 606 K. This excess, could result from sources other than warm dust, such as Br γ or other line emission within the K band. However, there is no similar bright lobe in H α or the low excitation line emission, suggesting that the excess is not

associated with the gas emission.

Balick and Preston (1987) propose a model of two pairs of bipolar lobes with axes that intersect at the center of the nebula (Figure 2.33). The ellipses visible in the images represent the places where the lobes intersect. This model was motivated mainly by the observed structure of the nebula in optical and radio images. In order to evaluate their model and others, they studied the velocity structure of NGC 6543 in $H\alpha$ and [NII]. The images they present also show this apparent structure of two overlapping ellipses whose major axes are at a 90° angle with respect to each other, seen in Figure 2.30. Several features are defined, including a [NII] nucleus, ellipse, and N and S caps and tails. The ellipse shows a clear expansion outward from the nucleus, at a projected velocity of 20 km/sec, with the south side approaching, and a true velocity of 30 km/sec, assuming the ellipse is a tilted circular feature. The lobes, visible in the $H\alpha$ and [OIII] images, and the [NII] caps have little net observable motion.

The bright lobes in the K and H images presented here are in the same spatial position in the model as the northern intersection of the lobes, and the limb-brightened edges of two of the lobes. If the material responsible for the emission was present mainly on the surfaces of the lobes and the intersections of the lobes, one would expect a higher flux from these regions. This enhancement is present in the radio and optical images of the nebula. However, the NIR emission is above what is expected if the emission is solely

from recombination emission, since the near-IR flux is predominately from a single position in the nebula. The excess NIR emission from the northern lobe could be from other sources besides hot dust, such as line emission in the K band. However, such emission would be expected to be distributed similar to the optical line emission. If the emission is from dust, these near-IR images suggest that the dust is mostly localized in this N lobe, and is not well mixed with the gas in the nebula.

2.5.3 Conclusions: NGC 6543

We have observed the PN NGC 6543 at H and K with a resolution of 0!56 per pixel. Calibrated images are presented showing the distribution of the NIR flux. The following conclusions can be drawn:

1. The structure of the nebula visible in the optical and radio images is present in the near-IR images. However, the relative brightness is very different between the near-IR and other images, with a bright lobe present to the north of the central star.
2. The emission from the bright N lobe may be due to dust emission in the nebula, which was not previously observed with broad-beam spectroscopy since the excess emission is a small percentage of the total near-IR flux of the nebula.

2.6 NGC 2392

The planetary nebula NGC 2392 (the "Eskimo" nebula) is a multiple-shell nebula of roughly elliptical shape, shown in Figure 2.34. The bright nebular ring has a complex structure, consisting of two shells that are at points connected by filaments. The ellipsoid is flattened on the south edge. Surrounding this bright nebular shell is a faint outer shell, with roughly twice the diameter of the inner ring. This outer shell is not continuous and consists of bright radial filaments around most of its circumference, except for a shell fragment on the south edge, which is a short continuous arc. This entire structure is enclosed in a faint roughly circular halo (Balick 1987, Balick, Preston, and Icke 1987, Barker 1991).

The isovelocity images of Balick, Preston, and Icke (1987) have shown that the nebula is a roughly ellipsoidal expanding shell, with the major axis of the ellipsoid aligned with the observer's line of sight. The outer filamentary shell and the largest diameter of the inner shells is roughly at zero systemic velocity. The largest velocity regions are close to the position of the central star for both positive and negative velocities.

The characteristics of the IR emission from NGC 2392 are not complex or unusual. In the near-IR region, broad beam spectrophotometry has shown no IR excess over what is expected from recombination emission and stellar flux (Willner, Becklin, and Visvanathan 1972, Cohen and Barlow 1974). The mid-

and far-IR spectrum shows no feature emission, and a weak IR continuum (Volk and Cohen 1990). From the *IRAS* observations of the cool dust, Lenzuni, Natta and Panagia (1989) determined a temperature of 75K, moderate for most PN.

2.6.1 Observations: NGC 2392

The PN NGC 2392 was observed in the K and H band on March 7-8, 1990 with the 64x64 Hg:Cd:Te array camera on the Steward Observatory 2.3 m telescope. For the H image, no calibration star image was obtained due to clouds so the image was scaled assuming the total flux of the nebula is .21 Jy (Khromov 1974). The calibration factor that resulted from this assumption was consistent with calibration factors for this filter obtained on previous nights. The images were taken as alternating on- and off-source 45 sec integrations. Off-source frames were obtained by nodding the telescope 1 arcmin to the north. Small (0.5 to 2") offsets were introduced before each on-source frame. The final image at each wavelength was constructed from 45-50 of these individual images. The IR standard star HD 84800 was used for flux calibration. The nearby star SAO #079428 was observed as a PSF reference for the nebula images.

2.6.2 Results and Discussion: NGC 2392

Contour images of NGC 2392 are presented in Figure 2.35, and grayscale images are shown in Figure 2.36. As with NGC 6543, many of the features visible in the optical images are seen in the images at H and K. The central star dominates the flux, and the ellipsoidal nebula surrounds it, offset slightly to the north. The southern end of the nebula seems somewhat flattened, just as in the optical images (Balick 1987), and the double shell structure is visible to the north of the central star. The faint halo and filaments of emission outside the main shell that are prominent in the optical images are not seen here, but may be too faint to detect in these images. The 1 sigma noise in the images is $.17 \text{ mJy/arcsec}^2$ at H and $.04 \text{ mJy/arcsec}^2$ at K.

The striking features of the nebula, however, are the bright lobes of emission to the NW of the central star in the K image. The lobes are located on the outer rim of the main nebula, the northern lobe on the outer shell only, and the southern lobe on the intersection between the inner and outer shells. Table 2.10 gives the fluxes for the various components of the system. Column 2 gives the total flux for the system. Column 3 and 4 give the excess flux for the northern and southern bright lobe, respectively. This is the excess flux over what is observed in the nebula on the opposite side of the shell. The percentages given for each lobe are the percent of the total nebular flux coming from the lobe. Column 5 gives the flux of the central star.

Table 2.10 Photometry of NGC 2392

Filter	Flux (Jy)				
	Star + Nebula	Star	Nebula	Bright lobe North	excess South
H	.21	.164	.046	.000 (0%)	.001 (2%)
K	.211	.039	.171	.007 (4%)	.008 (5%)

As with NGC 6543, the spatial distribution of the flux at K suggest that there is a region of excess emission above what is expected from recombination emission from the ionized zone. However, a similar excess is not seen in the H filter. If the excess is due to dust emission from that location of the nebula, it would imply that the dust is much cooler here than in NGC 6543. Again, the excess emission could also result from line emission from that location in the nebula.

2.6.3 Conclusions: NGC 2392

The PN NGC 2392 was observed at H and K, and calibrated images at these wavelengths have been presented. The following conclusions can be drawn:

1. The images show the near-IR source morphology to be similar to the optical appearance, with a flattened ellipsoidal structure surrounding the central star. The outer filaments and halo were not detected at the sensitivity of these

images.

2. The NW lobe of the nebula shows enhanced IR emission above what would be expected from the optical morphology. The effect is slightly visible in the H image but is readily apparent at K. One possible source of this excess is hot dust emission in this lobe of the nebula, which is not hot enough to have significant emission in the H band.

2.7 AFGL 2688

The object AFGL 2688 (the "Egg Nebula") is a bipolar nebula with symmetric lobes, oriented approximately 15° east of north (Figure 2.37). Optically, the north and south lobe sizes are $4.8''$ and $2.9''$ respectively, the southern lobe being about 2 magnitudes fainter than the northern lobe (Ney *et al.* 1975, Crampton *et al.* 1975). The lobes are approximately circular in shape, separated by about $8''$, with pairs of "horns" extending out from the ends away from the center of the nebula. AFGL 2688 is thought to be one of a class of proto-planetary nebulae (PPN), whose central star is evolving from a red giant with rapid mass loss (Zuckerman 1978).

The optical emission from the lobes is highly polarized, 50% and 62% for the northern and southern lobes, respectively, and oriented perpendicular to the axis of the nebula. The polarization, along with the optical spectrum, is consistent with the lobes being a reflection nebula illuminated by an F-type star (Ney *et al.* 1975).

Bipolar nebulae are thought to form from expansion of material through an existing distribution that is concentrated in the equatorial plane of the system (Balick 1987). This buildup of mass in the plane could be a result of mass loss from a binary system in its rotational plane, or from other mechanisms (see Figure 2.1). The material surrounding the star is in the form of a disk with a large equatorial density enhancement. The stellar wind quickly

breaks out and forms a hole in the polar regions of the disk. The hole is small and initially confines the expansion to be solely in two narrow lobes. As the system evolves, the hole allowing material to escape grows, so the lobes will grow wider. The evolved system will consist of a faint outer bipolar halo, with a nearly toroidal disk of material near the central star system.

The infrared emission in AFGL 2688 is in excess of that expected from a simple reflection nebula, and has been attributed to thermal emission from dust. The IR spectrum of AFGL 2688 cannot, however, be fit to a single blackbody, indicating that there are several components of dust with different temperatures. The near-IR emission is also due to scattered starlight from the obscured central source; the average polarization at $2.2\ \mu\text{m}$ is 20% (Ney *et al.* 1975). Color temperatures of 200K and 120K have been derived for the wavelength ranges 8-13 μm and 16-24 μm , respectively. The IR spectrum is relatively featureless, with no UIR, SiC, or silicate absorption detected. The mid- to far-IR emission is fairly compact, concentrated in the center of the nebula between the two lobes. Ney *et al.* (1975) determined the size at $12.5\ \mu\text{m}$ to be $1!0 \pm 0!3$ in R.A. and $1!5 \pm 0!2$ in Dec. Observations reported in Deutsch (1990) and Deutsch *et al.* (1991) confirmed that the source was compact, with deconvolved sizes of $1!37$ in R.A. and $1!40$ in Dec. Gatley, DePoy, and Fowler (1988), with B. Balick and B. Zuckerman, have imaged AFGL 2688 at 1.25 and $2.122\ \mu\text{m}$, and found the IR emission to be distributed in the optical lobes, as well as emission from the equatorial region surrounding the obscured central star.

2.7.1 Observations: AFGL 2688

The PPN AFGL 2688 was observed at J, H, K, and Br γ on December 12-14, 1989 with the 64x64 Hg:Cd:Te array camera. The images were taken as alternating on- and off-source 20 sec integrations (40 second integrations at J). Off-source frames were obtained by nodding the telescope 1 arcmin to the north. Small (0.5 to 2") offsets were introduced before each on-source frame. The final image at each wavelength was constructed from 32-40 of these individual images. The IR standard star HD 203856 was used for flux calibration. The nearby star SAO 070805 was observed as a PSF reference for the nebula observations.

2.7.2 Discussion: AFGL 2688

Calibrated contour maps of AFGL 2688 at J, H, K, and Br γ are presented in Figure 2.38. Grayscale images are shown in Figure 2.39. The structure of the nebula in the near-IR is similar to the optical structure. The nebula appears bipolar, with the north lobe brighter than the southern lobe. The "horns" of emission that extend out from the ends of the nebula are visible in some of the contour and grayscale images.

The contour images, however, show that the lobes, instead of being

circular and of uniform brightness, are roughly elliptical, with the peak emission located closer to the center of the nebula than the center of the elliptical lobes. The asymmetry between the lobes may be in part due to the orientation of the source, where the N lobe is tipped toward the observer at an angle of less than 30° (Kawabe *et al.* 1987). The spacing of the peak is different in the J, H, and K images. This is illustrated in Figure 2.40, which shows profiles of the source along the major axis of the nebula in the three bands. The profiles have been normalized to the maximum flux in each image, located in the northern lobe. The source separations are in sequence from largest to smallest J, H, and K. Also, the relative brightness of the southern lobe varies in each of the images.

The profiles in Figure 2.40 show other interesting characteristics which vary as a function of wavelength. In each of the profiles, there is a peak for each lobe, and then as the intensity drops off as one moves further away from the center. At a certain point, there is a "knee" in the profile where the intensity begins to drop off more rapidly. In the K image, the profile even begins to level off before beginning to drop off rapidly. This knee in the profile occurs in both the northern and southern lobe moving out from the lobe peak. The knee is at different locations and relative intensities, being further from the lobe peak and of lower relative intensity as the wavelength increases. Table 2.11 summarizes the results on source separations and brightness.

Table 2.11 AFGL 2688 Lobe Parameters¹

Filter	Peak Sep.	Rel. Flux of S. Lobe	Peak-Knee Distance		Knee-Peak Flux ratio	
			N	S	N	S
J	6.53	.39	2.49	1.33	.558	.73
H	5.86	.35	2.93	2.36	.356	.43
K	4.68	.25	4.06	3.27	.215	.44

¹All distances are in arcsec.

The peak separation is the distance between the peaks of the northern and southern lobes. The relative flux of the southern lobe is the peak value of the southern lobe when the northern lobe has been normalized to 1. The peak-knee distance is the separation between the lobe peak and the knee outward from that peak, for each of the lobes. Similarly, the relative brightness of the knee is the ratio between the intensity at the knee to the value at the peak for that particular lobe. The numbers show that the knee-peak separation increases and the knee-peak relative brightness decreases as the wavelength is increased.

A feature that is not present in the optical images is weak IR emission from positions to either side of the minimum between the main lobes, at approximately 6" to either side. This is most apparent in the Br γ and K images of Figures 2.38 and 2.39 which show the fainter lobes to be located symmetrically on an axis perpendicular to the major axis of the nebula, running through the center. There is a faint tail which extends from the eastern minor lobe to the northern lobe. The low flux also precludes any detailed comparison of the structure of the minor lobes. Table 2.12 summarizes the flux measured

in each of the four lobes. The lobes are identified as N, S, E, and W, with the N and S lobes being the main lobes as visible in the optical photograph, and the E and W lobes are the ones detected in the Br γ and K images.

Table 2.12 AFGL 2688 Fluxes (mJy)						
Filter	Total	N	S	Lobes E	W	3 σ Noise (mJy/($''$) ²)
J	270	179	60035
H	288	198	79025
K	324	224	68	7.4	3.8	.009
Br γ	318	222	60	5.1	3.9	.093

The total flux does not equal the sum of the lobes, since there is a faint halo enveloping the entire system that is not included in the lobe fluxes. This halo extends out from the edge of the lobes by approximately 6" in all directions, so the general shape is ellipsoidal, with the major axis parallel to the major axis of the system. The halo emission is shown in Figure 2.41, where the image at K is plotted with a lower level contour and larger field than in Figure 2.38. The image has been smoothed using bilinear interpolation with a 2x2 instrument pixel window to help show the outer contour levels more clearly. The relative distribution of the emission in the K filter and the Br γ filter is the same, to the accuracy of the data. The similarity of the distribution is also apparent in the contour images in Figure 2.38, where the two images have been plotted with the same contour levels.

As mentioned previously, AFGL 2688 has been imaged previously by

Gatley, DePoy, and Fowler (1988). Their image at J is apparently identical to the image presented here, and their image at $2.122 \mu\text{m}$ (H_2), in which the continuum had not been subtracted, is very similar to the images at K and Br γ . The Br γ filter in the Hg:Cd:Te camera has a center frequency near the wavelength of Br γ emission at $2.166 \mu\text{m}$, with a width of $.2 \mu\text{m}$. In the near-IR spectrum by Thronson (1982), no evidence of Br γ emission is detected. The spectrum is dominated by emission from H_2 rotation-vibration lines. In particular, strong emission was detected from the $V = 1 - 0 S(1)$ H_2 line at $2.122 \mu\text{m}$ which falls within the bandpass of the Br γ filter. Therefore, the "Br γ " filter is sampling flux from the H_2 line as well as the surrounding continuum.

The K filter covers a bandpass of approximately $.5 \mu\text{m}$, which includes the bandpass of the Br γ filter. The K filter also includes emission from several additional H_2 lines, although these lines are much fainter than the H_2 line at $2.122 \mu\text{m}$. There should then be a contribution of H_2 line flux to the total flux detected in the K filter. If the minor lobes were due solely to H_2 emission, one would expect a difference in the ratios of the major to minor lobe flux in the K filter ($\Delta\lambda=.5 \mu\text{m}$) and the $2.166 \mu\text{m}$ filter ($\Delta\lambda=.2 \mu\text{m}$), since the filters contain a different amount of continuum flux but the same amount of line flux. However, since the absolute value and the relative distribution of the flux is the same in the narrow bandwidth "Br γ " and the wide K filter, the flux observed is likely of a similar nature in both the major and minor lobes, and no significant difference in the spatial distribution between the H_2 emission feature and continuum flux is detected.

2.7.3 Comparison to Other Observations, Models of AFGL 2688

Heiligman *et. al* (1986) and Kawabe *et al.* (1987) have spatially resolved the CO emission from the nebula. Heiligman *et. al* detect an extension of the source parallel to the major optical lobes, centered between them. They also find that much of the emission is extended over a scale $>30''$. Kawabe *et. al*, however, have found the emission to be extended perpendicular to the major axis of the system, centered between the main lobes. Their observations support a model in which there is an equatorial disk of material which confines the fast wind to be along the major axis of the nebula. Their model is illustrated in Figure 2.42. The central star is surrounded by a toroidal disk which is located at the equatorial plane. The disk confines the fast wind to flow along the polar axes of the system, creating expanding shells along the polar axis. The shell is cleared of material by the wind, allowing the star to directly illuminate the walls of the shell and creates the visible reflection nebulae.

A number of observations support the model of an equatorial disk. Ney *et al.* (1975) have reported that the optical emission is highly polarized at a position angle normal to the lobes, consistent with reflection of starlight from the central source. The obscuration of the central source points to a higher density in the equatorial plane. Several observers have reported evidence of a disklike structure. Nguyen-Q-Rieu, Winnberg, and Bujarrabal (1986) mapped

the NH_3 and the $J = 21 - 20$ line of HC_7N in AFGL 2688 with 4" resolution. They found the NH_3 emission to be from the region between the optical lobes, with a size of $2'' \times 12''$ with the long axis perpendicular to the polar axis. The emission is distributed in two maxima about the center, implying a toroidal structure. Kawabe *et al.* (1987) have reported CO $J = 1 - 0$ emission centered between the optical lobes, unresolved in the direction parallel to the polar axis, but extended perpendicular to the polar axis of the system with a size of 20-25". They also observe absorption toward AFGL 2688, indicating that the system is surrounded by a cool cloud of CO as well.

Bieging and Nguyen-Q-Rieu (1988) mapped the HCN emission in AFGL 2688, and found the emission to be extended roughly perpendicular to the polar axis of the system. The velocity structure observed implies a rotation of the toroid of approximately 1.2 km s^{-1} at a radius of 3.75 or $5.6 \cdot 10^{16} \text{ cm}$ (assuming a distance of 1 kpc). Nguyen-Q-Rieu and Bieging (1990) observed the spatial distribution of H^{13}CN , HC_3N , and SiS in AFGL 2688. The molecular envelopes were seen to be elongated E-W, roughly aligned with the equatorial axis.

The near-IR images here also support this general model. The main lobes of reflected light are the dominant structure. The fact that the peak separations are smaller at the longer wavelength implies that the extinction within the source is higher closer to the center of the nebula, where the expanding disk will obscure some emission from the reflection nebula. The emission detected from the faint lobes to the east and west of the nebula in the equatorial plane

may be either light scattered from the central star, or thermal emission from dust in an equatorial disk.

2.7.4 Conclusions: AFGL 2688

1. The PPN AFGL 2688 was imaged at J, H, and K. The overall structure in these images is very similar to the optical image, with a bright northern lobe and fainter southern lobe. However, in the Br γ and K image, fainter lobes are observed in the equatorial plane of the system, at equal distances to either side of the main axis of the nebula. This emission, along with the main lobes, is continuum emission in the spectral region covered by the K filter. Also, a faint outer halo is observed which envelopes all the lobes and is roughly elliptical.
2. The detailed structure of the lobes is different at J, H, and K, with the lobe peaks having a smaller separation, and the lobes a larger size (as measured by the peak-knee distance) for larger wavelength. The Br γ and K filter images are nearly identical, with no significant spatial variations in flux intensity detected.
3. The observations presented here are consistent with the general model for AFGL 2688 of an equatorial high density region confining the outflow of gas to be along the polar axis of the system.

2.8 M 2-9

The PN M 2-9 (the "Butterfly Nebula") is a bipolar nebula that is classified as "butterfly" (Balick 1987) or "bow tie" (Zuckerman and Gatley 1988). It is a member of a class of objects (including AFGL 2688) that are considered precursors to the PN stage. At optical wavelengths, M 2-9 is a highly symmetric nebula, with two conical shaped extensions to either side of the center of the nebula, with the major axis of the system oriented N - S and extending approximately 20" in both directions. There is also a bright core located at the center of the nebula. The structure of the nebula has changed significantly from the period 1952 to 1972 (Allen and Swings 1972), with several of the condensations in the nebula having moved by several arcsec, and a brightening in the wings and perhaps the core as well. The nebula has also been seen to change its appearance on timescales of 2-4 years (van den Bergh 1974, Kohoutek and Surdej 1980, Aspin and McLean 1984), with knots of emission in the nebula brightening or fading.

A number of factors point to its classification as a PPN. The central star type of B1 (Calvet and Cohen 1978) places it at the beginning of the sequence of nuclei of PN. The high density core and the unusual nebular shape also point toward an object evolving into a PN. Its highly variable structure and magnitude show that it is a rapidly evolving object. Finally, the strong infrared continuum observed is common to many objects considered to be PPN.

The IR emission from the nebula is mainly concentrated in the bright core. The near-IR spectral structure resembles that from a 800K blackbody (Allen and Swings 1972). Near-IR emission at J, H, and K was detected and imaged over the entire area of the optical nebula by Aspin, McLean, and Smith (1988). The emission in the lobes at J is similar to the optical, with bright knots visible.

2.8.1 Observations: M 2-9

The PN M 2-9 was observed at 8.8 and 9.8 μm on April 30 - May 4 1991 with MIRAC on the Steward Observatory 1.5 m telescope. For these observations, the long dimension of the array was oriented N-S, along the long axis of the nebula. Six channels were in operation, so a 6x32 section of the array was being sampled. The final image at each wavelength was constructed from 50-60 individual 20 sec. (on-source) integrations. The chop throw was 25" to the west, at 10 Hz, and the nod beam was 30" to the south.

2.8.2 Results and Discussion: M 2-9

Calibrated contour images are presented in Figure 2.43. The mid-IR emission from M 2-9 is in general very compact, with most of the flux coming from the core of the nebula near the central star. The total flux detected from

the central source is consistent with previous large beam observations, indicating that there is not significant mid-IR flux coming from the lobes of the nebula. This is consistent with previous near-IR observations by Allen and Swings (1972), who determined that at least 90% of the 2 μm flux originates from within 3" of the core. Table 2.13 gives a summary of the photometry results from the MIRAC observations.

Table 2.13 Photometry of M 2-9			
Flux (Jy)			
Wavelength (μm)	These Observations	Previous Obs. ³	1 σ U.L. to lobe flux (Jy/arcsec ²)
8.8	31.2	35 ¹	.029
9.8	36.0	37 ²	.011

¹8.6 μm , Cohen and Barlow 1974.

²10.8 μm , Cohen and Barlow 1974.

³Fluxes adjusted for magnitudes of α Boo given in Table A6.1.

The agreement of the current flux measurements to previous results shown in the above table indicates that the IR flux from the core has not significantly changed since the earlier measurement. This is in contrast to the rapid changes in the optical appearance of the lobes above and below the central core.

2.8.2.1 Size and Shape of M 2-9

Evidence for extended emission of the core of M 2-9 at near-IR wavelengths has been previously reported from speckle interferometry (Dyck

1987). The source is reported to be partially resolved, with FWHM sizes of $1.2''$ and $1.09''$ at K and L at a PA of 90° , and a FWHM size of $1.13''$ at L and a PA of 0° .

The nebular images presented here show the source to be compact and centered on the bright optical condensation at the center of the nebula. However, the nebular images are significantly more extended than the point source α Boo. This can be seen more clearly from the source profiles, shown in Figure 2.44. A profile has been taken in the direction that shows the greatest extension in the M 2-9 images, at a PA of 62° , measured from a line passing through the center of the nebula S-N, 62° CCW (towards the east). The nebula is larger at both wavelengths, with source FWHM sizes of $3.12''$ and $2.16''$ for 8.8 and $9.8 \mu\text{m}$, respectively, for M 2-9, compared to $2.10''$ and $2.12''$ for the 8.8 and $9.8 \mu\text{m}$ images of α Boo.

These source profiles show that the size of M 2-9 is larger at $8.8 \mu\text{m}$ than at $9.8 \mu\text{m}$. If the emission is due to thermal emission from a single population of grains, one would expect that the size would increase with longer wavelength. The FWHM size of a point source should also be slightly larger at longer wavelengths, further increasing the size of the longer wavelength image. This effect is seen in the profiles of α Boo, which is slightly larger at $9.8 \mu\text{m}$ than at $8.8 \mu\text{m}$.

The mid-IR emission from M 2-9, however, is most likely not from a

single population of grains. The *IRAS* Low Resolution Spectra (LRS) of M 2-9 shows that there is emission from UIR features at 7.7, 8.6, and 11.3 μm (Volk and Cohen 1990). Our 8.8 μm filter samples the emission from the 8.6 μm feature as well as from the broad wing of the 7.7 μm feature. The 9.8 μm filter samples the continuum emission between the UIR features at 8.6 and 11.3 μm . The larger image at 8.8 μm suggests that the UIR feature emission is more spatially extended than the mid-IR continuum emission. This is consistent with observations of other more evolved PN where the UIR emission has been seen to be more extended than the continuum emission, such as BD+30°3639 (this work) and NGC 7027 (Aitken and Roche 1983, Tresch-Fienberg 1985).

2.8.2.2 Structure of M 2-9

As in other BP nebulae, the structure of M 2-9 is thought to consist of a equatorial toroid that has confined the outflow into two opposing lobes (see discussion in the introduction of section 2.7). Evidence for the existence of this equatorial structure has been seen by Aspin, McLean, and Smith (1988) who detected a reddened structure in their near-IR images that was oriented roughly perpendicular to the major axis of the system.

The mid-IR emission seen here in M 2-9 may therefore be related to this inner disk that is confining the expansion of material into the bipolar lobes. The direction of largest extent of the 8.8 and 9.8 μm images presented here is

roughly aligned with the equatorial plane of the system. Figure 2.45 shows an H α image of M 2-9 from Balick (1987) with the overlaid contour lines of the 8.8 μ m image, showing the alignment of the system.

2.8.3 Conclusions: M 2-9

1. Mid-IR imaging of the core of M 2-9 have shown the emission to be concentrated near the core of the nebula, consistent with previous observations. The images presented here show the source to be slightly extended in a direction roughly perpendicular to the major axis of the nebula.
2. The emission at 8.8, which samples UIR features present in the spectrum of M 2-9, is more spatially extended than the emission at 9.8 μ m which samples the continuum emission. This is consistent with the UIR features being emitted by a second population of carriers that is spatially distinct from the population of grains responsible for the mid-IR continuum emission.
3. These observations of a structure extended in the equatorial plane of the system provide evidence for a circumstellar disk as predicted in models of bipolar nebula formation. This disk-like structure is much more compact than the structures detected previously in the near-IR.

2.9 Comparison of the Planetary Nebulae Properties

The planetary nebula observations presented here cover a wide range of nebular types, ages, and morphologies. The PN presented here have been grouped according to their IR properties. The four groups discussed are as follows:

1. The "IR-active" nebulae, including BD+30°3639 and J 900. These are carbon-rich nebulae, with a $C/O > 1$. These PN are characterized by strong near- and mid-IR continuum emission in excess of that expected from the star and the nebular gas alone. The nebulae show strong UIR emission in all the usual UIR bands. The nebula NGC 7027 is also included in this category.
2. The moderately carbon-rich nebulae, including IC 418. The previously studied PN NGC 6572 is also in this class. These nebulae have a $C/O \approx 1$, and show weak UIR and continuum emission in the near- and mid-IR. These nebulae also have a spectral feature near $11\ \mu\text{m}$ attributed to SiC emission.
3. The "IR-quiet" nebulae, including NGC 2392 and NGC 6543. These nebulae typically have $C/O < 1$, and display little or no excess near- or mid-IR continuum emission. There is usually no evidence of UIR feature emission.
4. Protoplanetary nebulae, including AFGL 2688 and M 2-9. These PPN are bipolar nebulae with near- and mid-IR continuum emission attributed to

dust, as well as UIR feature emission. The nebulae have a bright mid-IR core of emission, with near-IR emission from the lobes. AFGL 2688 has little near-IR flux from the core region, whereas M 2-9 has strong near-IR emission from the core.

This grouping of nebulae is similar to that of Lenzuni, Natta, and Panagia (1989) whose classes of C2 = Carbon rich, C1 = Moderately carbon-rich, and O = Oxygen-rich correspond to the groups 1, 2, and 3 presented here.

2.9.1 BD+30°3639, J 900, and IC 418

These three nebulae are all classified as carbon-rich, young PN, with IR excess emission due to dust. They are also morphologically similar, having an overall circular or ellipsoidal appearance, with two symmetric lobes of emission superimposed on a ringlike structure. Also included in this class of objects are the well-studied PN NGC 7027 and NGC 6572.

Continuum emission from dust has been detected in all of these nebulae at both near- and mid-IR wavelengths. The near-IR emission and continuum mid-IR emission is in general confined to the ionized region of the nebulae, as defined by the optical and high-resolution radio continuum images of the nebulae. Detailed comparison between the images often shows small differences, however, which may indicate that the dust has a slightly different

location. For example, in the images of IC 418 presented here, the emission is more extended at K than at J, with a different distribution in the lobes.

Emission from spectral features in the near- and mid-IR often show distinct differences from the continuum emission. This has been demonstrated before for other PN. In NGC 7027, Woodward *et al.* (1989) concluded that the UIR feature emission at 3.28 and 3.4 μm is spatially distinct from the continuum emission, being slightly more extended than the continuum. The UIR emission was also determined to extend beyond the ionized region of the nebula, as defined by the Br α flux at 4.052 μm . The UIR emission in the mid-IR is also spatially distinct and located on the outer edge of the ionized zone (Aitken and Roche 1983, Arens *et al.* 1984).

In BD+30°3639, there is evidence of the 3.28 μm UIR feature being spatially distinct from the ionized zone, as defined by the Br γ emission (Roche 1989). The UIR features at 7.7, 8.6, and 11.3 μm have also been found to be distinct from the dust continuum and ionized regions of the nebula (Bentley *et al.* 1984, Hora *et al.* 1990, this work). The distribution of the UIR emission is similar in the different UIR features at 3.3, 7.7, and 11.3, being in general more extended than the continuum and ionized regions.

The PN in group 2 also show spatial variations of the components of IR emission. Previous studies of the nebula NGC 6572 have shown distinct variations in its mid-IR flux as a function of wavelength, with evidence for

extended emission in the UIR feature at $11.3\ \mu\text{m}$ (Hora *et al.* 1990). The PN IC 418 and NGC 6572 both exhibit a feature in the mid-IR attributed to SiC emission. IC 418 is unique in that the emission from this feature seems to originate from *within* the ionized region, as defined by the optical and near-IR observations, with mid-IR emission detected from the position of the central star.

Cohen *et al.* (1986) found strong correlations between emission in each of the UIR bands, indicating a single class of chemical species is responsible for the emission. The studies of the spatial distribution of UIR emission have supported this. The similarities in the distribution of the UIR feature emission imply a common carrier, while the differences between the UIR features and the continuum IR emission suggest that a second population of emission species is responsible for the IR continuum.

The characteristics of the IR emission from these PN can be understood in terms of the varying carbon abundance in the nebulae, as indicated by the C/O ratio. In the study by Cohen *et al.* (1986), a strong correlation was found between the fraction of the nebular far-IR emission emitted in the $7.7\ \mu\text{m}$ UIR feature and the C/O ratio. Their figure is reproduced here in Figure 2.46. Nebulae with high C/O ratios, such as NGC 7027, BD+30°3639, and J 900, have strong UIR features. Nebulae with low C/O ratios, such as IC 418 and NGC 6572, have much weaker UIR emission, and the mid-IR spectra contain features attributed to SiC.

This correlation can be understood as follows (Salpeter 1974, Frenklach, Carmer, and Feigelson 1989). The CO molecule is assumed to be stable in stellar atmospheres, and would contain all of the available atoms of the least abundant element. Therefore, for oxygen-rich nebulae, all the carbon will be locked up in CO and none would be available to condense out. For nebula with $C/O > 1$, all the oxygen is locked into CO, and carbon would be available to condense into particles, the total amount depending on the size of the C/O ratio. Particles will form in the atmosphere and circumstellar region of an evolving AGB star when the temperature cools sufficiently, below approximately 3000K. SiC will be the first particles to form where there is sufficient Si abundance, and SiC may serve as nucleation sites for amorphous carbon particles and PAH formation. The PAH molecules will form at a much lower temperature, in the narrow temperature range of 900-1100K.

The correlation between C/O ratio and $f(7.7\mu\text{m})$ seen in Figure 2.46 from Cohen *et al.* (1986) points to a carbonaceous origin for the UIR features, and implies that the formation of the UIR carriers is sensitive to the carbon abundance in the circumstellar region.

The spatially resolved observations of the IR emission support a model where the carriers of the UIR features are different than the source of the continuum dust emission, because of the different spatial distributions. In the nebulae studied here, the UIR emission is more extended than the continuum dust emission, although it is certainly overlapping the ionized zone and may

be contained within it. The fact that the emission is more extended could be either because of the order of UIR carrier formation and expansion from the central star, or because of the destruction of the UIR carriers on the interior edge of the shell from absorption of UV flux from the central star.

All the characteristics described above are consistent with the UIR emission being from a mixture of PAH molecules. They have characteristic bands in each of the UIR feature emission regions, and although no one PAH has been observed to match the spectrum of an astronomical source, the most likely case is that a mixture of PAHs, at various temperatures, molecule sizes, and states of hydrogenation are responsible for the emission in each object. Frenklach and Feigelson (1989) have shown in modelling the conditions in carbon-rich circumstellar envelopes that PAH molecules can form under the expected conditions. The PAH molecules will be susceptible to dissociation by absorption of UV photons (Duley 1987), with smaller molecules being easiest to dissociate. This may explain why the UIR emission is located on the outer edge of PN -- they may be destroyed by UV flux on the inner side of the PN shell. There is other evidence of an anticorrelation of UIR emission to objects with high UV flux (Roche 1987, Puget and Léger 1989).

2.9.2 NGC 2392 and NGC 6543

These two nebulae are grouped together because of their similar near-IR

emission characteristics, since in other respects they are quite different. NGC 6543 is a type "peculiar" PN, simply because it is a morphologically unique object that does not fall easily into any of the categories containing highly symmetric nebulae. NGC 2392 has a simpler shape, roughly elliptical, although it also has its complexities, having a double shell, surrounded by filaments of emission and enclosed in a larger halo.

The two nebulae are similar in their near-IR emission in that no IR excess is detected at K in broad-beam measurements (Willner, Becklin, and Visvanathan 1972, Cohen and Barlow 1974). The observed emission could be accounted for by recombination emission from the ionized region of the nebula and flux from the central star. In addition, no evidence of warm dust emission in the mid-IR is detected. The *IRAS* LRS data presented by Volk and Cohen (1990) show little continuum emission from dust, and no UIR feature emission. NGC 6543 does show several forbidden line transitions, such as the [S IV] line at 10.5 μm , and the [ArIII] line at 9.0 μm . The lack of UIR features is consistent with C/O ratios for NGC 2392 and NGC 6543 of .58 and 1.0 (Pottasch 1983), respectively.

One of the most unusual characteristics of the IR emission is shown in the data presented here, that the near-IR emission in these nebulae, instead of being distributed roughly the same as the optical and radio continuum emission, is highly concentrated in a particular area of the nebula, compared to the nebular recombination emission. The amount of excess near-IR emission

in these regions is small compared to the total flux in the nebula, so if this is a sign of excess emission from dust, this could easily have been missed in broad-beam photometry of the PN at these wavelengths. This unexpected concentration of the near-IR flux was seen in both H and K bands in both of these nebulae. If this is emission due to hot dust, its distribution is quite different from that of the gas in the nebula.

2.9.3 AFGL 2688 and M 2-9

The two bipolar nebulae, M 2-9 and AFGL 2688, are morphologically very similar. Both nebulae have been postulated to be approximately 1 kpc distant (although estimates vary widely) and are roughly the same angular size, so it would seem that they are possibly at a similar point in their evolution. However, the objects have quite different characteristics in other respects. For example, the optical spectrum of AFGL 2688 shows Na I D lines in emission, and strong [S II] emission is detected. Bands of SiC₂ are seen in absorption, which have been observed in carbon stars of high carbon abundance (Humphreys *et al.* 1975, Cohen and Kuhi 1977). The spectrum has been characterized as a F5 Ia supergiant, with some anomalous features superimposed.

At wavelengths longward of 4100 Å, the continuum of AFGL 2688 is depressed and strong anomalous absorption is seen, comparable to what has

been yseen previously in the spectra of carbon stars (Crampton *et al.* 1975). The absorption is attributed to bands of C_3 , and the Swan bands of C_2 are seen in emission. The observed light from both lobes is highly polarized (50% or larger in the optical), indicating that the lobes are reflection nebula illuminated by the obscured source (Ney *et al.* 1975). The lobes are fairly featureless, with no distinct filaments or small clumps of emission. The source has shown variability, increasing in brightness between 1920 and 1977 by approximately 2 magnitudes, and has increased in size by $\sim 1''$ (Gottlieb and Liller 1976).

On the other hand, the optical spectrum of M 2-9 is characterized by numerous FeII, [FeII], and [FeIII] emission lines. Strong emission lines of [OIII], [OI], He I and the Balmer series are seen in the core, along with weaker emission from lines of [NeIII], [SIII], [SII], SiII, and [NiII] (Walsh 1981). The central star has been tentatively identified as B1 (Calvet and Cohen 1978). Distinct knots of emission are present, which have been seen to change on timescales of 2 to 20 years, implying large velocities and rapid evolution (Allen and Swings 1972, van den Berg 1974, Kohoutek and Surdej 1980, Aspin and McLean 1984). The polarization of the optical emission is lower, approximately 16% for permitted lines and continuum, and 2% for forbidden lines, implying that $\sim 60\%$ of the continuum and permitted line emission and $\sim 10\%$ of the forbidden line emission from the lobes is scattered emission from the core (Schmidt and Cohen 1981, Aspin and McLean 1984).

No continuum 5 GHz emission has been detected from AFGL 2688,

implying the absence of an ionized region (Ney *et al.* 1975). However, radio continuum emission has been detected at several wavelengths from the compact core of M 2-9, and from the lobes at 20 cm (Kwok *et al.* 1985). The 20 cm emission was essentially coincident with the core and the bright knots of emission seen in the optical images of the lobes. Molecular line radiation has been detected in both nebulae. Kawabe *et al.* (1987) have mapped the CO $J = 1 - 0$ emission from AFGL 2688 and found three structures: a central compact core elongated in the equatorial plane of the system and centered on the IR core, spurs of emission from the outer edge of the northern optical lobe, and blueshifted emission along the polar axis of the system. Structures perpendicular to the polar axis in the equatorial plane have also been detected in NH₃, HC₇N, and HCN (Nguyen-Q.-Rieu, Winnberg, and Bujarrabal 1986, Bieging and Nguyen-Q.-Rieu 1988). CO $J = 1 - 0$ and $J = 2 - 1$ emission has been detected in M 2-9 (Bachiller *et al.* 1988, Bachiller, Martin-Pintado, and Bujarrabal 1990). The emission is concentrated in the core, and the $J = 2 - 1$ emission is unresolved in a 13" beam.

Both of the BPN presented here show strong IR emission. The nebula AFGL 2688 emits most of the near-IR emission from the lobes, with no detectable emission from the central source. The lobe emission is 20% polarized, indicating a significant contribution from scattered light from the central star (Ney *et al.* 1975). In M 2-9, however, the core emits strongly in the near-IR, with the emission from the lobes not detected until the IR camera observations of Aspin, McLean, and Smith (1988). The mid-IR emission is

centrally concentrated in both sources, with the emission in M 2-9 extended primarily perpendicular to the equatorial plane, and the emission in AFGL 2688 extended slightly in both the polar and equatorial directions (Deutsch 1990).

The mid-IR emission in both objects shows at least two different components: thermal continuum emission and UIR feature emission. In M 2-9, the sizes of the images presented here give evidence of a different spatial distribution of the UIR emission, with the UIR emission more spatially extended than the continuum emission.

The morphologies of these nebulae are perhaps a result of a similar mechanism, where a fast stellar wind has been confined by a circumstellar disk to flow primarily along the polar axis of the system, and has created roughly symmetric lobes of emission. This does not suggest, however, that these nebulae are necessarily at a similar point in an evolutionary sequence. The differences seen between these nebulae and other BPN are in part due to the differences in the central star and its mass loss history and current rate.

Many of the observational differences between M 2-9 and AFGL 2688 can be understood considering the central stars of the nebulae. The hotter star in M 2-9 results in the high excitation emission observed, both emitted from the nebula and scattered from the central star. The star in M 2-9 is also responsible for the radio continuum emission detected from the ionized gas (Kwok *et al.* 1985). The excitation of optical emission lines near the source causes the central

emission in M 2-9, whereas in AFGL 2688 there is no optical emission centered between the lobes.

Another nebula in this class is NGC 6302, a bipolar PN which has two bright lobes of emission on opposite sides of the central star, similar to AFGL 2688 and M 2-9. NGC 6302 is considered to be at a later stage of evolution than AFGL 2688, since it is larger, less dense, and more highly ionized. Lester and Dinerstein (1984) mapped the source at 2.2 and 10.2 μm and found that most of the emission is concentrated between the two optical lobes, with the emission more extended in the equatorial plane of the system. They conclude that the observed IR disk is not the structure responsible for confining the flow, since the estimated density is not high enough to keep it from being disrupted by the stellar wind at the expected velocity and mass loss rate. Instead, they suggest that the observed disk is either the expanded remnant of the toroid that confined the outflow, or it is the material remaining after the biconical wind has blown out the material in the direction of the flow.

The near-IR structures observed in M 2-9 and AFGL 2688 are similar to that observed in NGC 6302, since they are much larger than the expected size of the confining toroid. In AFGL 2688, the equatorial emission is well separated from the central region, implying that it is no longer responsible for confining the outflow. The mid-IR structures, however, are centrally concentrated and barely resolved in both objects, so it is possible that the mid-IR emission is directly from the structure that is confining the outflow into

bipolar lobes.

It should be mentioned that the identification of these objects as protoplanetary nebulae is not yet completely established. Balick (1989) has suggested that M 2-9 shares more similarities with objects such as η Car, or the nova RR Tel, some symbiotic stars, or the P Cyg star AG Car. The observational characteristics of AFGL 2688 have also been compared to some Herbig Haro objects, although its classification as a protoplanetary is now fairly well established.

2.10 Conclusion

The first part of this dissertation provides a description of MIRAC capabilities and performance. The camera is a significant advance over the previous generation of mid-IR array cameras in sensitivity, format, and ease of use, and its performance is on the same level as similar state-of-the-art detector cameras currently being operated. MIRAC is an extremely versatile instrument that has a wide range of possible applications, from the study of star formation regions, planetary nebulae, and circumstellar disks to the investigation of extragalactic nuclei and star formation in galaxies.

The observations presented here have shown that infrared imaging of PN can be a very useful technique in gaining understanding of these objects. Data on PN and PPN of vastly different morphological types and evolutionary stages have been presented here, showing a wide range of IR characteristics. Important information has been revealed by this study of the dust distribution within the nebula.

The observations of BD+30°3639 presented here have confirmed the results of previous investigations that have shown the images taken in the UIR feature wavelengths to be slightly more spatially extended than the continuum emission. This has been the case in other PN where the spatial distribution of the UIR emission has been studied, such as NGC 7027, and J 900 in this study. The location of the UIR features on the outer edge of the ionized zone indicates

that the UIR emission carriers may be destroyed on the inner edge of the nebular shell.

In IC 418, the near-IR structure, although similar to the optical images, shows a trend of larger source size with increasing wavelength, due to the contribution of dust emission. The H and K images show evidence of emission from an extended halo around IC 418 of approximately 40". The spatial distribution of the mid-IR emission is significantly different from the distribution of the near-IR or optical images. The 11.7 μm emission peaks within the ring of the nebula as defined by the near-IR images, showing that the flux is coming from within the ionized zone. A central peak of emission is seen, in excess of what is expected from the central star or outer nebula shell, indicating emission from near the central star.

Both of the PN NGC 6543 and NGC 2392 have a small IR excess in the near-IR, but the spatial distribution has been seen in the images presented here to be very non-uniform. Both have emission excesses at particular locations in the nebular shells. These locations are at the intersection points of the multiple shells of the nebulae, which suggests some density enhancement in these regions. Further study of these nebulae must be done to determine if the source of the excess emission regions is due to continuum emission from hot dust, or from line emission from the ionized gas.

In the bipolar nebulae AFGL 2688 and M 2-9, evidence for structures in

the equatorial planes of the systems have been detected in the near- and mid-IR. These structures are thought to be responsible for directing the outflow from the central star to be primarily in opposing directions, along the poles of the system. In AFGL 2688, the equatorial emission is seen in the K and Br γ filters. In M 2-9, the mid-IR flux shows a bright central core which is extended in the equatorial direction. The image taken in the filter which samples the UIR feature emission is larger in spatial extent, consistent with the behavior of UIR emission in the other PN studied here. The detection of the equatorial structures in both of these nebula have confirmed an important element in the models of bipolar nebula formation.

In summary, infrared cameras such as MIRAC and the Hg: Cd: Te systems available at Steward Observatory have proved to be very effective in studying the infrared emission from planetary nebulae. In the observations presented here, the images have revealed important information on the spatial distribution of dust and ionized gas in the nebulae. Using MIRAC, we will be able to extend this study to many other nebulae, as well as a wide variety of other astronomical applications.

FIGURES - PART 2

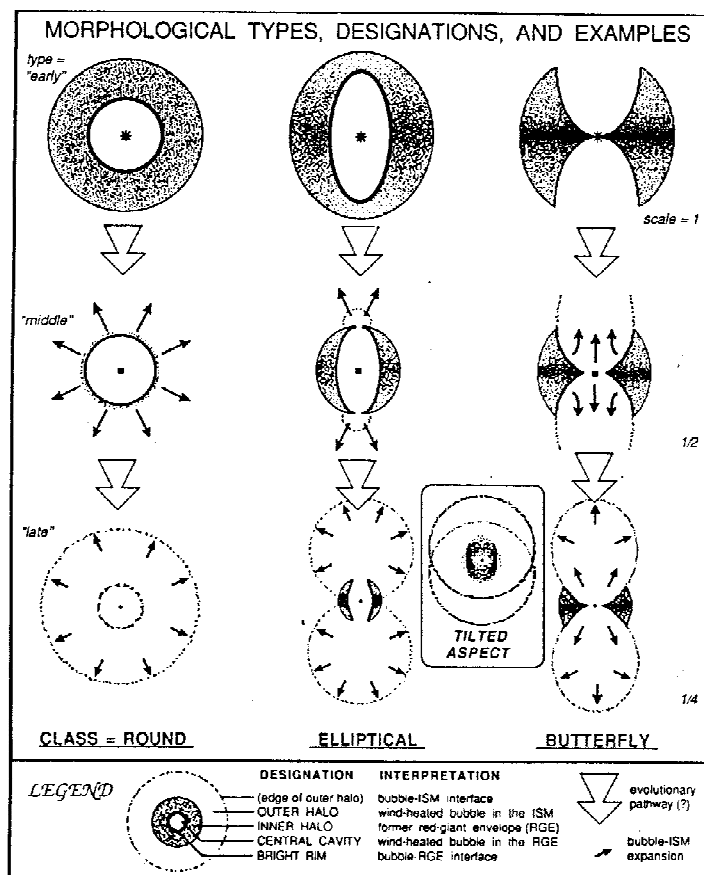


Figure 2.1. Planetary nebulae types and models. Schematic illustration of two-dimensional cuts through the centers of various morphological archetypes of PN (Balick 1987).

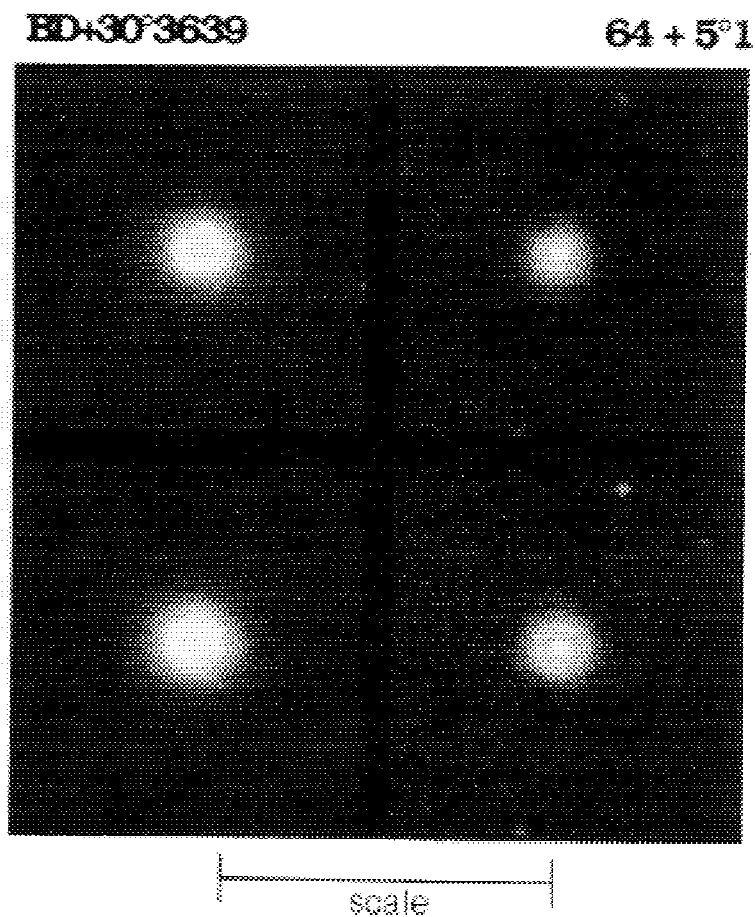


Figure 2.2. CCD images of the planetary nebula BD+30°3639, from Balick (1987). The scale line shown has a length of $37''.5$. The images were taken at the wavelengths of the following lines, in the order clockwise from the upper left: H α , [OIII], He II, and [NII].

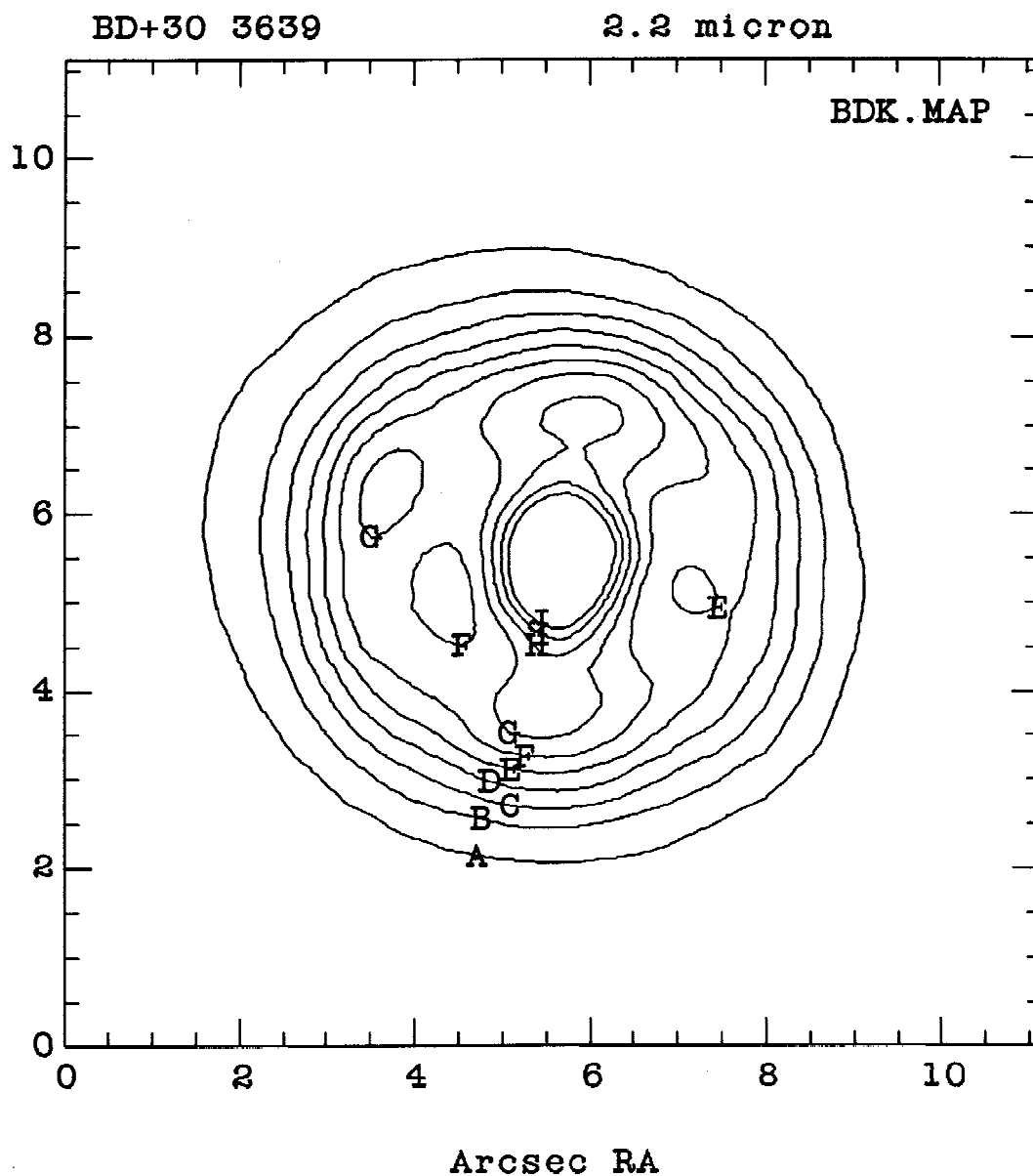


Figure 2.3. Contour images of the planetary nebula BD+30°3639. The contour level spacings in the mid-IR maps were chosen to be spaced evenly between a minimum and the maximum value of the map.

2.3a. $\lambda = 2.2 \mu\text{m}$, contour level spacing 2.5 mJy/arcsec^2 , minimum level 2.5 mJy/arcsec^2 .

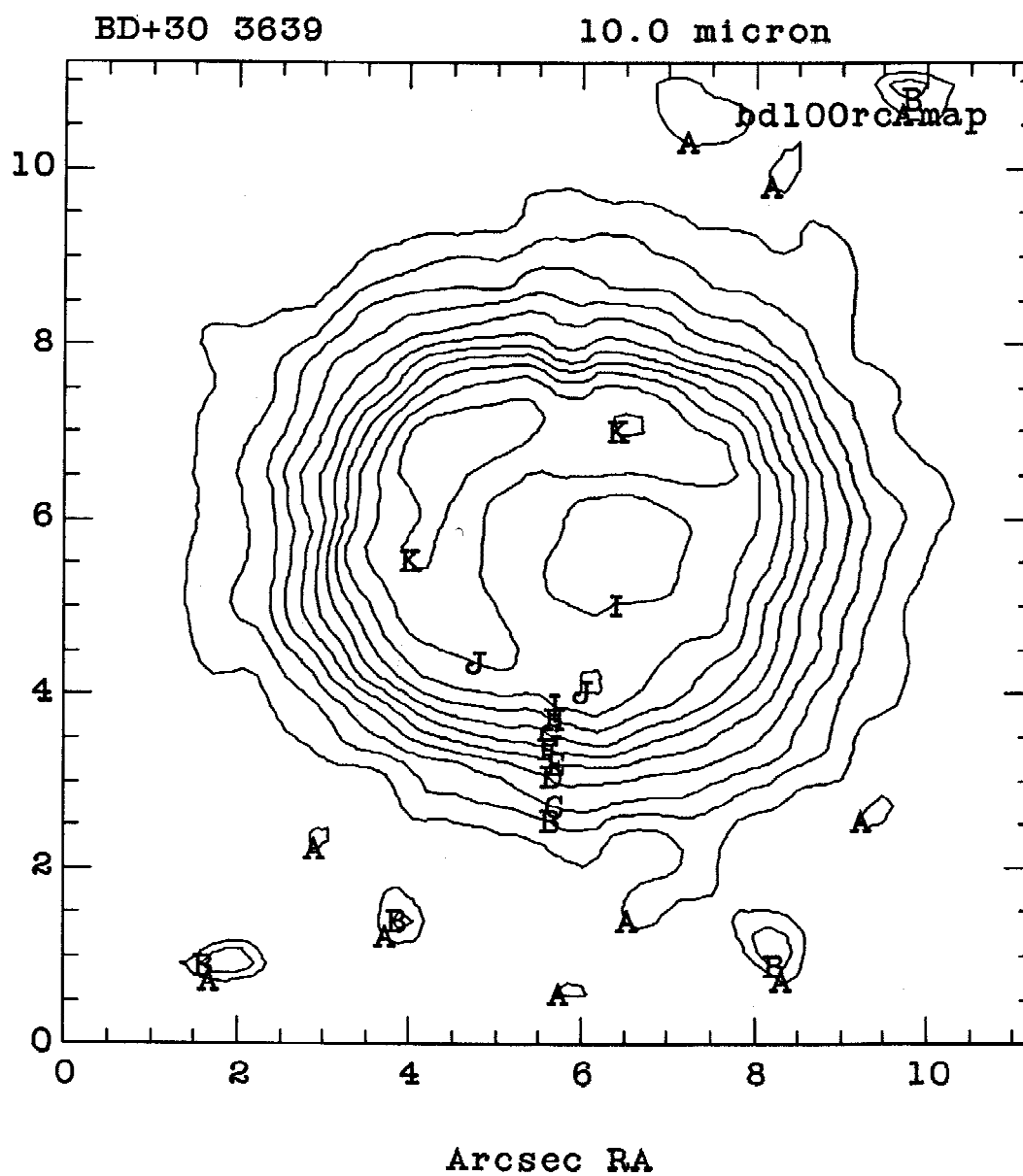


Figure 2.3b. $\lambda = 10.0 \mu\text{m}$, contour level spacing 150 mJy/arcsec^2 , minimum level 200 mJy/arcsec^2 .

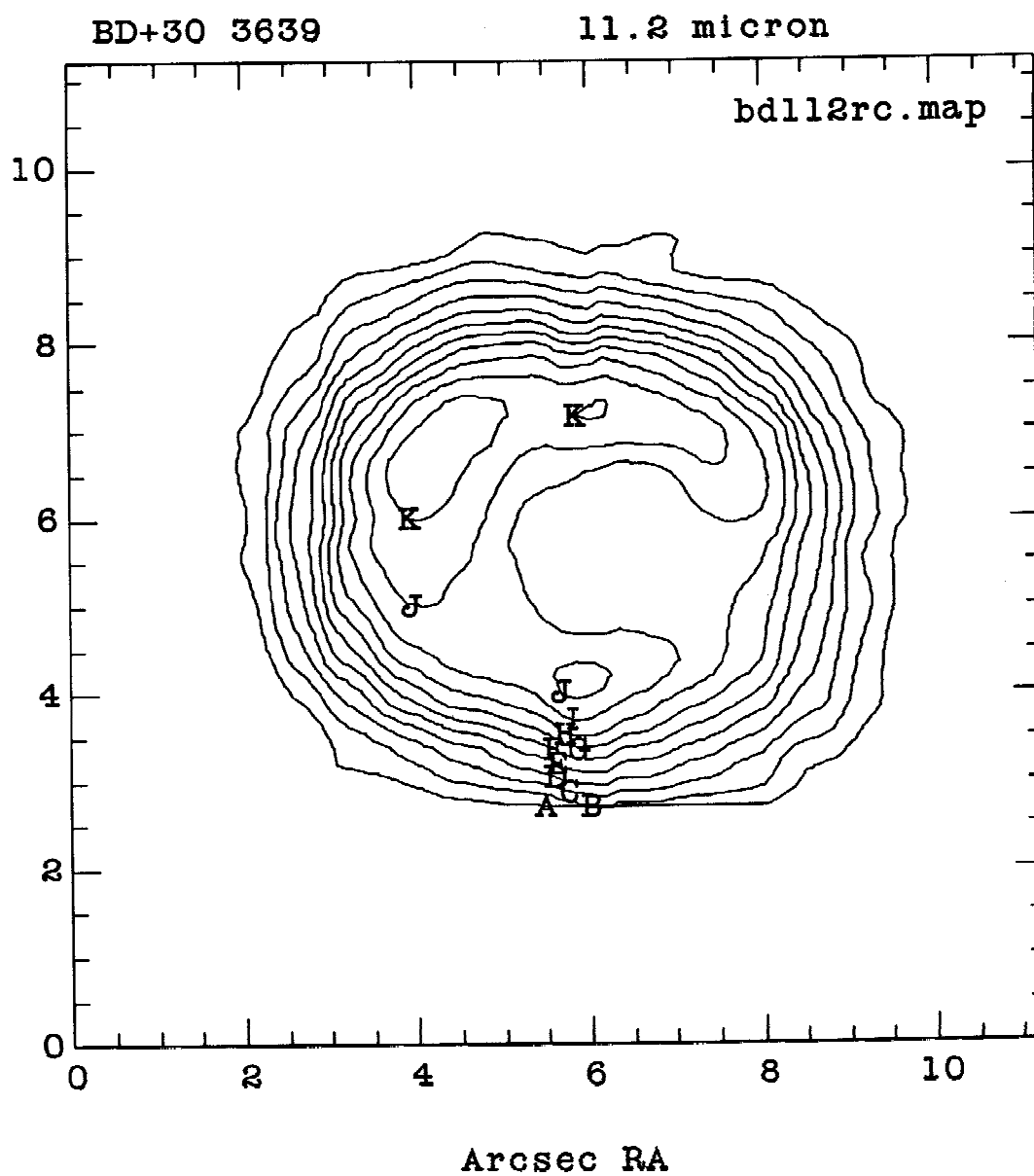


Figure 2.3c. $\lambda = 11.2 \mu\text{m}$, contour level spacing 200 mJy/arcsec^2 , minimum level 500 mJy/arcsec^2 .

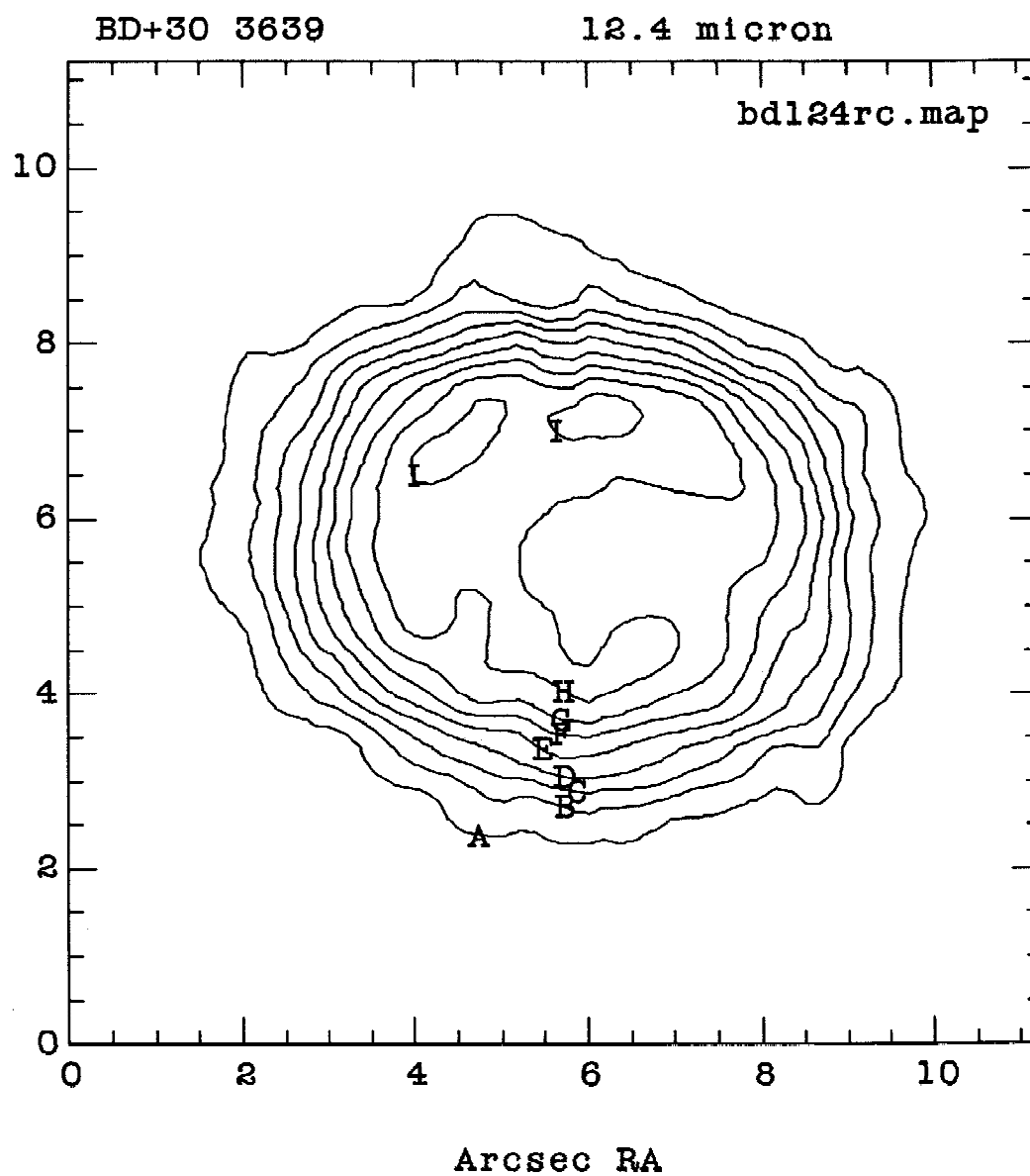


Figure 2.3d. $\lambda = 12.4 \mu\text{m}$, contour level spacing 250 mJy/arcsec^2 , minimum level 450 mJy/arcsec^2 .

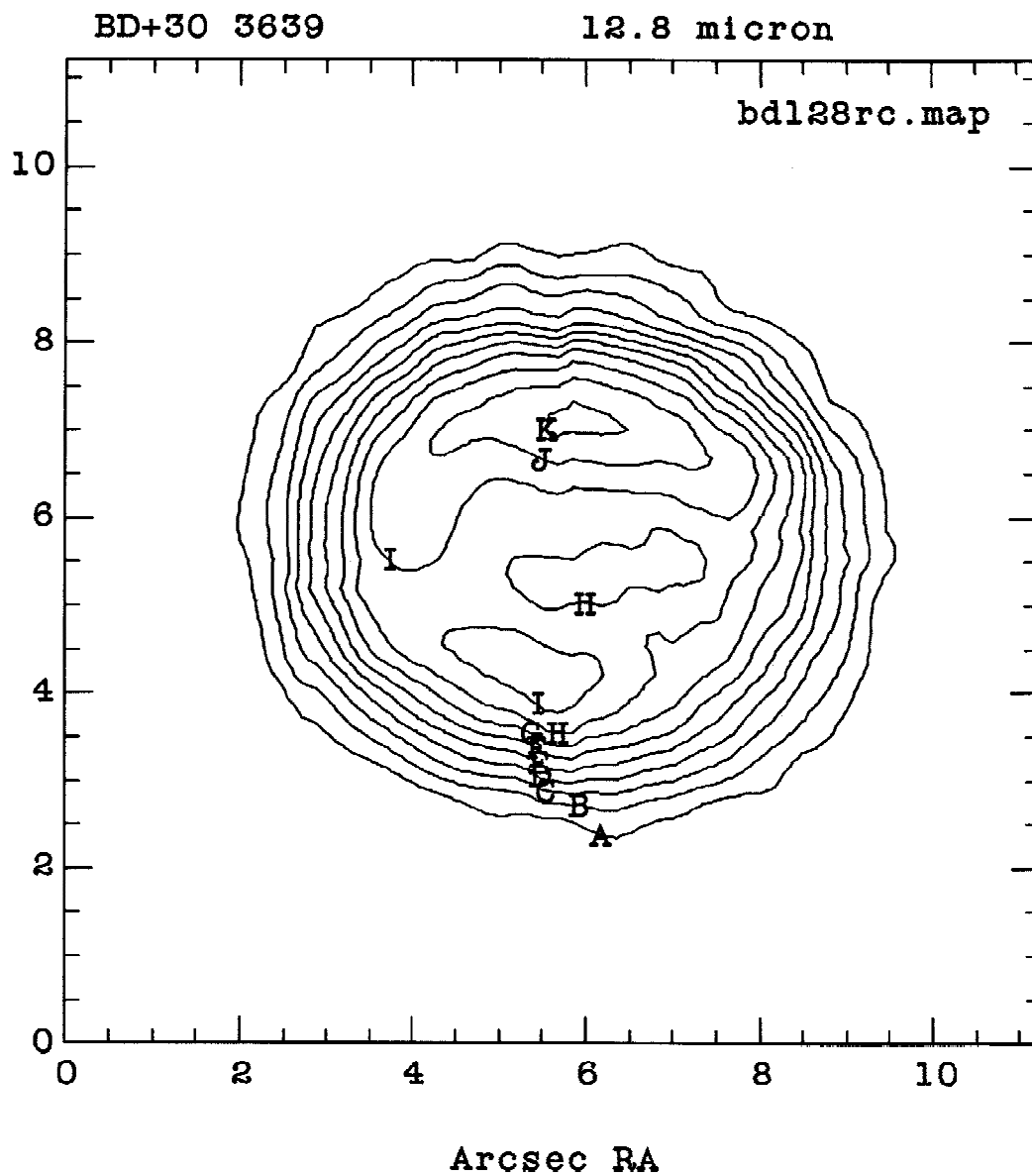


Figure 2.3e. $\lambda = 12.8 \mu\text{m}$, contour level spacing 400 mJy/arcsec^2 , minimum level 900 mJy/arcsec^2 .

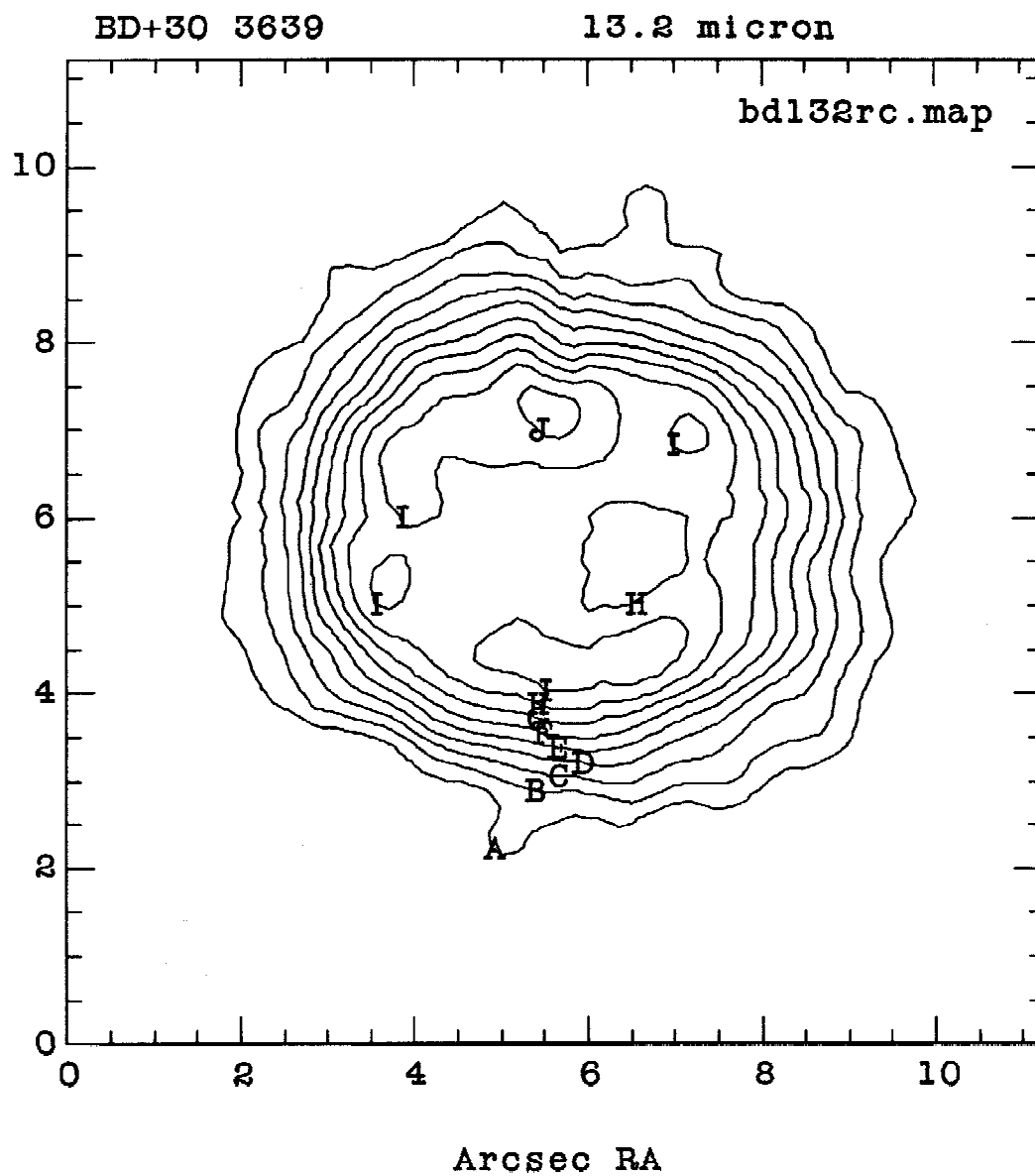


Figure 2.3f. $\lambda = 13.2 \mu\text{m}$, contour level spacing 300 mJy/arcsec^2 , minimum level 600 mJy/arcsec^2 .

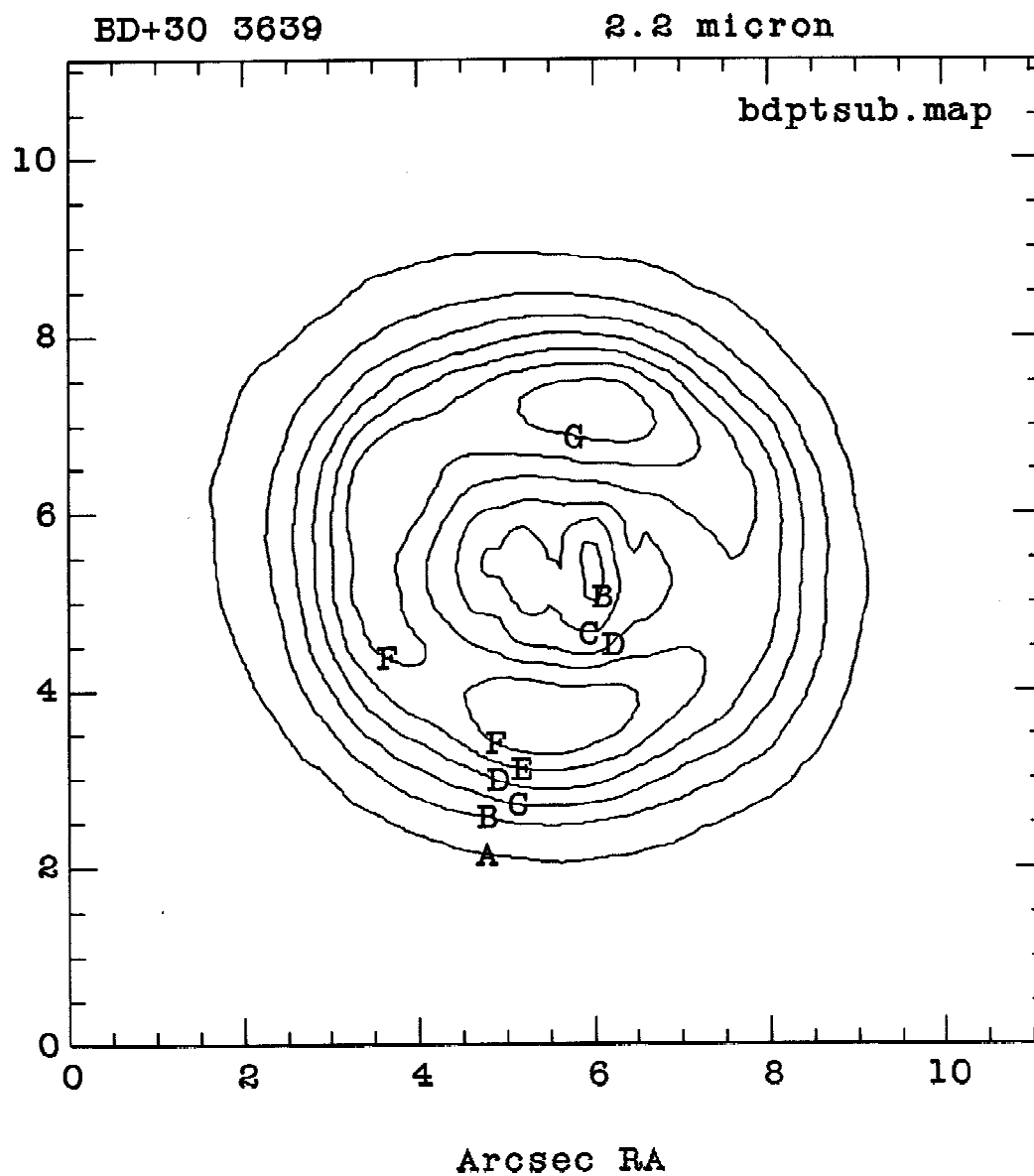


Figure 2.4. Contour image of BD+30°3639 at 2.2 μm , where the central star contribution has been subtracted, showing the nebula alone. Contour levels are evenly spaced at 2.5 mJy/arcsec², with a minimum level of 2.5 mJy/arcsec².

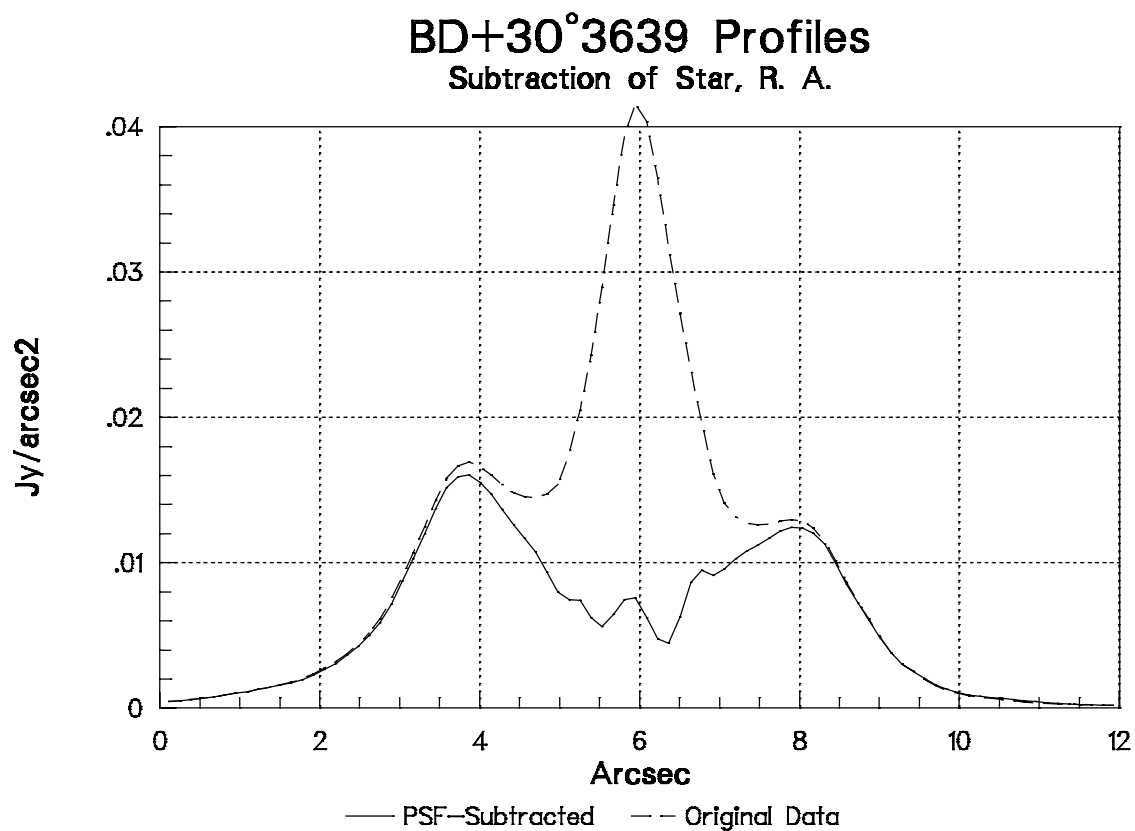


Figure 2.5. Profiles of the 2.2 μm image of BD+30°3639, showing the original data and the profile after the star was subtracted. The profiles pass through the center of the nebula.

2.5a. Right Ascension profiles.

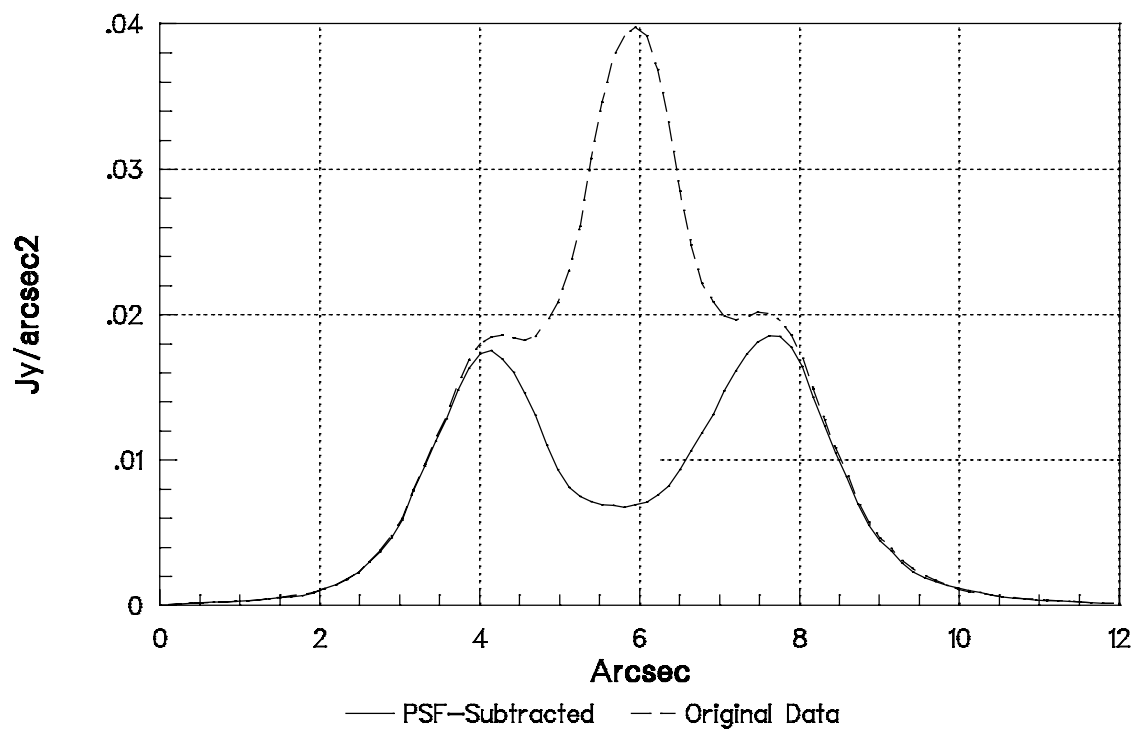


Figure 2.5b. BD+30°3639 Declination profiles.

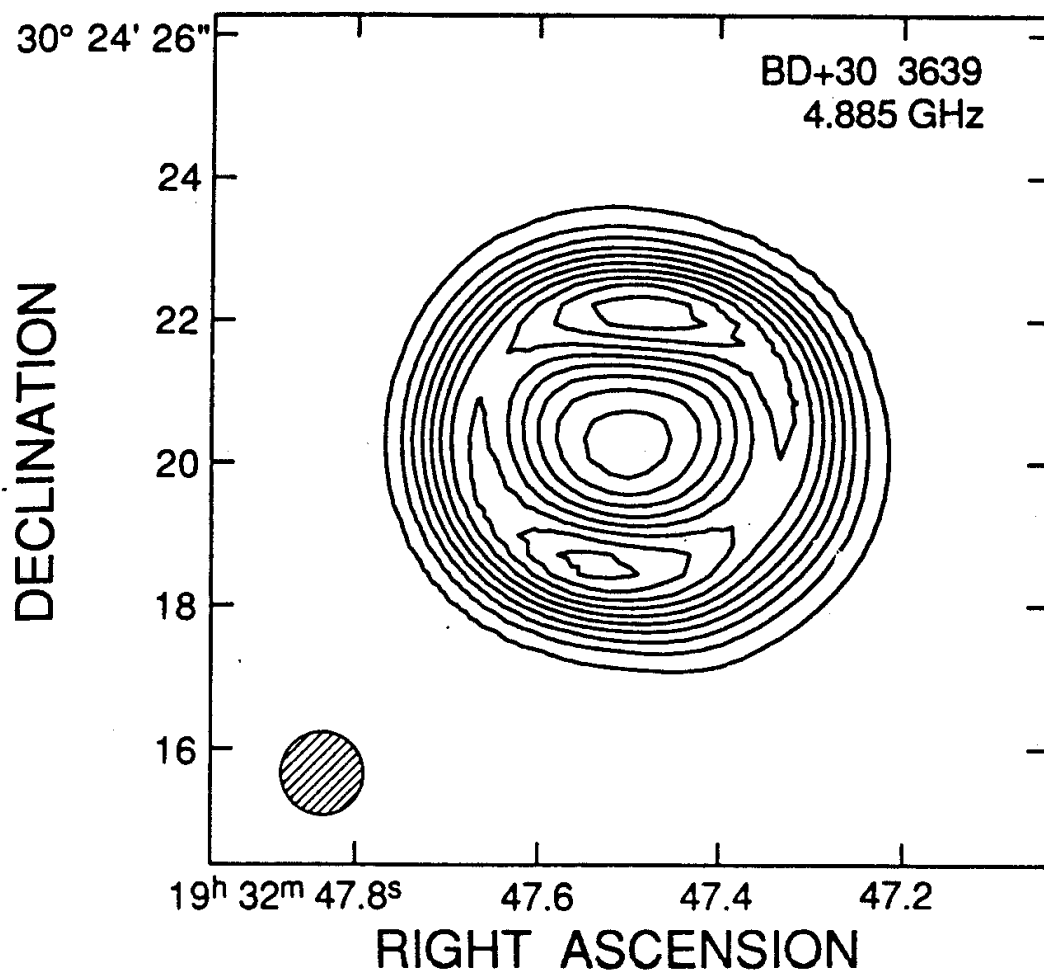


Figure 2.6. Contour image of BD+30°3639 at 4.885 GHz, from Masson (1989). The Gaussian beam size for this image is 0!96, and the contour level spacing is 5 mJy/beam.

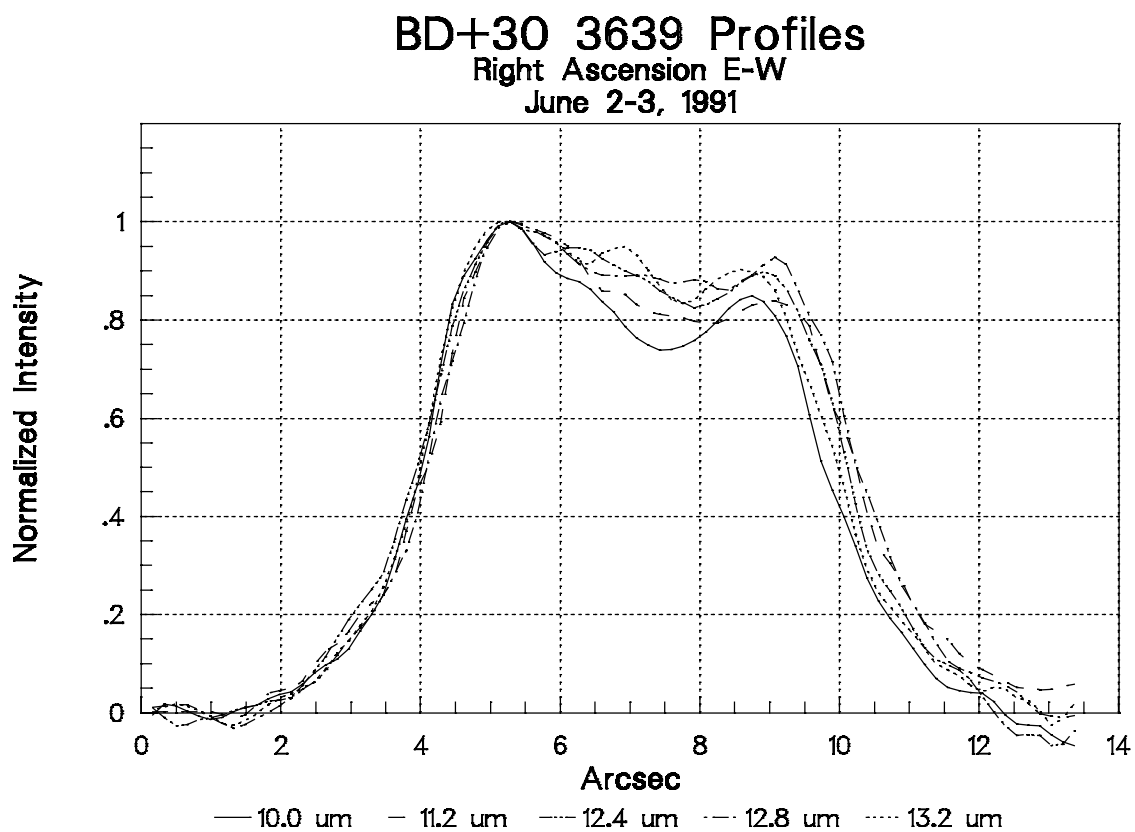


Figure 2.7. Profiles of the mid-IR images of BD+30°3639.

2.7a. Profiles in R. A., from east to west. The profiles have been normalized to the eastern peak, and the eastern peaks have been aligned to show the differences in spatial extent. The profiles are overall very similar, but it can be seen that the 10.0 and 13.2 μm profiles are the narrowest.

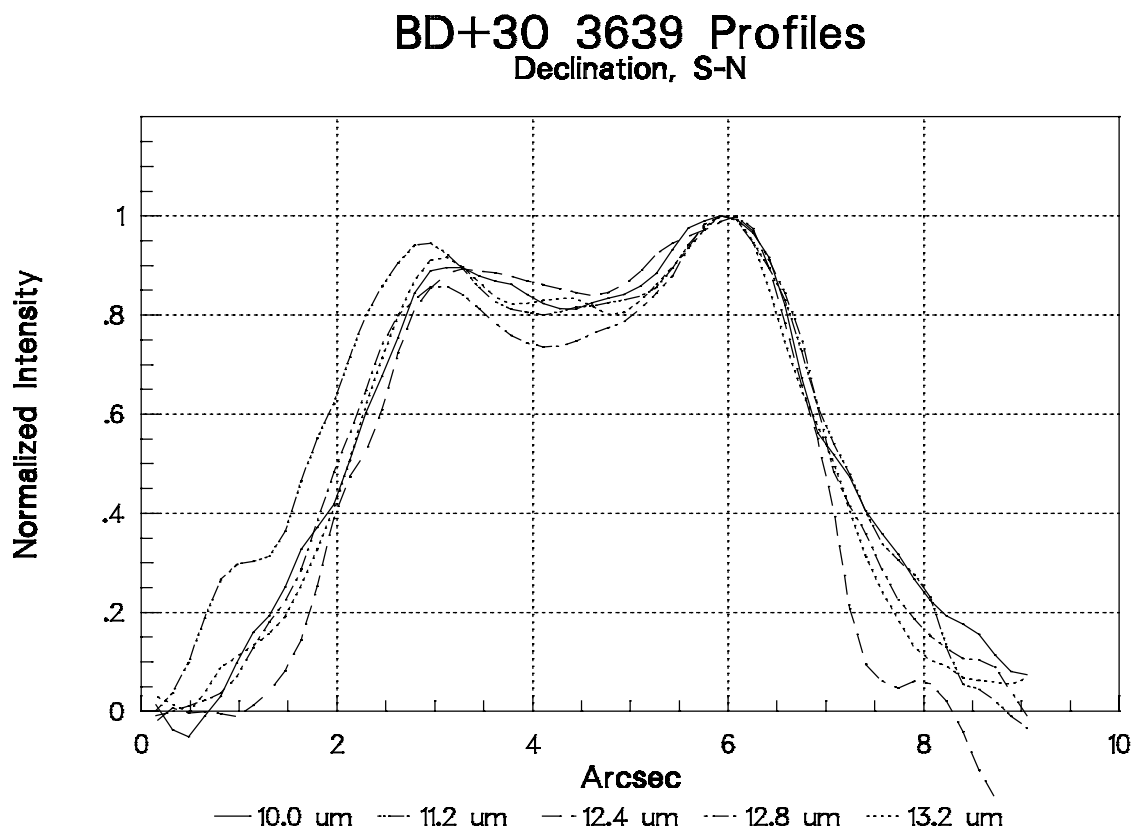


Figure 2.7b. Profiles of the mid-IR images of BD+30°3639 in Declination, from south to north. The profiles have been normalized to the north peak, and the north peaks have been aligned. As in the R. A. profiles the sizes are similar, but the 11.2 μm profile is clearly wider than the others.

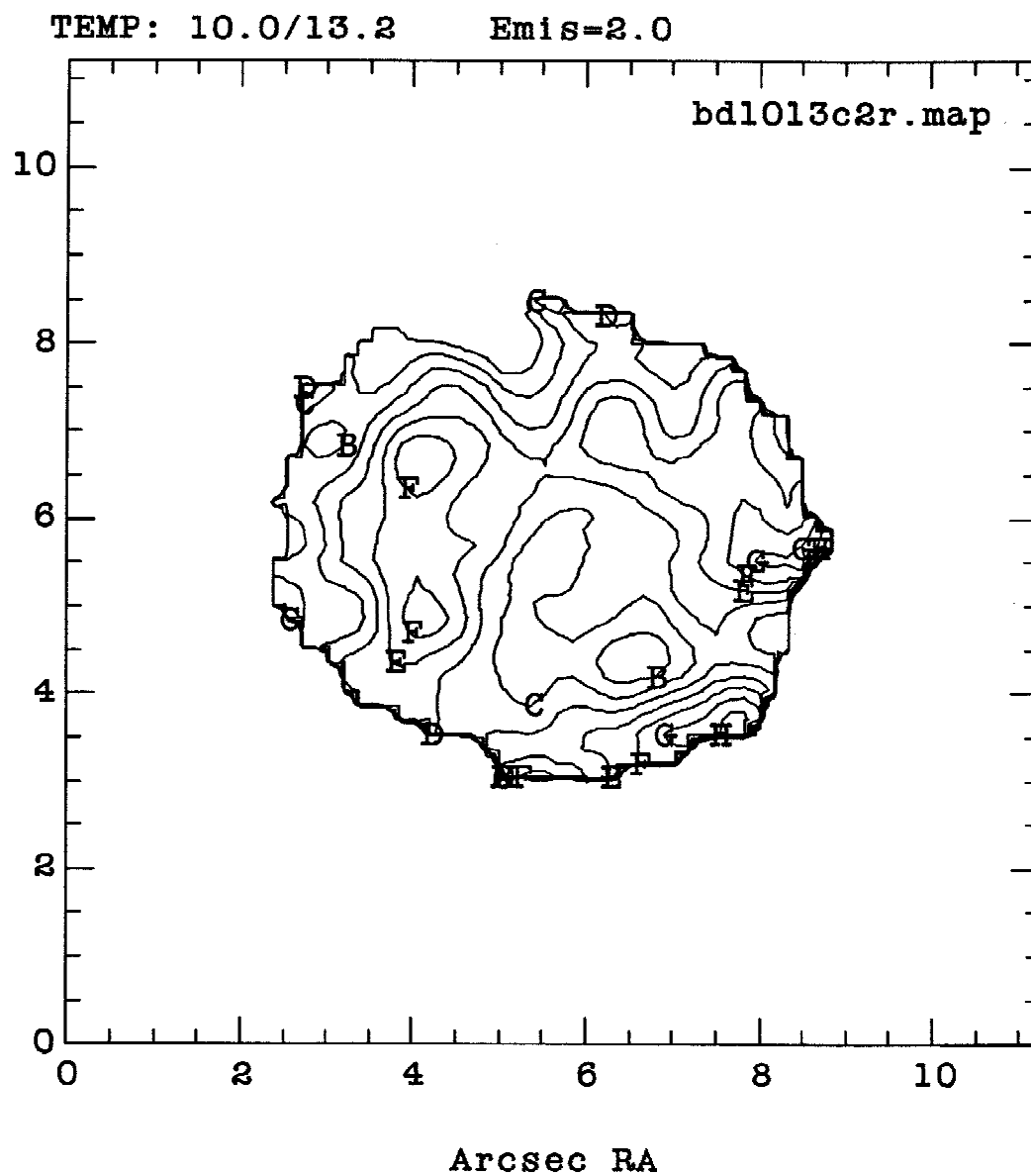


Figure 2.8. Temperature image of BD+30°3639, calculated from the 10.0 and 13.2 μm images. Contour levels are evenly spaced at 4°K per level, with a minimum level of 160K.

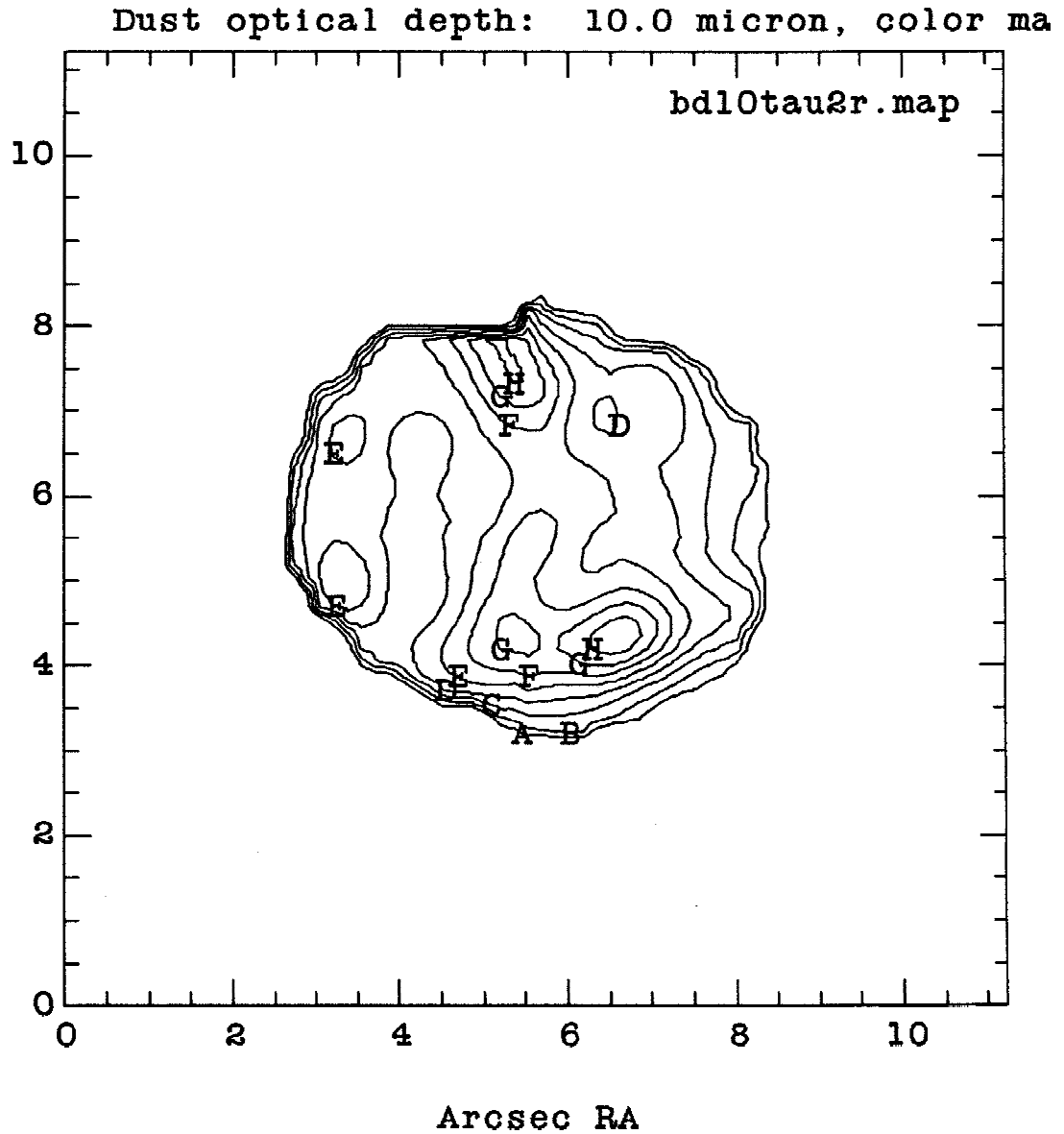


Figure 2.9. Dust opacity image of BD+30°3639, calculated from the temperature image of Figure 2.8 and the 10.0 μm intensity image. Contour levels are evenly spaced at $1 \cdot 10^{-3}$, with a minimum value of $3 \cdot 10^{-3}$.

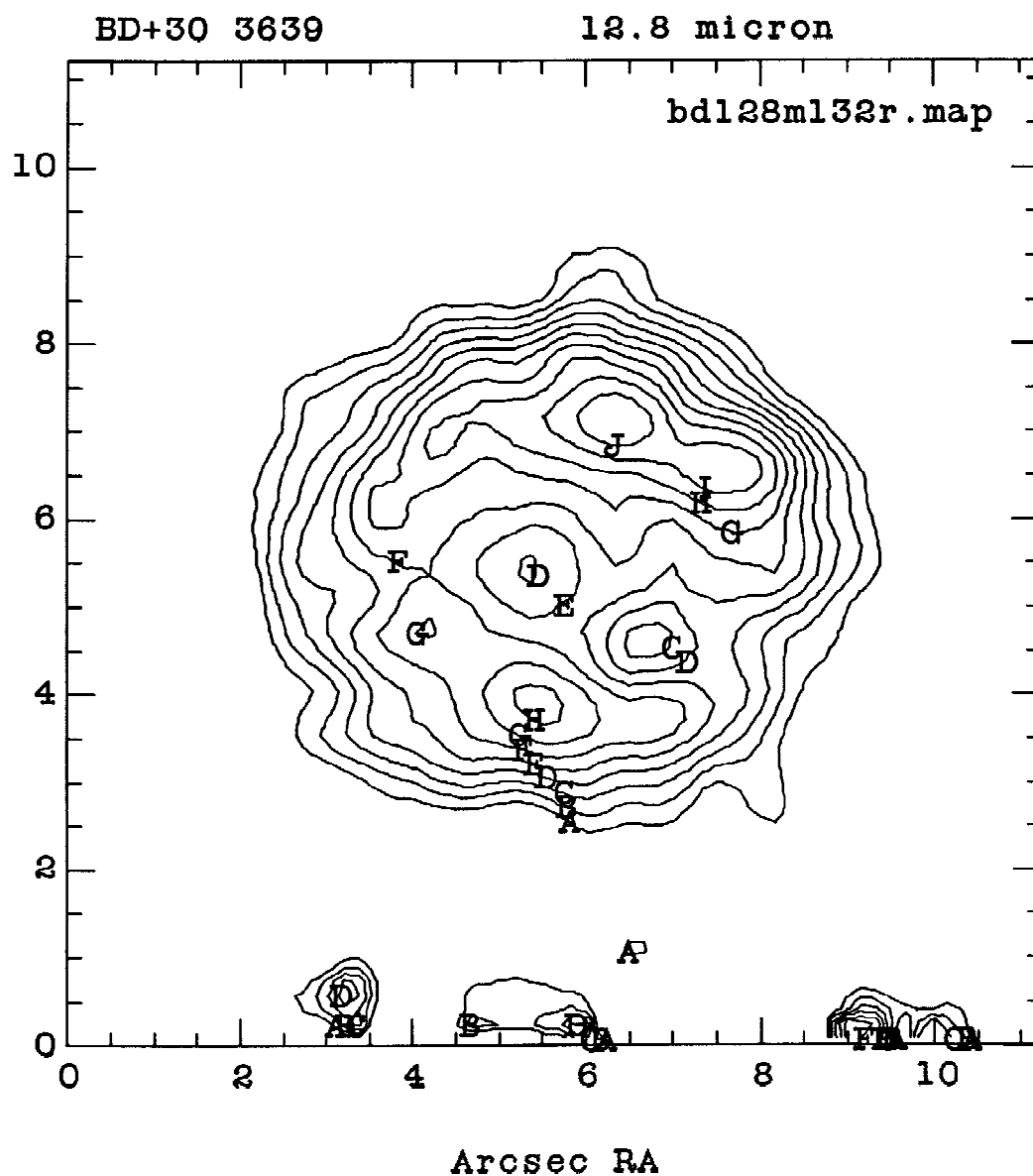


Figure 2.10. Contour image of the 12.8 μm feature of BD+30°3639, calculated from the 12.8 μm image and a scaled 13.2 μm image from Figure 2.3. The contour level spacing is 150 mJy/arcsec², with a minimum level of 300 mJy/arcsec².

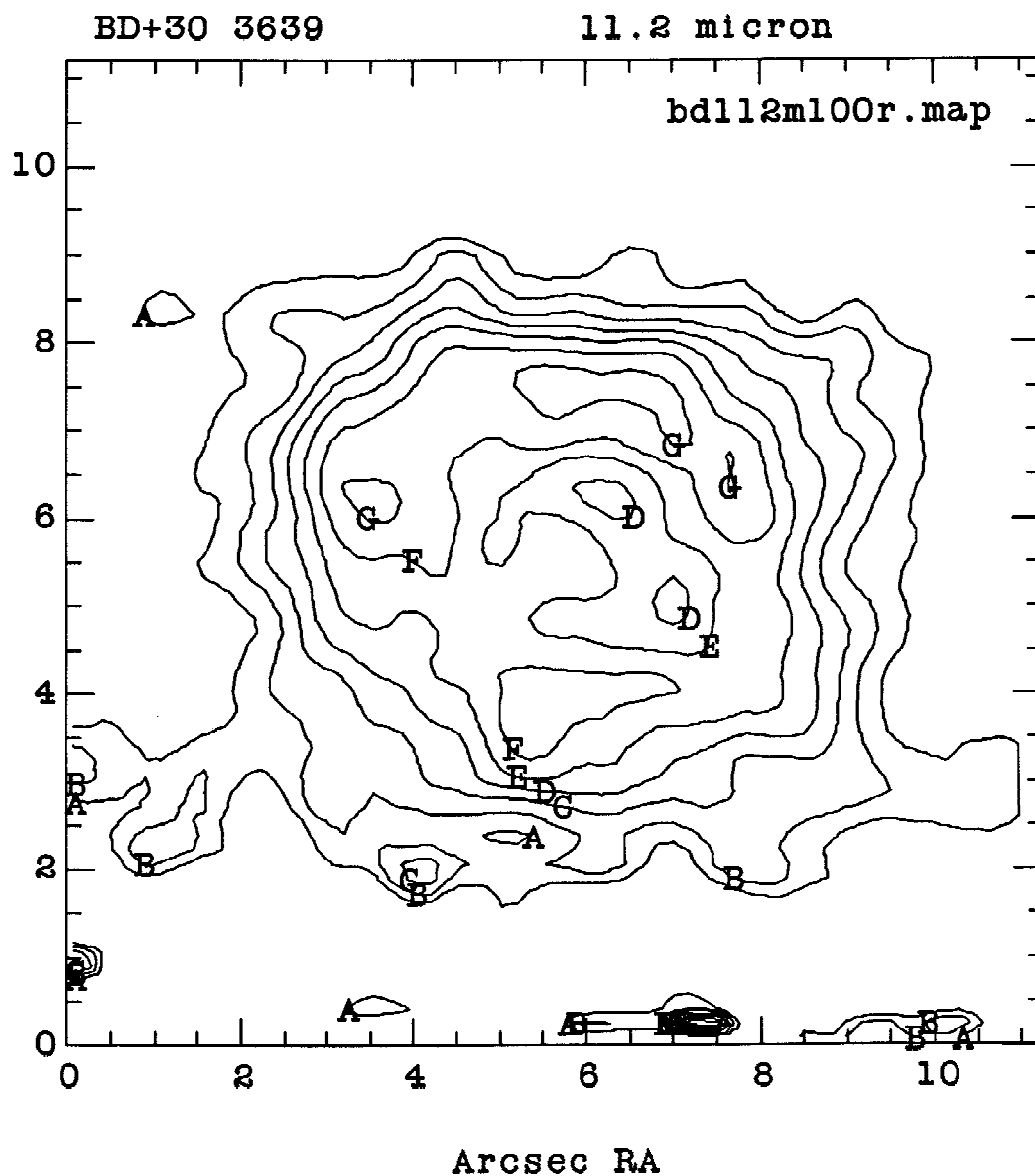


Figure 2.11. Contour image of the 11.2 μm feature of BD+30°3639, calculated from the 11.2 μm image and a scaled 10.0 μm image from Figure 2.3. The contour level spacing is 100 mJy/arcsec², with a minimum level of 100 mJy/arcsec².

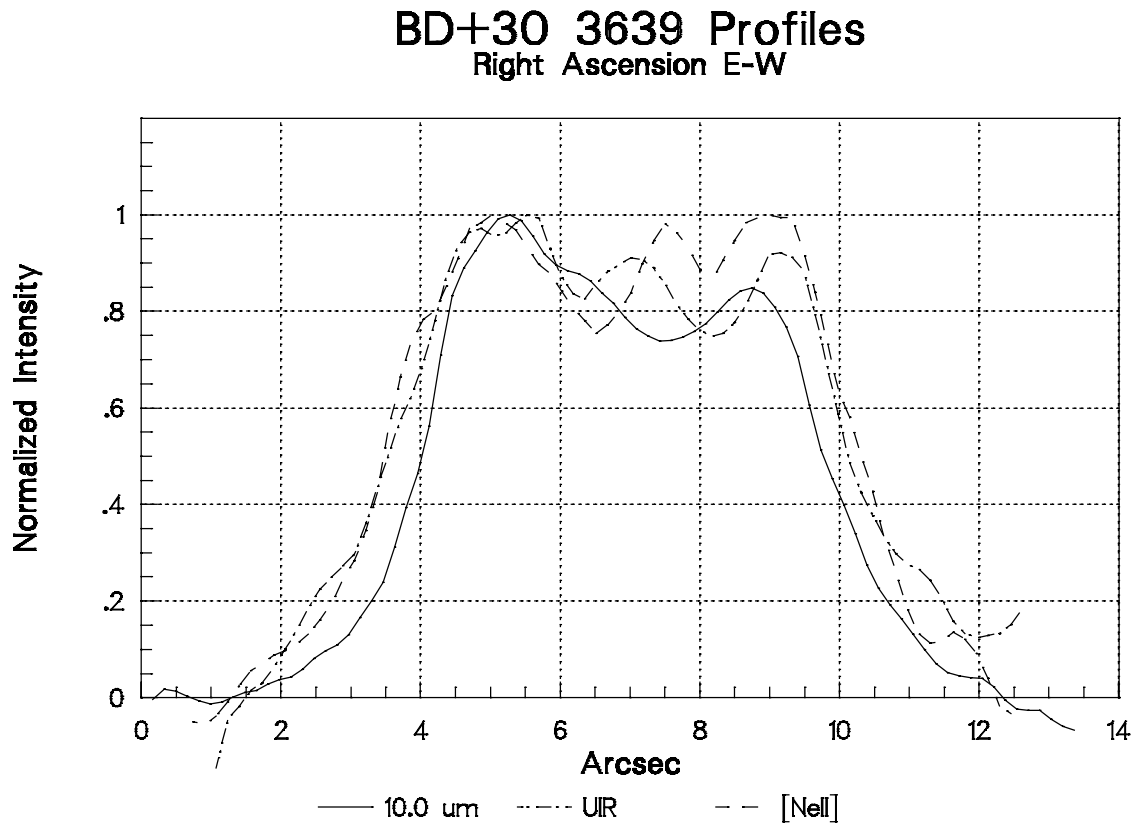


Figure 2.12. Profiles of BD+30°3639 in the [NeII] and UIR feature images of Figure 2.10 and Figure 2.11, along with the continuum profile of the 10.0 μm image of Figure 2.3. These profiles have been aligned to the center position of the nebula. 2.12a. Profiles in Right Ascension, with east at the left. Profiles have been normalized to the eastern peak. The UIR and [NeII] profiles are wider than the continuum profile at 10.0 μm , both in FWHM and peak separation.

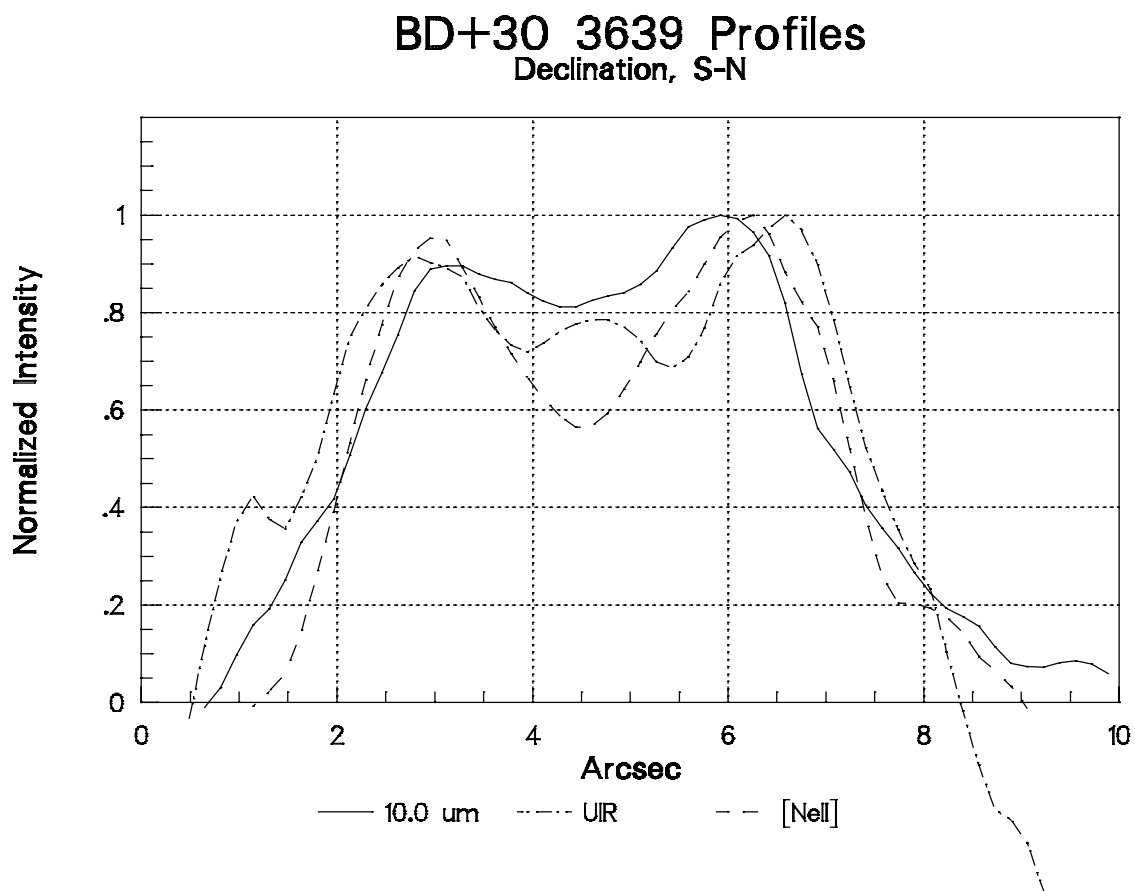


Figure 2.12b. Profiles in Declination, with south at the left. Profiles have been normalized to the north peak. Here again the UIR feature profile is wider than the 10.0 μm continuum profile. However, the [NeII] profile is only slightly wider than the continuum.

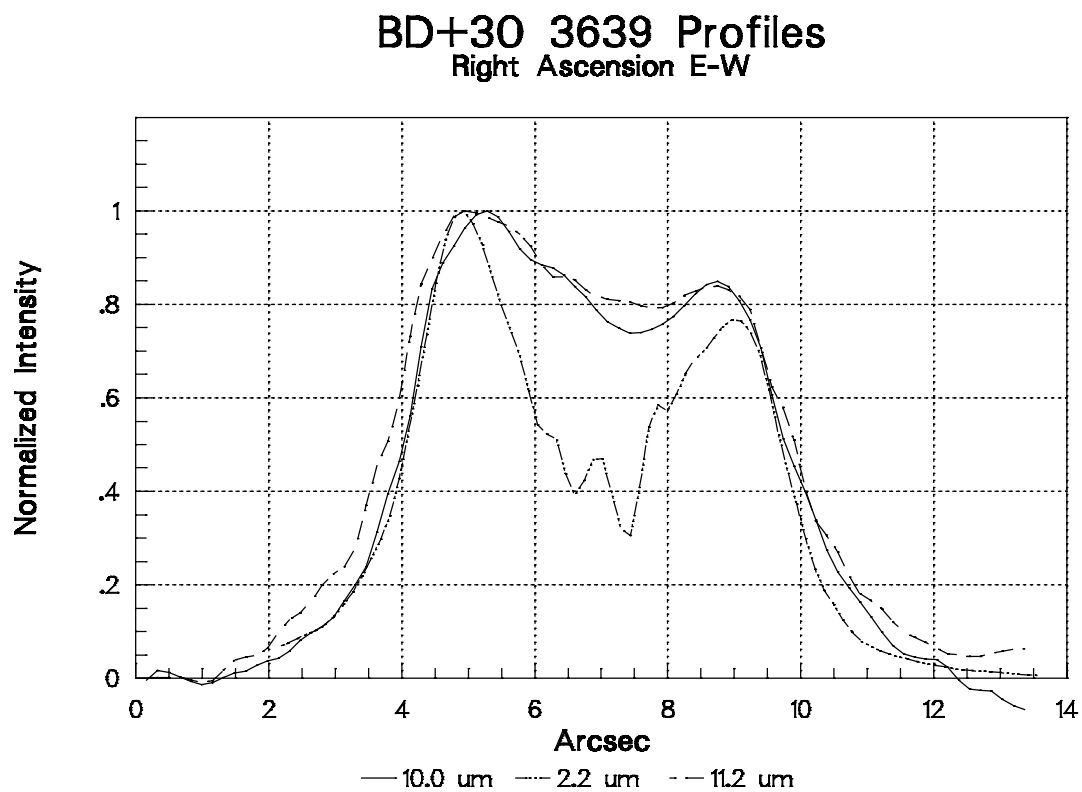


Figure 2.13. Profiles of the 2.2 μm star-subtracted image of BD+30°3639, along with the profiles at 10.0 and 11.2 μm . These profiles have been aligned to the center position of the nebula.

2.13a. Profiles in Right Ascension, with east at the left. The profiles have been normalized to the east peak.

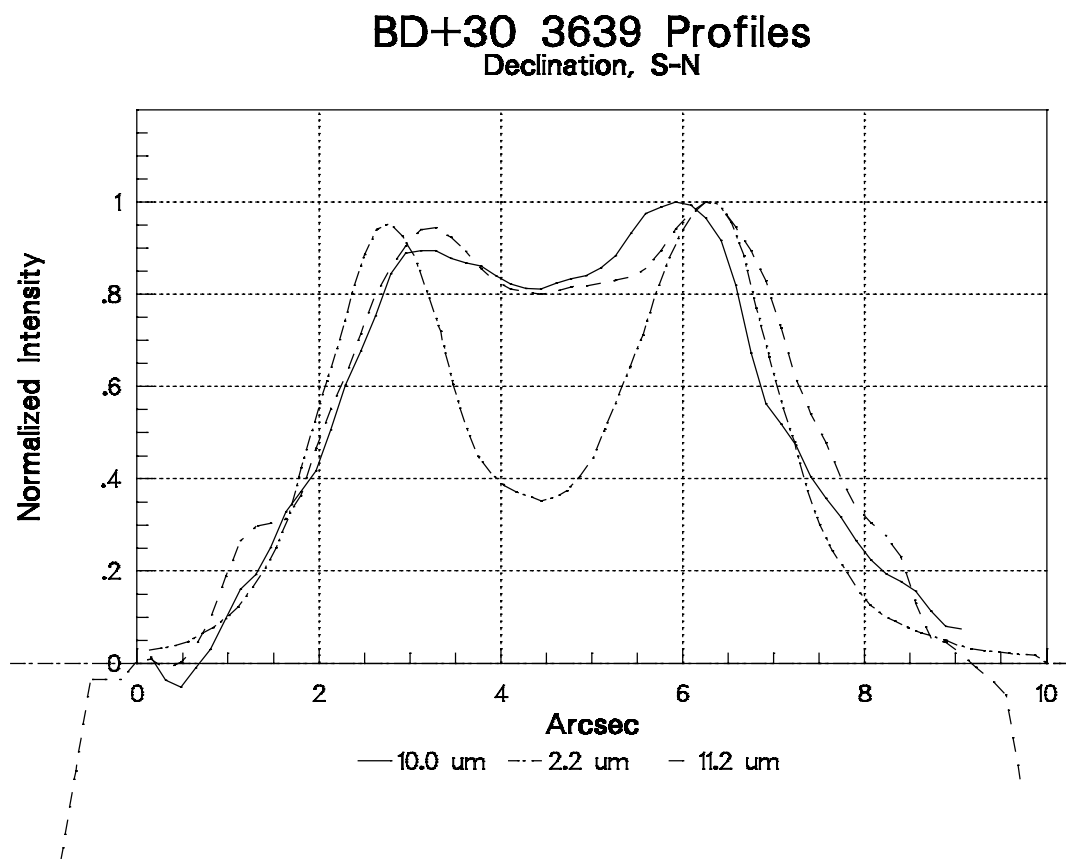


Figure 2.13b. Profiles in Declination, with south at the left. The profiles have been normalized to the north peak.

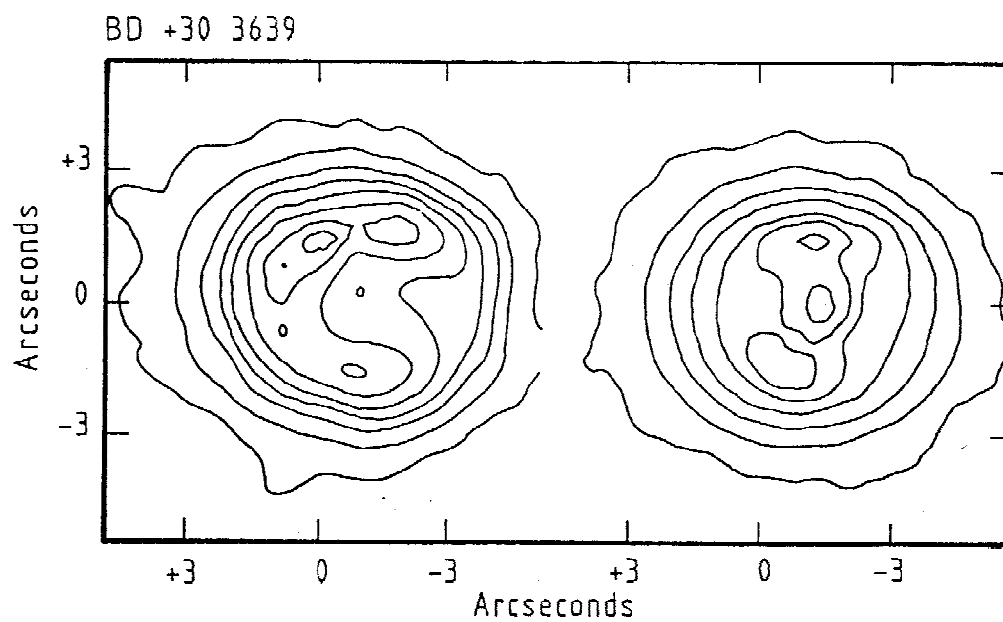


Figure 2.14. Contour images of BD+30°3639, from Roche (1989). The left image is at 3.28 μm , and the right image is at Br γ .

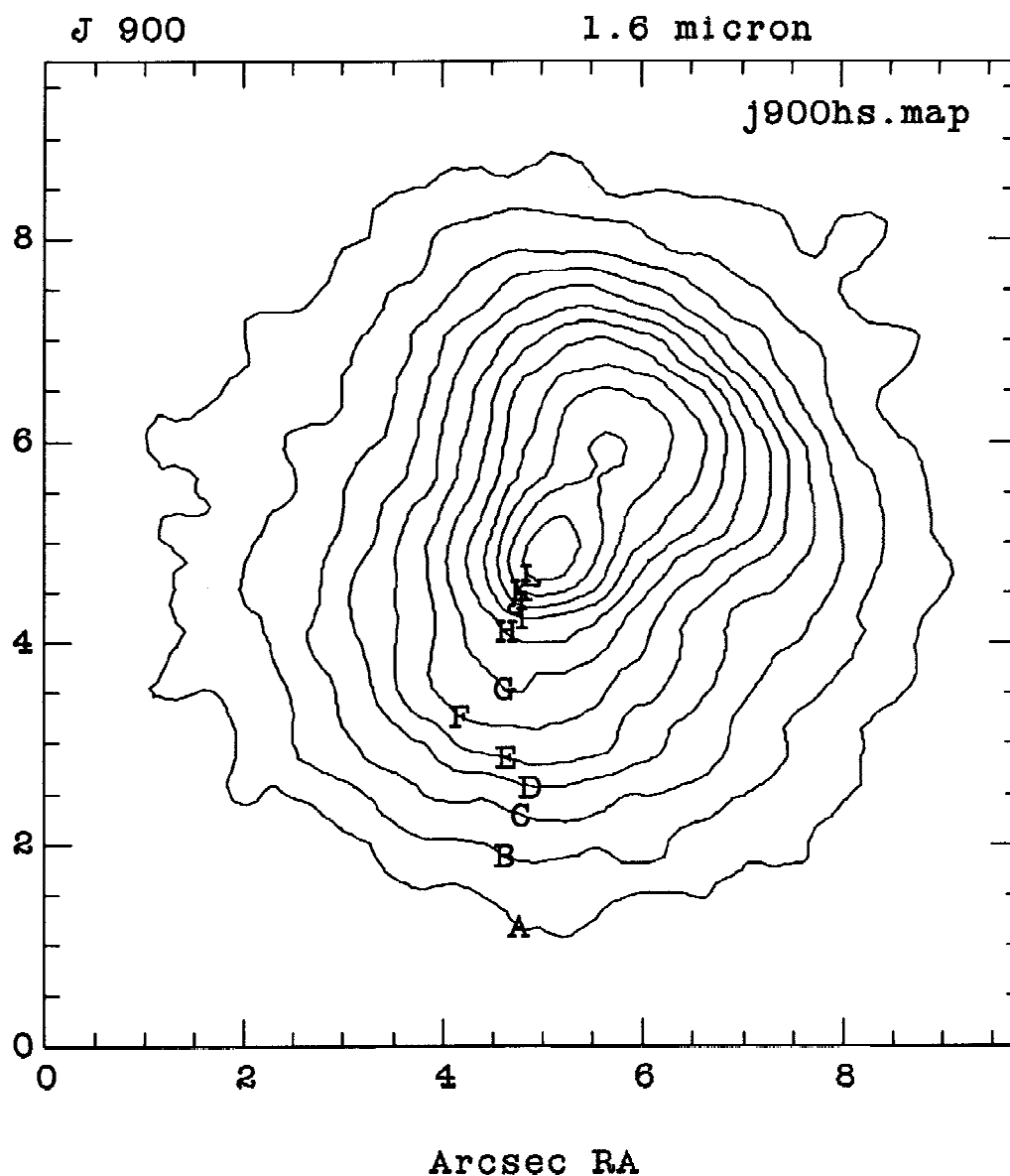


Figure 2.15. Contour images of the PN J 900. The contour levels are evenly spaced, as described below for each image. Both images show an elongation of the PN in the SE-NW direction.

2.15a. J 900 H contour image. Minimum contour level = $.15 \text{ mJy/arcsec}^2$, contour level spacing = $.15 \text{ mJy/arcsec}^2$.

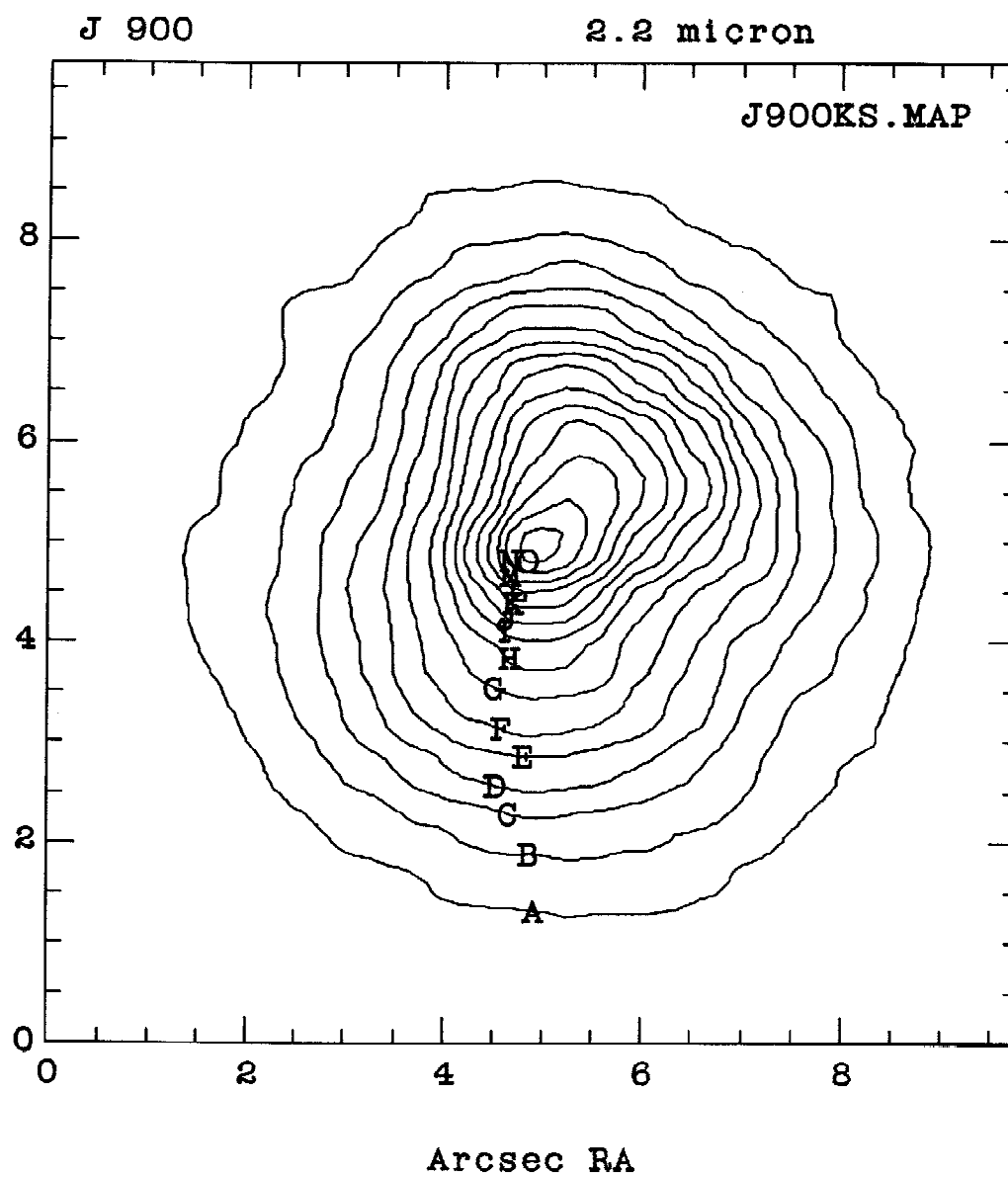


Figure 2.15b. J 900 K contour image. Minimum contour level = $.5 \text{ mJy/arcsec}^2$, contour level spacing = $.5 \text{ mJy/arcsec}^2$.

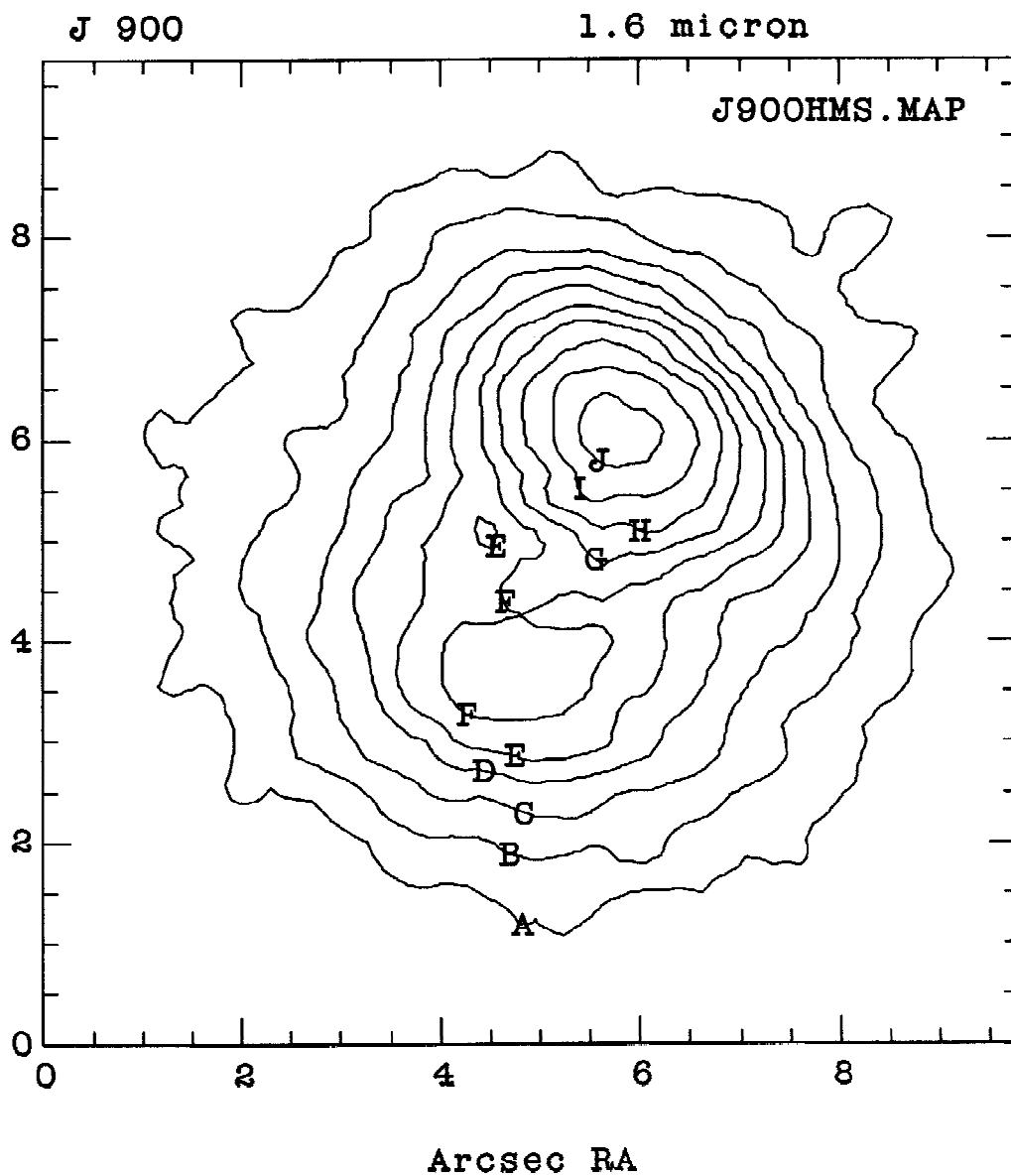


Figure 2.16. Contour images of the PN J 900, in which the central star has been subtracted. Contour levels are evenly spaced, as described below for each image.

2.16a. J 900 H PSF-subtracted image. Minimum contour level = $.15 \text{ mJy/arcsec}^2$, contour level spacing $.15 \text{ mJy/arcsec}^2$.

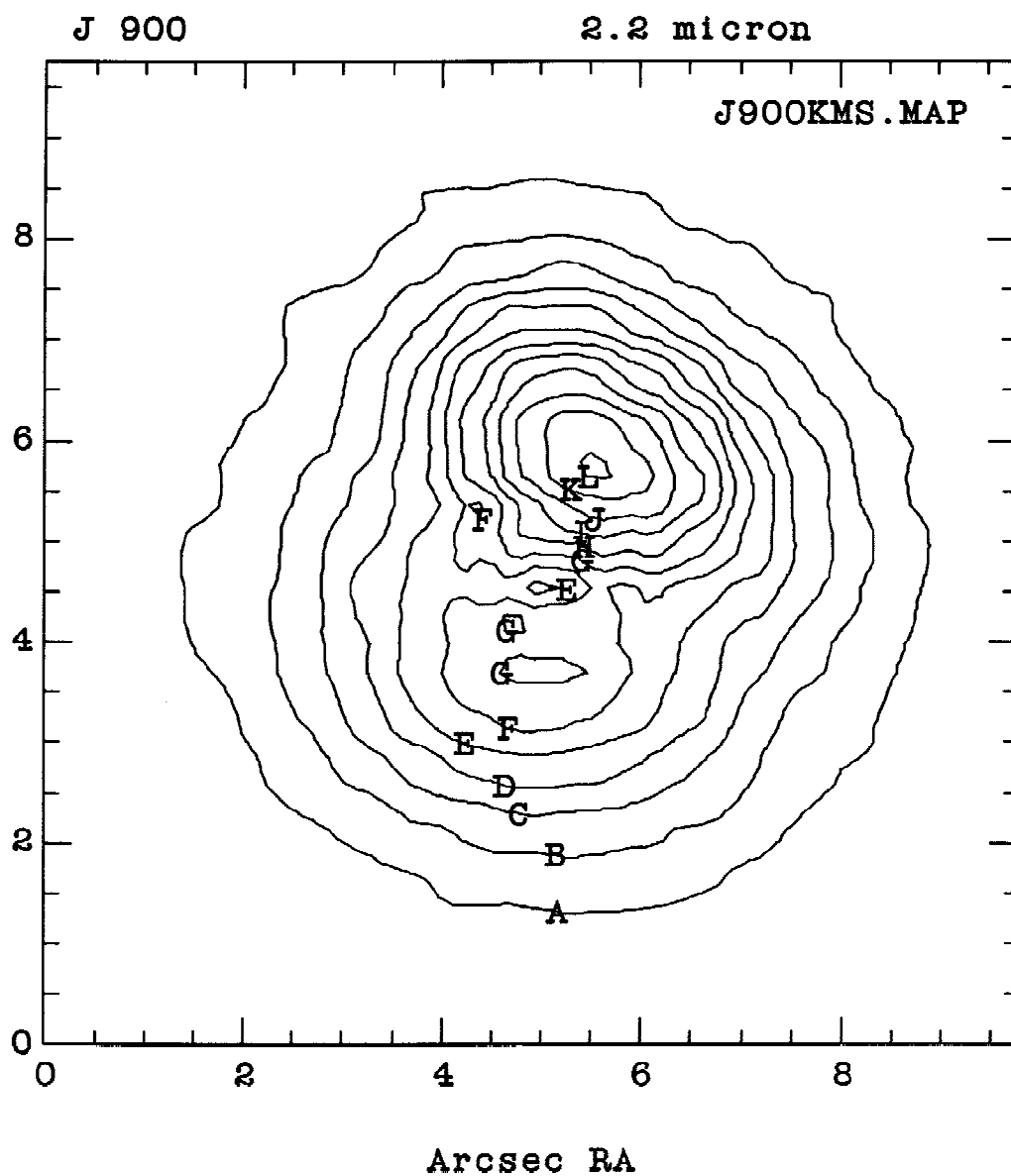


Figure 2.16b. J 900 K contour image, in which the central star has been subtracted. Minimum contour level = $.5 \text{ mJy/arcsec}^2$, contour level spacing = $.5 \text{ mJy/arcsec}^2$.

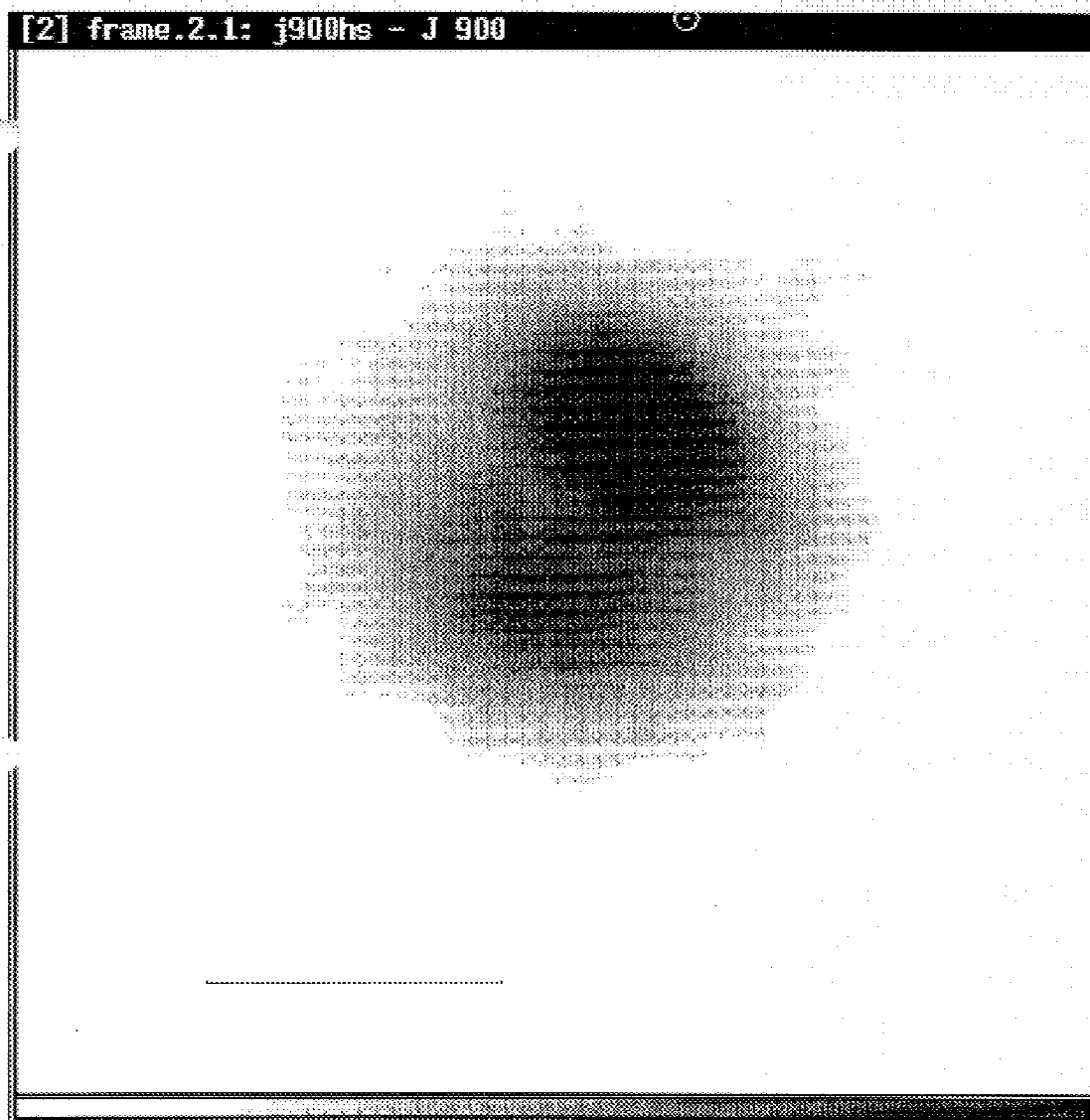


Figure 2.17. Grayscale images of the PN J 900, in which the central star has been subtracted. The line at the bottom of the figure is 5 arcsec long.
2.17a. J 900 H PSF-subtracted image.

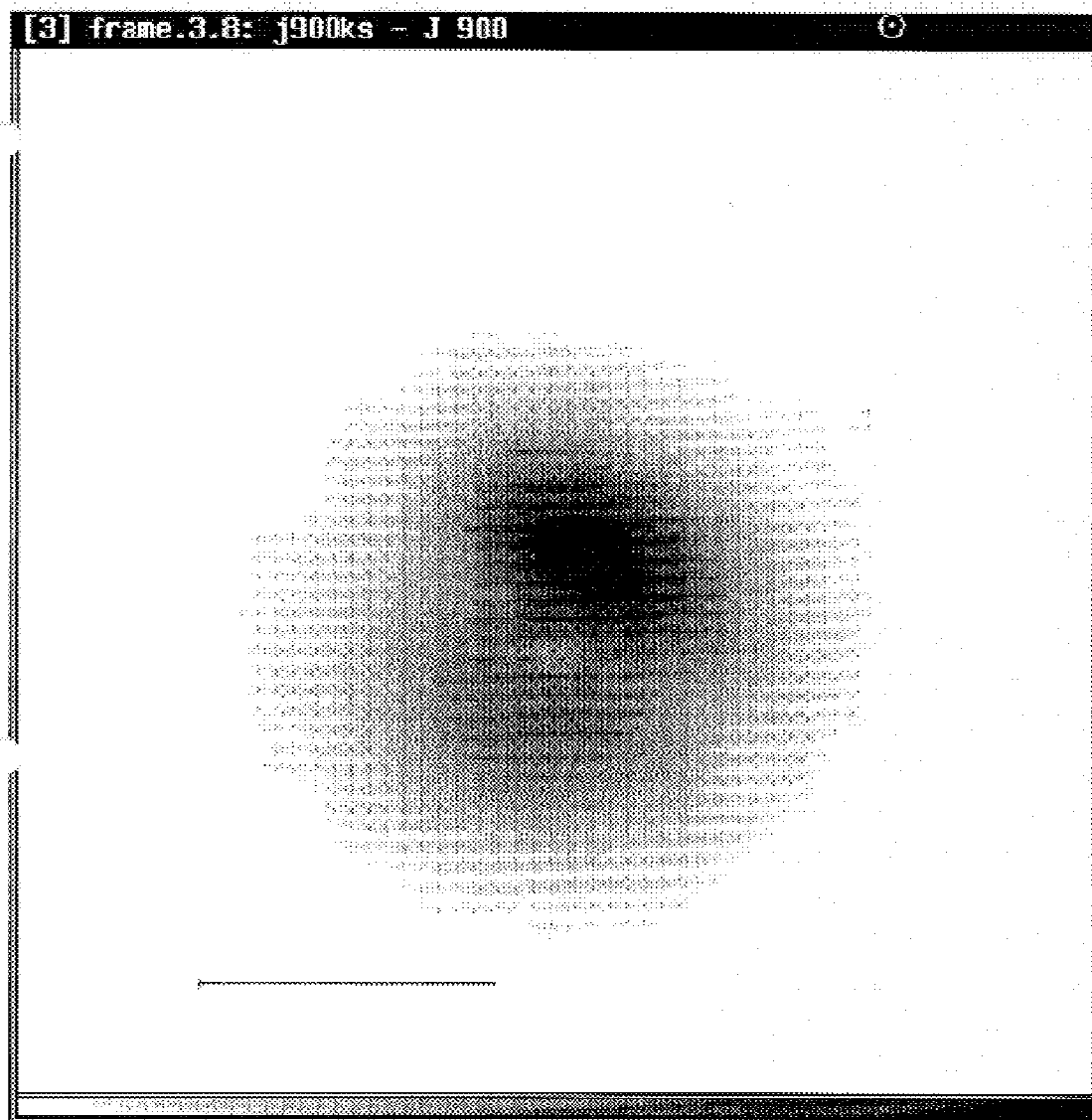


Figure 2.17b. J 900 K grayscale image, central star subtracted.

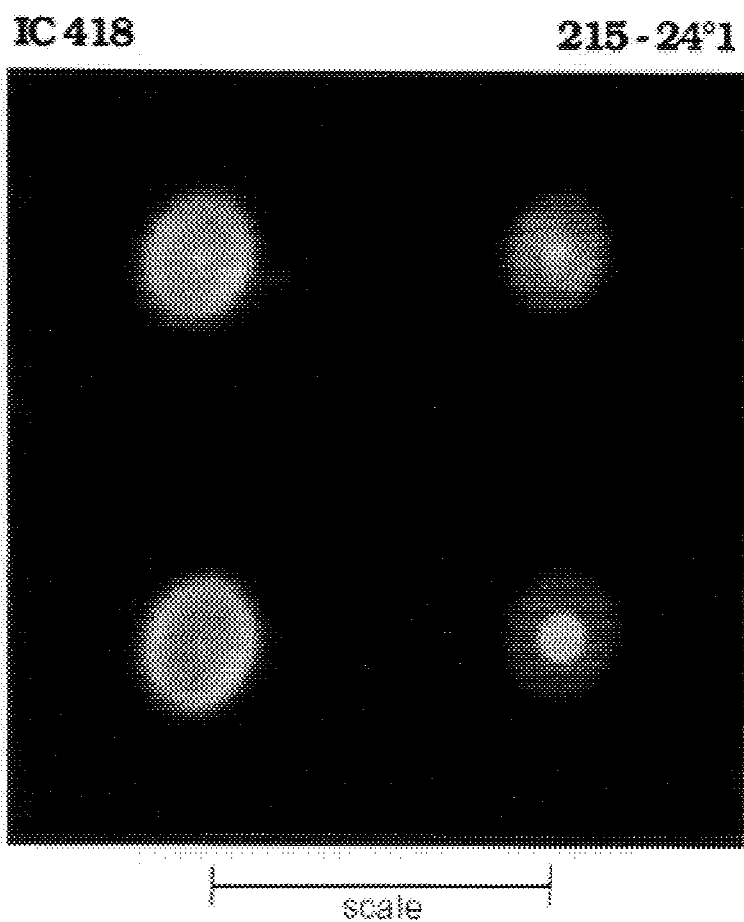


Figure 2.18. CCD images of IC 418, from Balick (1987). The scale line shown has a length of 37". The images were taken at the wavelengths of the following lines, in the order clockwise from the upper left: H α , [OIII], He II, and [NII].

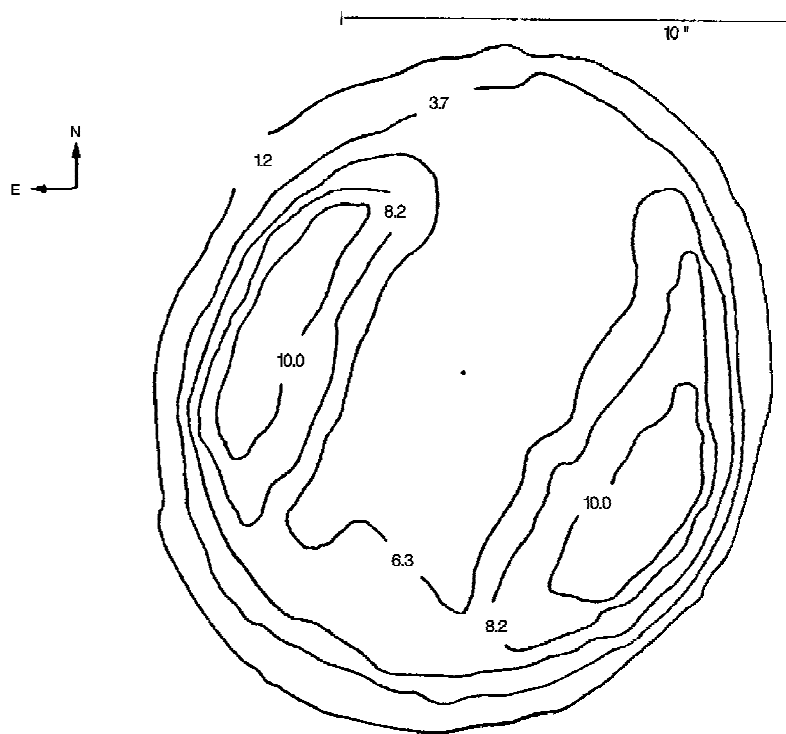


Figure 2.19. H β contour image of IC 418 (Louise *et al.* 1987). The central star has been subtracted from this image to reveal the nebular structure. A line drawn through the lobes passing through the center of the nebula has a PA of 68°.

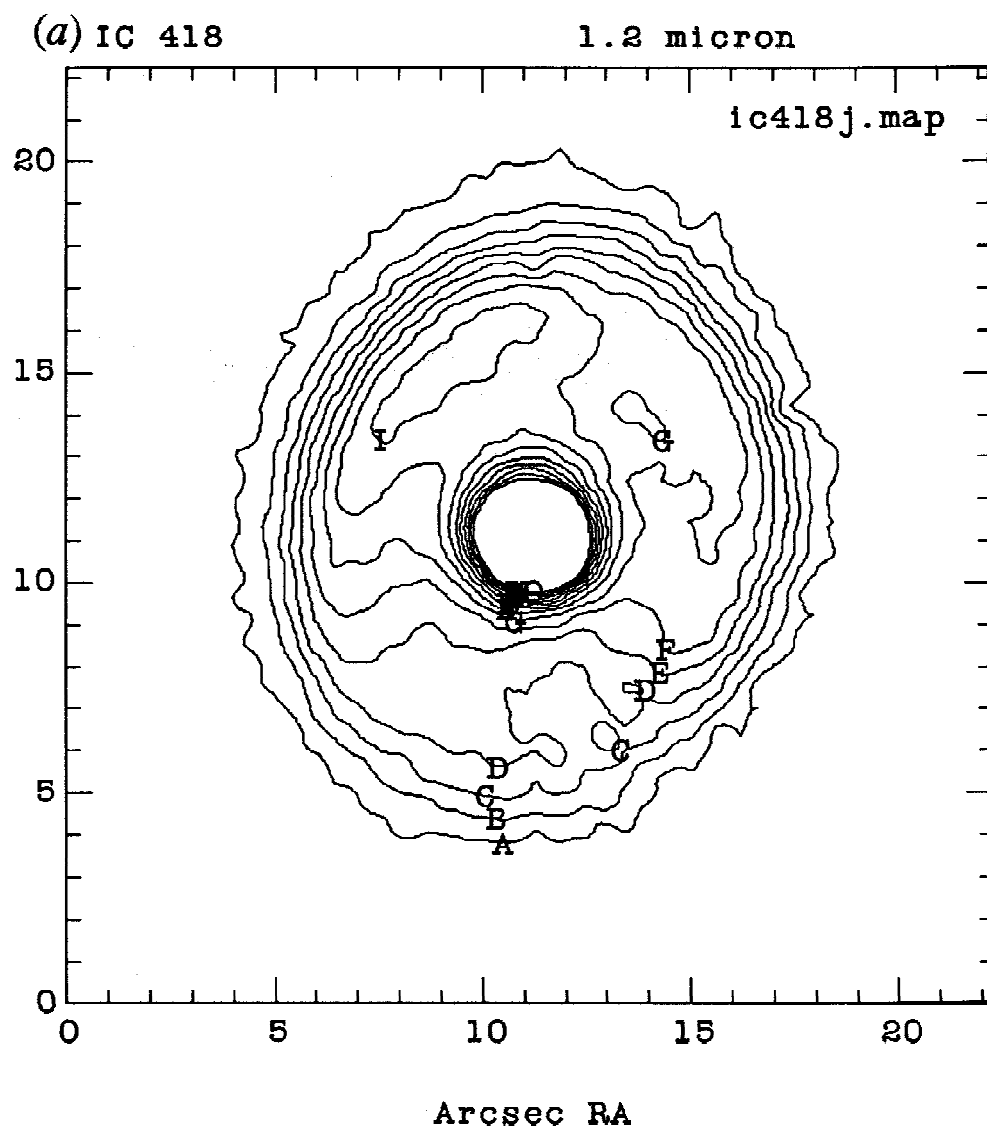


Figure 2.20. Calibrated contour images of IC 418 at J, H, and K. There are fifteen levels displayed with a constant spacing between them. The spacing has been chosen to display the nebula structure, so the levels cut off before the peak of the central star is reached. The position angle (PA) of the lobes given for each image is the angle E of N of a line drawn through the peak of the lobes, passing through the center of the nebula.

2.20a. J image, contour level spacing of $.75 \text{ mJy/arcsec}^2$, with the lowest level $.75 \text{ mJy/arcsec}^2$. The PA of the lobes is 25° .

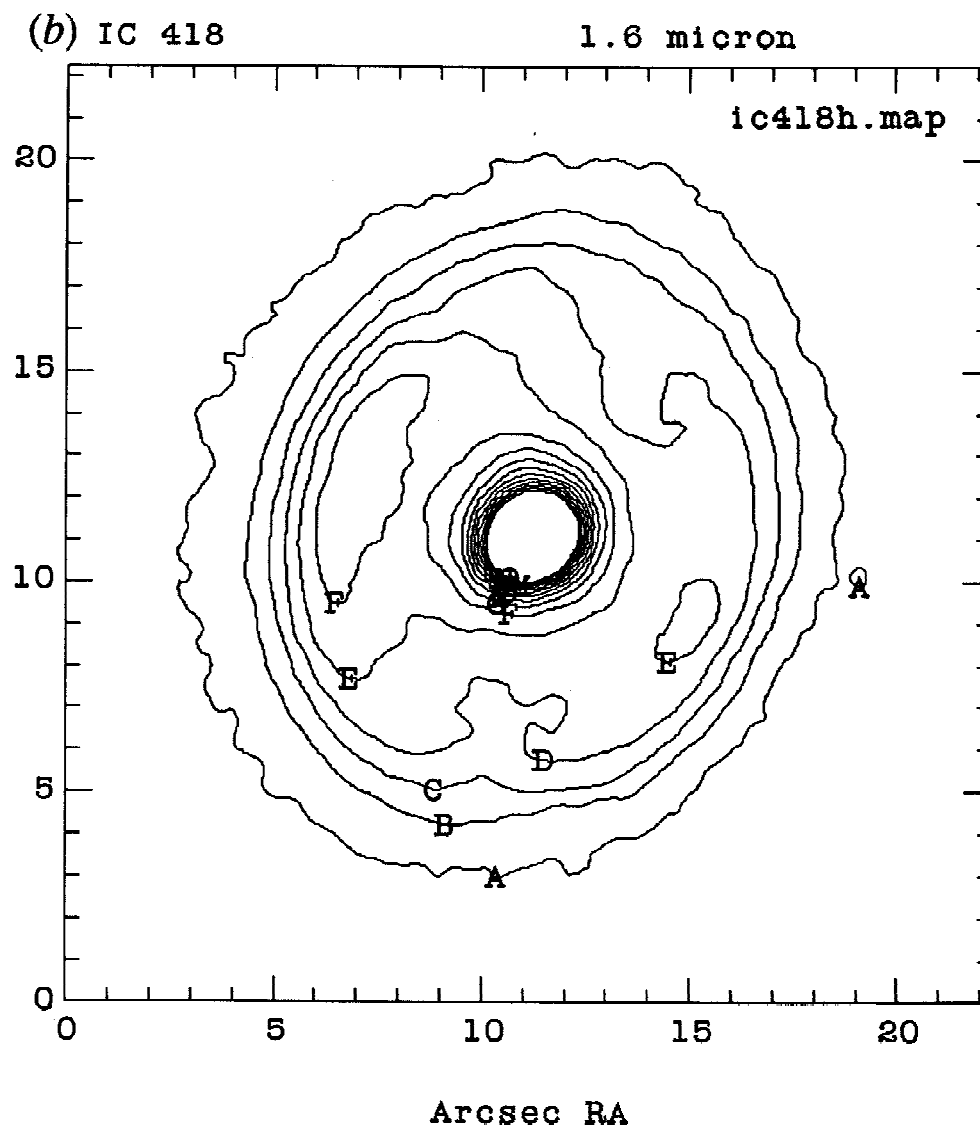


Figure 2.20b. H image, contour level spacing $.75 \text{ mJy/arcsec}^2$, lowest level $.75 \text{ mJy/arcsec}^2$. The PA of the lobes is 70° .

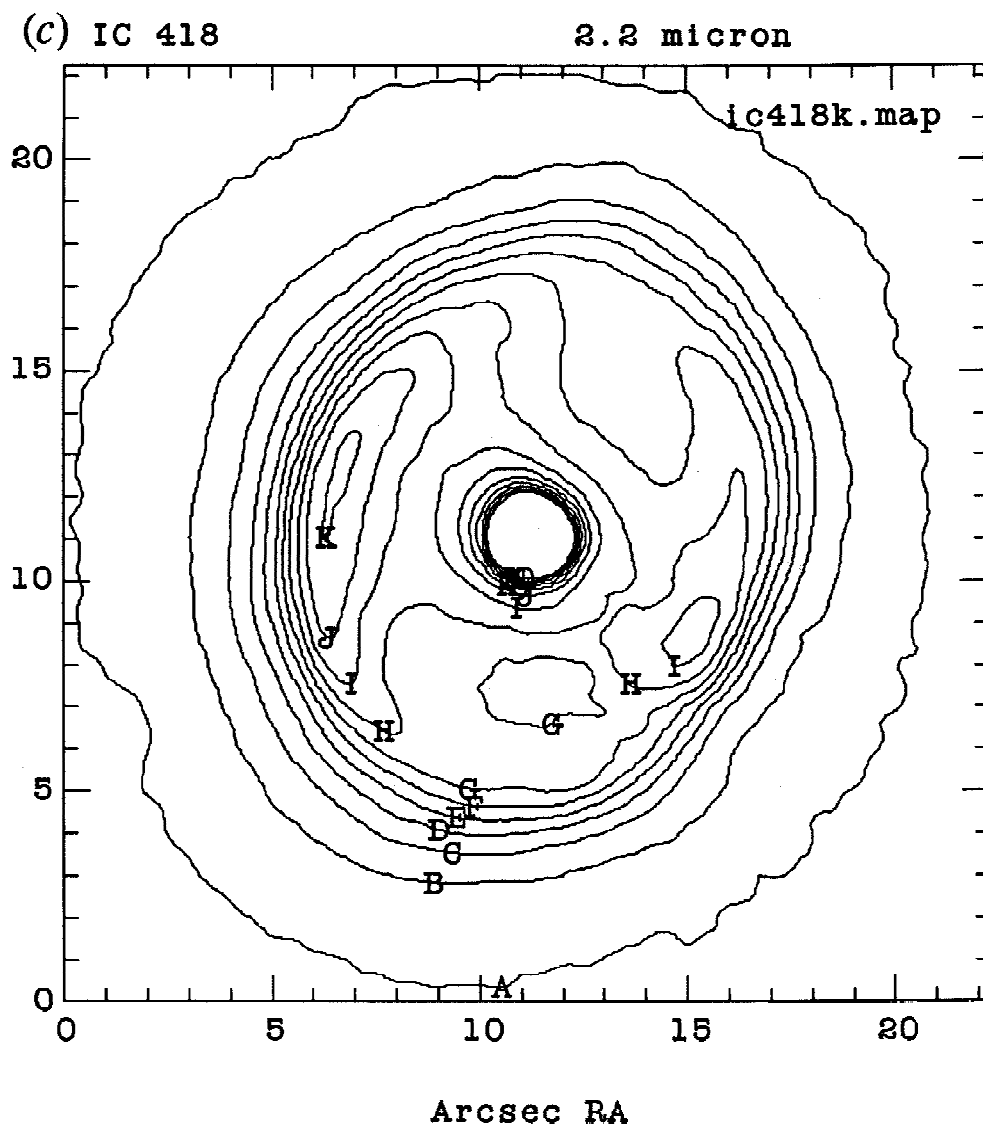


Figure 2.20c. K image, contour level spacing $.75 \text{ mJy/arcsec}^2$, lowest level $.75 \text{ mJy/arcsec}^2$. The PA of the lobes is 76° .

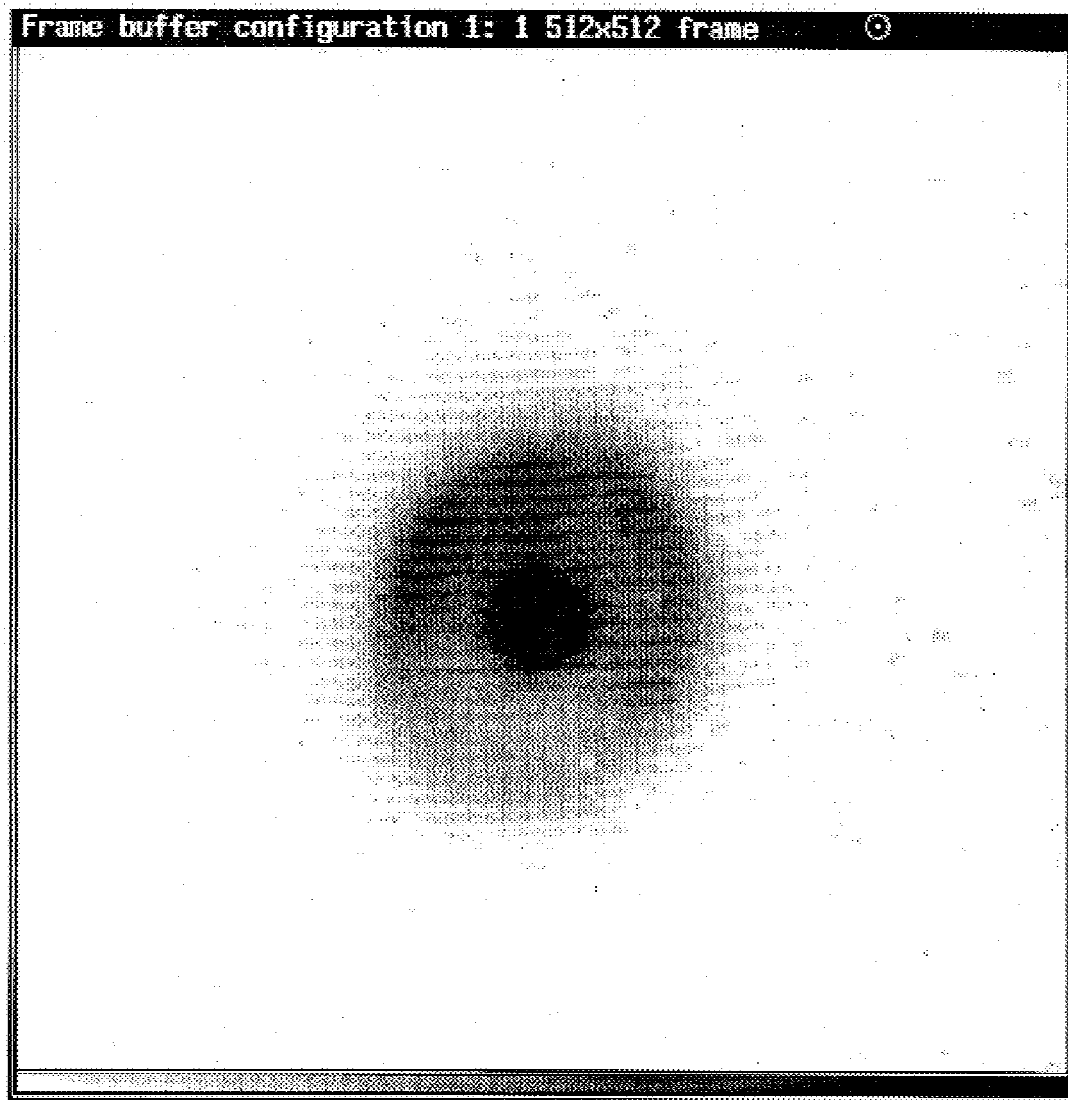
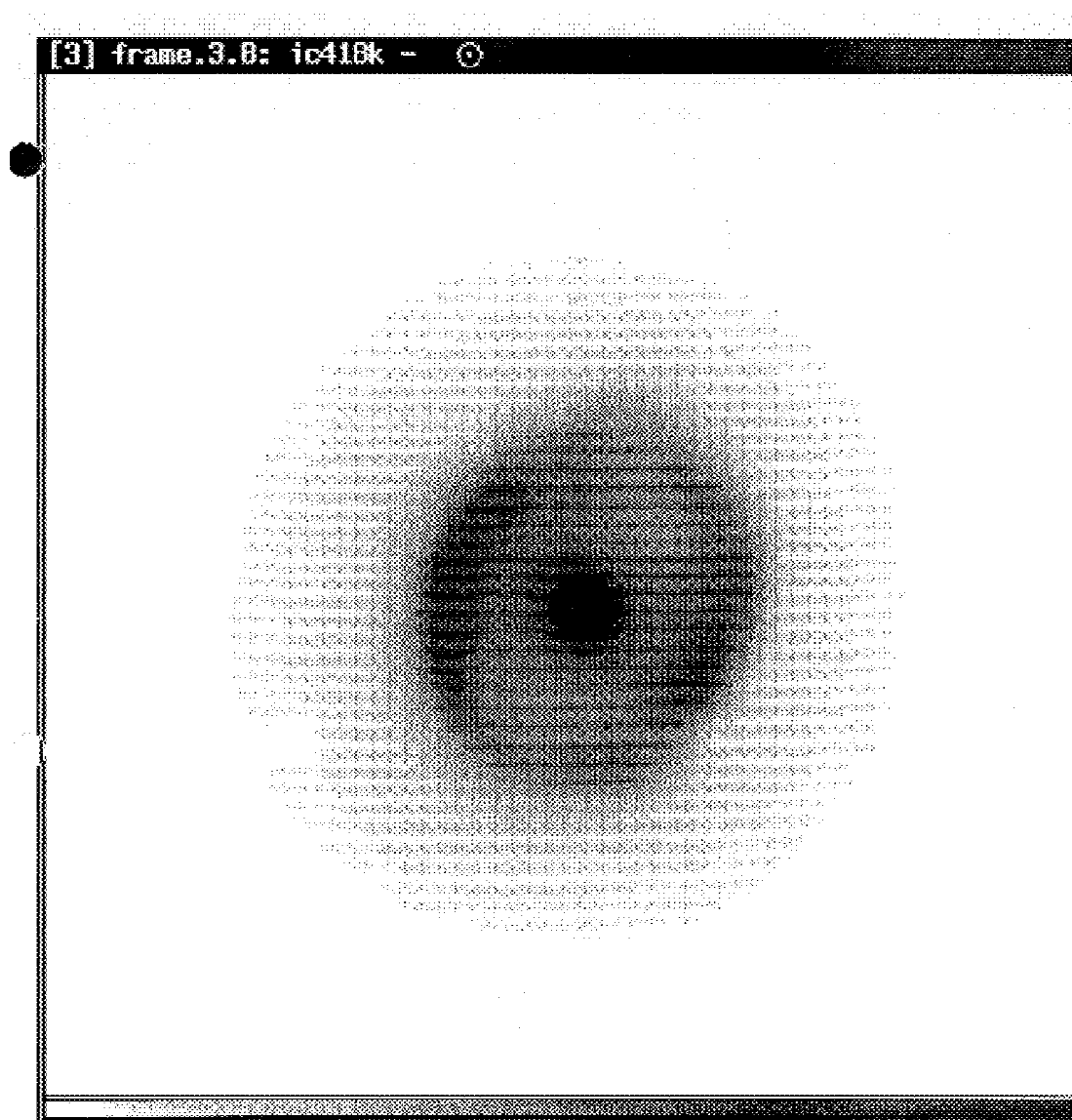


Figure 2.21. Grayscale images of IC 418. The gray levels have been selected in each image to show the nebular structure, saturating the central star.
2.21a. IC 418 J grayscale image. The main lobe appears as a dark condensation on the NE portion of the ring. This lobe extends to a point directly N of the central star.



2.21b. IC 418 grayscale image at K. The two lobes are visible in the ring, primarily to the E and W of the central star. The halo is seen to extend beyond the nebula. The "hole" in the left side of the nebula in the outer gray level is due to a faint star in the off-source field.

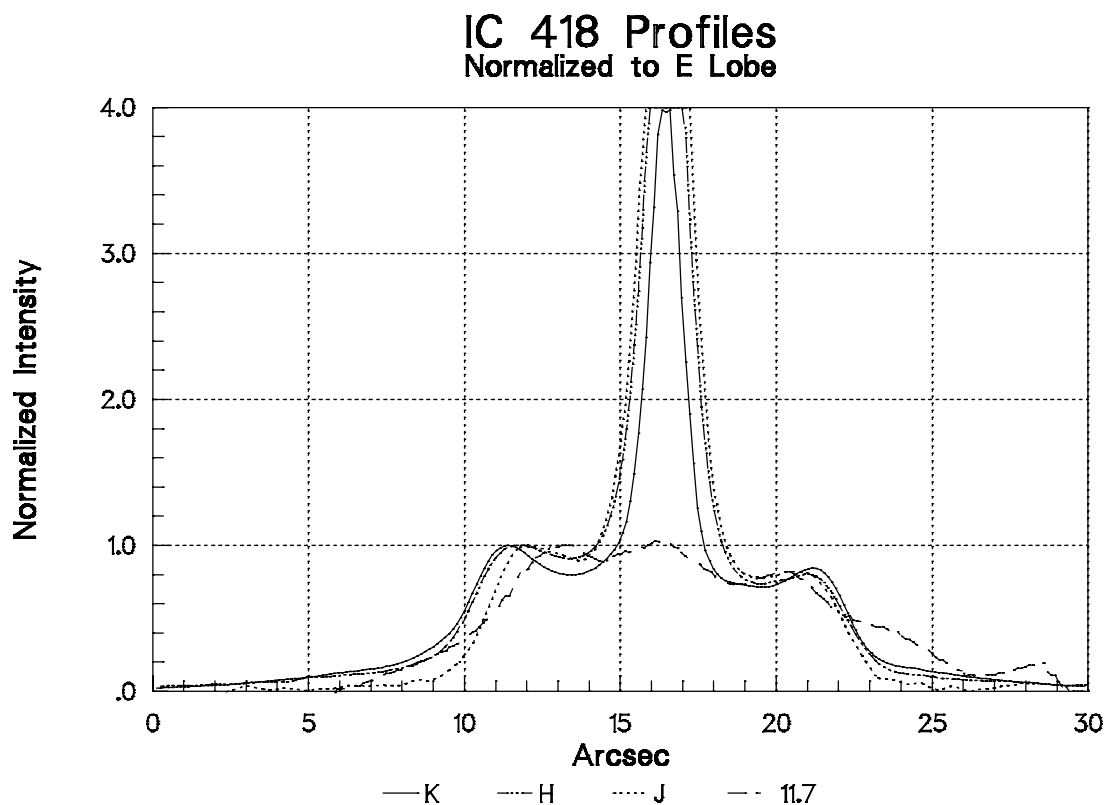


Figure 2.22. Profiles of IC 418 through the major lobes ($PA = 70^\circ$). The profiles have been normalized so that the NE lobe peak is 1.0, and the profiles aligned to the central star. Each wavelength is assigned a different line type, shown below the figure. The K image profile has the largest spatial extent, followed by the H, J, and $11.7 \mu m$ image profiles.

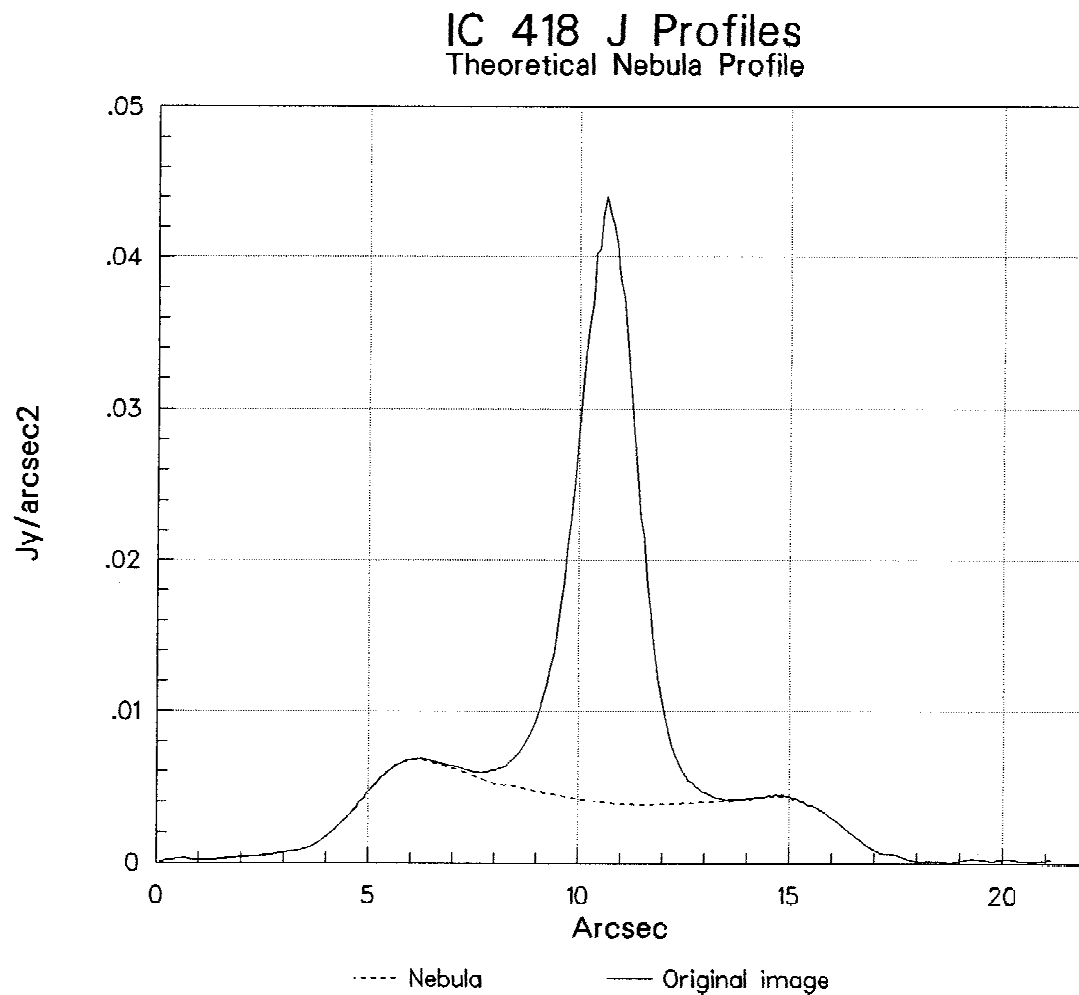


Figure 2.23. Theoretical nebula profile for IC 418, J image. The solid line is the profile from Figure 2.22. The dotted line below the standard star is the assumed profile of the flux from the outer nebular shell alone, without the emission from near the central star.

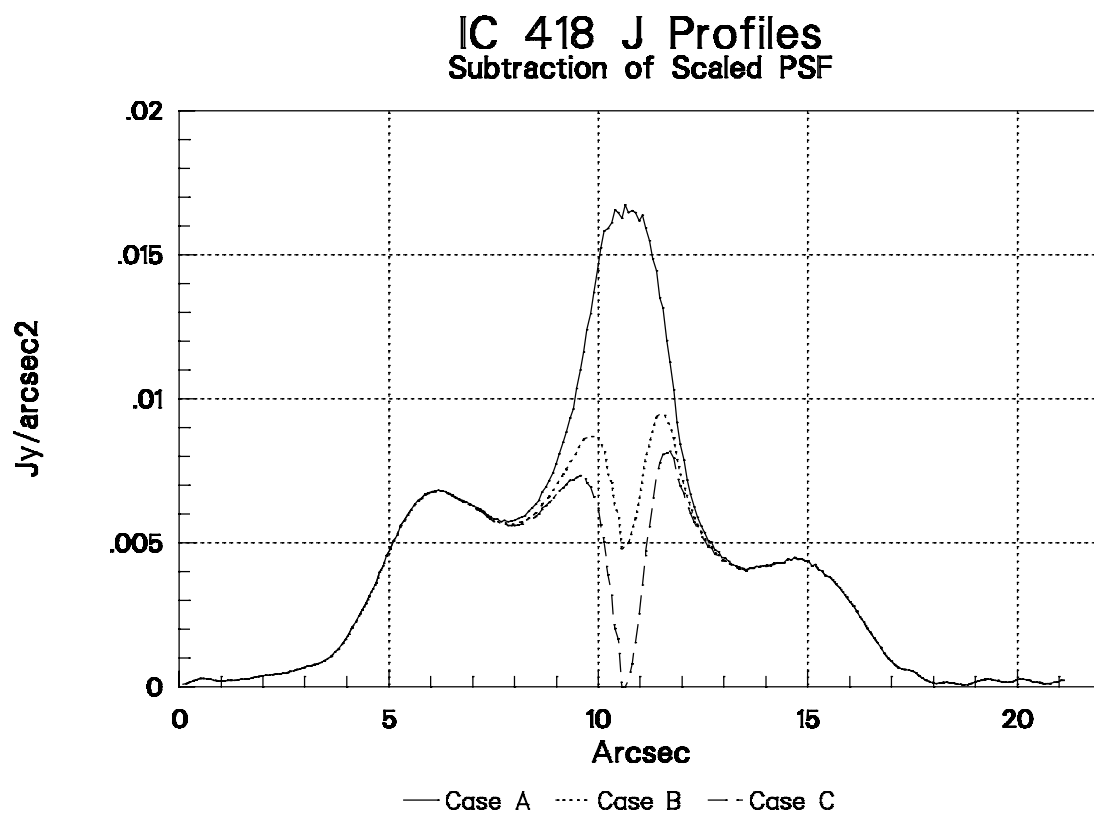


Figure 2.24. PSF-subtracted profiles of IC 418, showing different central star subtractions. In each figure, the solid line is the central star scaled so that there is no central hole. The dotted line is the central star subtracted to the level of the theoretical outer shell profile, as shown above in Figure 2.23. The dashed line is the peak of the star subtracted to the zero level.

2.24a. IC 418 J profiles.

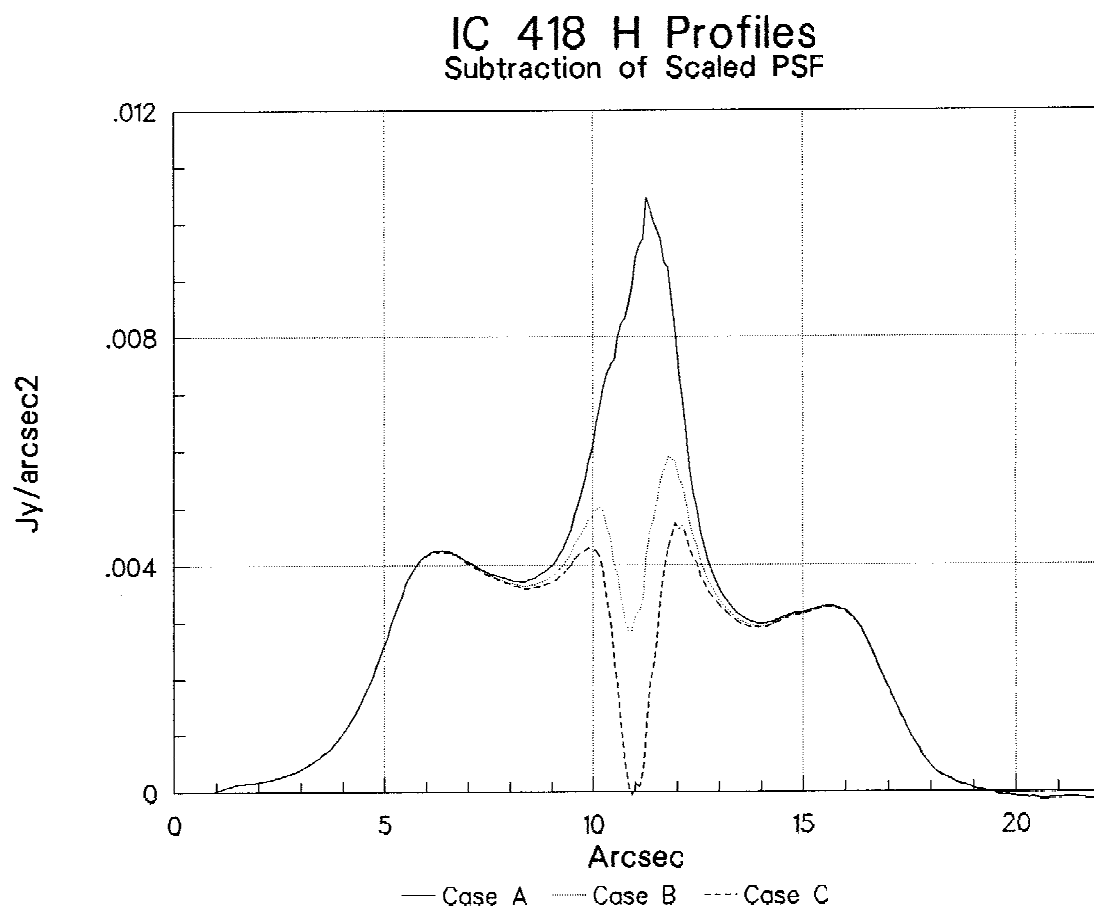


Figure 2.24b. IC 418 H profiles (see main caption to Figure 2.24).

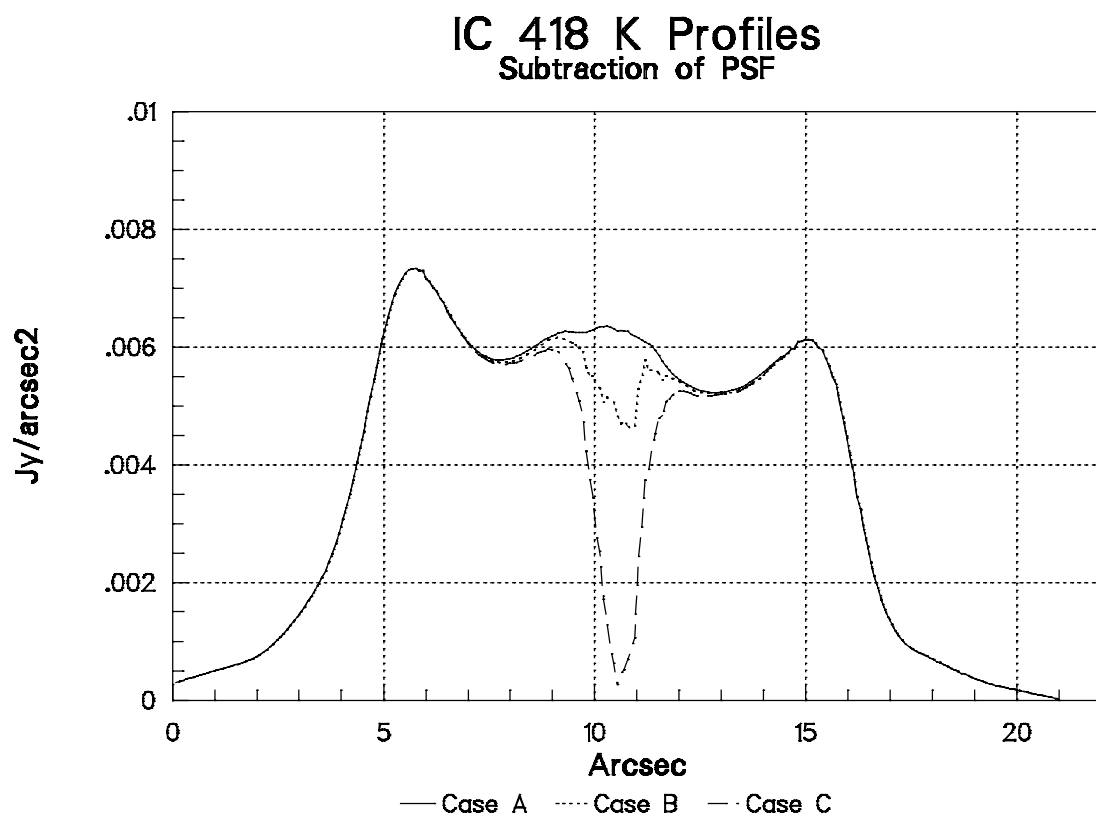


Figure 2.24c. IC 418 K profiles (see main caption to Figure 2.24).

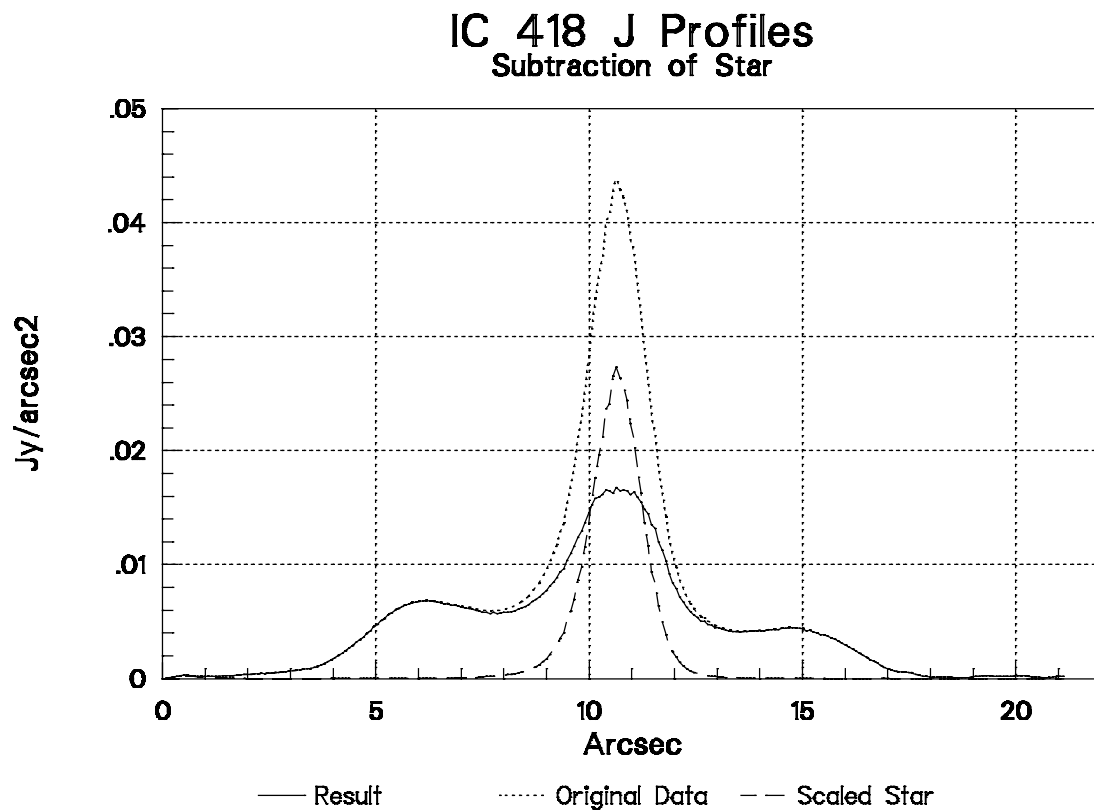


Figure 2.25. PSF-subtracted profiles of IC 418. These profiles show the original data (dotted line), the scaled standard star (dashed line), and the resulting profile when the star is subtracted (solid line). The solid line in this figure is the same as the solid line in Figure 2.24.

2.25a. IC 418 J PSF-subtracted profiles.

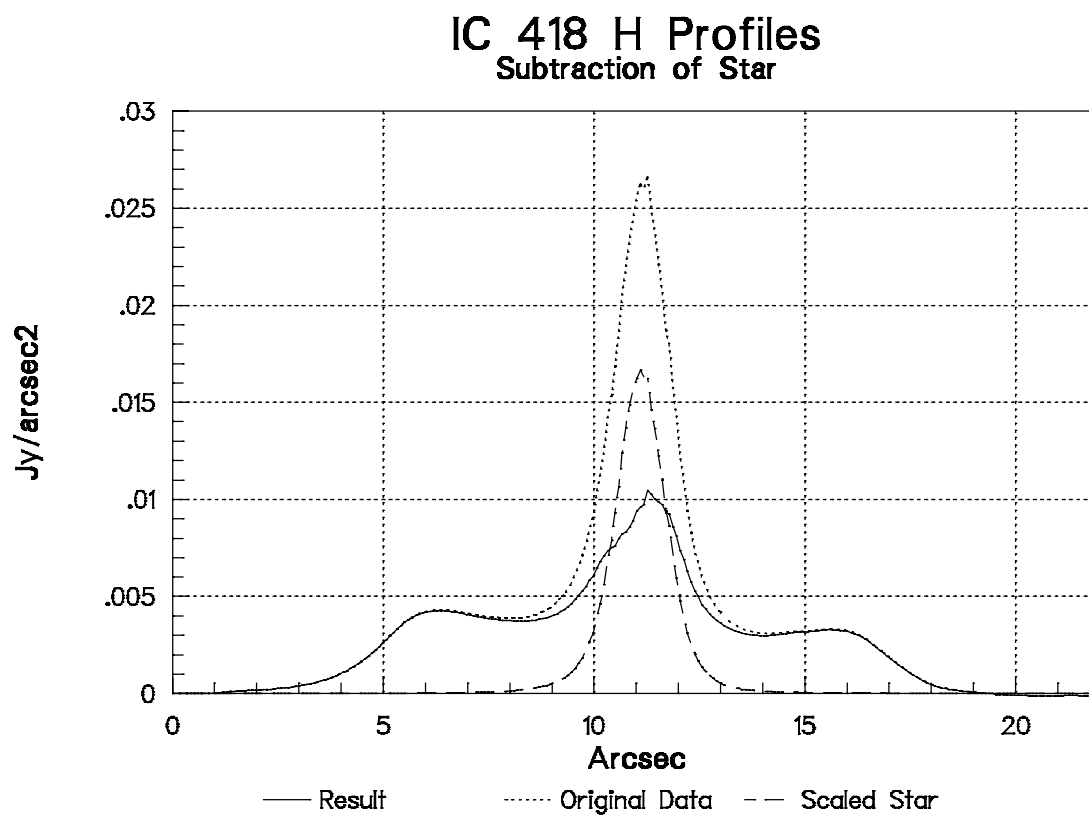


Figure 2.25b. IC 418 H PSF-subtracted profiles (see main caption of Figure 2.25).

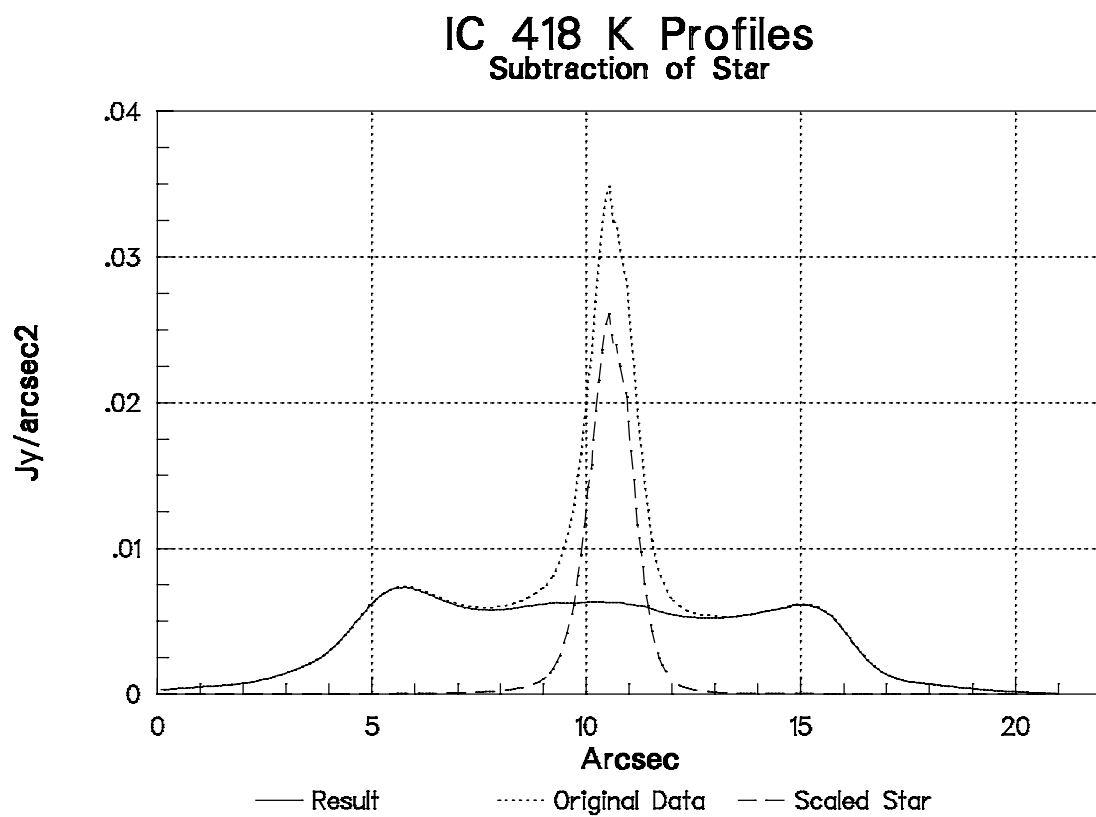


Figure 2.25c. IC 418 K PSF-subtracted profiles (see main caption to Figure 2.25).

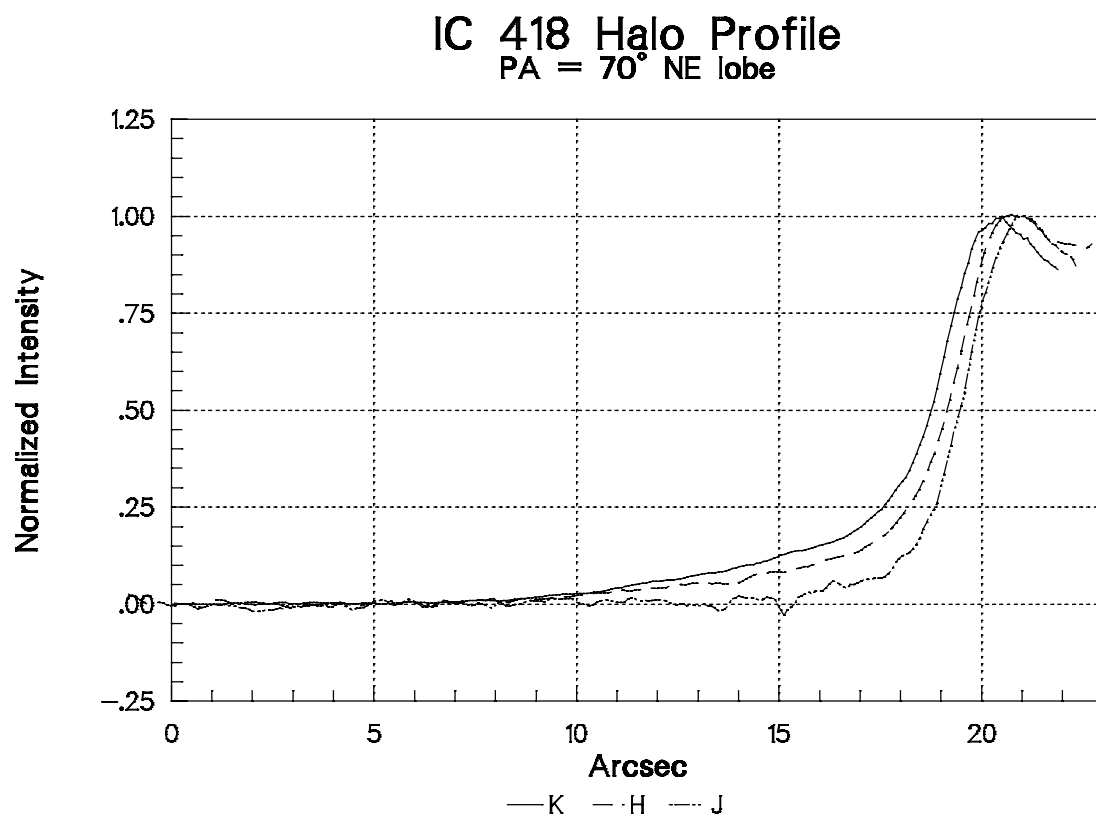


Figure 2.26. Profiles of IC 418 halo, in the same direction as previous profiles, extending further to the NE and including the NE lobe peak. The profiles have been aligned on the central star. The profiles show the halo emission in H and K, and the much weaker emission in the J profile beyond the nebular shell.

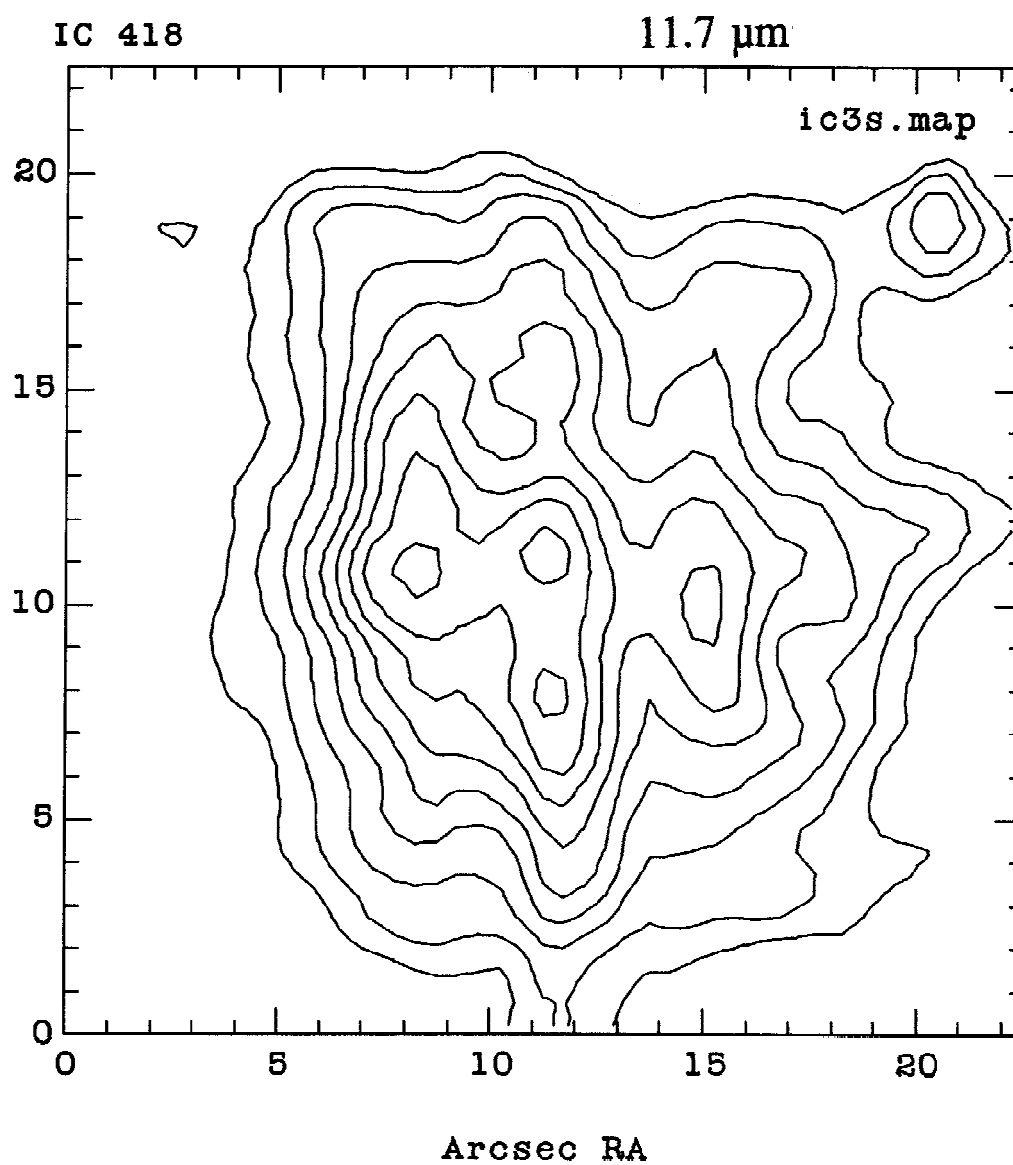


Figure 2.27. Contour image of IC 418 at 11.7 μm , from MIRAC observations. The contour levels are evenly spaced at 140 mJy/arcsec² per level, starting at 100 mJy/arcsec².

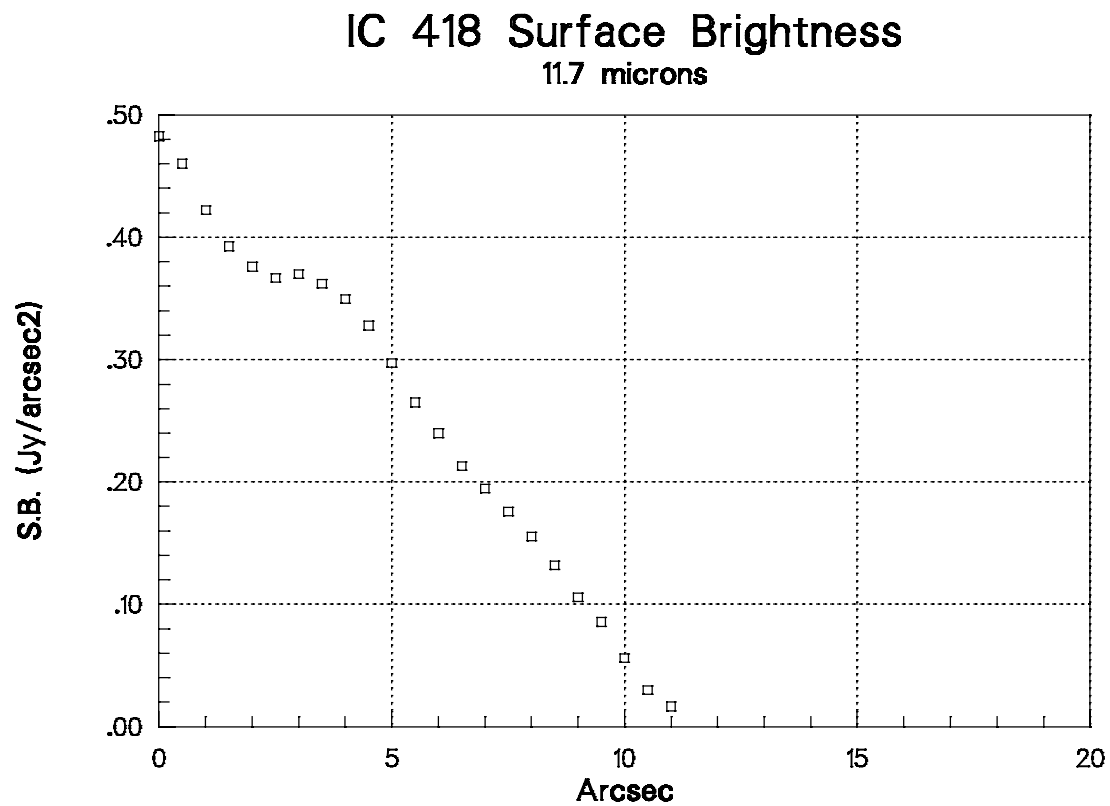


Figure 2.28. Observed surface brightness of IC 418 at 11.7 μm , determined from the image in Figure 2.27. The surface brightness in Jy/arcsec^2 is plotted as a function of distance from the center of the nebula in arcsec.

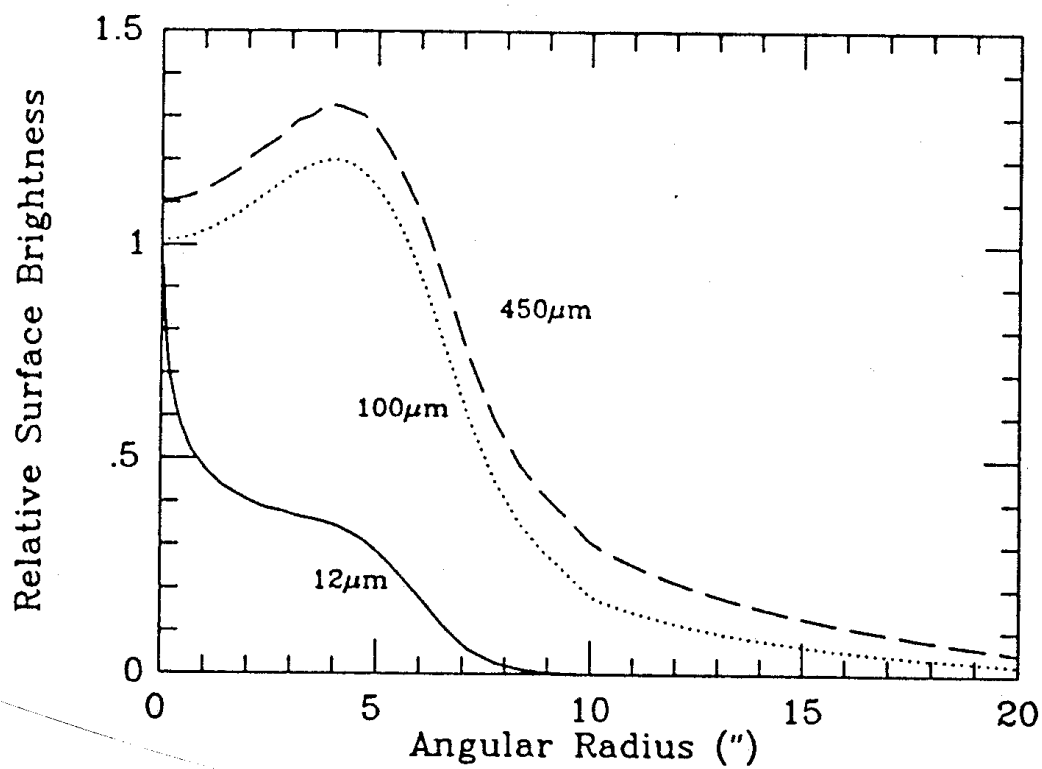


Figure 2.29. Surface brightness of IC 418, from Hoare (1990). This plot is from the amorphous carbon model of IC 418 that includes a neutral halo.

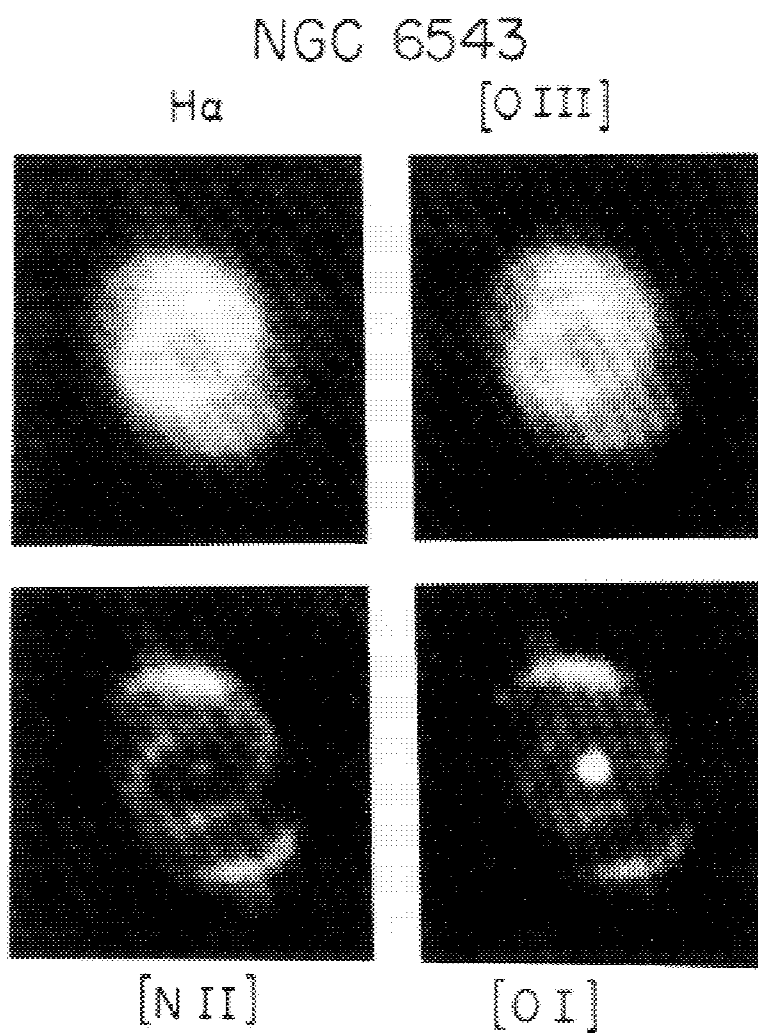


Figure 2.30. Images of the planetary nebula NGC 6543, from Balick and Preston (1987).

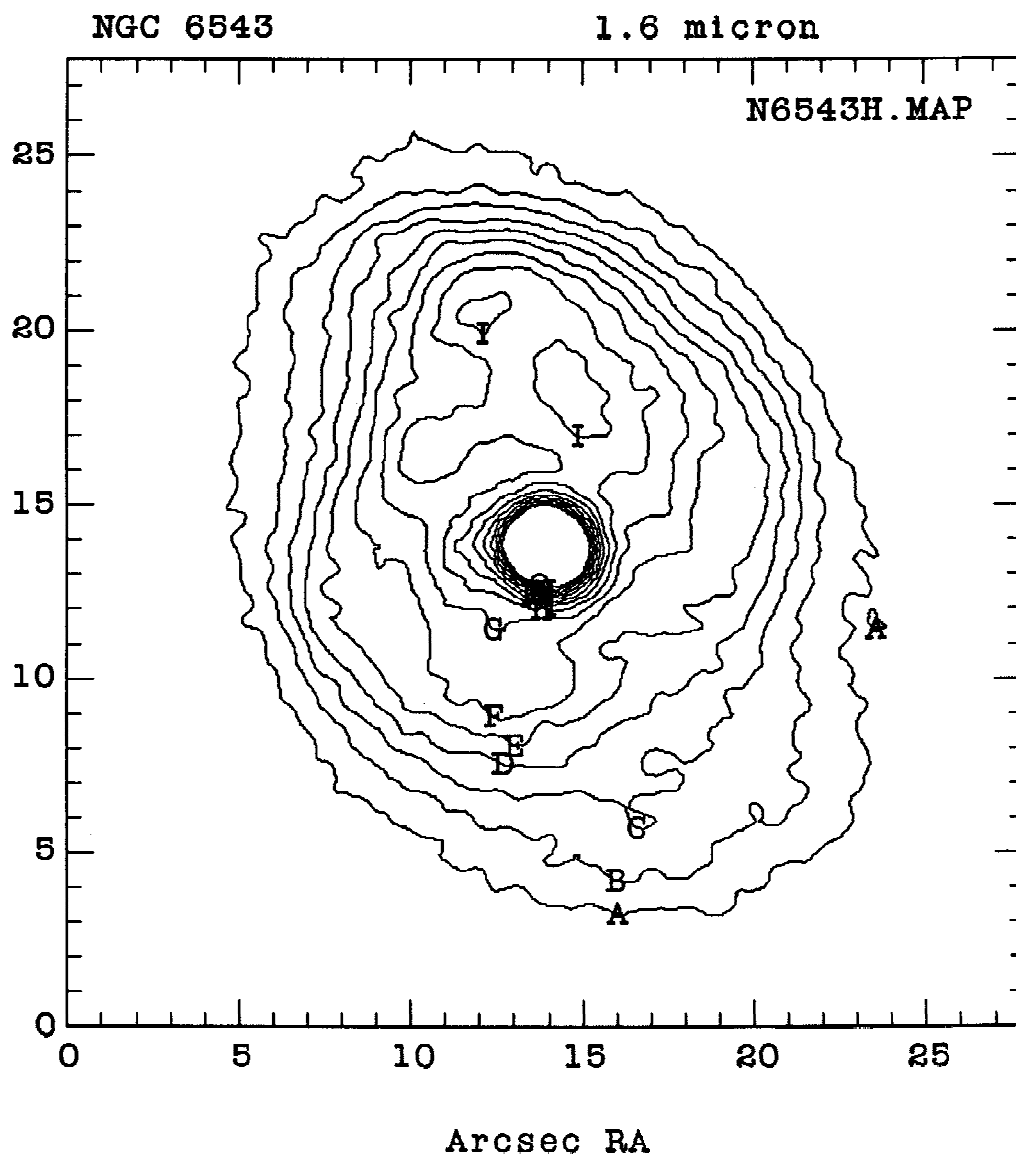


Figure 2.31. Contour images of the planetary nebula NGC 6543. The contour level spacing is at even intervals of $.15 \text{ mJy/arcsec}^2$, with a minimum level of $.15 \text{ mJy/arcsec}^2$.

2.31a. NGC 6543 H contour image.

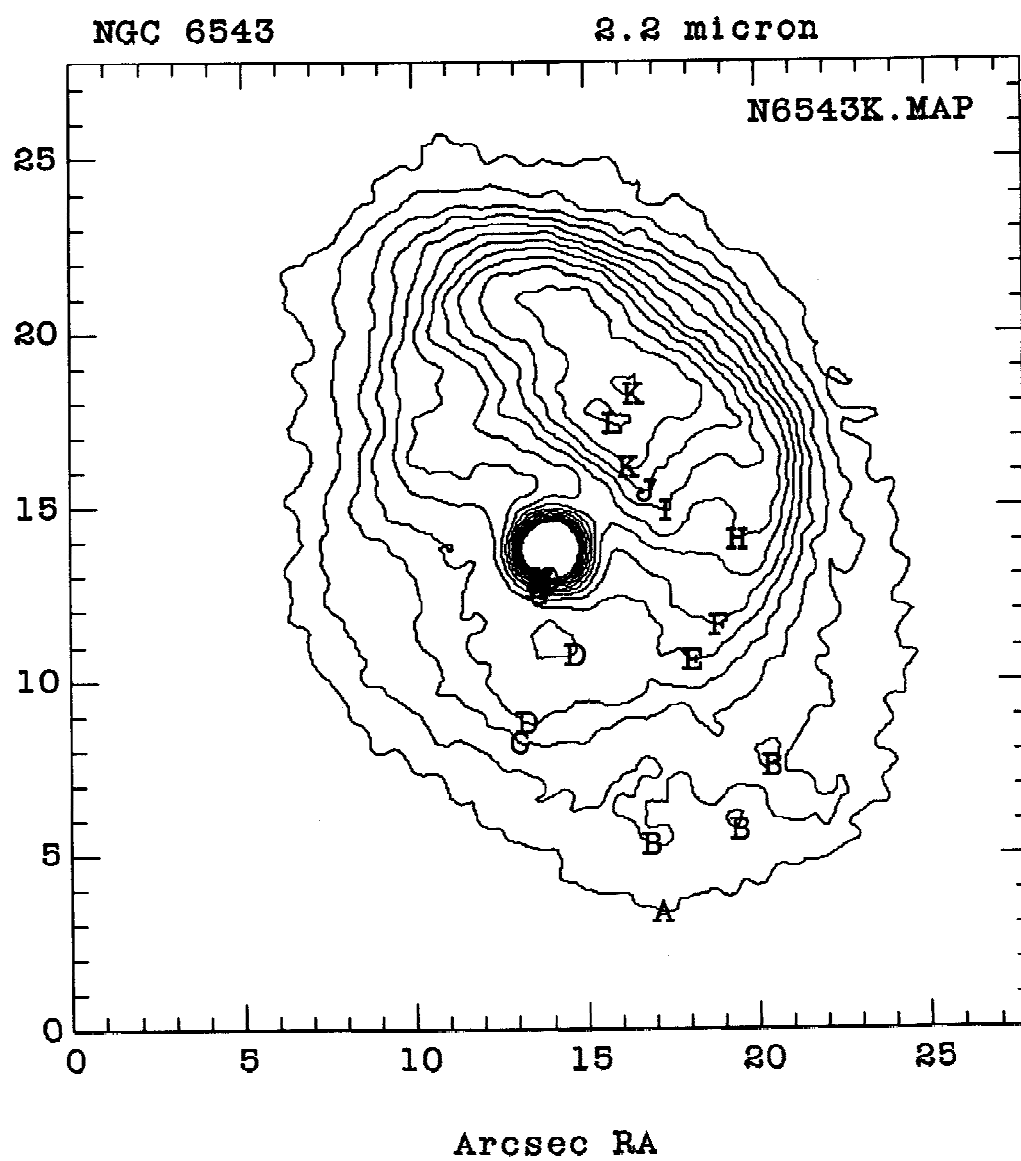


Figure 2.31b. NGC 6543 K contour image (see main caption of Figure 2.31).

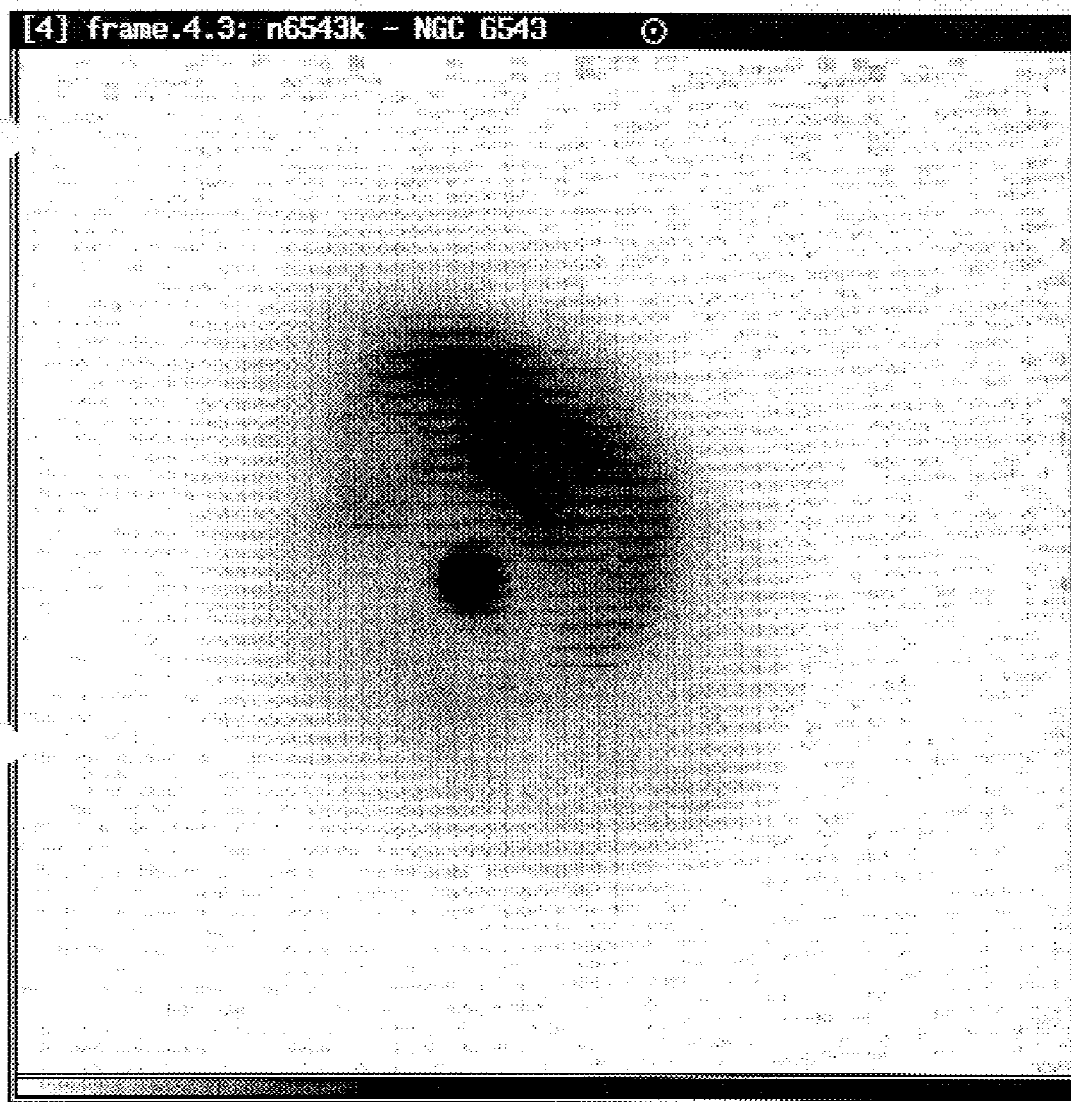


Figure 2.32. Grayscale image of NGC 6543 in the K filter. The gray levels have been set to saturate the bright lobe, so that the faint structure is visible. The faint halo enveloping the bright inner shells is also visible.

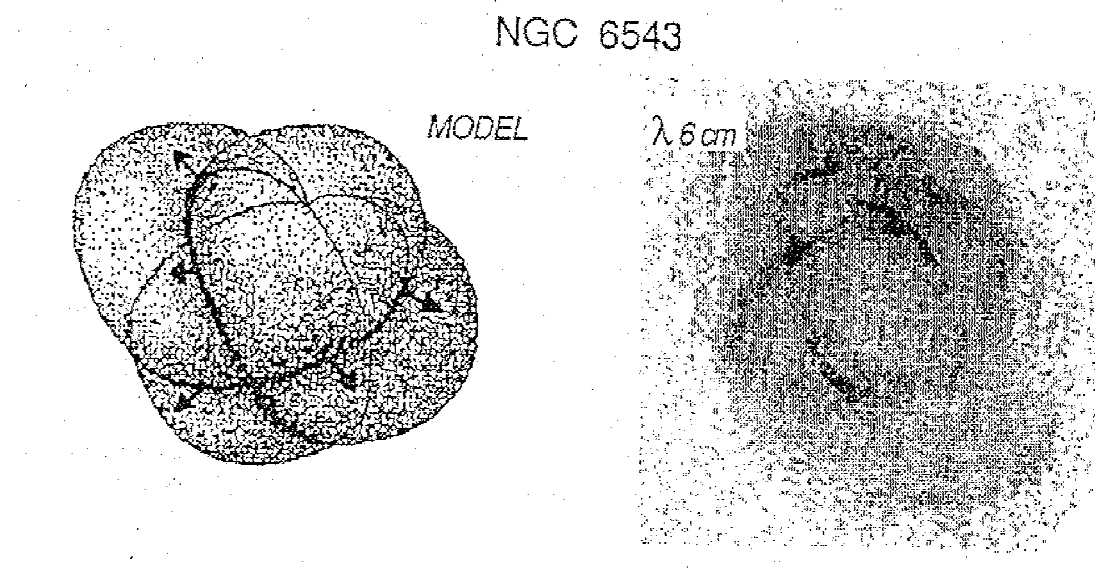


Figure 2.33. Model of the structure of NGC 6543, from Balick and Preston (1987). The model consists of four separate lobes, at the inclination angle shown. The observed morphology results from an intensity enhancement along the points where the lobes intersect. The 6 cm image of NGC 6543 is shown for comparison.

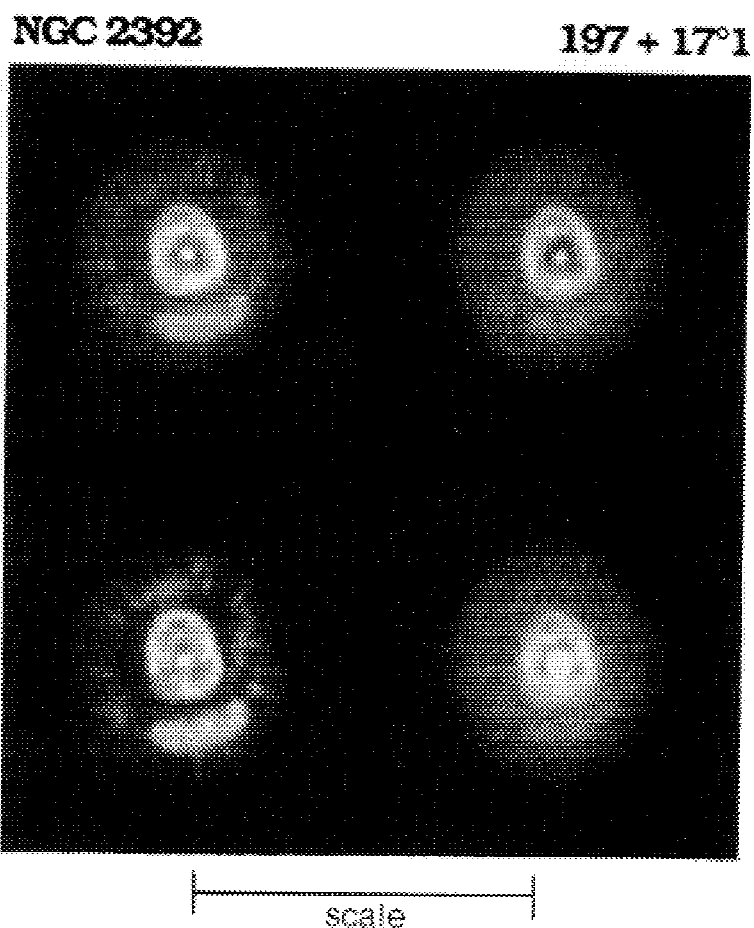


Figure 2.34. CCD images of NGC 2392, from Balick (1987). The scale bar shown has a length of 75". The images were taken at the wavelengths of the following lines, in the order clockwise from the upper left: H α , [OIII], He II, and [NII].

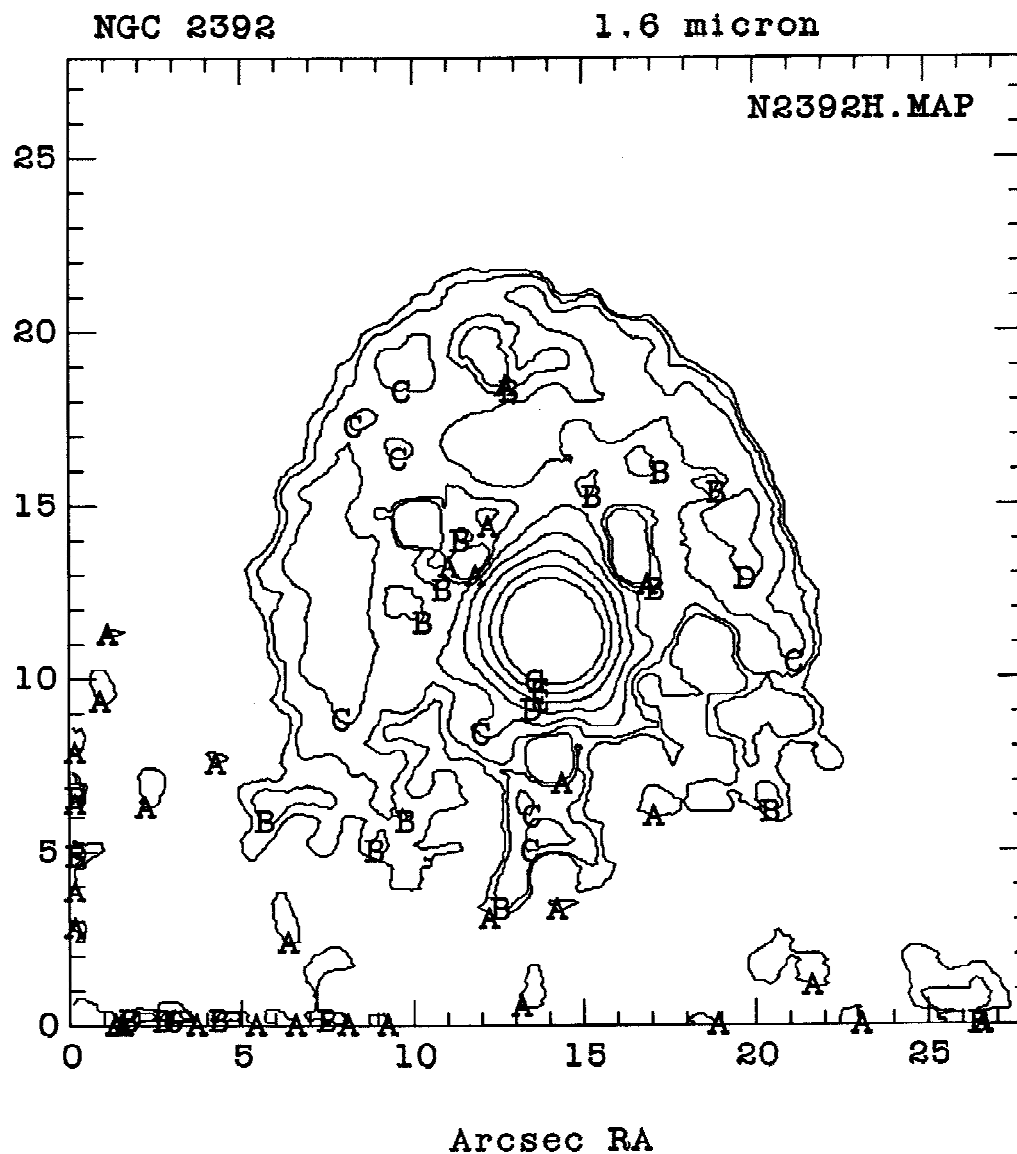


Figure 2.35. Contour images of NGC 2392. The contour levels are logarithmically spaced, with the levels as given for each image. The contour levels do not show the peak of the central star.

2.35a. NGC 2392 H contour image. The contour levels are (in mJy): A = .07, B = .102, C = .150, D = .218, E = .320, F = .468, G = .684.

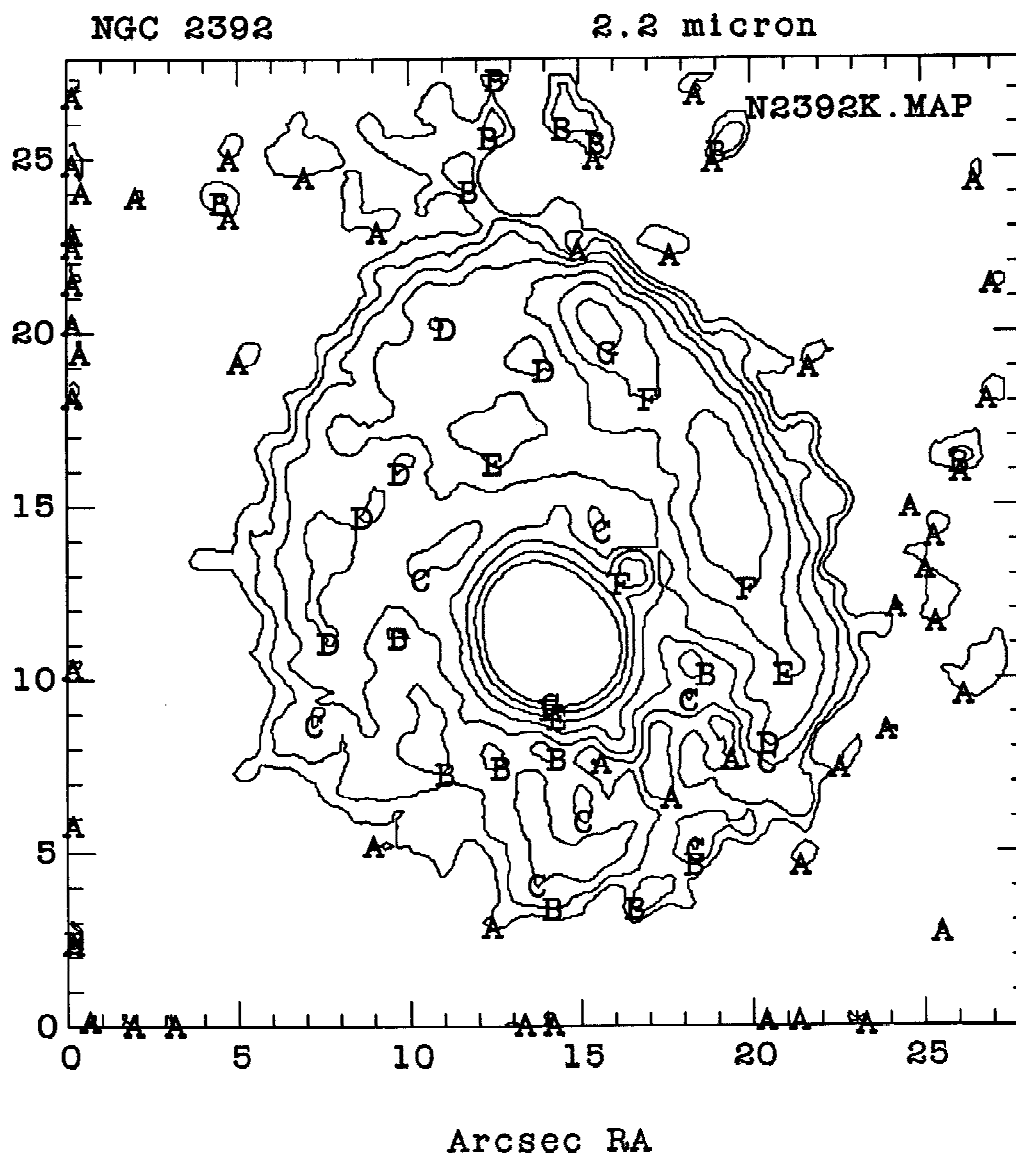


Figure 2.35b. NGC 2392 K contour image. The contour levels are (in mJy): A = .07, B = .102, C = .150, D = .218, E = .320, F = .468, G = .684.



Figure 2.36. Grayscale images of NGC 2392. The bar shown at the bottom of the figure has a length of 10". The gray levels have been chosen to show the nebular structure, so the central star is saturated in this image.

2.36a. NGC 2392 H grayscale image.

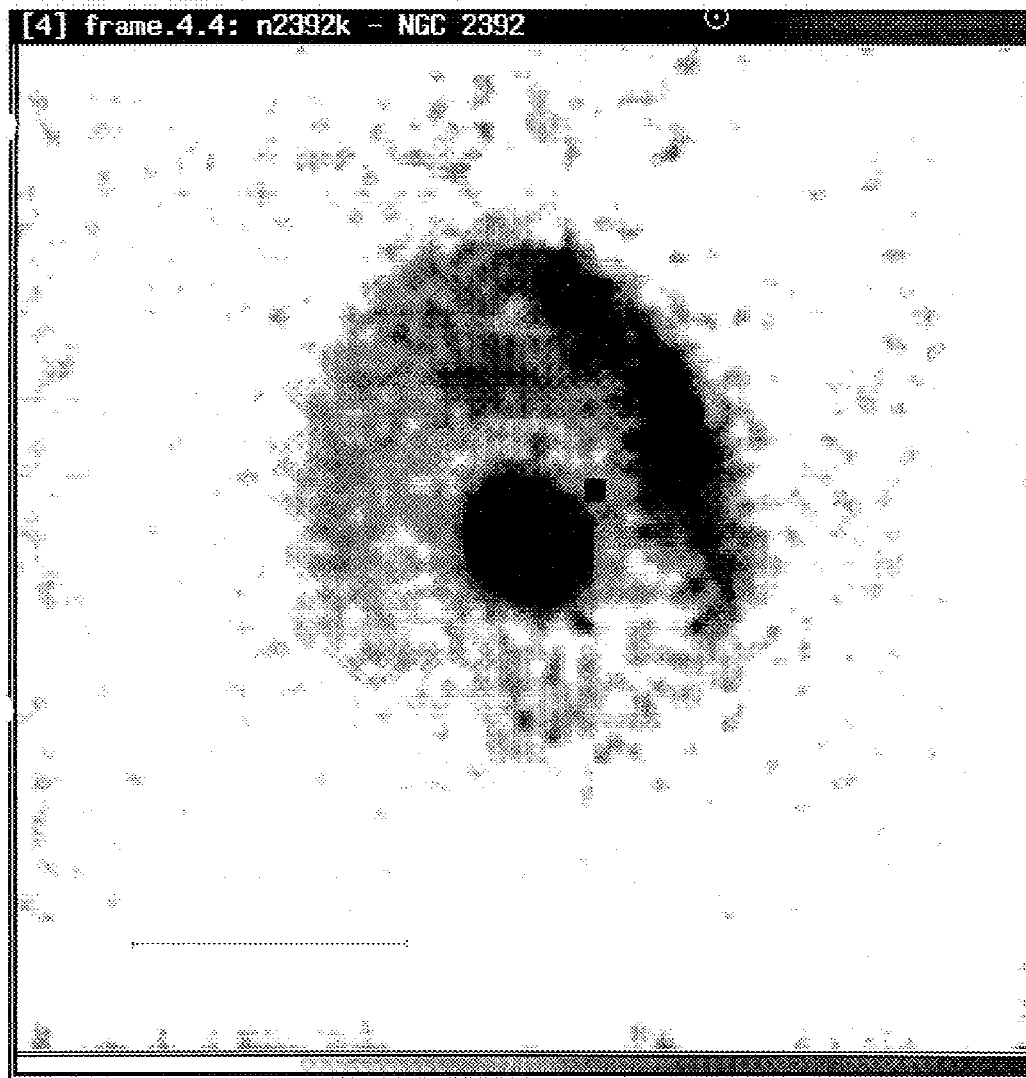


Figure 2.36b. NGC 2392 K grayscale image (see main caption to Figure 2.36).



Figure 2.37. Optical image of AFGL 2688, from Ney *et. al* (1975).

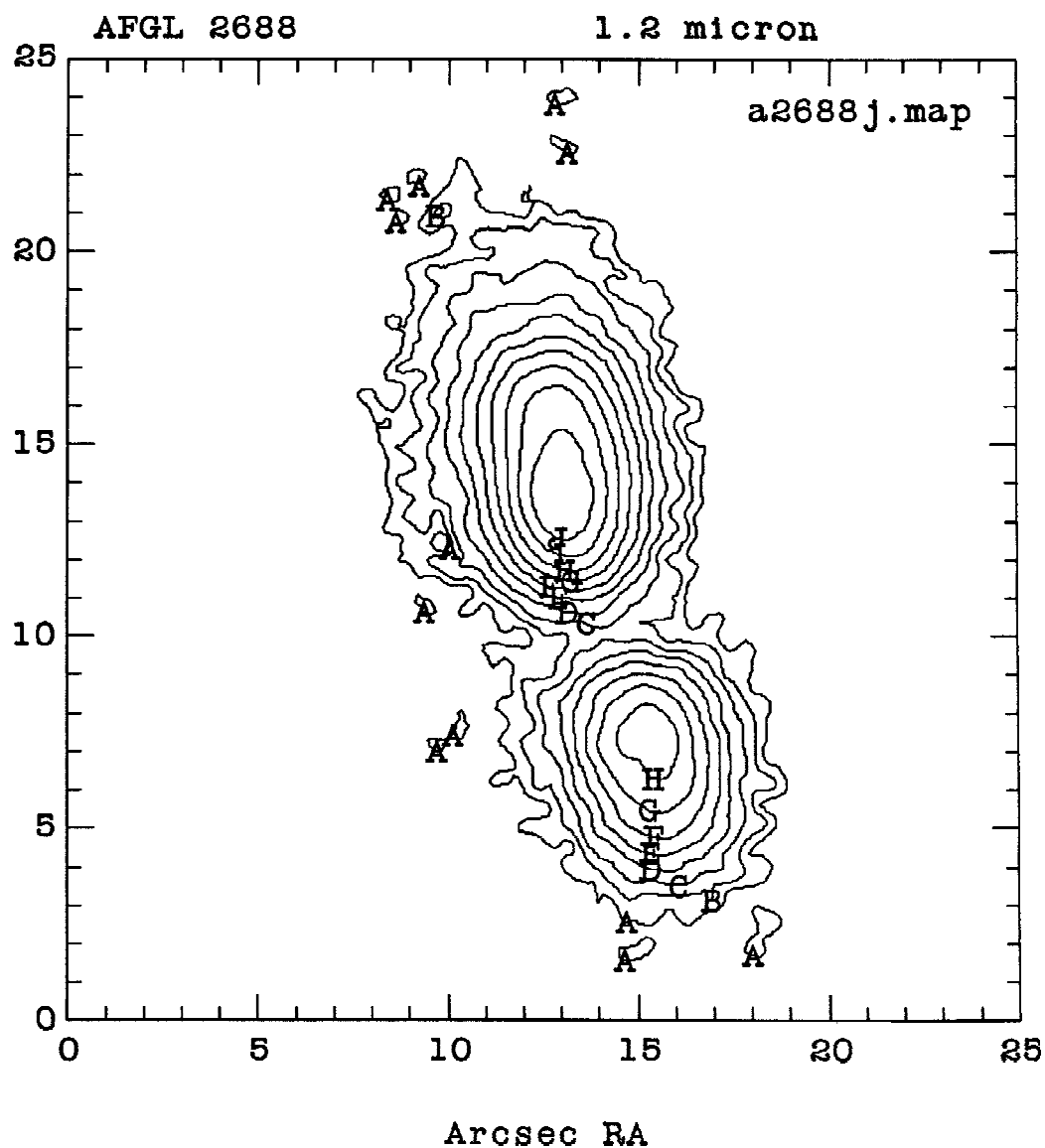


Figure 2.38. Contour images of AFGL 2688. Contour levels are logarithmically spaced, at the levels given for each image.

2.38a. AFGL 2688 J contour image. Contour levels are set to the following values, in mJy/arcsec²: A = .3, B = .447, C = .668, D = .998, E = 1.49, F = 2.22, G = 3.32, H = 4.95, I = 7.40, J = 11.0.

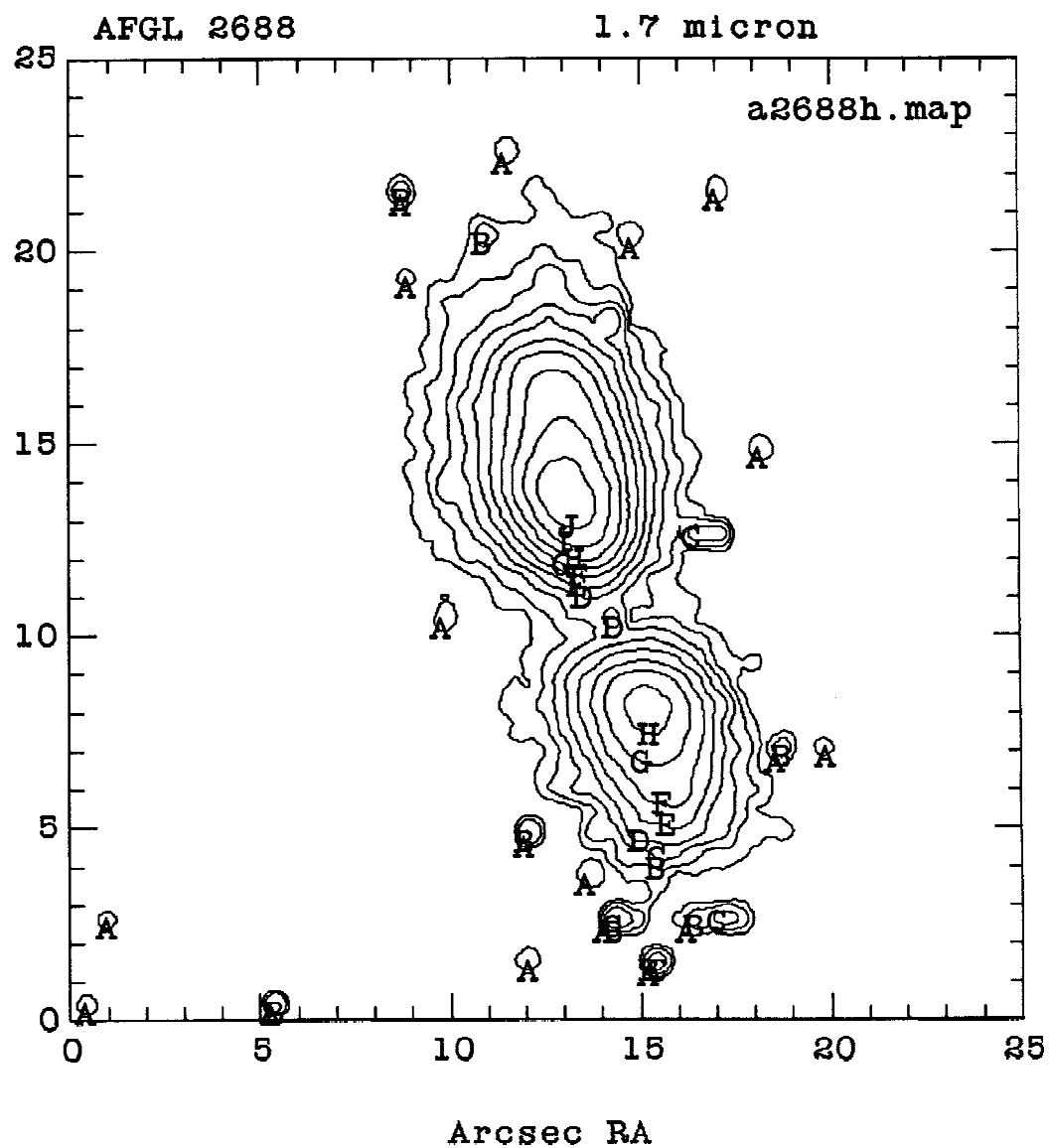


Figure 2.38b. AFGL 2688 H contour image. Contour levels are set to the following values, in mJy/arcsec²: A = .4, B = .594, C = .883, D = 1.31, E = 1.95, F = 2.90, G = 4.30, H = 6.39, I = 9.50, J = 14.1.

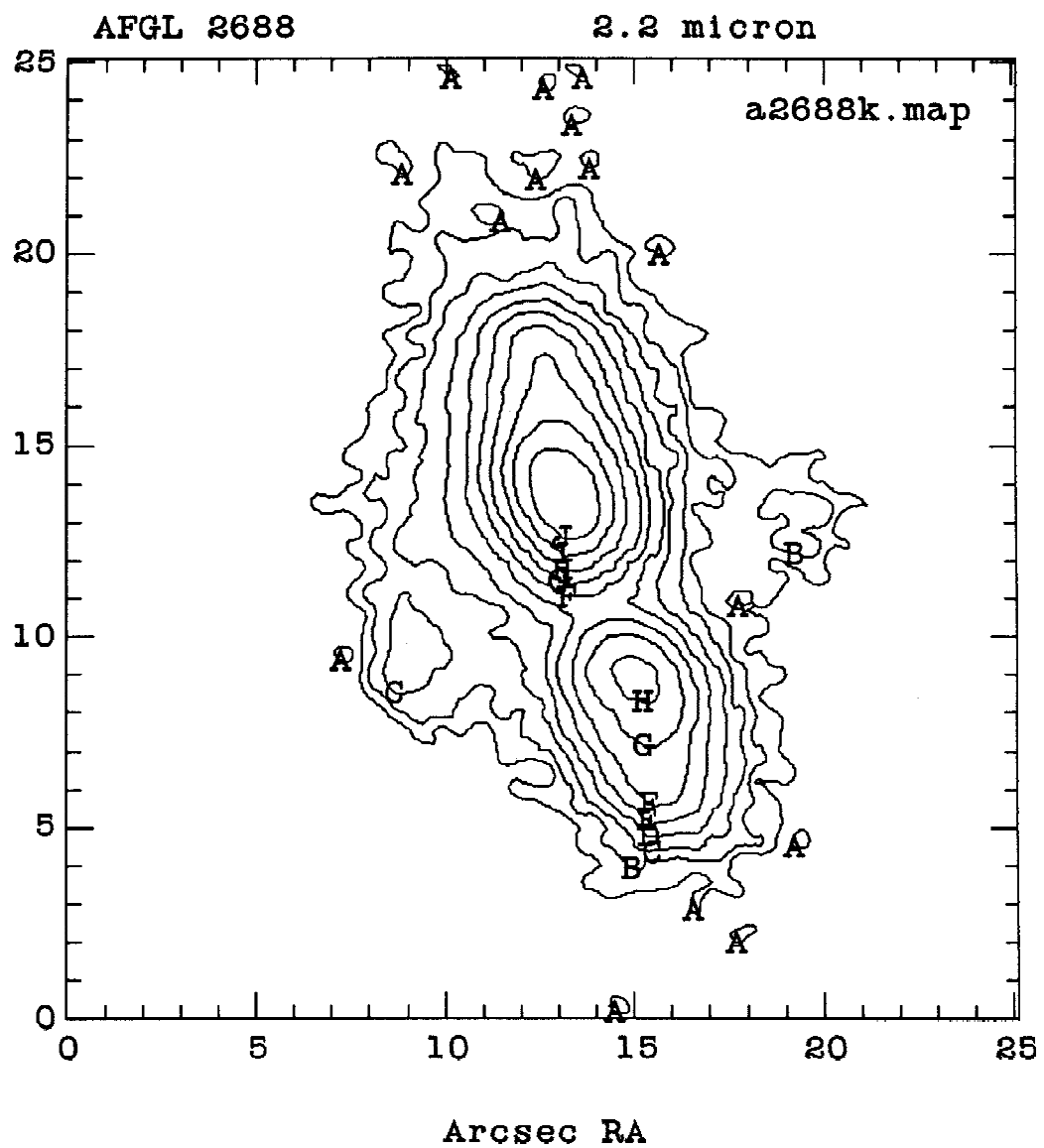


Figure 2.38c. AFGL 2688 K contour image. Contour levels are set to the following values, in mJy/arcsec²: A = .2, B = .324, C = .523, D = .847, E = 1.37, F = 2.22, G = 3.58, H = 5.80, I = 9.39, J = 15.2.

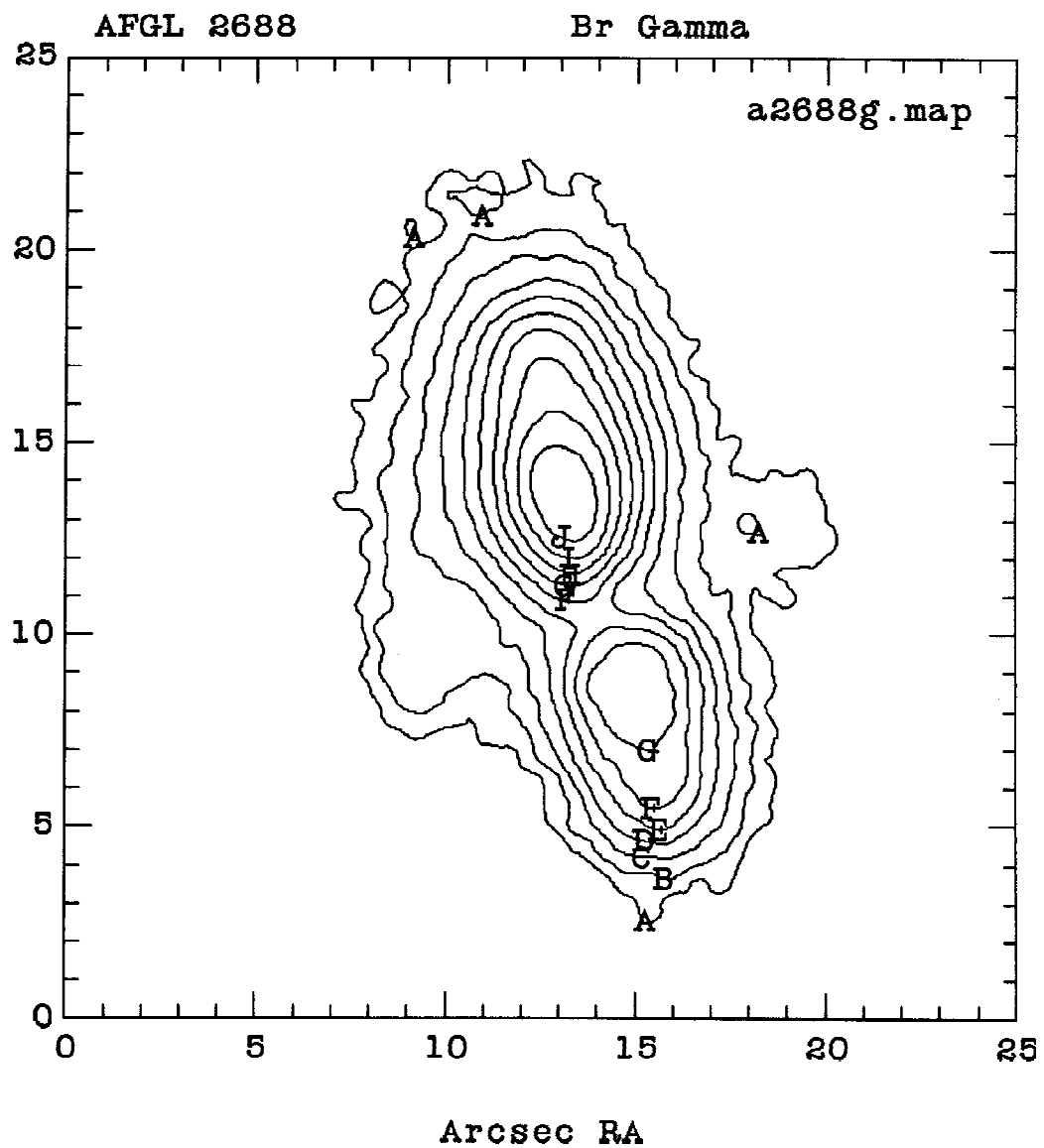


Figure 2.38d. AFGL 2688 Br γ contour image. Contour levels are set to the following values, in mJy/arcsec². A = .2, B = .324, C = .523, D = .847, E = 1.37, F = 2.22, G = 3.58, H = 5.80, I = 9.39, J = 15.2.

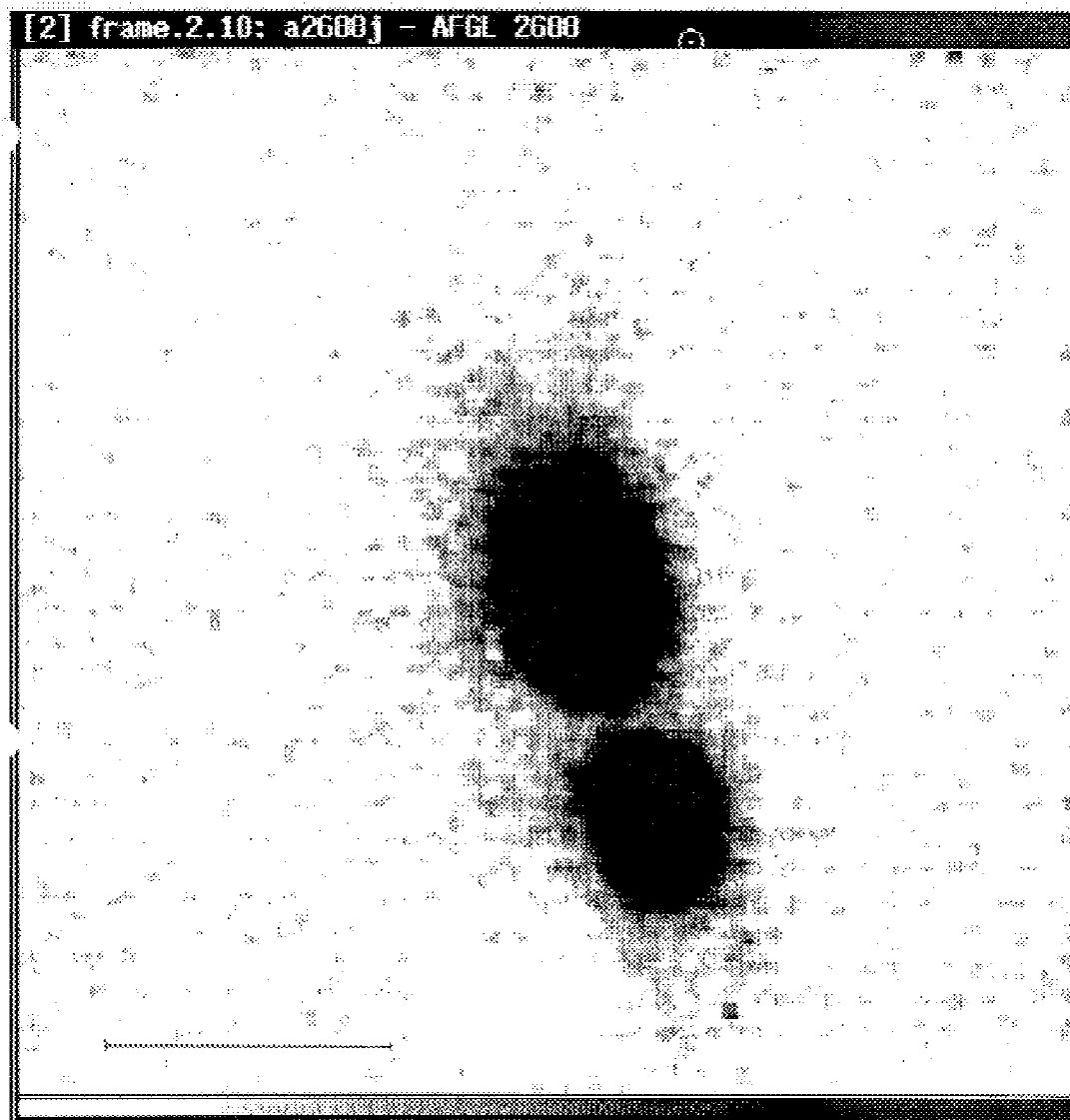


Figure 2.39. Grayscale images of AFGL 2688. The bar at the bottom of the figure has a length of 10".

2.39a. AFGL 2688 J grayscale image.

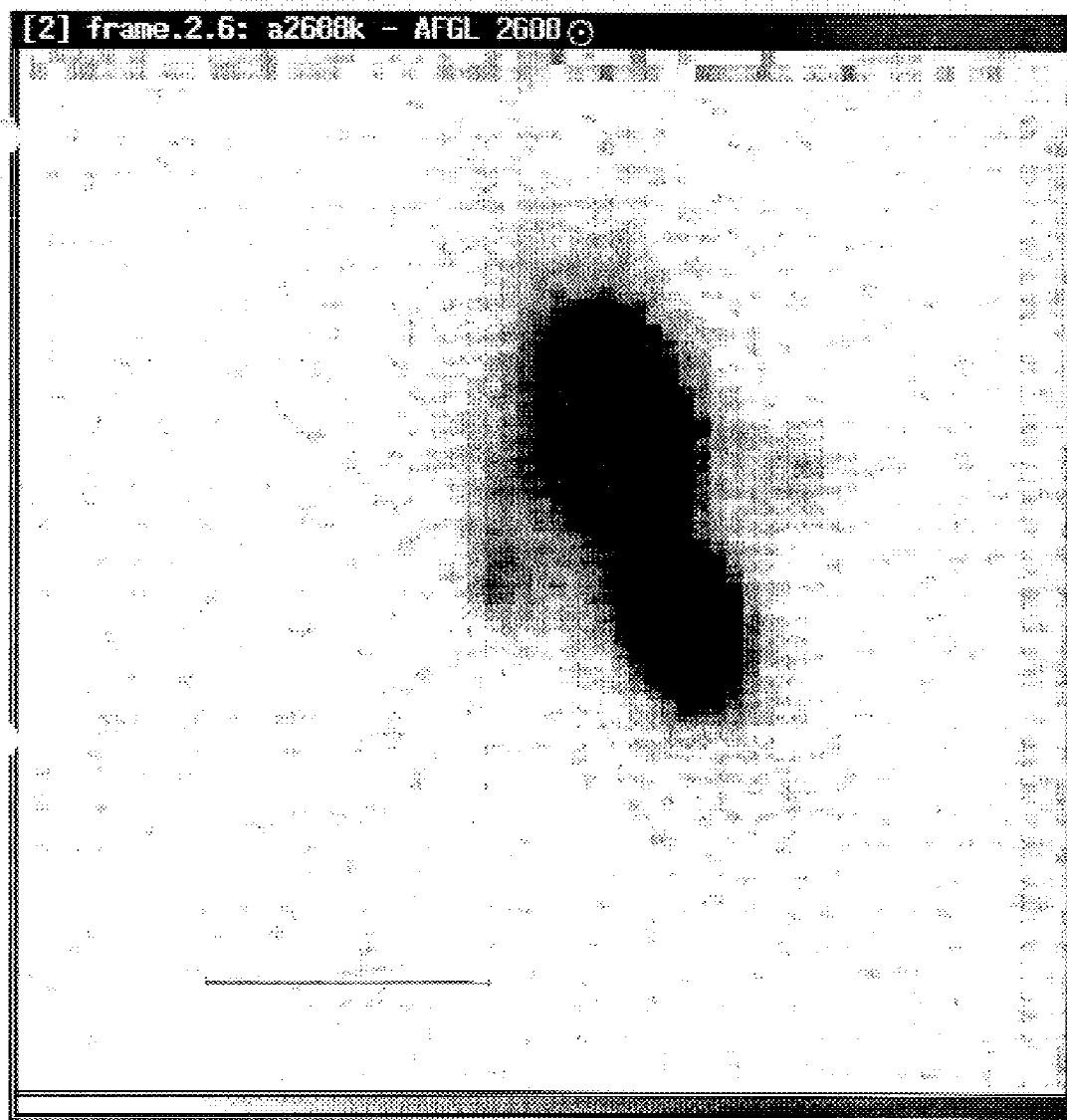


Figure 2.39b. AFGL 2688 K grayscale image.

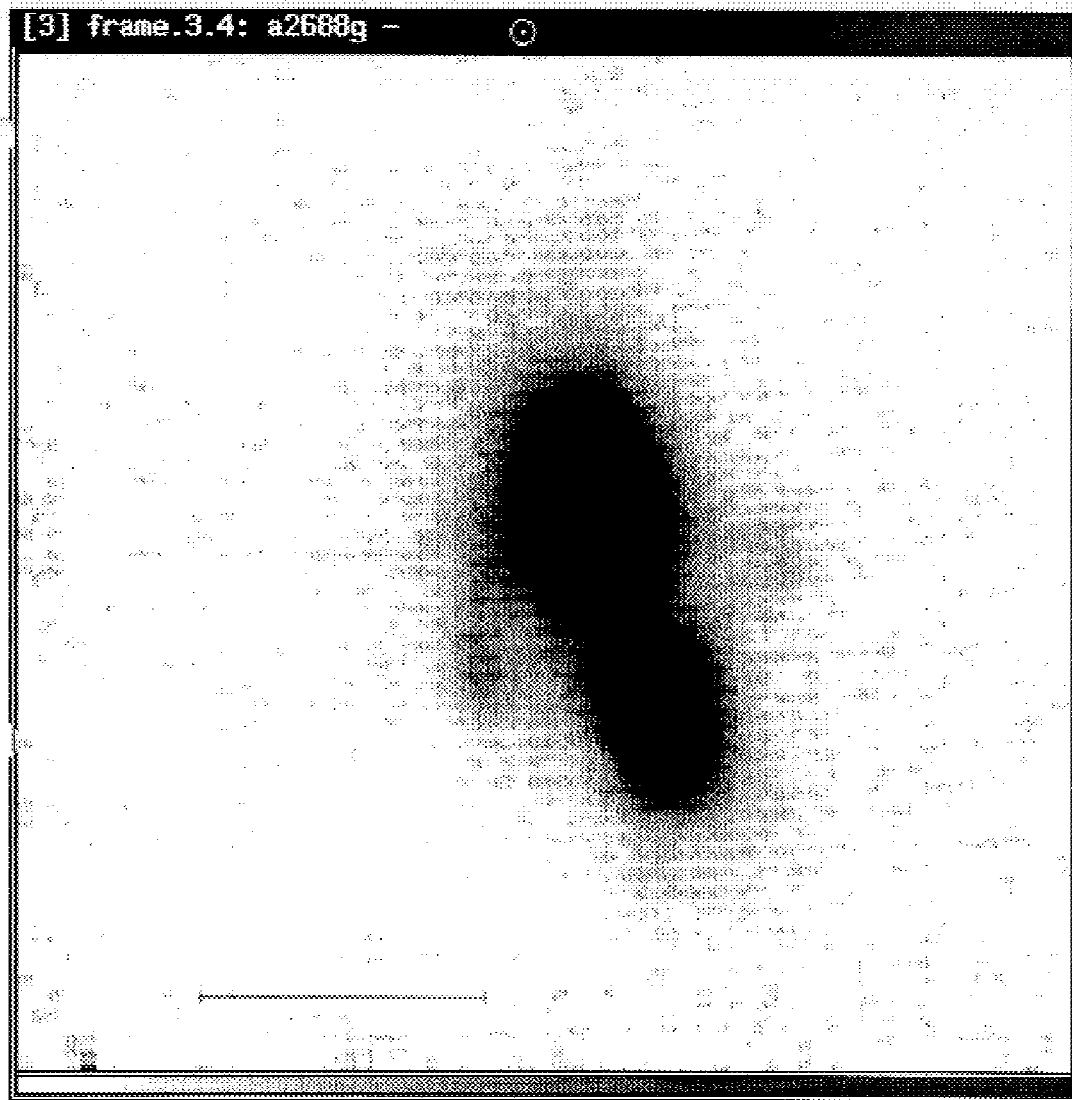


Figure 2.39c. AFGL 2688 Br γ grayscale image.

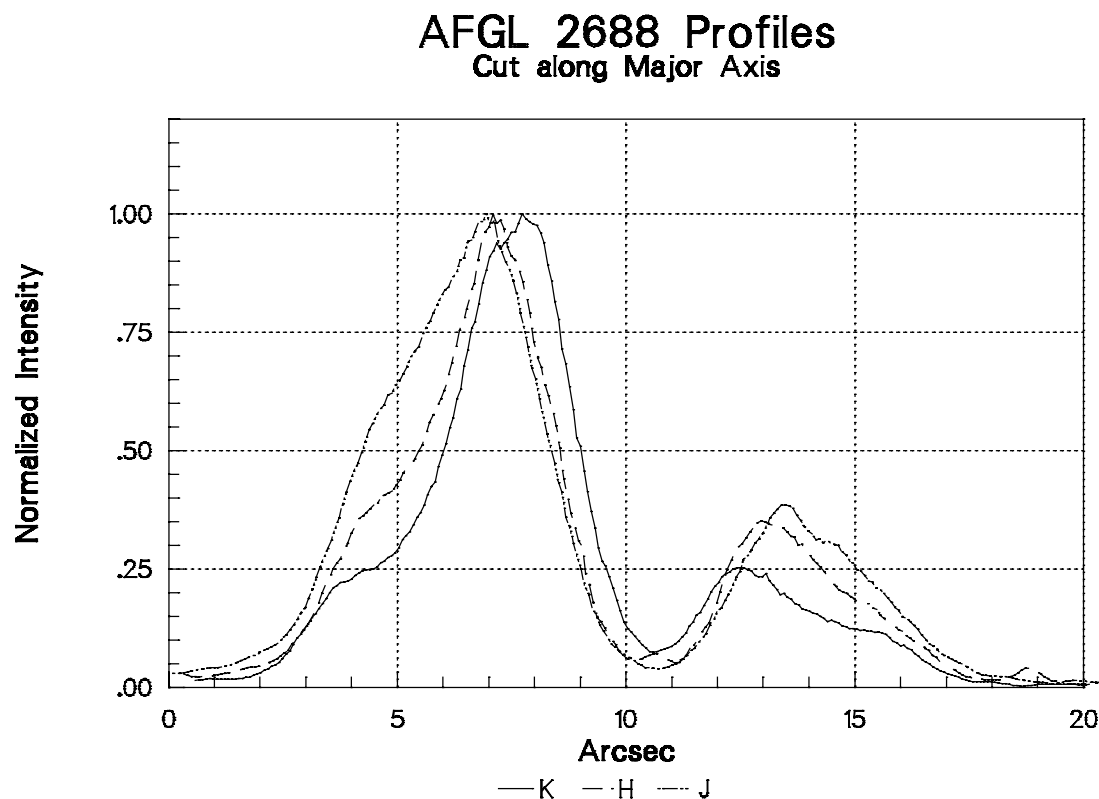


Figure 2.40. Profiles through the major axis of AFGL 2688. The left side of the profile is at the NE corner of the nebula, and the right side is the the SW end of the major axis. The profiles were aligned to match the minimum between the two lobes. In the H profile, there is a small local maximum at this position. The profiles were normalized to the intensity of the brightest (NE) lobe.

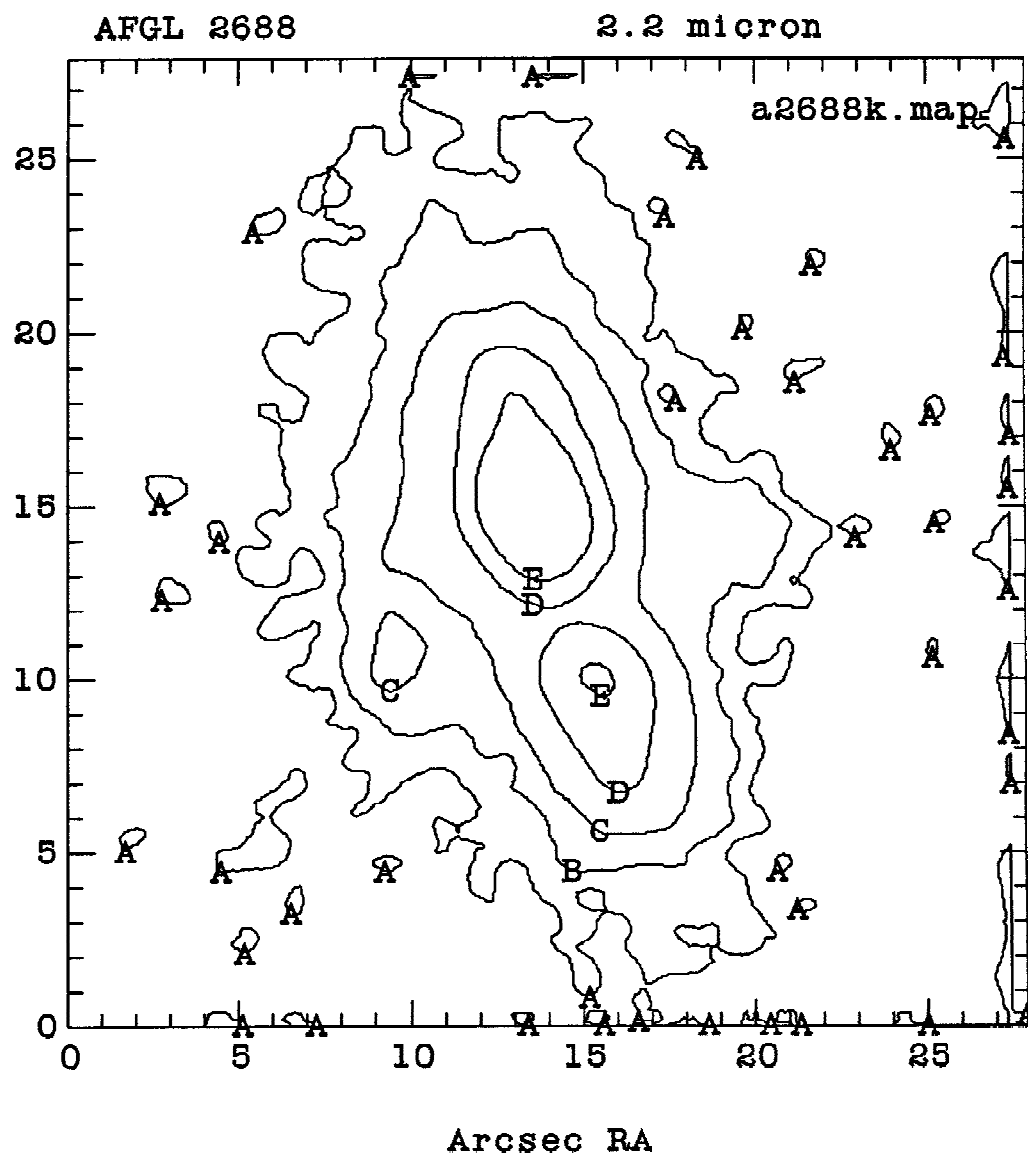


Figure 2.41. Contour image of AFGL 2688 at K showing the halo emission. This is the same data as in Figure 2.38c, which has been smoothed using a bilinear interpolation and plotted with lower contour levels. The contour levels are as follows, in $\text{mJy}/\text{arcsec}^2$: A = .1, B = .2, C = .523, D = 2.2, E = 5.8.

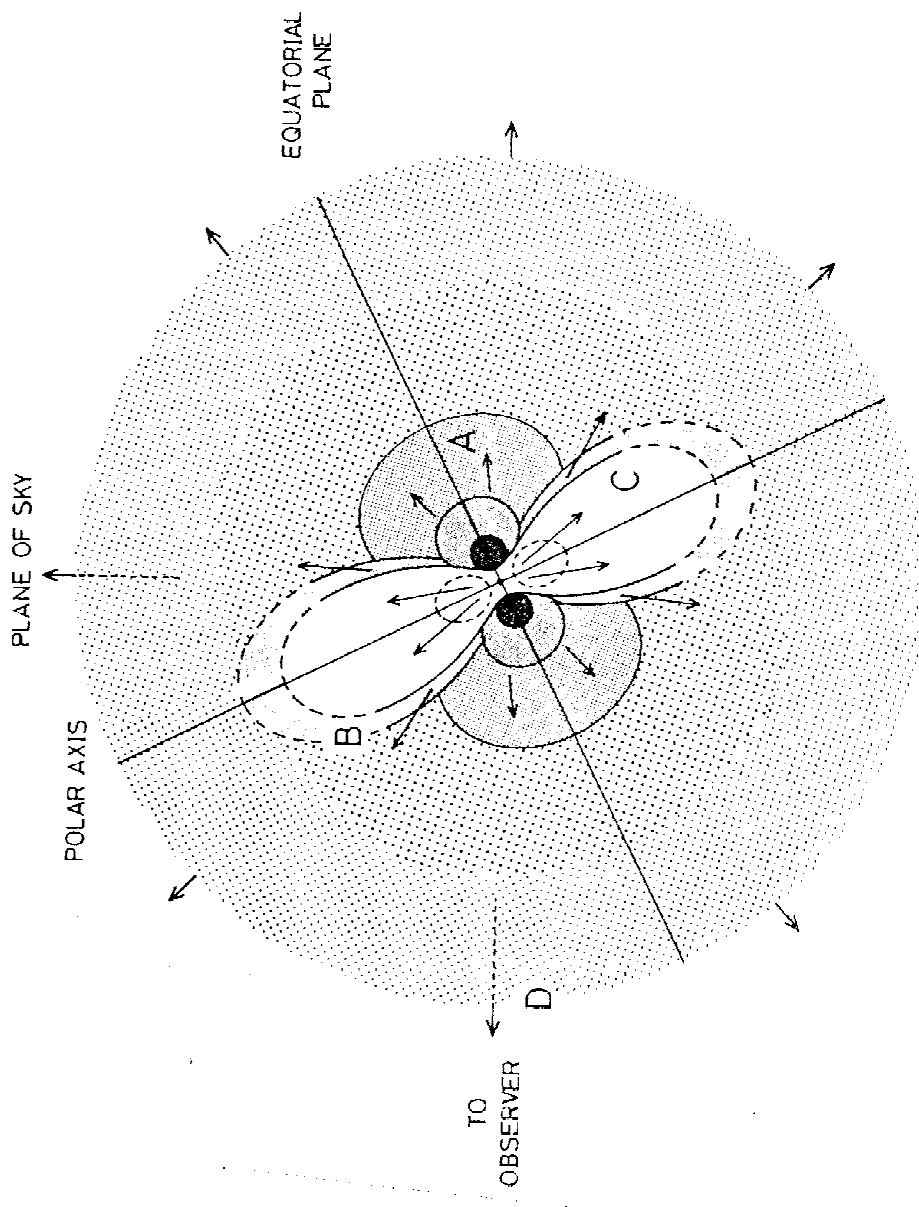


Figure 2.42. Model of AFGL 2688 from Kawabe *et al.* (1987). Region A is the expanding disk in the equatorial plane of the system. Region B shows the shells expanding in the polar direction. Region C shows the wind cavity interior to region B. Region D is the cold expanding envelope which causes the self-absorption in the source.

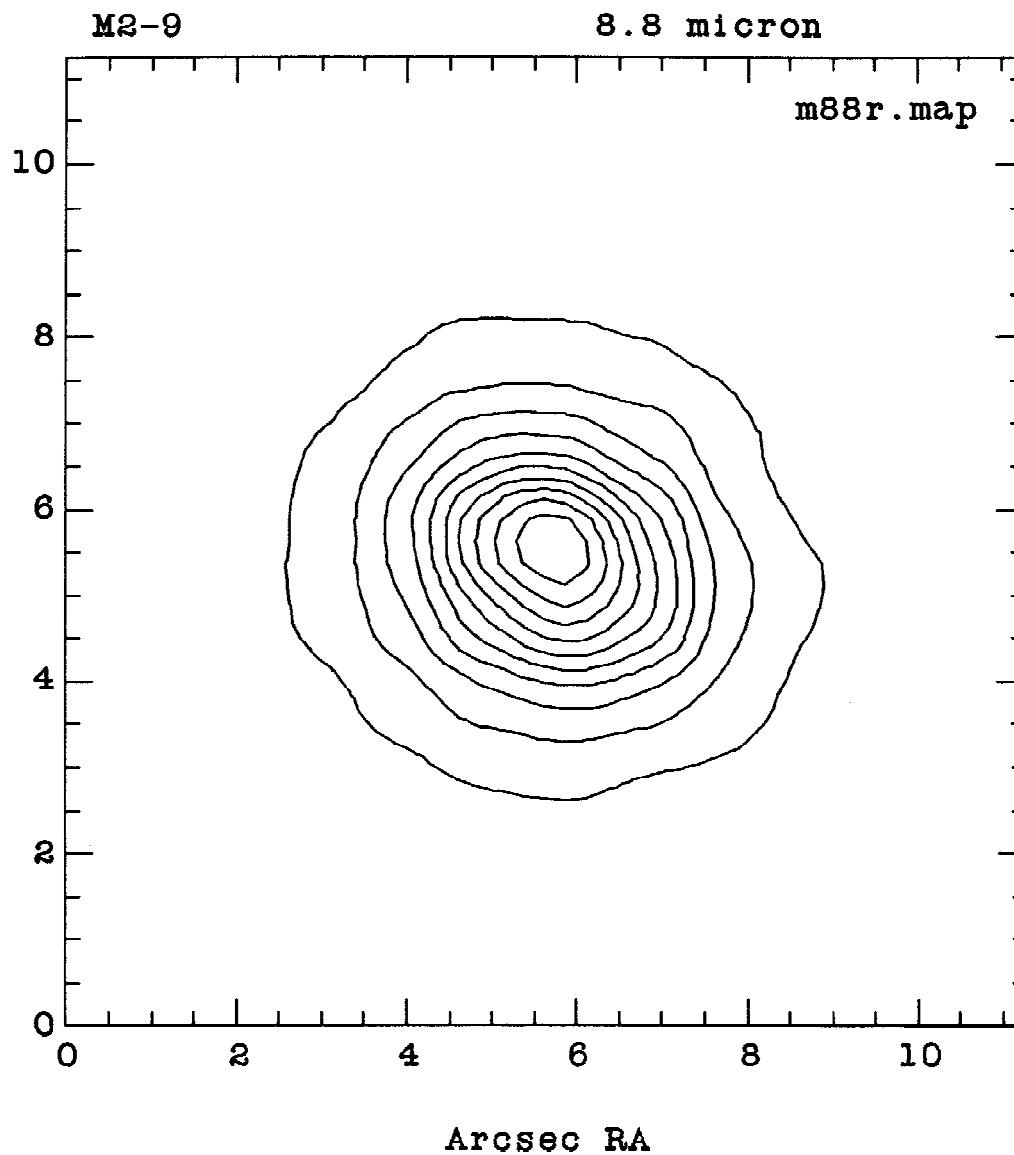


Figure 2.43. Mid-IR contour images of M 2-9. The contour levels are evenly spaced, as indicated below.

2.43a. Contour image of M 2-9, $\lambda = 8.8 \mu\text{m}$. Minimum contour level = .3 Jy/arcsec², contour level spacing .3 Jy/arcsec².

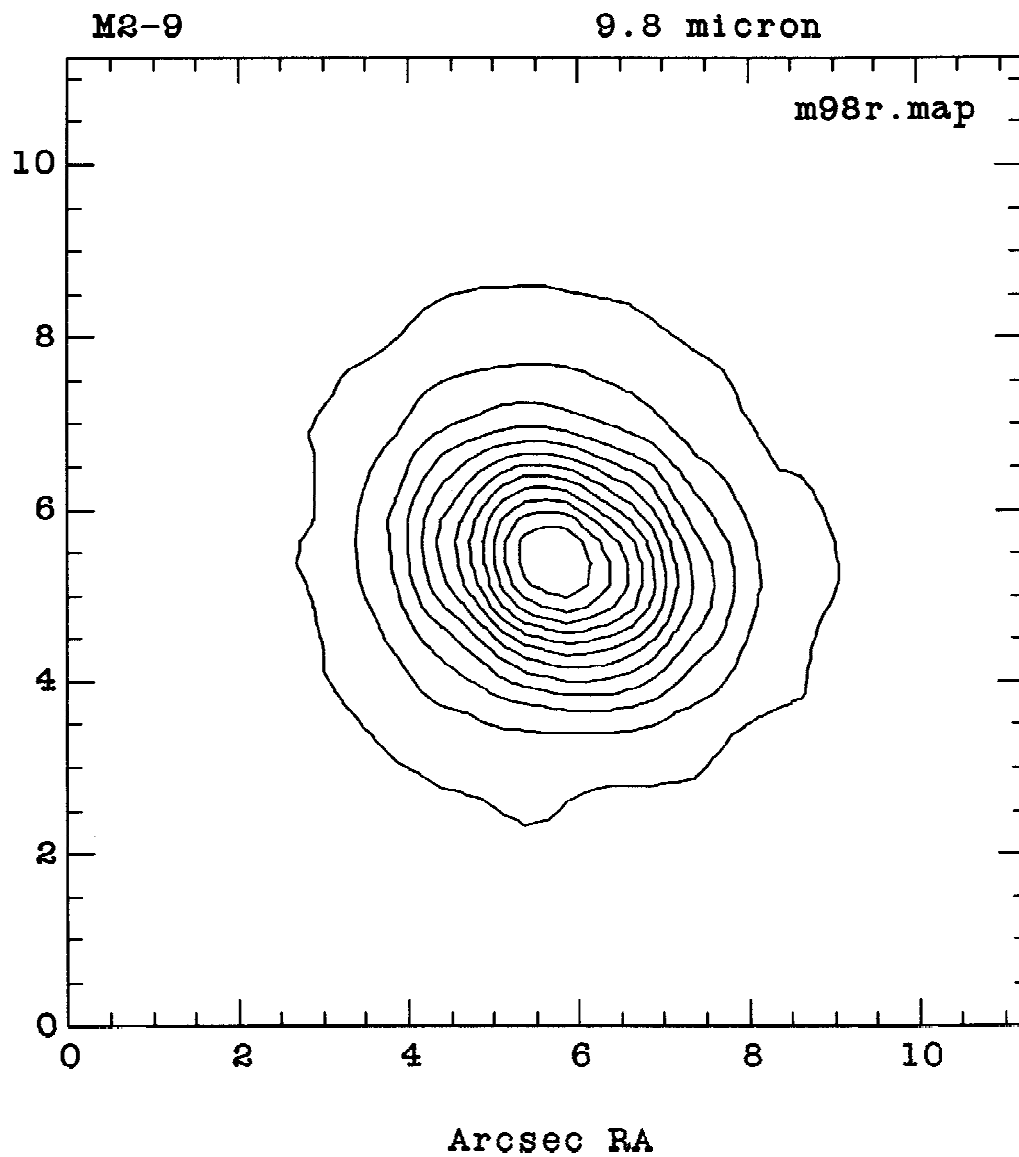


Figure 2.43b. M 2-9 contour image, $\lambda = 9.8 \mu\text{m}$. Minimum contour level = .3 Jy/arcsec², contour level spacing .3 Jy/arcsec².

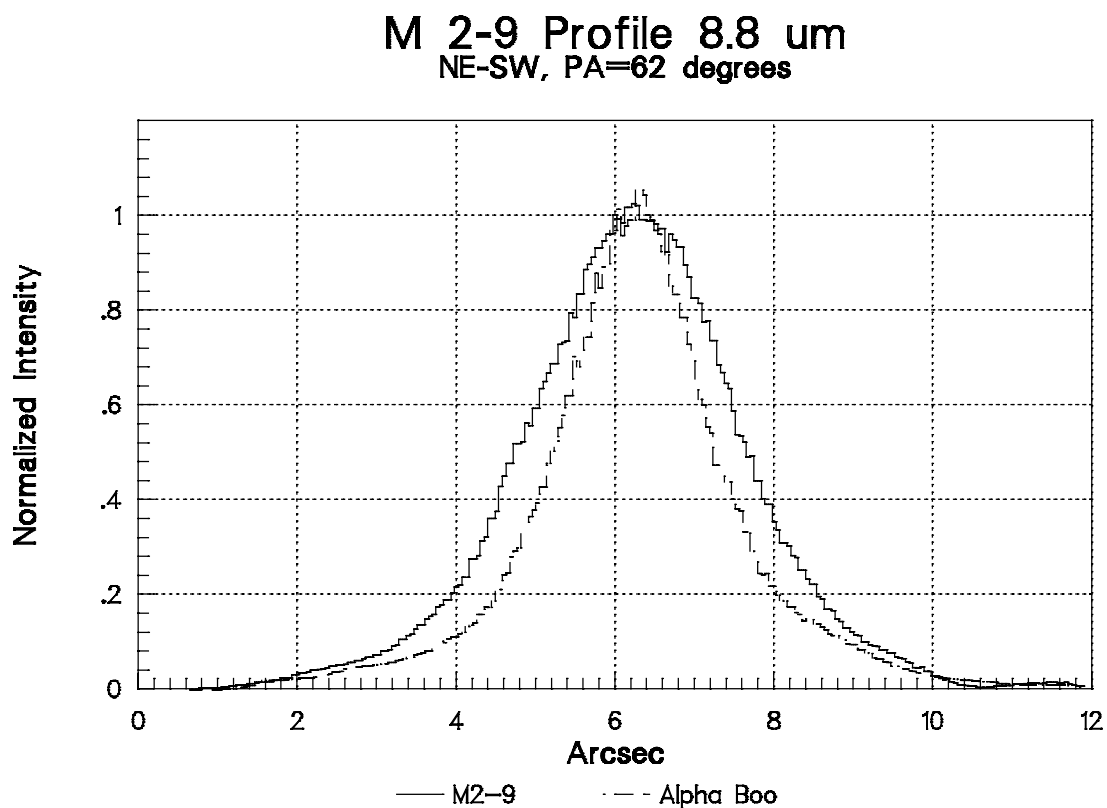


Figure 2.44. Source profiles of M 2-9 at 8.8 and 9.8 μm , with profiles of α Boo at the the same position angle for comparison. The profiles are normalized and aligned to the peak intensity value. The direction of the profiles is from NE to SW, at a PA of 62 degrees.

2.44a. Profiles of M 2-9 and α Boo at 8.8 μm .

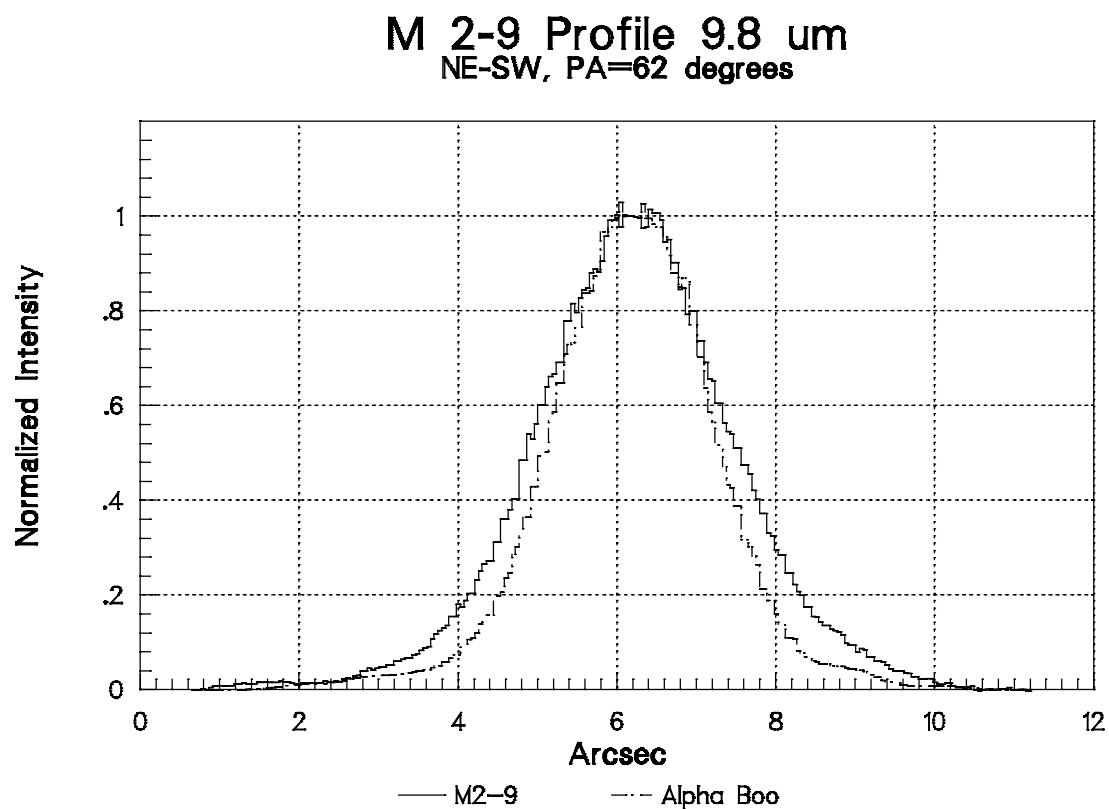


Figure 2.44b. Profiles of M 2-9 and α Boo at 9.8 μ m (see main caption to Figure 2.44).

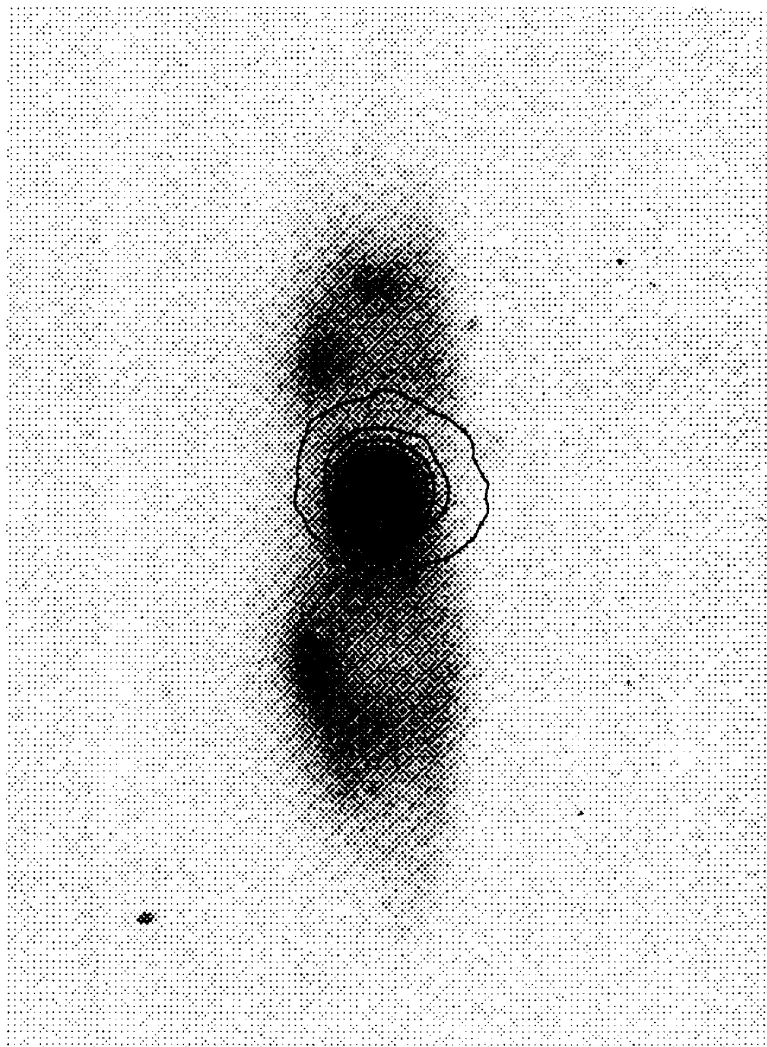


Figure 2.45. Overlay of 8.8 μm image of M2-9 on negative optical image from Balick (1987). The direction of extended emission is roughly aligned with the equatorial plane of the system.

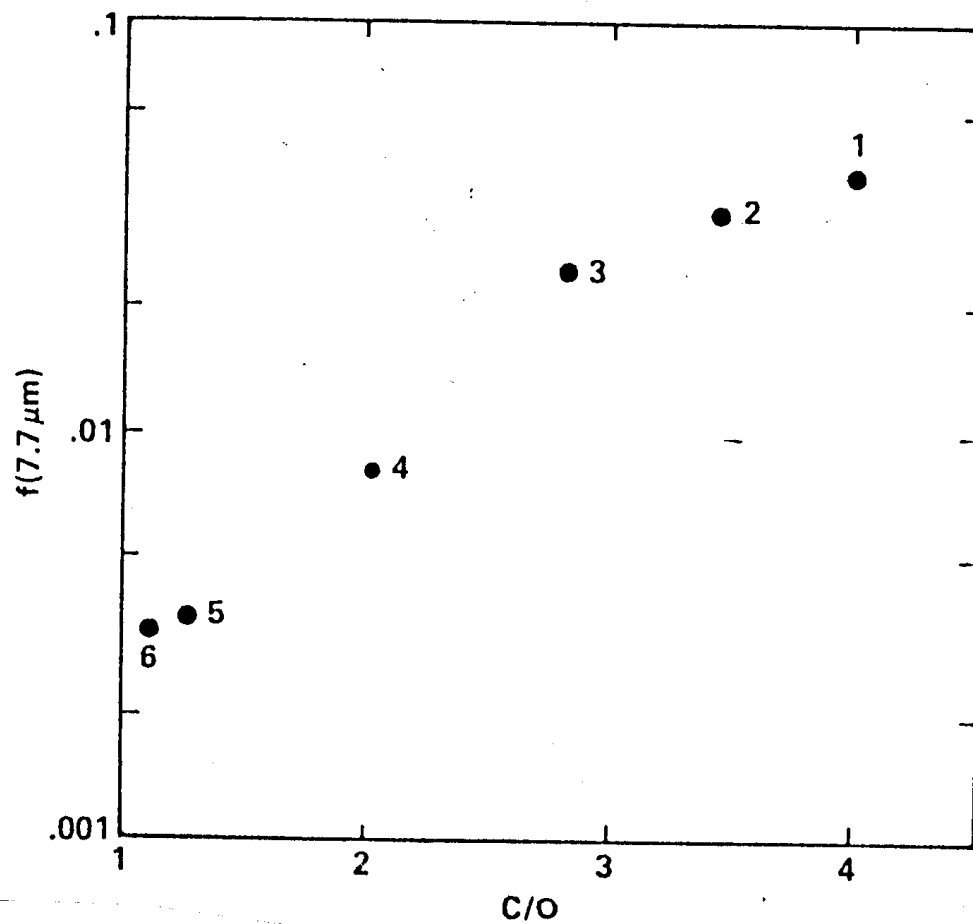


Figure 2.46. UIR correlation plot, from Cohen *et al.* (1986). This plot shows the correlation between $f(7.7\mu\text{m})$ (the fraction of nebular far-IR luminosity radiated by the $7.7 \mu\text{m}$ UIR band), and the nebular C/O ratio.

APPENDIX 1. MIRAC SYSTEM RESPONSIBILITIES AND FUNDING SOURCES

<u>Item</u>	<u>Responsibility</u>	<u>Funding</u>
1. Hughes CRC 444A Array	NRL	NRL, SDIO
2. Optics design, evaluation and testing, filter selection	U/A	U/A, SI, NSF
3. Cryostat layout, baffle design, geometrical configuration	U/A	U/A
4. Cryostat, optics and filters fabrication	NRL	NRL, SDIO
5. Electronics design, fabrication and debugging for detector timing, bias supplies, and signal amplification, detector temperature control, signal processing computer interface	SAO	SAO, SI, U/A, NSF, SDIO(parts)
6. Camera control and data computer, high speed computer digital I/O and parallel processor, camera/computer interface	U/A	U/A, NSF, SAO, SI
7. Software for camera control, data acquisition and display	U/A	U/A, NSF
8. Guider box for mechanical and optical interface between telescope and camera	U/A	U/A, NSF

Abbreviations:

U/A - University of Arizona

SDIO - Space Defense Initiative Organization Sensor Office/USAF Phillips
Laboratory

NRL - Naval Research Laboratory

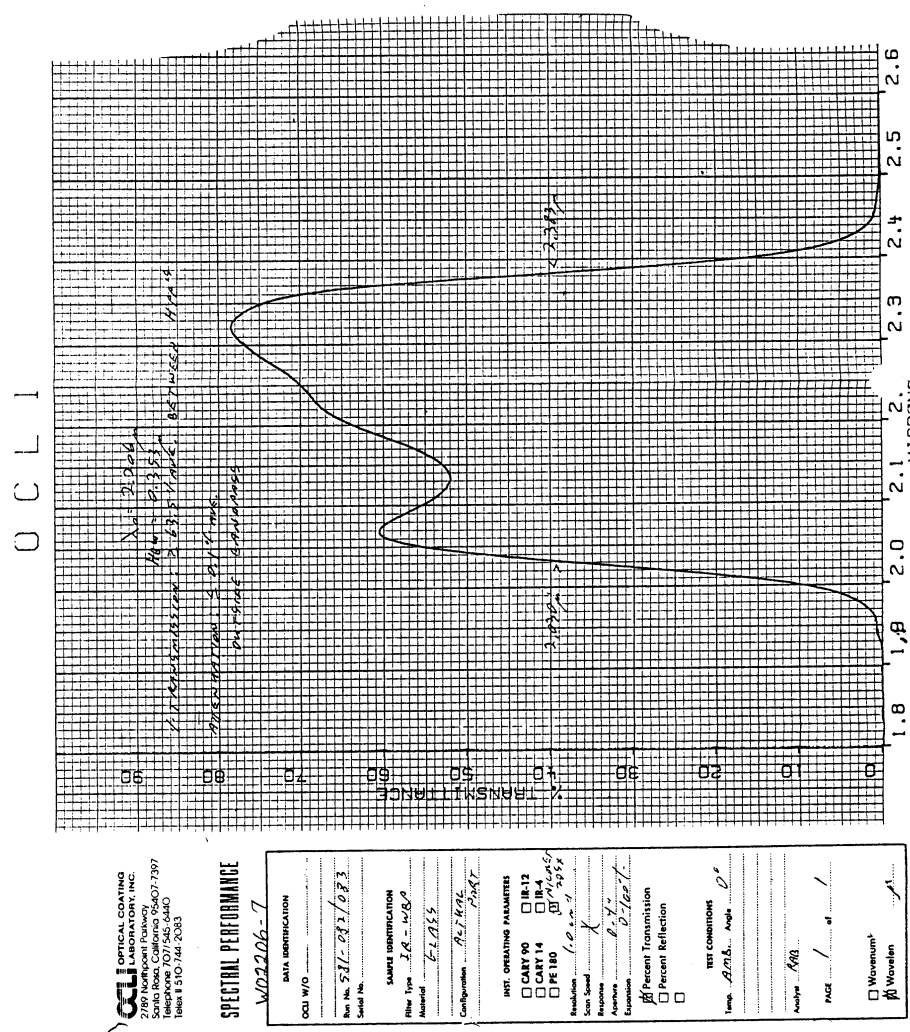
NSF - National Science Foundation, grant # AST-8820904

SAO - Smithsonian Astrophysical Observatory

SI - Smithsonian Institution Scholarly Studies Grants and
Visitors Program, grants #1240S821, 1240S921

APPENDIX 2. MIRAC FILTERS

The following figures display the MIRAC filter transmission plots. Most of these plots were provided by OCLI, except for the dewar windows which were measured using a Beckmann Acculab 6 spectrophotometer at NOAO. These are measurements of the filter transmission at the indicated temperatures, and are not the camera filter/detector bands, which must fold in the response of the detector.

Figure A2.1 2.2 μm filter.

Optical Coating Laboratory, Inc.

ASTRONOMY "L" FILTER W/O # Run # 1114-027/029 lot#1

Unit: micron

Peak %T = 96.4% at 3.955

Half power points: 48.2%T @ 3.529 48.2%T @ 4.152

Average %T between half power points = 89.5%

Half band width = 0.622 % Band width = 16.203%

Center wavelength = 3.841

5.0%abs T @ 3.478 80.0%rel T = 77.1% @ 3.558 Left slope = 2.298%

5.0%abs T @ 4.207 80.0%rel T = 77.1% @ 4.133 Right slope = -1.761%

Test conditions: temp=77Kdeg. angle=0 PE983

Instrument operating parameters: res=4.0cm-1 apert=.8"

Atten: <=.1%Tabs

Analyst K.P.

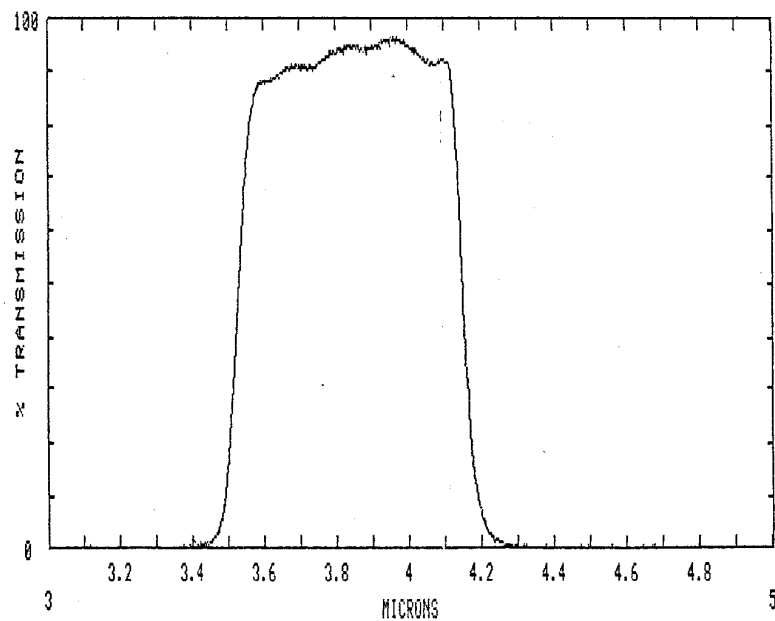


Figure A2.2 3.8 μ m filter.

Optical Coating Laboratory, Inc.

STOCK FILTER W/O #

Run # 381-088/104 IR-WE

Unit: micron

Peak %T = 87.6% at 4.812

Half power points: 43.8%T @ 4.409 43.8%T @ 5.012

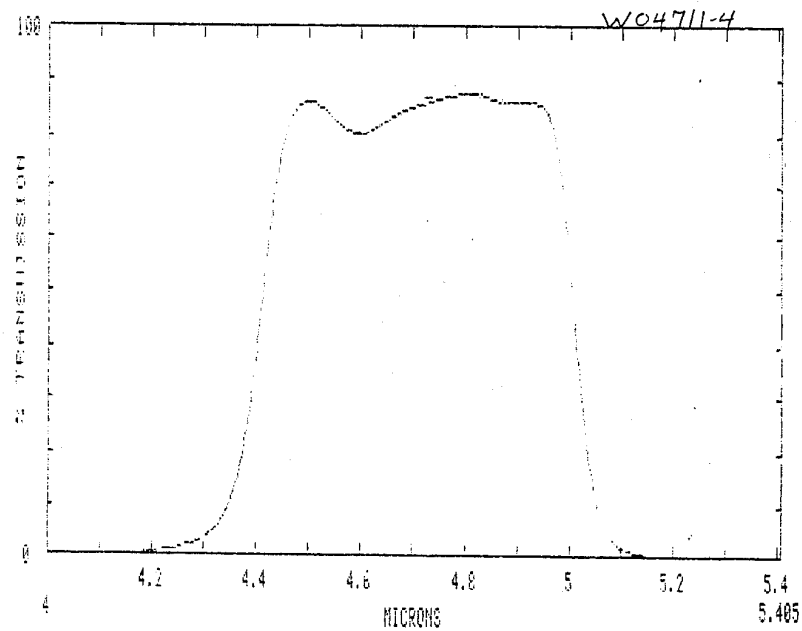
Half band width = 0.603 % Band width = 12.802%

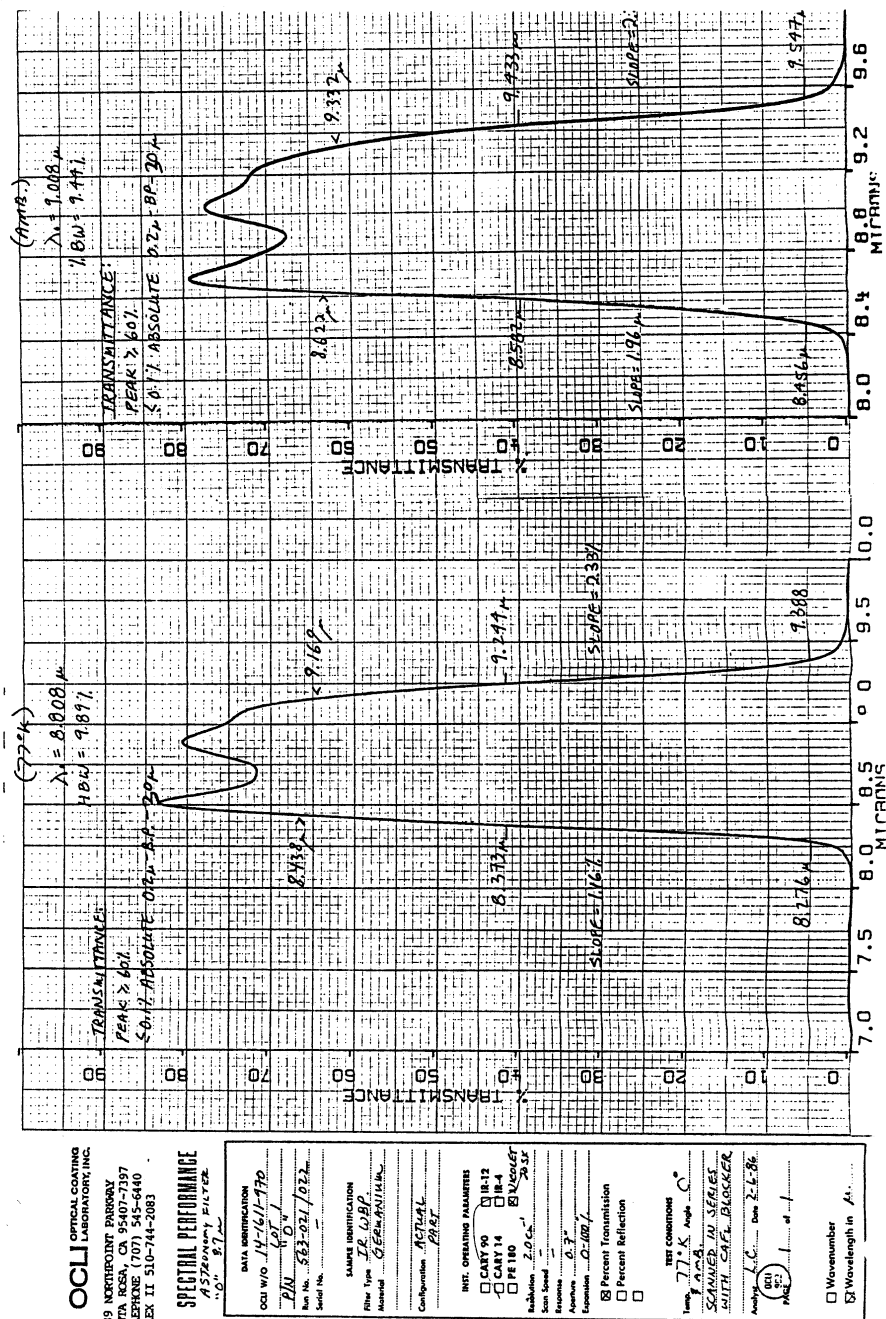
Center wavelength = 4.711 AVE. %T BETWEEN H.P.'S $\geq 80\%$

Test conditions: temp= AMB. angle= 0 deg.

Instrument operating parameters: res.= 3.0cm-1

aperture= 0.7"

Analyst KABFigure A2.3 4.6 μ m filter.

Figure A2.4 8.8 μ m filter.

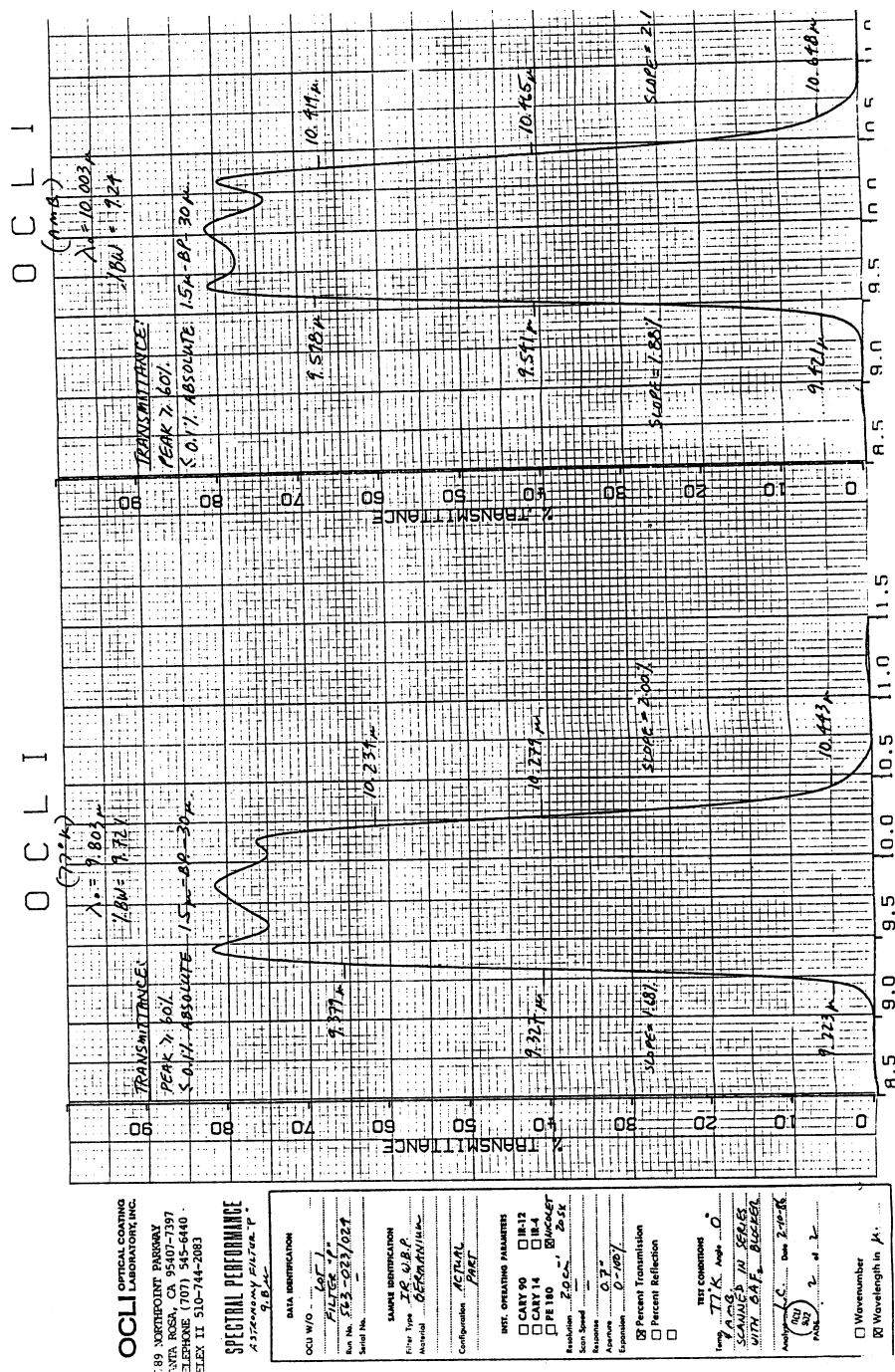


Figure A2.5 9.8 μm filter.

SPECTRAL PERFORMANCE

SPECTRAL PERFORMANCE

Astronomy filter
11gⁿ 12.5 μ

DATA IDENTIFICATION

LOT # 1 PLATE 5
DATE SEP-02/1980

Run On 50 Vol. 50 Vol. 50 Vol. 50 Vol.
Run Time 10 Min. 10 Min. 10 Min. 10 Min.

STATUS INFORMATION

W.P. 2
RECEIVED SEP-ANALYSIS

ANALYSIS

ANALYST THAT

NET OPERATING PARAMETERS

☐ CARRY OVER ☐ R-12
☐ R-14 ☐ R-16
☐ R-18 ☐ R-20
☐ R-22 ☐ R-24

PERCENT TRANSMISSION 2.0
PERCENT REFLECTION 2.0

TEST CONDITIONS

WAVELENGTH 77.7 nm
TEMPERATURE 0 °C

SCANNERS IN SERIES 1

DATE SEP-02-86

WAVELENGTH 2 nm

WAVELENGTH 2 nm

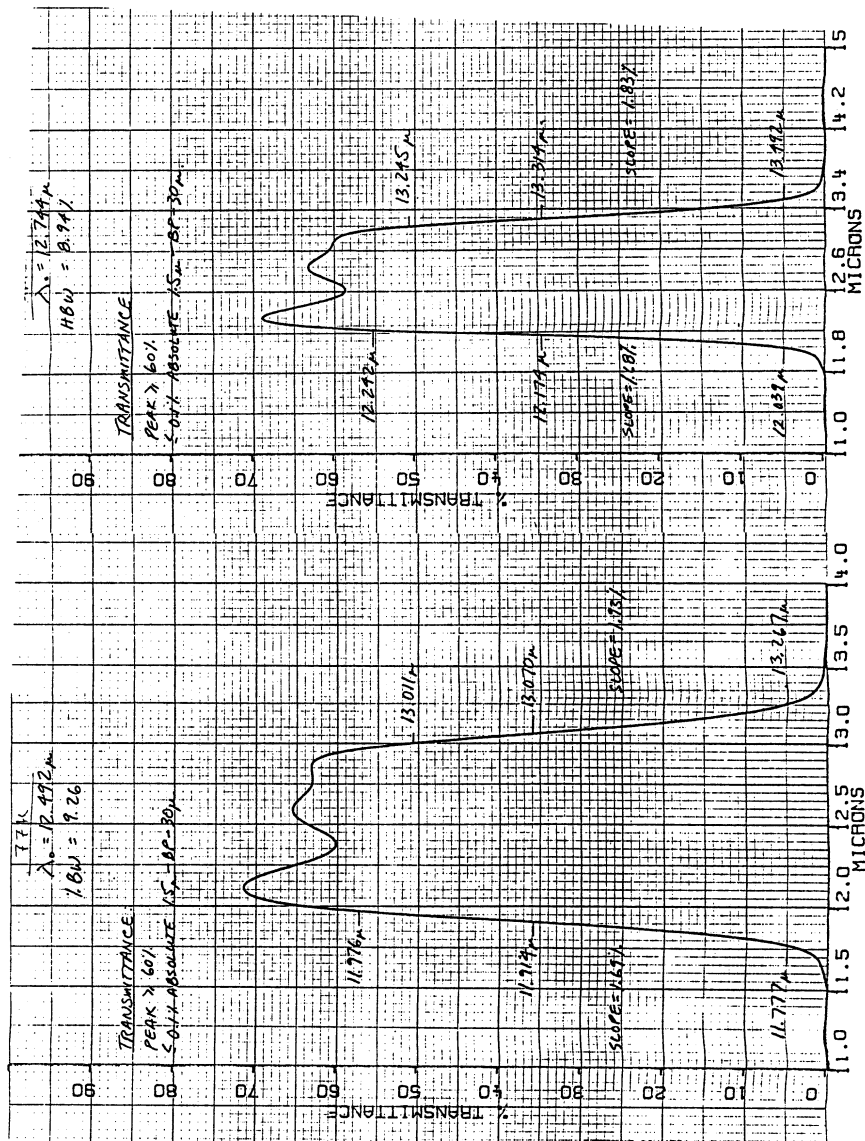


Figure A2.7 12.5 μm filter.

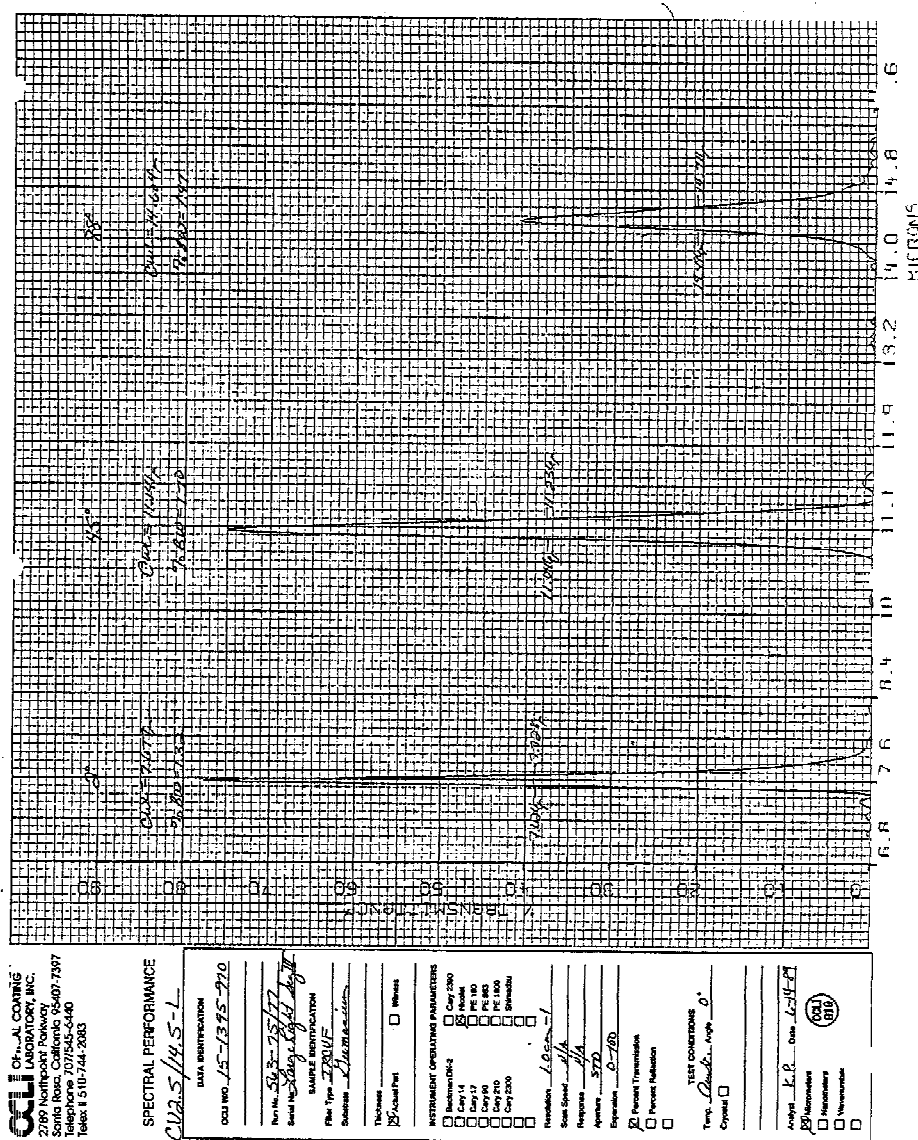


Figure A2.8 7.9-14.5 μm CVF.

Optical Coating Laboratory, Inc

STOCK FILTER CATALOG

Run # 1114-179/179 10cm

Unit: micron

Peak %T = 91.7% at 10.970

Half power points: 45.8%T @ 8.155 45.8%T @ 12.995

Average %T between half power points = 80.6%

Half band width = 4.840 % Band width = 45.770%

Center wavelength = 10.575

5.0%abs T @ 7.946 80.0%rel T = 73.3% @ 8.498 Left slope = 6.938%

5.0%abs T @ 13.283 80.0%rel T = 73.3% @ 12.857 Right slope = -3.299%

Test conditions: temp=amb angle=0 PE1800

Instrument operating parameters: res=3.0cm-1 aper=1"

Atten=<.1%T 1.0-80-17.0um

Analyst K.P.

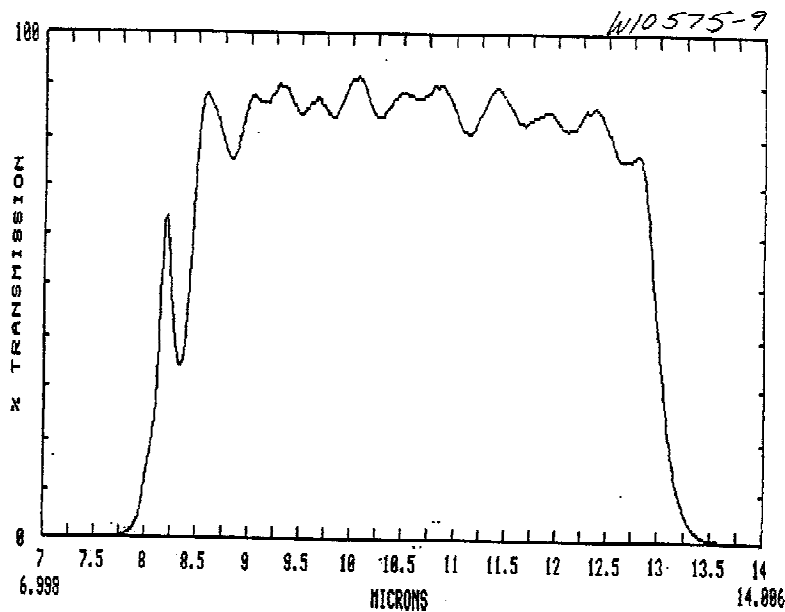


Figure A2.9 8-13 μm filter ("N" band).

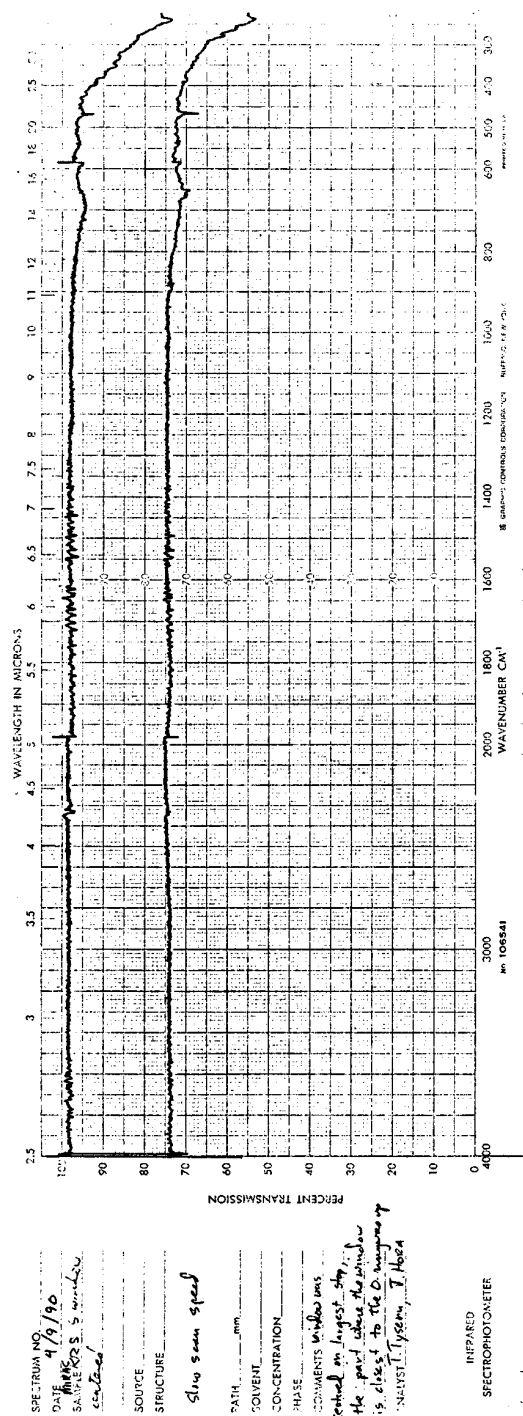


Figure A2.10 MIRAC KrS-5 window.

APPENDIX 3. CRC 444A ROW DECODER CODE

The following table shows the transformation between the sequential row address and the address code necessary to send to the detector. This conversion is done by a EEPROM on the MIRAC controller. In this table, the ROW is the row address of the pixel, from 0 to 65. There are two extra rows which together with the two edge columns form a border around the detector, and only the rows numbered 1 to 64 are read out. The binary code indicates the voltage on each of the address lines. A "1" indicates -4 V, and a zero (0) indicates 0 V.

Table A3.1 CRC 444A Row Decoder Code

A1.....A8	Row	A1.....A8	Row
11110000	0	10100110	32
11101000	1	10100011	33
11011000	2	11000011	34
10111000	3	01100011	35
01111000	4	00110011	36
00111100	5	00011011	37
01011100	6	00101011	38
10011100	7	01001011	39
10101100	8	10001011	40
11001100	9	10000111	41
11100100	10	01000111	42
11010100	11	00100111	43
01110100	12	00010111	44
10110100	13	00001111	45
10110010	14	00011101	46
01110010	15	00101101	47
11100010	16	10001101	48
11010010	17	01001101	49
11001010	18	01100101	50
01101010	19	11000101	51
00111010	20	10100101	52
10011010	21	10010101	53
01011010	22	01010101	54
01010110	23	00110101	55
10010110	24	00111001	56
10001110	25	01011001	57
01001110	26	10011001	58
00101110	27	11001001	59
00011110	28	10101001	60
00110110	29	01101001	61
01100110	30	01110001	62
11000110	31	10110001	63
		11010001	64
		11100001	65

APPENDIX 4. MIRAC ELECTRONICS COMMAND SUMMARY

I. Serial word format

All serial words are 32 bits long, Manchester encoded, and transmitted at 1.25 MHz, MSB first. Within a field, data are right (LSB) justified. Three bits are used as synchronization bits and one bit used as parity by the Manchester encoder, so 28 bits remain available to be used to send commands and data.

A. Command word format (from APB to camera):

sync	sync	code field	data field	parity
1.5 bits	1.5 bits	5 bits	23 bits	1 bit

The command word is separated into a "code field" and a "data field". The code field contains a 5-bit word that the electronics controller uses to determine which command is being sent. The data field transmits the parameter (if any) for the command. See the command set summarized below.

B. Data word format (from camera to APB):

sync	sync	FIFO	COADD	data	parity
1.5 bits	1.5 bits	2 bits	2 bits	24 bits	1 bit

The data field consists of two FIFO bits, two COADD bits, and 24 bits of data. The FIFO bits are the "FIFO FULL" and "FIFO EMPTY" memory status flags. If the data are not being read rapidly enough from the FIFO memory so that the memory is overfilling, the FIFO FULL flag will be set. Similarly, if a read is attempted from the FIFO memory when there is no data present, the FIFO EMPTY flag will be set. The COADD bits designate which area of memory the data word is from. There are three areas of memory, the first area containing the single sample or delta reset result, or the first sample of a double or triple sample. The second area contains the second sample of the double or triple sample, and the third area contains the third sample of the triple sample. The current sample mode determines which of these areas are used.

II. Command set

Table A4.1 is a summary of the commands available. Group 1 commands can be sent to the camera regardless of the camera mode. Group 2 commands are accepted by the camera only when not currently imaging.

Table A4.1 MIRAC Electronics Command Summary

Code field	Command	Data field length(bits)
Group 1:		
01001	Load column register	5
01010	Start coimage	0
01000	Stop coimage	0
01011	Read FIFO, n-word block	8
01100	FIFO reset	0
Group 2:		
10001	Set # of frames/coimage	12
10010	Set clock rate	4
10011	Set sample mode	2
10100	Set array extent	1
10101	Set bandwidth	3
11001	Set delay cycles	16
11010	Freeze row counter	7
11101	Master reset	0
The following are no longer implemented:		
10110	Set gain	3
10111	Select alt. offset	1
11000	Write to EEPROM	16

The following is a brief description of some of the commands and the data fields used:

Load column register - this command selects which column will be read out by the next "Read FIFO" command. Columns are numbered 0-19.

Read FIFO - this command initiates a transfer of data from the camera electronics to the APB. The "Load column register" command must have already been sent with the desired column. The data field contains the number of bytes to send minus 1 (n-1). The number of words depends on the observing mode and the number of pixels to be read out. For example, if in double sample mode, 64 pixels per column, then the number of words $n = 64 * 2 = 128$. A separate Read FIFO command must

be issued for every column to be read out.

Set # of frames/coimage - this sets the number of frames that will be coadded into a single coimage. The data field contains the number of frames minus 1 (n-1). Valid numbers for n are 1 to 4096.

Set clock frequency - this sets the base clock frequency that determines the frame rate of the camera. The base oscillator frequency of 15 MHz is divided down by the power of two sent in this command, i.e., the clock frequency is given by

$$clock\ freq. = \frac{15}{2^n} MHz$$

Valid numbers for n are 0 to 15.

Set array extent - chooses whether the full array (64 pixels per column) or half the array (32 pixels per column) is to be used.

Set bandwidth - This chooses which bandwidth-limiting filter capacitor is used at the input stage of the signal processor board. There are eight possible settings:

Table A4.2 Available Bandwidth Filters

Command	Bandwidth (KHz)
0	1440
1	700
2	350
3	175
4	87
5	44
6	11
7	.07

Set delay cycles - This determines the number of pixel delay cycles between each detector readout. This is the parameter that controls the so-called "burst" mode, where the detector is read out at the chosen clock frequency, separated by a number of pixel delays. Valid values are 0-65535.

Freeze row counter - This command turns off the pixel addressing going to the detector, so that a single row is reset. The pixels are numbered 0-63, 64 unfreezes the counter (for the normal mode of operation).

Master reset - this command stops the camera if it is imaging, resets frame counters and row addresses, and initializes the mode of the camera.

APPENDIX 5. PHOTOMETRY OF SAO STARS

The following stars were observed to measure the instrumental point source response for the PN observations. The magnitudes of these stars were determined from these data, and are presented in table A5.1. The stars are identified by their SAO star catalog number, and the magnitude of each of the stars at the wavelengths observed is given.

TABLE A5.1 SAO STAR PHOTOMETRY				
SAO STAR	J	MAGNITUDE H	K	
17713	...	6.7	7.5	
57384	...	6.6	...	
68520	11.0	
70805	11.5	
70809	10.8	
79428	7.0	
95673	6.3	
150440	3.65	6.2	...	
150445	8.7	8.5	9.6	
151362	...	4.8	...	

APPENDIX 6. MAGNITUDES OF CALIBRATION STARS

The near-IR images presented in this thesis were calibrated using the stellar magnitudes listed in Elias *et al.* (1982). For the mid-IR images, the magnitudes of the flux standards were taken from various source in the literature, given below in table A6.1. In the cases where a measurement has not been reported at the wavelength of interest, an interpolation between published values was done to obtain the magnitude at that wavelength. For both the near- and mid-IR, the flux in Jy was calculated assuming that the zero magnitude star emits as a 10000 K blackbody source.

Table A6.1 IR Standard Star Magnitudes

Star	Magnitude [μm]									
	[8.8]	[9.8]	[10.0]	[11.2]	[11.7]	[12.4]	[12.5]	[12.8]	[13.2]	
α Boo	-3.17	-3.15	-3.26	...	-3.33	
γ Dra	-1.3	-1.44	-1.44	-1.48	-1.52	-1.52	-1.52	-1.52	-1.52	
β Peg	-2.51	
α Tau	-3.05	

References:

- α Boo: Hanner et. al 1984
- γ Dra: Gehrz and Woolf 1971, Gehrz 1972, Rieke, Lebofsky, and Low 1985
- β Peg: Hackwell and Gehrz 1974
- α Tau: Hackwell and Gehrz 1974

Table A6.2 Adopted Fluxes for Zero Magnitude

Wavelength (μm)	Flux (Jy)
1.25	1650
1.68	1070
2.25	673
8.8	51.6
9.8	42.0
10.0	40.4
11.2	32.5
11.7	30
12.4	26.5
12.5	26
12.8	24.4
13.2	23.6

REFERENCES

- Acker, A. 1978, *Astron. Astrophys. Suppl. Ser.*, **33**, 367.
- Aitken, D. K. and Roche, P. F. 1982, *M. N. R. A. S.*, **200**, 217.
- Aitken, D. K., and Roche, P. F. 1983, *M. N. R. A. S.*, **202**, 1233.
- Allen, D. A., and Swings, J. P. 1972, *Ap. J.*, **174**, 583.
- Aller, L. H., and Czyzak, S. J. 1983, *Ap. J. Supp.*, **51**, 211.
- Arens, J. F., Lamb, G. M., Peck, M. C., Moseley, H., Hoffmann, W. F., Tresch-Fienberg, R. M., and Fazio, G. G., 1984 *Ap. J.*, **279**, 685.
- Aspin, C., and McLean, I. S. 1984, *Astron. Astrophys.*, **134**, 333.
- Aspin, C., McLean, I. S., and Smith, M. G. 1988, *Astron. Astrophys.*, **196**, 227.
- Bachiller, R., Gómez-González, J., Bujarrabal, V., and Martin-Pintado, J. 1988, *Astron. Astrophys.*, **196**, L5.
- Bachiller, R., Martin-Pintado, J., and Bujarrabal, V. 1990, *Astron. Astrophys.*, **227**, 188.
- Balick, B. 1987, *A. J.*, **94**, 671.
- Balick, B. 1989, *A. J.*, **97**, 476.
- Balick, B., and Preston, H. L. 1987, *A. J.*, **94**, 958.
- Balick, B., Preston, H. L., and Icke, V. 1987, *A. J.*, **94**, 1641.
- Ball, R., Arens, J. F., Jernigan, G., and Keto, E. 1991, in *Astrophysics with Infrared Arrays*, ed. R. Elston (San Francisco: Astronomical Society of the Pacific), 171.

- Bally, J., Arens, J. F., Ball, R., Becker, R., and Lacy, J. 1987, *Ap. J.*, **323**, L73.
- Barker, T. 1991, *Ap. J.*, **371**, 217.
- Barlow, M. J. 1983, in *IAU Symp. No. 103, Planetary Nebulae*, ed. by D. R. Flower (Dordrecht: Reidel), p. 105.
- Basart, J. P., and Daub, C. T. 1987, *Ap. J.*, **317**, 412.
- Becklin, E. E., Beckwith, S., Gatley, I., Matthews, K., Neugebauer, G., Sarazin, C., and Werner, M. W. 1976, *Ap. J.*, **207**, 770.
- Bentley, A. F., Hackwell, J. A., Grasdalen, G. L., and Gehrz, R. D. 1984, *Ap. J.*, **278**, 665.
- Bianchi, L., Cerrato, S. and Grewing, M. 1987, *Astron. Astrophys.*, **169**, 227.
- Biegging, J. H., and Nguen-Quang-Rieu 1988, *Ap. J.*, **324**, 516.
- Bevington, Philip R., 1969, *Data Reduction and Error Analysis for the Physical Sciences* (New York: McGraw-Hill), Chapters 8,9.
- Bignell, R. C. 1983, in *IAU Symp. No. 103, Planetary Nebulae*, ed. by D. R. Flower (Dordrecht: Reidel), p. 69.
- Calvet, N., and Cohen, M. 1978, *M. N. R. A. S.*, **182**, 687.
- Cohen, M, and Barlow, M. J. 1974, *Ap. J.*, **193**, 401.
- Cohen, M., Allamandola, L., Tielens, A. G. G. M., Bregman, J., Simpson, J. P., Witteborn, F. C., Wooden, D., and Rank, D. 1986, *Ap. J.*, **302**, 737.
- Crampton, D., Cowley, A. P., and Humphreys, R. M. 1975, *Ap. J. (Letters)*, **198**, L135.
- D'Antona, F., Mazzitelli, I., and Sabbadin, F. 1987, in *Planetary and Proto-Planetary Nebulae: From IRAS to ISO*, ed. by A. P. Martinez (Dordrecht: Reidel), 121.
- Deutsch, L. K., 1990, *Ph. D. Thesis*, Harvard.

- Deutsch, L. K., Hora, J. L., Hoffmann, W. F., and Fazio, G. G., 1991, *in preparation*.
- Dinerstein, H. L., and Sneden, C., 1988, *Ap. J.* **335**, L23.
- d'Hendecourt, L. B. and Léger, A. 1987, in *Polycyclic Aromatic Hydrocarbons and Astrophysics*, eds. A. Léger, L. d'Hendecourt, and N. Boccara (Dordrecht: Reidel), p. 203.
- Dwek, E., Sellgren, K., Soifer, B. T., and Werner, M. W. 1980, *Ap. J.*, **238**, 140.
- Duley, W. W. 1985, *M. N. R. A. S.*, **215**, 259.
- Duley, W. W. 1987, in *Polycyclic Aromatic Hydrocarbons and Astrophysics*, eds. A. Léger, L. d'Hendecourt, and N. Boccara (Dordrecht: Reidel), p. 373.
- Dyck, H. M. 1987, in *Late Stages of Stellar Evolution*, ed. by S. Kwok and S. R. Pottasch (Dordrecht: Reidel), 19.
- Elias, J. H., Frogel, J. A., Matthews, K., and Neugebauer, G., 1982, *A. J.* **87**, 1029.
- Flower, D. R., and Penn, C. J. 1981, *M. N. R. A. S.*, **194**, 13P.
- Forrest, W. J., Merrill, K. M., Russell, R. W., and Soifer, B. T. 1975, *Ap. J.*, **199**, L181.
- Forrest, W. J., Houck, J. R., and McCarthy, J. F. 1981, *Ap. J.*, **248**, 195.
- Fowler, A. M., and Joyce, R. R. 1990, *Proc. SPIE Vol. 1235 Instrumentation in Astronomy VII*, ed. by D. L. Crawford, (Bellingham: SPIE), 151.
- Frenklach, M., and Feigelson, E. D. 1989, *Ap. J.*, **341**, 372.
- Frenklach, M., Carmer, C. S., and Feigelson, E. D. 1989, *Nature*, **339**, 196.
- Gathier, R., Pottasch, S. R., and Goss, W. M. 1986, *Astron. Astrophys.*, **157**, 191.
- Gatley, I., DePoy, D. L., and Fowler, A. M. 1988, *Science*, **242**, 1264.

- Gehrz, R. D. 1972, *Ap. J.* **178**, 715.
- Gezari, D. Y., Foltz, W. C., Woods, L. A., and Woodbridge, J. B. 1988, *Proc. SPIE*, **973**.
- Gezari, D. Y., Foltz, W. C., Woods, L. A., and Varosi, F. 1991, *submitted to Optical Engineering*.
- Gillett, F. C., Low, F. J., and Stein, W. A. 1967, *Ap. J. (Letters)*, **149**, L97.
- Gillett, F. C., and Stein, W. A. 1969, *Ap. J. (Letters)*, **155**, L97.
- Gillett, F. C., Forrest, W. J. and Merrill, K. M. 1973, *Ap. J.*, **183**, 87.
- Goebel, J. H., and Moseley, H. 1985, *Ap. J.*, **290**, L35.
- Gottlieb, E. W., and Liller, W. 1976, *Ap. J.*, **207**, L135.
- Hackwell, J. A., and Gehrz, R. D. 1974, *Ap. J.*, **194**, 49.
- Hanner, M. S., Tokunaga, A. T., Veeder, G. J., and A'Hearn, M. F. 1984, *A. J.* **89**, 162.
- Heiligman, G. M., Berge, G. L., Claussen, M. J., Leighton, R. B., Lo, K. Y., Masson, C. R., Moffet, A. T., Phillips, T. G., Sargent, A. I., Scott, S. L., Scoville, N. Z., Wannier, P. G., and Woody, D. P. 1986, *Ap. J.*, **308**, 306.
- Hildebrand, R. H. 1983, *Q. J. R. A. S.*, **24**, 267.
- Ho, P. T. P., Turner, J. L., Fazio, G. G., and Willner, S. P. 1989, *Ap. J.* **344**, 135.
- Hoare, M. G., 1990, *M. N. R. A. S.*, **244**, 193.
- Hoffmann, W. F., Fazio, G. G., Tresch-Fienberg, R. M., Deutsch, L. K., Gezari, D. Y., Lamb, G. M., Shu, P. K., and McCreight, C. R., 1987, in *Infrared Astronomy with Arrays*, ed. C. G. Wynn-Williams and E. E. Becklin (Honolulu: University of Hawaii), p. 241.
- Hora, J. L., Deutsch, L. K., Hoffmann, W. F., and Fazio, G. G. 1990, *Ap. J.*, **353**, 549.

- Humphreys, R. M., Warner, J. W., and Gallagher, J. S. 1976, *Publ. Astr. Soc. Pacif.*, **88**, 380.
- Icke, V., Preston, H.L., and Balick, B. 1989, *A. J.*, **97**, 462.
- Jay, D., Tresch-Fienberg, R., Fazio, G. G., Gezari, D. Y., Hoffmann, W. F., Lamb, G. M., Shu, P. K., and McCreight, C. R. 1989, *A. J.*, **97**, 809.
- Kaler, J. B., and Jacoby, G. H. 1991, *Ap. J.*, **372**, 215.
- Kawabe, R., Ishiguro, M., Kasuga, T., Morita, K.-I., Ukita, N., Kobayashi, H., Okumura, S., Fomalont, E., and Kaifu, N. 1987, *Ap. J.*, **314**, 322.
- Keto, E., Jernigan, G., Ball, R., Arens, J., and Meixner, M. 1991a, *Ap. J. (Letters)*, **374**, L29.
- Keto, E., Ball, R., Arens, J.F., Jernigan, G., and Meixner, M. 1991b, *Appl. Optics*, submitted.
- Khromov, G. S. 1974, *Sov. Ast.*, **19**, 195.
- Kohoutek, L., and Surdej, J. 1980, *Astron. Astrophys.*, **85**, 161.
- Kohoutek, L. 1989, in *I.A.U. Symposium 131, Planetary Nebulae*, ed. S. Torres-Peimbert (Dordrecht: Kluwer Academic Publishers), p. 29.
- Kohoutek, L., and Surdej, J. 1980, *Astron. Astrophys.*, **85**, 161.
- Knapp, G. R., Phillips, T. G., Leighton, R. B., Lo, K. Y., Wannier, P. G., and Wooten, H. A. 1982, *Ap. J.*, **252**, 616.
- Knapp, G. R., Rauch, K. P., and Wilcots, E. M. 1990, in *The Evolution of the Interstellar Medium*, ed. Leo Blitz (San Francisco: Astronomical Society of the Pacific), 151.
- Kwok, S., Purton, C. R., Matthews, H. E., and Spoelstra, T. A. T. 1985, *Astron. Astrophys.*, **144**, 321.
- Kwok, S., Hrivnak, B. J., and Milone, E. F. 1986, *Ap. J.*, **303**, 451.

- Léger, A., and Puget, J. L. 1984, *Astron. Astrophys.*, **137**, L5.
- Lenzuni, P., Natta, A. and Panagia, N. 1989, *Ap. J.*, **345**, 306.
- Lester, D. F., and Dinerstein, H. L. 1984, *Ap. J.*, **281**, L67.
- Livio, M., Salzman, J., and Shaviv, G. 1979, *M. N. R. A. S.*, **188**, 1.
- Louise, R., Macron, A., Pascoli, G., and Maurice, E., 1987, *Astron. Astrophys. Supp. Ser.* **70**, 201.
- Martin, W. 1987, *Astron. Astrophys.*, **182**, 290.
- Masson, C. R. 1989, *Ap. J.*, **346**, 243.
- McCaughrean, M., and Gezari, D. 1991, in *Astrophysics with Infrared Arrays*, ed. R. Elston (San Francisco: Astronomical Society of the Pacific), 301.
- Méndez, R. H., Kudritzki, R. P., Herrero, A., Husfeld, D. and Groth, H. G. 1988, *Astron. Astrophys.*, **190**, 113.
- Merrill, K. M, and Stein, W. A. 1976, *Publ. Astr. Soc. Pacif.*, **88**, 285.
- Monk, D. J., Barlow, M. J., and Clegg, R. E. S. 1989, in *I.A.U. Symposium 131, Planetary Nebulae*, ed. S. Torres-Peimbert (Dordrecht: Kluwer Academic Publishers), p. 197.
- Morris, M. 1981, *Ap. J.*, **249**, 572.
- Moseley, H. 1980, *Ap. J.*, **238**, 892.
- Natta, A., and Panagia, N. 1976, *Ap. J.*, **248**, 189.
- Ney, E. P., Merrill, K. M., Becklin, E. E., Neugebauer, G., and Wynn-Williams, C. G. 1975, *Ap. J. (Letters)*, **198**, L129.
- Nguyen-Quang-Rieu, Winnberg, A., and Bujarrabal, V. 1986, *Astron. Astrophys.*, **165**, 204.

- Nishimura, T., Low, F. J., and Shivanandan, K. 1984, in *The Ninth International Conference on Infrared and Millimeter Waves*, Takarazuka, Japan, October 22-26.
- Nishimura, T., Low, F. J., and Shivanandan, K. 1985, in *IEEE Transactions on Magnetism*, **MAG-21**, 451.
- Odenwald, S., Shivanandan, K., and Thronson, H. 1991, preprint.
- Osterbrock, D. E. 1989, *Astrophysics of Gaseous Nebulae and Active Galactic Nuclei* (Mill Valley, University Science Books).
- Phillips, J. P., Sanchez Magro, C., and Martinez Roger, C., 1984, *Astron. Astrophys.* **133**, 395.
- Phillips, J. P., Mampaso, A., Vilchez, J. M., and Gomez, P., 1986, *Astrophys. Space Sci.* **122**, 81.
- Pottasch, S. R. 1983, in *IAU Symp. No. 103, Planetary Nebulae*, ed. by D. R. Flower (Dordrecht: Reidel), 391.
- Pottasch, S. R. 1984, *Planetary Nebulae* (Dordrecht: Reidel).
- Pottasch, S. R., Preite-Martinez, A., Olon, F. M., Mo Jing-Er, and Kingma, S. 1986, *Astron. Astrophys.*, **161**, 363.
- Puetter, R., Jones, B., and Pina, R. 1990, "*Final Report: NAG 2-580 'Low Background Array Testing'*".
- Pwa, R., Pottasch, S. R., and Mo Jing-Er 1986, *Astron. Astrophys.*, **164**, 184.
- Reay, N. K., Atherton, P. D., and Taylor, K. 1983, *M. N. R. A. S.*, **203**, 1087.
- Reay, N. K., and Worswick, S. P., 1979, *Astron. Astrophys.* **72**, 31.
- Rieke, G. H., Lebofsky, M. J., Thompson, R. I., Low, F. J., and Tokunaga, A. T. 1980, *Ap. J.*, **238**, 24.
- Rieke, M. J., Rieke, G. H., and Montgomery, E. F. 1987, in *Infrared Astronomy with Arrays*, ed. C. G. Wynn-Williams and E. E. Becklin (Honolulu:

- University of Hawaii), p. 213.
- Roche, P. F. 1987, in *Polycyclic Aromatic Hydrocarbons and Astrophysics*, eds. A. Léger, L. d'Hendecourt, and N. Boccarda (Dordrecht: Reidel), p. 307.
- Roche, P. F. 1989, in *I.A.U. Symposium 131, Planetary Nebulae*, ed. S. Torres-Peimbert (Dordrecht: Kluwer Academic Publishers), p. 117.
- Russell, R. W., Soifer, B. T., and Merrill, K. M. 1977, *Ap. J.*, **213**, 66.
- Sakata, A., Wade, S., Onaka, T., and Tokunaga, A. 1987, *Ap. J. (Letters)*, **320**, L63.
- Salpeter, E. E. 1974, *Ap. J.*, **193**, 579.
- Seab, C. G. 1988, in *Dust in the Universe*, eds. M. E. Bailey and D. A. Williams, (Cambridge: Cambridge University Press), 303.
- Schmidt, G. D., and Cohen, M. 1981, *Ap. J.*, **246**, 444.
- Schönberner, D. 1987, in *Planetary and Proto-Planetary Nebulae: From IRAS to ISO*, ed. by A. P. Martinez (Dordrecht: Reidel), 113.
- Smith, M. G., Geballe, T. R., Aspin, C. McLean, I. S., and Roche, P. F. 1989, in *I.A.U. Symposium 131, Planetary Nebulae*, ed. S. Torres-Peimbert (Dordrecht: Kluwer Academic Publishers), 178.
- Soker, N., and Livio, M. 1989, *Ap. J.*, **339**, 268.
- Stephens, J. R. 1980, *Ap. J.*, **237**, 450.
- Stetson, S. B., Reynolds, D. B., Stapelbroek, M. G., and Stermer, R. L. 1986, *SPIE vol. 686 Infrared Detectors, Sensors, and Focal Plane Arrays*, 48.
- Taylor, A. R., and Pottasch, S. R., 1987, *Astron. Astrophys.* **176**, L5.
- Taylor, A. R., Pottasch, S. R., and Zhang, C. Y. 1987, *Astron. Astrophys.*, **171**, 178.
- Taylor, A. R., Gussie, G. T., and Pottasch, S. R., 1990, *Ap. J.* **351**, 515.

- Telesco, C. M., Joy, M., and Sisk, C. 1990, *Ap. J. (Letters)*, **358**, L17.
- Terzian, Y. 1978, in *I.A.U. Symp. #76 Planetary Nebulae Observations and Theory*, ed. by Y. Terzian (Dordrecht: Reidel), p. 115.
- Thronson, H. A. 1982, *A. J.*, **87**, 1207.
- Tielens, A.G.G.M., Allamandola, L. J., Barker, J. R., and Cohen, M. 1987, in *Polycyclic Aromatic Hydrocarbons and Astrophysics*, eds. A. Léger, L. d'Hendecourt, and N. Boccarda (Dordrecht: Reidel), p. 273.
- Torres-Peimbert, S., and Pena, M. 1981, *Rev. Mex. Astron. Astrof.*, **6**, 301.
- Treffers, R., and Cohen, M. 1974, *Ap. J.*, **188**, 545.
- Tresch-Fienberg, R. M 1985, *Ph. D. Thesis*, Harvard.
- Tresch-Fienberg, R. M., Fazio, G. G., Gezari, D. Y., Hoffmann, W. F., Lamb, G. M., Shu, P. K., and McCreight, C. R. 1987, *Ap. J.*, **312**, 542.
- van den Bergh, S. 1974, *Astron. Astrophys.*, **32**, 351.
- Volk, K., and Cohen, M. 1990, *A. J.*, **100**, 485.
- Walsh, J. R. 1981, *M. N. R. A. S.*, **194**, 903.
- Walton, N. A., Pottasch, S. R., Reay, N. K., and Spoelstra, T. 1989, in *I.A.U. Symposium 131, Planetary Nebulae*, ed. S. Torres-Peimbert (Dordrecht: Kluwer Academic Publishers), 301.
- Whitelock, P. 1985, *M. N. R. A. S.*, **213**, 59.
- Willner, S. P., Becklin, E. E., and Visvanathan, N. 1972, *Ap. J.*, **175**, 699.
- Willner, S. P., Jones, B., Puetter, R. C., Russell, R. W., and Soifer, B. T. 1979, *Ap. J.*, **234**, 496.
- Woolf, N. J. 1969, *Ap. J. (Letters)*, **157**, L37.
- Zhang, C. Y., and Kwok, S. 1991, submitted to *Ap. J.*

Zuckerman, B. 1978, in *I.A.U. Symp. #76 Planetary Nebulae Observations and Theory*, ed. by Y. Terzian (Dordrecht: Reidel), p. 305.

Zuckerman, B., and Aller, L. H. 1986, *Ap. J.*, **301**, 772.

Zuckerman, B., and Gatley, I. 1988, *Ap. J.*, **324**, 501.